The Phase Dependent Optoelectronic Properties of Ternary I-III-VI_2 Semiconductor Nanocrystals and Their Synthesis

By

Alice Dorinda Penrice Leach

Dissertation
Submitted to the Faculty of the
Graduate School of Vanderbilt University
in partial fulfillment of the requirements
for the degree of

DOCTOR OF PHILOSOPHY
in
Interdisciplinary Materials Science
May, 2017
Nashville, Tennessee

Approved:

Janet E. Macdonald, Ph.D.
Richard F. Haglund, Ph.D.
D. Greg Walker, Ph.D.
James E. Wittig, Ph.D.
David W. Wright, Ph.D.

DEDICATION

"I'd far rather be happy than right any day." — Douglas Adams

To my friends and family who have made the last four years the happiest of my life.

ACKNOWLEDGEMENTS

This work was supported financially by the IMS program at Vanderbilt University, NSF Career Award Sus-ChEM-1235105, and the U.S.-Israel Binational Science Foundation grant number 2012276. Portions of this work were performed at the Vanderbilt Institute of Nanoscale Science and Engineering, using facilities renovated under TN-SCORE (DMR 0907619) and NSF EPS-1004083. Computational resources were provided by the National Science Foundation through XSEDE resources under grant numbers TG-CHE150005 and TG-DMR130121. Financial support for travel to academic conferences to present the research described in this dissertation was provided by the Graduate School at Vanderbilt.

Graduate work can be an incredibly isolating experience, I am fortunate that my time at Vanderbilt has been just the opposite, filled with joy by friends, colleagues, and family.

Janet, your kindness, curiosity, and boundless enthusiasm have shown me what it is to be a mentor. Thank you for giving me the chance to work in your lab and guiding me on this journey. You have kept my feet on the ground and my head in the clouds, the perfect balance for graduate school. It has been a privilege working with you and I am proud to be your number three. I would also like to thank the members of my committee Dr. Richard Haglund, Dr. Greg Walker, Dr. James Wittig, and Dr. David Wright for their support, guidance and the delicious snacks.

To the Macdonald group, you have made my PhD an unforgettable experience, I will miss you all enormously. To my fluffy friends Manuel, Alyce, Ron, Arnie, and Grand Moff Tarkin thank you for always being there when I needed you. Mike, my brewing buddy, couldn't have done it without you. Shane, thank you for being so kind, welcoming, and guiding me through my first rotation. Elijah is so lucky to have you as a father. Evan, you are such a great

role model not only as a PhD student, but as a scientist and husband, don't work too hard. Jordan, you may be low key, but your science definitely isn't. I look forward to seeing all your future achievements. Nikki, you are an incredibly smart, mature, and talented young woman. You also have great taste in music. Good luck with all your future endeavors, I know you will be great no matter which career path you choose. Summer, thanks for showing me there's more to life than just grad school. Suresh, thank you for some insightful discussions, your extensive knowledge of nanocrystals is impressive. Emil, we only met recently, but working with you remotely and in person was a real pleasure, look forward to seeing you at more races over the summer. Stephanie, you deserve every success, never forget that. Also call me anytime and we can hit up Hattie B's. Andrew, the marathon we experienced together was more than just that run. You are such a kind, loving and generous man, and I hope that the future brings you nothing but happiness. Bryson, our time together was too short, but you made my first couple of years here the best! Laura, your energy and passion carried me through some difficult research days, Georgia Tech is so lucky to have you. This work could not have been completed without assistance from undergraduate and rotation students including Matthew, Nazharie, Margaret, and Cara, thank you all for making my job so enjoyable.

Thank you also to Dr. Uri Banin and his group at the Hebrew University of Jerusalem, especially Adam, Yehonadav, Yorai, Kathy, Shira, Orian, and Itzik for teaching me so much and for being so kind during my visits. To Dr. Xiao Shen, your patience and mentorship taught this experimentalist to understand computational chemistry, a vital part of this dissertation. Thank you Dr. Pantelides for encouraging Xiao and now Andy to work with the Macdonald lab. This collaboration has been invaluable to our research. Andy, thank you for all the advice regarding

calculations and beer. I look forward to continuing to work with you on the computer stuff. Jeremy, thank you for teaching me to love the Scintag.

To the VINSE staff and community, thank you for your constant support, helpful advice, and valuable collaboration. Particularly, Dr. James McBride for your endless patience and assistance with the TEM; Dr. Anthony Hmelo for your wisdom and assistance with the XRD; Dr. Dmitry Koktysh for your assistance with the fluorimeter; and Dr. Kurt Heinrich for giving me a chance. I cannot wait to join the team.

To my materials science family, thank you for making Nashville my home away from home. Sarah, you take such good care of all of us, I would not have made it through even the first semester without you. Alisha, thanks for all the cookies and caffeine. They fueled this dissertation. Claire, thanks for being a great roommate, friend and running buddy. Thank you also for introducing me to the joy of dance. Kristin, thank you for offering me a place to live, I would probably not be at Vanderbilt if it weren't for you. Matt, Kevin, and Keith, I am so lucky to have joined the program at the same time as you. Thanks for all the great food, great beers, and great conversation. Robin, thank you for your wise words and unwavering support, I am proud to call you my friend. To all the rest of my friends and colleagues in the IMS program and beyond, it was a real pleasure spending my time in Nashville with you.

To the tribal council, Danielle and Alex, I am so lucky to call you my best friends. Your wisdom, honesty, humor, and support have brought me so much happiness and steered me through some challenging times. May there be a thousand more beers and a thousand more runs. Bailey, I can't wait to watch the Kanga grow up and become the wonderful man I know you and Stephen will guide him to be. Stephen, thank you for your friendship and for putting up with us.

To my parents, Beverly and Charles, there is no way in which I can thank you enough. You have shown me that if I work hard, have fun, and be myself, anything is possible. Thank you for your support and guidance in all my endeavors, and most of all for my education. Through your love and sacrifice, I have received a world class education and this is the greatest gift I will ever receive. To my brother Felix, you have always been an inspiration to me. Your support and example have taught me so much about being a good scientist and mentor. To Lindsey and Dexter, without you Nashville would have been a lonely place. Thank you for good concerts, good food, and good advice. To Costy and Car, you are the best friends a girl could ask for. You always believed in me. My only regret is that this PhD led me so far away from you.

Finally, to my partner Bradly, the best thing about graduate school was that it brought you into my life. Thank you for being my rock. I love you.

TABLE OF CONTENTS

Page

LIST OF TABLES

Table Page

LIST OF FIGURES

Figure Page

1. INTRODUCTION

1.1 Introduction to Nanomaterials

As humanity seeks to address global challenges, such as the availability of clean water, the prevention and treatment of disease, and the demand for sustainable energy, the development of new technology has become imperative.[1, 2] One of the primary limitations to the growth of many future technologies is the availability of materials with appropriate properties and performance.[3] The need for superior performance has driven researchers to push the boundaries of existing materials, resulting in the development of new systems that tackle countless global concerns. One of the most promising areas of research is in nanoscale materials. Efforts to synthesize structures with smaller and smaller dimensions are motivated by two principal factors. Firstly, when a material reaches nanometer (nm) length scales, it exhibits unique physical properties with respect to the bulk. In these structures, which can consist of only hundreds to thousands of atoms, quantum mechanical effects start to dominate the bulk properties of a material.[4-8] These new electronic and optical properties are of fundamental interest to the scientific community and can be harnessed in applications. Secondly, the small size of these materials can enhance existing applications. For example, in the microelectronics industry, the reduction in size of transistors, following Moore's law, has allowed computers to significantly increase in processing power, while shrinking in size.[9] In another example, the large surface area of nanomaterials can be used to enhance catalytic activity.[10]

Nanomaterials are typically defined as structures which possess at least one dimension sized from 1 to 100 nm.[11] Both carbon and metal nanostructures have demonstrated exceptional physical properties, and are used extensively in commercial products.[12] 0D, 1D, and 2D carbon

nanomaterials (fullerenes, carbon nanotubes, and graphene, Figure 1.1a) exhibit unique properties, which arise from their small size, dimensionality, and sp^2 hybridized carbon binding.[13] The most common fullerene is Buckminsterfullerene, C_{60}, which consists of twelve pentagonal and twenty hexagonal sp^2 hybridized carbon rings, forming a spheroid shape. The covalent bonds in C_{60} impart high stability to these molecules, thus they can withstand incredibly high pressure and temperature and have been used to strengthen composite materials.[14] Fullerenes are also good electron acceptors, have been used extensively in biomedicine and as n-type semiconductors in organic photovoltaics.[15, 16] Carbon nanotubes have very high electrical conductivity, tensile strength and flexibility; thus they are utilized in consumer products including rechargeable batteries, water filters, automotive parts, and sporting goods.[17] Graphene also possesses unusually high strength and conductivity. It is less available commercially; however, remains an immensely popular field of research with a Nobel Prize awarded in 2010 and €1 billion in research funding pledged by the European Commission in 2013 for the development of graphene.[18, 19] Potential applications for graphene include display screens, electric circuits, solar cells and drug delivery.[20]

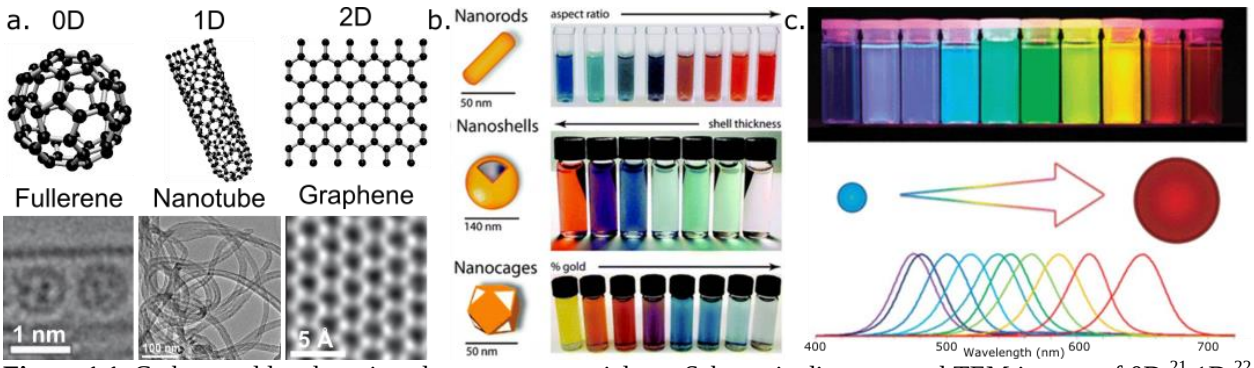

Figure 1.1. Carbon, gold and semiconductor nanomaterials; **a.** Schematic diagrams and TEM images of 0D,[21] 1D,[22] and 2D carbon nanomaterials;[23] **b.** Images showing colloidal gold nanostructures with different structures, and the variety of colors that arise from their surface plasmon resonance modes;[24] and **c.** ZnCdSeS alloyed semiconductor quantum dots with size-tunable light emission and their fluorescence spectra.[25] Reproduced with permission from references 21, 22, 23, 24, and 25 respectively. Copyright 2011 Royal Society of Chemistry, 2006 American Chemical Society, 2011 Nature Publishing Group, 2012 Royal Society of Chemistry, and 2010 Royal Society of Chemistry respectively.

Metallic materials show a number of interesting properties at the nanoscale.[26] Perhaps the most well-known phenomena are the bright colors of metallic nano-colloids, which have been utilized throughout history in the coloring of glass. Copper, silver, and gold nanoparticles have been identified in glass dating from as early as the Bronze Age (1000 BCE).[27] The bright colors observed from these nanoparticles are the result of a surface plasmon resonance: an oscillation of free electrons that is a consequence of the formation of a dipole in the particle due to electromagnetic waves.[28] This leads to strong electromagnetic fields at the particle surfaces and consequently enhances all radiative properties such as absorption and scattering. As such, while bulk gold is a yellow, non-magnetic, inert metal, gold nanoparticles are red/ pink in color, catalytic, insulating, and magnetic.[29] The wavelengths of light scattered and absorbed and thus the color of the particles can be tuned by changing their size and morphology (Figure 1.1b). Additionally, the strongly absorbed light is converted to heat quickly via a series of nonradiative processes. This heat can be harnessed for use in photothermal applications.[30] Amongst other applications, engineered gold nanoparticles are used in nanoelectromechanical systems, bioengineering, electronic textiles, and nonlinear optics.[31] Nanoscale silver also exhibits plasmonic properties, but is primarily used for its antimicrobial properties. Silver nanoparticles have been incorporated into wound dressings, clothing, food packaging, and surgical tools, as a biocide.[32] Both gold and silver nanoparticles are also widely used as catalysts in organic transformations, due to their high activity under mild conditions, and large surface area to volume ratio with respect to the bulk noble metals.[33, 34] Another useful catalytic metal is platinum, which is regularly utilized in the automobile and petroleum industries.[35] Due to its high cost, platinum metal is often finely divided to increase the catalytic surface area. This has

resulted in the well-known material platinum black (particle size ~ 20 μm) and platinum nanopowders (particle size ~ 200 nm), which are widely used in catalysis.

The focus of this dissertation will be semiconductor nanomaterials. They are made from a variety of different compounds and referred to as IV, II-VI, III-V or IV-VI, based on the periodic table groups into which these elements are formed. For example, Si is group IV; GaN is III-V; while CdS, CdSe and CdTe are II-VI semiconductors. Semiconductor nanomaterials are perhaps most well-known for their use in the microelectronics industry, in which devices are frequently manufactured with feature sizes at the nanoscale.[36] Interestingly, in this case, manufacturers are only leveraging the size of these devices; a microscale transistor does not behave in a manner significantly different to a nanoscale one. However, in other applications, semiconductor nanomaterials are synthesized for their unique physical properties. At the nanoscale, semiconductors can be isolated in structures and morphologies not found in the bulk.[37] Furthermore, once the semiconductor is smaller than a critical size, known as the Bohr exciton radius, it begins to exhibit quantum mechanical effects. Briefly, if charge carriers (electrons and holes) are confined to a length shorter than their characteristic bound length (the Bohr exciton radius, typically 2 - 10 nm), the valence and conduction band shift away from their bulk values, and the characteristic band gap of the material increases. As such, nanocrystals of the same material with different sizes absorb and emit light of different energies (Figure 1.1c). Furthermore, spatial confinement of the exciton (electron-hole pair) results in strong overlap between the electron and hole wave functions. This increases the probability of radiative recombination, resulting in exceptionally high quantum yield of emission.[4-8] A more detailed explanation of this phenomenon can be found in Section 2.2.1. Due to these properties,

semiconductor nanomaterials have attracted significant attention in research areas including energy conversion, sensing, electronics, photonics, and biomedicine.[38]

Traditionally, the fabrication of semiconductor materials utilizes growth substrates and ultra-high vacuum (UHV) conditions. These techniques can be used for the growth of nanocrystals, through the Stranski-Krastanov method, but the resulting particles are trapped in, or on, a solid state matrix.[39-41] In contrast, colloidal semiconductor nanocrystals (NCs) are grown in solution, resulting in free particles. They also have relatively low-cost, high-yield syntheses with exquisite control over the composition, size, shape, and crystal structure of the product.[42] Thus they are an excellent medium in which to study the fundamental properties of nanoscale semiconductors. This dissertation focuses on the syntheses and properties of a specific class of NCs with composition I-III-VI_2.

1.2 Research Motivation

NCs have quickly become one of the most versatile systems for studying the fundamental properties of nanoscale materials and for use in applications. They have been synthesized with control over size, composition, and morphology, allowing the elucidation of remarkable properties. For example, the unique surface chemistry of small colloidal CdSe nanocrystals causes the emission of white-light. Two fluorescence bands, one from the band edge and another at lower energy that originates from recombination at surface defects, combine to result in this broad emission, which can be exploited in solid-state lighting.[43]

Furthermore, NCs can act as artificial atoms, becoming the building blocks for new materials. The bottom-up self-assembly of NCs is a facile and flexible approach to superlattice formation.[44] While the mechanisms of self-assembly have yet to be completely understood, this technique has been leveraged to create NC superlattices with an array of unique, tunable

properties. Superlattices with enhanced optical,[45] electronic,[46] and magnetic[47] properties have already been demonstrated, suggesting that NC assembly could be an important tool in the development of next generation materials.

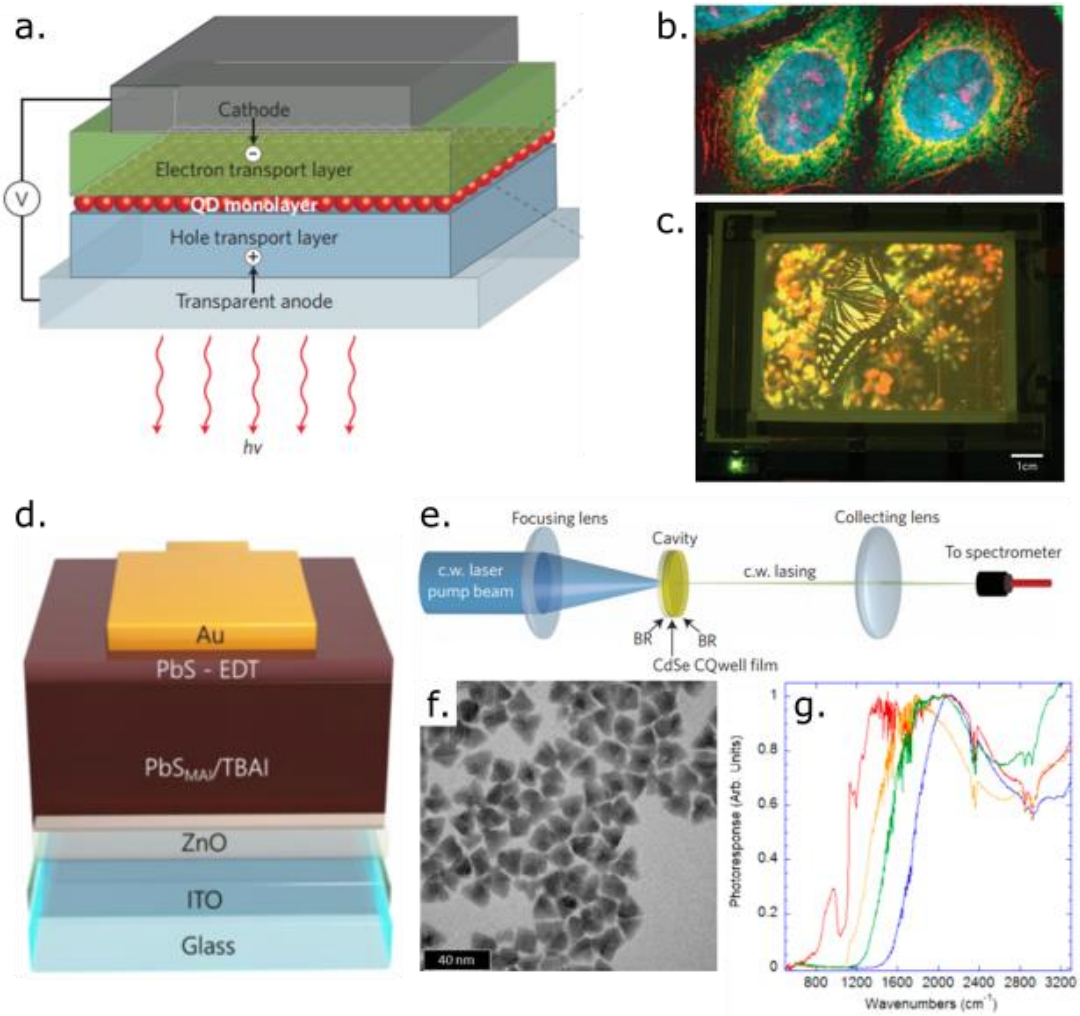

Figure 1.2. Applications of colloidal semiconductor nanocrystals; **a.** Schematic diagram of a prototypical QD-LED structure, comprising a monolayer of QDs sandwiched between an organic hole-transport layer and an organic electron-transport layer.[48] Reproduced with permission from reference 48. Copyright 2013 Nature Publishing Group; **b.** Pseudocolored image of five color quantum dot staining of human epithelial cells.[49] Quantum dots with emission at 705 nm, 655 nm, 605 nm, 565 nm, and 525 nm were used. Reproduced with permission from reference 49. Copyright 2005 Nature Publishing Group; **c.** Image of a 4-inch full-color QD display.[50] Reproduced with permission from reference 50. Copyright 2011 Nature Publishing Group; **d.** Schematic diagram of PbS quantum dot solar cell with record efficiency.[51] Reproduced with permission from reference 51. Copyright 2016 American Chemical Society; **e.** Schematic of a CdSe nanocrystal laser cavity.[52] Reproduced with permission from reference 52. Copyright 2014 Nature Publishing Group; **f.**TEM image and **g.** photocurrent response of thin films of HgTe quantum dots.[53] Reproduced with permission from reference 53. Copyright 2014 American Chemical Society.

NC self-assembly broadens the scope of a field already rich in applications. The high quantum yield and color purity of NC emission has led to their use in light-emitting diodes

(Figure 1.2a),[48] and as fluorescent labels in bio imaging (Figure 1.2b).[49] This property has also been exploited commercially with NCs used to produce displays with enhanced color (Figure **1.2**c).[50]

The Macdonald lab at Vanderbilt University is primarily focused on the use of NCs for capturing solar energy. This application exploits the high molar absorptivity and tunable band gap of NCs, which can be utilized in both photovoltaic and photocatalytic devices. In photovoltaics, NCs can be used as the light absorbing medium and are combined with a p-n junction and electrodes to produce a device. Record efficiencies of 10.6% have been achieved using PbS NCs in a solid-state device (Figure 1.2d.).[51] In photocatalysis, NCs are used to convert light energy to chemical energy. One of the most widely investigated catalytic applications for NCs is photochemical water splitting. Here, light absorbed by the NC results in the generation of electron-hole pairs. The photogenerated charges are then used to oxidize and reduce the constituent ions of water to oxygen and hydrogen respectively. 100% photon-to-hydrogen production efficiency has been achieved for Pt-tipped CdSe/CdS nanorods,[54] however, efficient removal of holes from the catalyst is currently a limiting factor. This barrier must be overcome to realize the complete splitting of water by NC photocatalysts.

More recently, NCs have found application in optics with NC lasers and photodetectors demonstrated. NCs are an attractive lasing medium due to their near-unity emission efficiencies, and narrow emission lines. Continuous-wave stimulated emission and lasing has been achieved in CdSe NC solids (Figure 1.2e).[52, 55] NCs can also be used to detect light. In fact, the use of NCs in infrared photodetectors represents a promising alternative to existing high-cost semiconductor technologies.[56] HgTe NC films have been produced with efficient photoconductivity in the mid-

wave and long-wave infrared spectral regions (Figure 1.2f-g).[53, 57] Currently work is focused on improving the infrared detectivity of devices.

Research has also been focused on extending the use of NCs in biomedicine. While more commonly used in cell-labeling and fluorescent imaging, NCs have recently been utilized in theranostics. Here, NCs are used as a platform that combines medical analysis with therapy. For example, with appropriate functionality, super-paramagnetic iron oxide NCs can be used as contrast agents for MRI (*e.g.* to indicate the presence of tumors). Additionally, upon irradiation, these NCs can be used to produce heat locally, destroying tumor tissue by hyperthermia.[58]

Scientists have barely scratched the surface of NC potential. Since the discovery of NCs in the 1980s, huge advances have been made in their synthesis and understanding, but at this stage fundamental research has primarily been focused on II-VI systems, in particular the heavy metal Cd-, Hg- and Pb-based chalcogenides. The commercial use of these well understood and promising NC materials could well be restricted due to the toxicity of the constituent elements. Furthermore, while the II-VI systems are well suited to certain applications (*e.g.* CdSe in display technology, and PbS in quantum dot sensitized solar cells), in others their properties are far from ideal. For example, in solar concentrators, higher efficiency is achieved when utilizing NCs with a large Stokes shift of emission to minimize reabsorption losses. Likewise, in deep tissue imaging, low toxicity NCs with tunable emission in the infrared spectral region are preferred. Therefore, researchers seek to expand the database of NCs across a broad range of semiconductor materials. Without the development of synthetic processes that produce uniform product NCs composed of these materials, a good understanding of their properties cannot be developed. Furthermore, without a complete understanding of the properties of each system at the nanoscale, their full potential in application cannot be realized.

The work in this dissertation serves not only to expand our library of NC materials to include new ternary I-III-VI_2 systems, but also develops our understanding of existing I-III-VI_2 NCs, which can inform refinements in their synthesis and cultivate their use in application.

1.3 Dissertation Outline

This thesis focuses on the synthesis and fundamental properties of ternary I-III-VI_2 semiconductor nanocrystals with metastable, anisotropic crystal structures. In Chapter 2, a brief overview of nanocrystal syntheses, properties and structures will be given. In Chapter 3, existing knowledge of the I-III-VI_2 materials of interest is summarized. In particular, the nanoscale syntheses and properties of these materials are discussed. In Chapters 4 and 5, a direct synthesis to luminescent, wurtzite $CuInS_2$ NCs is described. The mechanism behind the formation of the NCs is elucidated (Chapter 4) and the origin of their near-infrared luminescence is considered (Chapter 5). In Chapter 6, hybrid NCs of wurtzite $CuInS_2$ with Pt and Pd are synthesized, characterized, and their photoelectrical properties are studied. The study of the wurtzite structure is extended in Chapter 7 to include $CuFeS_2$ NCs. Finally, in Chapter 8 progress towards the synthesis of pseudo-wurtzite, orthorhombic $AgFeS_2$ NCs is detailed. This is the first time this metastable structure of $AgFeS_2$ has been observed. Additionally, the optical properties of the $CuFeS_2$ (Chapter 7) and $AgFeS_2$ (Chapter 8) systems are investigated and their dependence on NC composition noted.

2. COLLOIDAL SEMICONDUCTOR NANOCRYSTALS

Whilst thermodynamically stable colloidal nanoparticles, most notably colloidal gold, have been known since ancient times, modern scientific evaluation of nanoparticle solutions did not begin until the 19th century when Faraday investigated the optical properties of colloidal gold.[59] The study of colloidal semiconductor nanocrystals (NCs) began in earnest in the early 1980s, when size dependent behavior was observed in CdS NCs by Brus and the term 'quantum dots' was coined to describe confined NCs.[4-8] Since then, NCs have become one of the most versatile nanomaterials, due to the superb synthetic control that has been demonstrated over their composition and morphology[42] and their unsupported colloidal state. NCs are composed of a small inorganic semiconductor core (1-100 nm) surrounded by a layer of organic passivating ligands (Figure 2.1a). This corona of ligand molecules can be tuned to give the NCs solubility in a wide range of solvents, allowing them to be integrated into matrices or deposited on surfaces with ease.[60]

2.1 Nanocrystal Synthesis

Several synthetic strategies have been developed to produce high quality NCs, including hot-injection,[61] heat-up,[62] cation exchange,[63] and seeded growth methods.[64, 65] Amongst these, the hot-injection technique has been the most widely explored due to its simplicity and versatility. In this method, a cold solution of one ionic precursor is injected into a hot mixture of the coordinating solvent and the other ionic precursor(s). After injection, a burst of nucleation occurs due to the sudden availability of monomers at temperatures high enough to allow the formation of nuclei. As the precursors are consumed, the monomer concentration quickly falls below the nucleation threshold (Section 2.1.1), preventing the formation of additional nuclei. As a result, the remaining monomers only contribute to further growth of the existing nuclei.

Temporal separation between the nucleation and growth stages of particle formation allows the synthesis of NCs with high monodispersity and as a consequence highly uniform optical properties (Section 2.2.1). Heat-up methods have also been used extensively due to the large scale and low batch-to-batch variation attainable in these syntheses.[62] In this technique, all reactants are added to a single vessel and heated to the desired reaction temperature for nucleation and growth. This circumvents the pitfalls of mixing time and poor heat management inherent to hot-injection syntheses. However, in heat-up reactions, the nucleation and growth stages of particle formation can be hard to separate, often resulting in the observation of Ostwald ripening (Section 2.1.2). Therefore, the precursors, stabilizers and heating rates must be carefully selected to ensure that the product NCs are monodisperse.

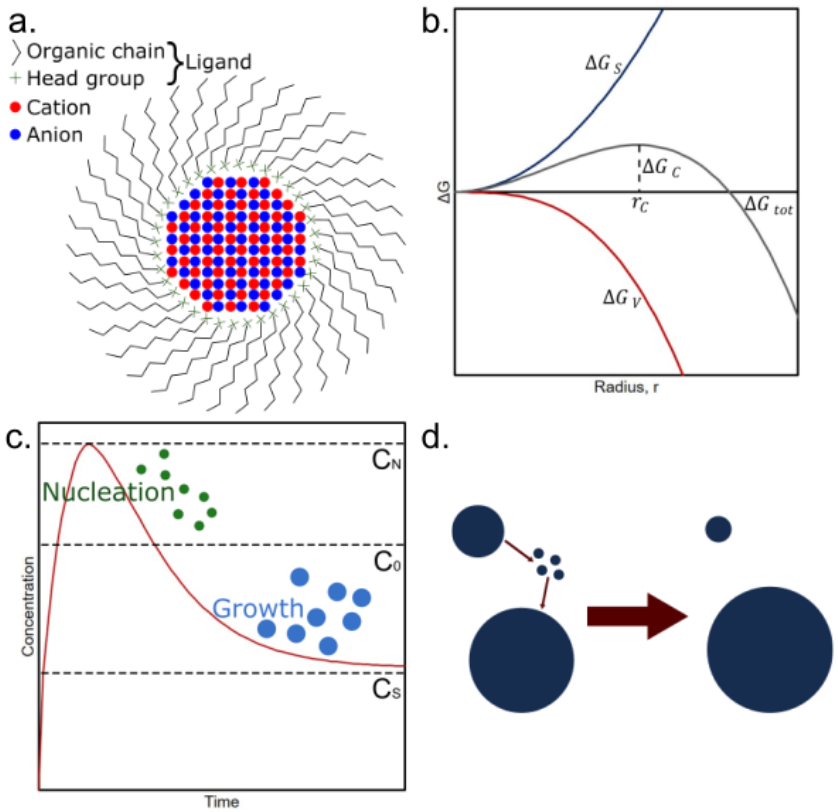

Figure 2.1. Nucleation and growth of semiconductor nanocrystals; **a.** Schematic diagram of a colloidal semiconductor nanocrystal; **b.** Classical nucleation theory shown using a plot of Gibbs free energy against radius of nucleus; **c.** Plot of concentration against time showing the La Mer model for burst nucleation; and **d.** Schematic diagram showing the process of Ostwald ripening.

Careful selection of stabilizers can also allow the synthesis of NCs with unusual morphology. A good example of this lies in the synthesis of anisotropic CdSe nanostructures. Different facets of wurtzite CdSe have different chemistry and, as a result, ligands often bind preferentially to different crystal facets. Phosphonic acid ligands bind preferentially to the non-polar facets, promoting growth in the [001] direction.[66, 67] In contrast, use of oleic acid as the ligand results in the formation of 2D CdSe sheets.[68]

2.1.1 Nucleation Theory

Classical nucleation theory suggests that the total free energy change during crystal formation (ΔG_{tot}) is the sum of two opposing components: the volume free energy of the nuclei (ΔG_V) and the surface free energy between the nuclei and solution (ΔG_S):

$$\Delta G_{tot}(r) = \Delta G_V + \Delta G_S \tag{2.1}$$

with r the radius of the nuclei, $\Delta G_V = \frac{4}{3}\pi r^3 \Delta g_V$ with Δg_V the volume energy of the nuclei (negative), and $\Delta G_S = 4\pi r^2 \gamma$ with γ the surface energy between the particle and the solution (positive).[69] The combination of favorable (ΔG_V) and unfavorable (ΔG_S) processes yields an energy barrier (ΔG_C), which must be overcome for nucleation to occur (Figure 2.1b). This occurs at a critical nuclei radius (r_C), after which growth occurs. When nuclei are smaller than r_C, growth does not occur and the nuclei tend to dissolve. The implication for NC synthesis is that lowering the particle surface energy (γ) allows the stabilization of smaller particles. A common method for achieving this is the use of surfactants that bind tightly to the nanoparticle surface.

The nucleation of crystals can also be related to the concentration of the precursor materials using the La Mer model.[70] In this case, the monomer concentration is increased to supersaturation (C_S); however, a nucleation event does not occur until the minimum

concentration for nucleation (C_0) is reached (Figure 2.1c). At this stage nucleation persists, as the monomer concentration increases until the maximum precursor concentration (C_N) is attained, followed by a decrease in precursor concentration as monomers are consumed. When the concentration falls below (C_0), nucleation stops and further concentration decreases correspond to the growth of existing nuclei. This behavior is frequently observed for hot-injection syntheses and tends to yield homogeneous NC samples, as nucleation occurs quickly allowing more uniform growth to follow.

2.1.2 Ostwald Ripening

Ostwald ripening is a thermodynamically-driven spontaneous process, in which small crystals or particles dissolve and reprecipitate onto the surfaces of larger crystals (Figure 2.1d).[71] The driving force here is the minimization of surface energy. Atoms or ions at the surface of particles are more energetically unstable than those within as they possess unsatisfied bonds. As a result, the system tries to lower its overall energy by minimizing the number of atoms at the particle-solvent interface. The resultant shrinking and growing of particles in solution results in an increase in the particle size distribution, often undesirable in NC synthesis due to the dependence of NC properties on particle size (Section 2.2.1). Ostwald ripening depends on the reversible solubility of the material, thus can only occur under conditions in which small particles are able to dissolve.

2.2 Nanocrystal Properties

At small sizes (1-10 nm), the properties of a semiconductor material change significantly. There are two major factors that influence these unique properties: quantum confinement, and surface effects.

2.2.1 Quantum Confinement

There are two ways to consider the problem of semiconductor confinement. The first approach, known as 'top-down', is to correct the bulk electronic properties of a semiconductor for a finite crystal size. The second, known as 'bottom-up', builds up the optoelectronic properties of the nanocrystal from the atomic orbitals. In this case, the nanocrystal is considered to be a large molecule or cluster.

In the top-down approach, the properties of a bulk semiconductor are first considered. In an unconfined semiconductor, an electron-hole pair is typically bound within a characteristic length called the Bohr exciton diameter. The Bohr exciton radius (a_0) can be calculated using the equation:

$$a_0 = \frac{\hbar^2 \varepsilon}{e^2}\left(\frac{1}{m_e^*} + \frac{1}{m_h^*}\right)$$

where m_e^* and m_h^* are the effective masses of electron and hole, respectively. Further, e is the electron charge and ε is the dielectric constant of the semiconductor. When the size of the semiconductor is smaller than twice this radius (approximately 2 - 20 nm), the charge carriers must exist at a distance closer than their lowest energy state. Increasing the spatial confinement of the exciton increases the energy of the excited state, resulting in a decrease in the wavelength of light absorbed and emitted by the NCs. Furthermore, the resulting system can be described by the particle-in-a-box model and, as a result, its energy levels become discretized. In a complete quantum mechanical treatment of confinement, the Bloch wavefunctions describing the bulk properties of the semiconductor are multiplied by an envelope function to correct for the confinement of electrons and holes (Appendix A). For a NC, the best model for the envelope function is the particle in a sphere. When an additional term is included to account for the

Coulomb interaction between electrons and holes, solution of the Schrodinger equation results in the Brus equation (2.2), which can be used to calculate the emission energy of a confined NC:

$$E_g(r) = E_g^0 + \frac{\hbar^2\pi^2}{2r^2}\left(\frac{1}{m_e^*} + \frac{1}{m_h^*}\right) - \frac{1.786e^2}{4\pi\varepsilon_0\varepsilon_r r} \qquad (2.2)$$

where E_g^0 is the band gap energy of the semiconductor, $\hbar$ is Planck's constant, r is the radius of the nanocrystal, m_e^* and m_h^* are the effective masses of the electron and hole respectively, ε_0 is the permittivity of space, and ε_r is the relative permittivity of the semiconductor.[5, 6]

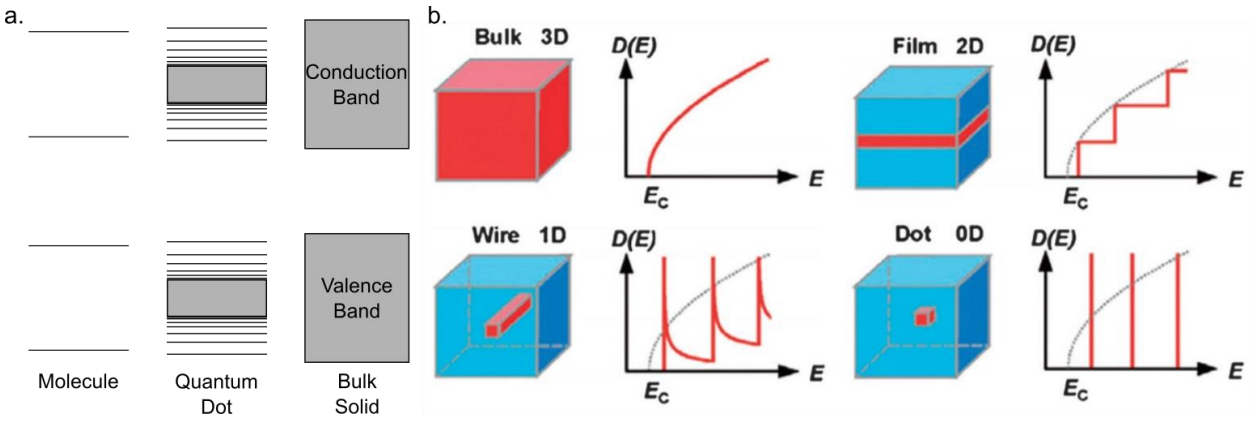

Figure 2.2. Quantum confinement effects; **a.** Energy levels of a molecule, quantum dot, and bulk semiconductor; **b.** Schematic illustration of the quantum confinement effect on the density of states of 3D bulk, 2D quantum well, 1D quantum wire, and 0D quantum dot species.[72] Reproduced with permission form reference 72. Copyright 2012 Royal Society of Chemistry.

The 'bottom-up' approach is based on the linear combination of atomic orbitals (LCAO).[73, 74] This theory suggests that the electron orbitals of a molecule (regions in which a charge carrier is likely to be found) can be determined using a combination of the orbitals of its constituent atoms. These atomic orbitals combine forming bonding and antibonding states at different energies. As more and more atoms are added, more and more energy levels are formed until a bulk system is reached. In the bulk, the separation of energy states is much smaller than the thermal energy so the collection of states is better described as a band (Figure 2.2a). In a semiconductor, the region between the highest occupied band and the lowest unoccupied band

are known as the band gap. A quantum dot contains a number of atoms between those of a molecule and the bulk. From LCAO theory it follows that when fewer atoms are present, fewer atomic orbitals combine and fewer energy states exist. This band-thinning leads to discrete energy levels near the band edges and an increase in the band gap (Figure 2.2a), also known as quantum confinement.

The quantum confinement effect has a strong dependence on the dimensionality of the NCs. The difference between bulk, 2D, 1D and 0D nanomaterials can be understood by considering the density of states (Figure 2.2b). With decreasing dimensionality, the carrier energy distribution changes from a square root dependence, to a step-like dependence, to sharp peaks, and finally to discrete energy levels.[75] This change corresponds to the number of dimensions in which an electron can move freely and the distribution of energies a charge carrier may occupy.

2.2.2 Surface Effects

The small size of colloidal NCs is inherently associated with a large surface area to volume ratio. The characteristics of the surface therefore play a dominant role in the properties of the system. Atoms at the surface of a NC have fewer direct neighbors than atoms in the bulk, resulting in the incomplete satisfaction of their binding orbitals by the crystal. Unbound orbitals are typically satisfied by ligand molecules or the formation of crystalline defects; however, the anisotropy of these features can result in the formation of localized surface states within the band gap. While these additional states can result in interesting properties such as white-light emission or surface magnetization,[76, 77] they can also act as trap states for generated charge carriers. Carrier trapping is detrimental to applications requiring luminescence or charge extraction, due to the reduction in quantum yield (QY) and number of mobile carriers respectively. Considerable

work has been focused on passivating these surface states by both tuning the organic ligand corona,[78] and coating the NC surface with inorganic materials (Section 2.3.2),[79] resulting in improved QY and colloidal stability. However, in order for NCs to meet their full potential in application, a more complete understanding of NC surfaces and their manipulation must be developed.[60]

2.3 Nanocrystal Structures

2.3.1 Crystal Structure

The physical properties of semiconductors originate from their atomic structure (Appendix A). This is of particular importance in nanomaterials, which due to their size can exist as polymorphs not seen in the bulk.[37] The II-VI semiconductors typically exhibit two stable structures, zinc blende (ZB) and wurtzite (WZ) (Figure 2.3). Zinc blende is based on a face-centered cubic lattice of S anions with cations filling half the tetrahedral interstitial sites. Wurtzite is similar, but based on a hexagonal close packed array of anions. An additional cubic structure, chalcopyrite (CP), is observed for the I-III-VI_2 materials, which contains ordered cations.

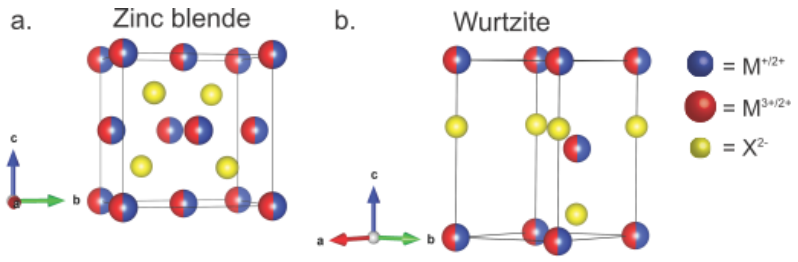

Figure 2.3. Characteristic crystal structures of II-VI semiconductors; **a.** Zinc blende; and **b.** Wurtzite.

The symmetry of a nanomaterial crystal structure can play a significant role in its properties. Firstly, anisotropic phases often promote the formation of NCs with anisotropic morphologies (*e.g.* rods or plates).[80] These 1D and 2D nanostructures are of great interest, as

they still exhibit behavior characteristic of quantum confinement, while maintaining at least one extended dimension in which charge carriers can propagate (Section 2.2.1). Furthermore, structural anisotropy can lead to a difference in the mobility of charge carriers along the lattice axes, promoting orthogonal charge separation.[81] This property is sought after in both photovoltaic and photocatalytic applications for which the recombination of charge carriers is undesirable.

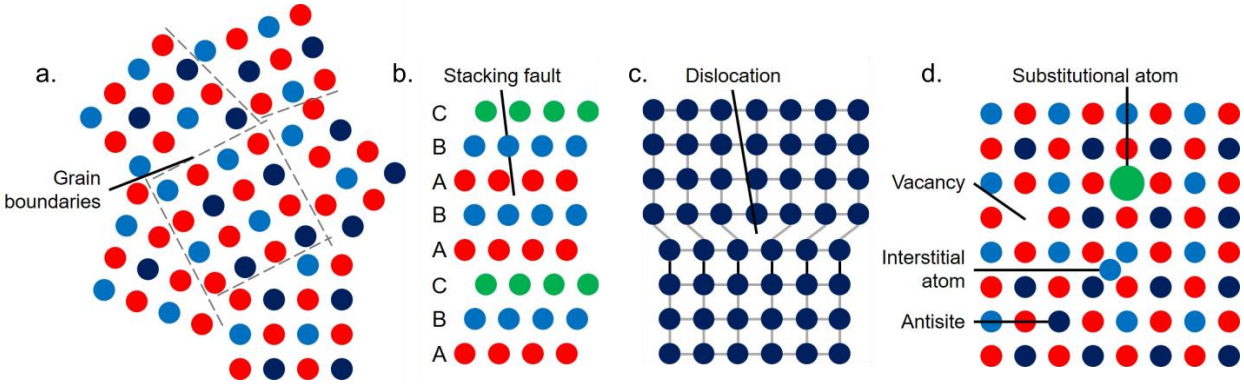

Figure 2.4. Crystallographic defects; **a.** Grain boundaries; **b.** A stacking fault; **c.** A dislocation; and **d.** Point defects.

Crystalline materials typically contain imperfections, known as defects. At the nanoscale, crystals consist of only hundreds or thousands of atoms, thus the defect concentration in a single nanoparticle is often significantly higher than that of the bulk. As such, these defects can have a large impact on the properties of the system. Lattice defects change the local electronic properties of a material. This can result in the formation of energy states within the band gap of the semiconductor. Planar defects (*e.g.* grain boundaries and stacking faults) and line defects (*e.g.* dislocations) are frequently observed in NCs and can be characterized using transmission electron microscopy (TEM) (Figure 2.4a-c).[82-84] These defects can act as carrier traps that introduce non-radiative paths to the system and, therefore, are usually undesirable in NCs. In contrast, point defects often introduce additional radiative decay paths into systems.[85-87] A well-known example of this is ZnO, which possesses a number of intrinsic and extrinsic radiative

defect levels. These levels emit light in a characteristically broad range within the visible region.[87] Point defects occur only at or around a single lattice point. A number of species exist including vacancies, interstitial atoms, substitutional atoms and antisite defects (Figure 2.4d). Vacancies (denoted V_X) are empty lattice sites. Interstitial defects (denoted X_i) are atoms at a position in the crystal lattice that is usually unoccupied. Substitutional atoms (denoted X_Y, atom X at a Y site) occur when an impurity atom sits at a regular site in the lattice. Similarly, antisite defects occur in ordered multinary materials when cations (or anions) of different types exchange positions. For example, in the ternary CP material $CuInS_2$, the antisite defects Cu_{In} and In_{Cu} exist.

Crystal structure can be characterized using X-ray diffraction (XRD). The wavelength of X-rays is of similar magnitude to the interatomic spacing in crystal structures. Therefore, Miller planes of ions in a crystal can act like a diffraction grating. Constructive interference between diffracted X-rays occurs at angles characteristic of a crystal with a certain interplanar spacing according to Bragg's law:

$$n\lambda = 2d \sin\theta \tag{2.3}$$

where n is an integer; λ is the wavelength of the incident radiation; d is the distance between atomic planes; and θ is the angle of incidence. Powder XRD, which is used throughout this thesis, relies on there being a sufficiently large number of crystallites in random orientations such that a portion will always be positioned at appropriate Bragg angles for reflection. The angle at which reflections are observed gives information about the unit cell and therefore the structure of the material. Diffractograms are visually compared to literature data and the International Centre for Diffraction Data (ICDD) database to determine the structure.

The diffractograms of NCs often show significant broadening due to the small crystallite size of the material. Thus it can be difficult to distinguish crystal structure for NCs using only XRD. Consequently, XRD is often used in tandem with other techniques such as high resolution transmission electron microscopy (HRTEM) and selected area electron diffraction (SAED) to determine phase.

When describing the crystal structure of a semiconductor, it is useful to consider the constituents atoms as an arrangement of cations and anions with ionic bonds between them; however, this description fails to define bonding within the system completely. Semiconductors contain mixed covalent-ionic bonding, known also as polar covalent bonding. The percentage of ionic character ($\%_{ionic}$) in a bond between atoms A and B is given by the equation:

$$\%_{ionic} = (1 - e^{-\frac{1}{4}(x_A - x_B)^2}) \times 100 \qquad (2.4)$$

where x_A and x_B are the electronegativities of atoms A and B respectively.

The $\%_{ionic}$ for the bonding in the materials studied in this dissertation are shown in Table 2.1. Values were calculated using equation 2.4 and Pauling electronegativity values reported by Allred *et al.*[88] All have large covalent character. To simplify the explanations of the mechanisms of formation studied here, materials are described throughout as consisting of cations and anions; however, the reader should be aware that binding in these systems is directional and involves the sharing of electrons. The covalent character of binding contributes to the stabilization of crystal structures in the materials studied here that are not seen in the bulk.

Bond	$\%_{ionic}$	$\%_{covalent}$
Cu-S	10.9	89.1
Ag-S	10.0	90.0
In-S	14.8	85.2
Fe-S	13.1	86.9

Table 2.1. Ionic and covalent character of bonds in $CuInS_2$, $CuFeS_2$ and $AgFeS_2$.

2.3.2 Core-Shell Structures

The nano-size of colloidal NCs results in a very high surface area to volume ratio. While this property can be advantageous for catalytic applications, it also results in an unusually large proportion of surface atoms. These atoms are typically passivated via complex formation with organic stabilizing ligands; however, complete satisfaction of the surface atoms is often not possible. Both organically passivated and unpassivated surface atoms can generate trap states within the band gap of the material, yielding fast non-radiative decay paths for photogenerated charge carriers.[60] In order to isolate the exciton from non-radiative relaxation via surface states and improve surface passivation, a layer, or 'shell', of a wider band gap semiconductor material is often grown over the core material (Figure 2.5a). This shell typically serves to increase the stability and QY of NCs. Furthermore appropriate choice of shell material can result in enhanced charge separation and spectral tunability for NC systems.[89]

Core-shell systems are labeled by their architecture and classified by their band alignments.[79] Typically, core-shell systems are reported with the core material first and the shell second, separated by the symbol @ for spherical particles, / for rod-shaped particles, or – for other morphologies (*e.g.* CdSe@CdS, CdSe/CdS, or CdSe-CdS representing a CdSe core with a CdS shell). Three distinct band conditions can be obtained, known as Type I, Reverse Type I, and Type II (Figure 2.5b). Type I systems have a shell material with a larger band gap than that of the core, leading to both electron and hole confinement in the core. These systems are typically used to improve the QY of NCs with the shell physically separating an optically active core from its surrounding medium. The inverse is true for Reverse Type I structures; the band gap of the shell material is smaller than that of the core and, depending on the thickness of the shell, the holes and electrons are partially or completely confined in the shell. This means

emission wavelength can be tuned by varying the shell thickness. However, Reverse Type I systems often suffer from low QY and rapid photobleaching.[90-92] Finally, in Type II systems either the valence band edge or the conduction band edge of the shell material is located within the band gap of the core. These systems are often used to enhance charge separation with one charge carrier localized in the core and the other localized in the shell.[93] Type II systems can also be leveraged to red-shift the emission wavelength of NCs.[89]

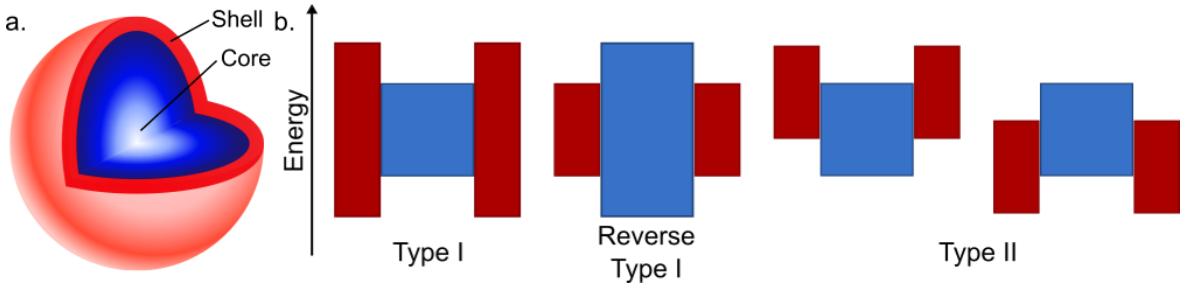

Figure 2.5. Core-shell nanoparticles; **a.** A schematic illustration of a core (blue) – shell (red) nanoparticle; **b.** Three types of core–shell NCs. The upper and lower edges represent the upper and lower energy levels of the core (blue) and the shell (red).

The choice of shell material cannot be based solely on optical properties. Shells often grow epitaxially and thus core and shell materials should crystallize in the same structure and have similar lattice parameters. Selection of a material with a poor lattice match can result in strain and the formation of defects within the shell or at the core-shell interface.[94] As a result of this, the wide band gap semiconductors ZnS (3.61 eV) and CdS (2.49 eV) are typically used as Type I shell materials for metal sulfide systems. These materials can crystallize in both WZ and ZB phases and possess a S-based anionic lattice, similar in dimensions to those of both the II-VI and I-III-VI_2 systems.

2.3.3 Hybrid Structures

Hybrid nanostructures combine distinct material components, often with dissimilar properties, into a single system. The resultant systems can display not only the properties of the

components, but also synergistic features such as enhancement and up-conversion of luminescence or improved catalytic function.[95] Examples of hybrid materials include multilayer core-shell nanoparticles for targeted drug delivery[96, 97] and plasmonic metal-silicon dioxide nanostructures for surface-enhanced Raman scattering.[98-100] However, in this thesis, work is focused on semiconductor-metal NC hybrids for photoinduced charge separation.

Given the complexity of hybrid systems, there are a variety of material parameters that must be considered in their synthesis, including lattice constant, crystal structure, facet polarity, interfacial energy, miscibility, surface defects, and surface reactivity.[101, 102]

When the lattice constants and crystal structure of the component materials do not differ significantly or when the interfacial energy is kept low, the formation of a large interface between the two materials is often observed, leading to core-shell type hybrids (Figure 2.6a). Typically, core-shell hybrid preparation techniques involve selective heterogeneous nucleation of the shell onto preformed NC cores.[102] Numerous methods to promote shell growth exist, including the alternating deposition of monolayers of each ionic species for semiconductor-semiconductor core-shells,[103] and transmetalation processes for metal-metal core-shell formation.[104, 105] However, for semiconductor-metal systems, shell formation is typically achieved by tuning the reactivity of the metal precursor in a classically dimeric synthesis.[106, 107] For example, Klimov *et al.* synthesized fluorescent, magnetic, Co@CdSe NCs by slow deposition of CdSe onto preformed Co NCs, followed by annealing.[107] The encapsulation of metallic NCs with a semiconductor has also been explored for the noble metal NCs. Shelling Ag or Au with SiO_2 or TiO_2 has been shown to tune the plasmonic features of the metallic core in a controlled manner, and to confer additional stability on the core (Figure 2.6b).[108-111] In the inverse case, metallic deposits on oxide and sulfide NCs have been shown to greatly enhance the

photocatalytic and photoelectrochemical properties of the semiconductor cores, due to the promotion of charge carrier separation via electron migration to the metal domain.[112-114] In this case, a complete shell of the metallic component can hinder light absorption, thus other more elaborate hybrid morphologies have been studied.

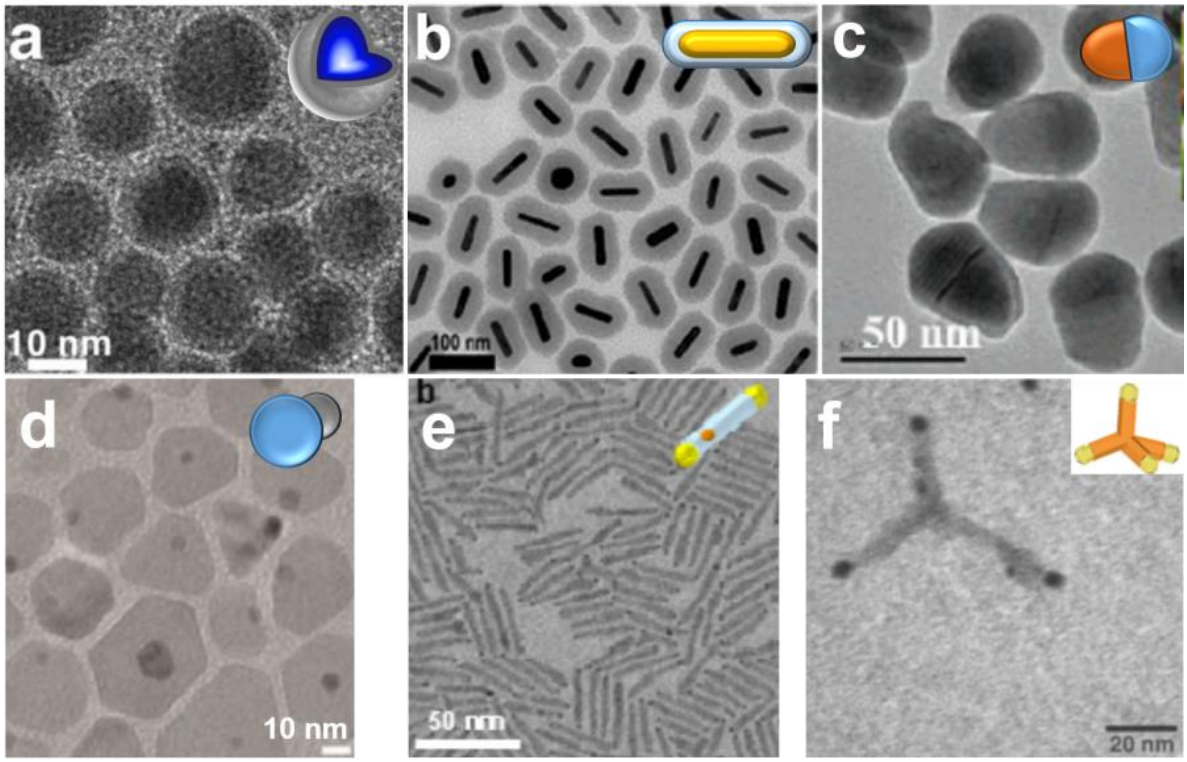

Figure 2.6. Hybrid nanoparticles; **a.** Co@CdSe core-shell hybrid nanoparticles;[107] **b.** Au@SiO_2 core–shell nanorods;[108] **c.** Cu−In sulfide heterostructured nanocrystals;[115] **d.** Pt-$CuInS_2$ dimeric hybrid nanocrystals;[106] **e.** CdSe-CdS nanorods with Au tips with 'dumbbell' morphology;[116] and **f.** Au tips on CdSe tetrapods.[117] Reproduced with permission from reference 107, 108, 115, 106, 116, and 117 respectively. Copyright 2005 American Chemical Society, 2006 American Chemical Society, 2006 American Chemical Society, 2015 American Chemical Society, 2009 American Chemical Society, 2004 American Association for the Advancement of Science respectively.

For hybrid components with limited miscibility, large interfacial energy, or differing surface reactivity, an anisotropic, oligomeric hybrid architecture is more likely to form. Systems with limited miscibility can be exploited to form heterodimers via phase segregation of a homogeneous mixture of the two materials. This method has been used extensively in metal sulfide syntheses with heterodimers of Co-Pd, Cu-In, and Ag-Fe sulfides synthesized under suitable conditions (Figure 2.6c).[115, 118, 119] However, colloidal dimeric systems are most

frequently synthesized via the nucleation of a precursor on an existing seed particle.[106, 120] For such reactions, seed particles are heated to a temperature just below the nucleation point of the second component. The seeds then act as nucleation points for the precursor, as the nucleation barrier, ΔG_{tot} (Section 2.1.1), is much lower at a surface. To minimize the interfacial energy between the two components, growth then proceeds via addition of precursor to the new material, forming two distinct domains (Figure 2.6d). This technique can be extended to a multitude of geometries (with different domain numbers, shapes and spatial arrangements) and component materials (including ternary and quaternary systems) by tuning the solvent polarity, concentration of reactants and reaction temperature,[120] and is further explored in Chapter 6 to produce $CuInS_2$-Pt hybrid NCs with different morphologies.[106]

Further geometric complexity can be achieved when the seed material possesses facets or edges with distinct reactivity or accessibility. Perhaps the most studied nanoscale examples of this are the WZ Cd chalcogenide systems. These anisotropic materials can be grown in rod or tetrapod morphologies with a high degree of control over their size and aspect ratio.[121, 122] The tips of both morphologies are polar facets with weakly bound ligands,[123] and thus are more reactive than the edge sites. This leads to the possibility of nucleating a second material exclusively at these facets (Figure 2.6e-f). Additionally, due to anisotropy in the crystalline *c*-direction, the two tips of a given rod are not chemically equivalent. Therefore, metallic domains can be selectively grown at one end of each rod.[116, 117, 124] 'Dumbbell' morphologies with a metallic tip at both ends represent a metastable intermediate, which can evolve into a single-tipped rod via a intraparticle Ostwald ripening mechanism (Section 2.1.2).[124] Similar selective growth on CdTe tetrapods can only be achieved by depositing the nanostructures on a substrate and partially masking them with a polymer layer.[125] Selective growth can also occur at high

energy surface defect sites.[116, 124] However, these defects can be efficiently suppressed by the binding of organic ligands.

3. TERNARY I-III-VI SEMICONDUCTOR NANOCRYSTALS [a]

Since its inception, the study of colloidal nanocrystals (NCs) has largely been focused on the II-VI systems (CdS, CdSe, CdTe, PbS, *etc.*). Exquisite control has been demonstrated over their synthesis and properties, however, concern has arisen regarding the toxicity and disposal of these heavy metal containing systems.[126] Recently both the III-V and ternary I-III-VI_2 systems have become the subject of further study. Expanding our library of NC materials, not only yields low toxicity alternatives to the II-VI NCs, but also facilitates additional tailoring of material properties to meet specific needs in application.[127] This dissertation is focused on the I-III-VI_2 materials: $CuInS_2$, $CuFeS_2$, and $AgFeS_2$.

3.1 Optoelectronic Properties of $CuInS_2$ NCs and Their Origin

3.1.1 Introduction

Copper indium sulfide, $CuInS_2$, represents a promising alternative to the II-VI systems. It has a direct band gap near the visible spectral region (E_g = 1.5 eV),[128] a large optical absorption coefficient ($\alpha > 10^5$ cm^{-1}),[129] and high photostability.[130] Furthermore, $CuInS_2$ NCs have been reported with tunable fluorescence covering the near-infrared (NIR) and visible spectral region,[131] high quantum yield (QY),[132] long luminescence decay time,[133] and large Stokes shift.[134] This has resulted in significant interest from the scientific community, who hope to exploit these properties.

$CuInS_2$ is often touted as a 'green' or 'safer' alternative to II-VI NCs. It is considered to be of low toxicity,[135] and Cu toxicity in humans requires much higher concentrations than Pb or Cd.[136] It should be noted, however, that in some aquatic ecosystems, Cu ions can be more toxic

[a] Portions of this chapter have been previously published in Leach, A.D.P. et al., *J. Phys. Chem. Lett.*, **2016**, *7* (3), pp 572–583. Copyright 2016 American Chemical Society.

than Pb,[137] and as such the ecological fate of any commercial product containing $CuInS_2$ should be considered carefully.

The chemistry of I-III-VI_2 NCs can be particularly complex due to the different properties of the two cations. In the case of $CuInS_2$, the ionic radii of Cu^+ (77 pm) and In^{3+} (80 pm) are similar,[138] yet, as soft and hard Lewis acids, respectively, their bond lengths to S and reactivity are distinct. Additionally, the composition of individual nanoparticles within the synthesized ensemble can differ, causing variability in the optoelectronic properties observed.[139] In order to harness the potential of $CuInS_2$ NCs, a complete understanding of the relationships between structure and properties must be developed.

Section 3.1 reports the optoelectronic properties of $CuInS_2$ NCs and summarizes current knowledge regarding their origin. A brief overview of synthetic strategy is presented, followed by a complete discussion of the crystallographic structures accessible to $CuInS_2$ and the mechanism of their formation. Progress towards understanding the optical properties of $CuInS_2$ NCs is then reviewed and the approaches used to tune these properties are reported. The applications of $CuInS_2$ NCs in photocatalysis, optoelectronic devices and biotechnology are also described. Finally the current challenges faced in this field are considered and possible areas for future work suggested. Discussion regarding the effect of shelling on $CuInS_2$ NCs (Section 3.1.7) was contributed by Dr. Janet Macdonald.

3.1.2 Synthesis of $CuInS_2$ NCs

A wide variety of synthetic techniques have been used to produce $CuInS_2$ NCs and have been reviewed thoroughly elsewhere.[140] The syntheses of ternary NCs can be particularly challenging due to the distinct reactivity of the two cations. In the case of $CuInS_2$, In^{3+} is a hard Lewis acid, whereas both Cu^+ and S^{2-} are soft in character. Therefore, if the reactivity of Cu^+

towards S is not attenuated, the formation of copper sulfide impurities can be observed.[140] Balance can be achieved by selecting two cationic stabilizers to control the reactivity of each cation (*e.g.* a thiol and a carboxylic acid control Cu^+ and In^{3+} respectively),[131, 141] or performing the reaction in an excess of Cu^+ stabilizer (*e.g.* using a thiol as both solvent and ligand).[133, 142] Alternatively, a single source precursor can be used, causing the simultaneous release of equimolar amounts of Cu and In ions,[143-145] thus promoting the formation of $CuInS_2$ over any competing binary compounds.

3.1.3 Structure of $CuInS_2$ NCs

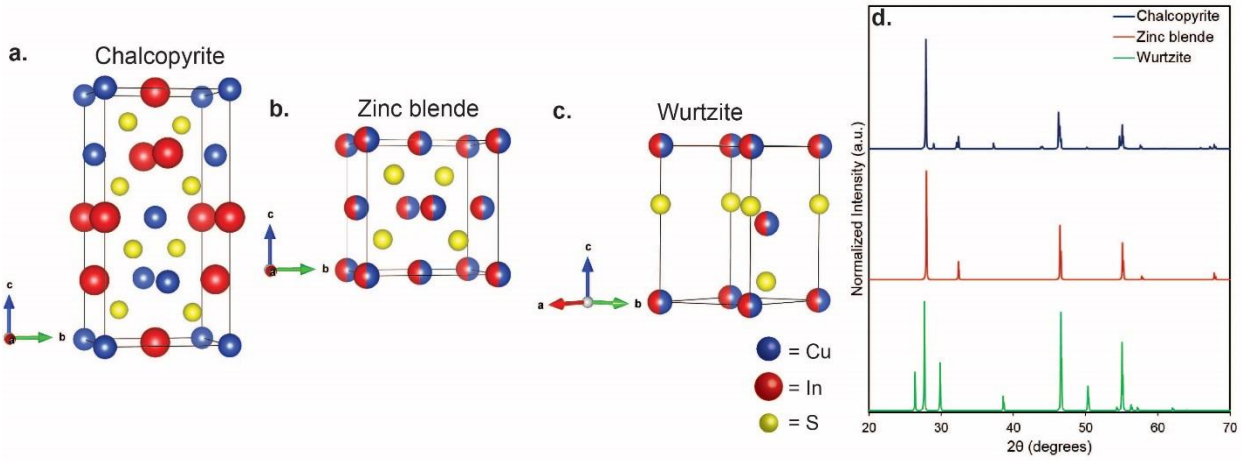

Figure 3.1. Structures of $CuInS_2$ NCs; **a.** Chalcopyrite; **b.** Zinc Blende; and **c.** Wurtzite $CuInS_2$; **d.** Their calculated XRD patterns.

Bulk $CuInS_2$ has the chalcopyrite structure, but $CuInS_2$ NCs have been reported to crystallize in three distinct crystal structures: chalcopyrite (CP), zinc blende (ZB), and wurtzite (WZ) (Figure 3.1).[145, 146] The microstructure of CP has been well studied and has a significant impact on the optoelectronic properties of $CuInS_2$ NCs with this structure.[128, 147] CP I-III-VI_2 materials exhibit cation-ordering (Figure 3.1a) with each S atom surrounded by two In and two Cu atoms. The different bond lengths ($R_{Cu-S} \neq R_{In-S}$) cause anion displacement from a close packed arrangement, leading to a tetragonal distortion of the crystal lattice. The structural

complexity of I-III-VI_2 CP semiconductors results in a low band gap energy[147] and an abundance of intrinsic defects,[128] causing their characteristic broad emission, in comparison to the II-VI ZB analogues.[134] In addition, deviations from 1:1:2 I:III:VI stoichiometry allow the growth of both n-type and p-type NCs, which have been used to increase the efficiency of $CuInS_2$-based photovoltaics,[148-150] and can influence the conductivity,[151] band gap,[134, 152] and luminescence properties[139, 149, 153] of the material.

The ZB structure is analogous to CP with related lattice parameters, $c_{CP} = 2c_{ZB}$, but is cation disordered (Figure 3.1b). Thus, in ZB NCs, cations can be easily exchanged for one another leading to compositions ranging far beyond those seen for CP with stoichiometries from $Cu_3InS_{3.1}$ to $CuIn_{2.2}S_{3.8}$ reported.[146] The flexible cationic ratio of ZB $CuInS_2$ can be advantageous for photovoltaic applications as the stoichiometry can be used to tune the optical band gap, and form n-type and p-type NCs. However, the ZB polymorph is difficult to isolate, with typical syntheses resulting in the formation of both ZB and WZ,[130, 154-157] and can be difficult to distinguish from CP. ZB and CP show similar lattice fringe spacing (0.32 nm) in high resolution transmission electron microscopy (HRTEM) and can only be distinguished by additional low intensity reflections in the CP diffraction pattern (Figure 3.1d). In the case of small NCs, broadening of reflections can prevent clear assignment.

In contrast, the WZ structure (Figure 3.1c) can be easily identified by both XRD (Figure **3.1**d) and lattice fringe spacing in HRTEM (0.34 nm). This structure is the hexagonal analogue of ZB with both consisting of a close packed anionic lattice with half the tetrahedral interstitial sites filled by cations. Remarkably, the $CuInS_2$ WZ structure is cation-ordered. This was reported by Shen *et al.*, who discovered a new form of crystalline order in NCs of $CuInS_2$.[158] These 'interlaced crystals' contain an uninterrupted, anionic lattice; however, within the cation

sublattice, several types of Cu and In ordering were observed, forming distinct phases in interlaced domains. This ordering has important implications for phonon and electron transport in NCs of WZ $CuInS_2$, as electronic motion is unaffected by interlaced phase boundaries, but phonons are likely to be scattered at these features.

Various mechanistic approaches have been used to form CP or ZB NCs,[142, 159, 160] however, high quality, monodisperse samples are typically prepared in organic solvents, using hot-injection or heat-up methods.[140] In contrast, the mechanism of WZ formation appears to be more defined. In particular, a Cu_2S intermediate has been identified as key in its synthesis. This was hypothesized by Pan *et al.* in 2008[146] and identified by Connor *et al.* in 2009,[161] who noted that WZ $CuInS_2$ nanorods were formed by the nucleation of Cu_2S nanodisks followed by epitaxial growth of $CuInS_2$ in the [002] direction. This finding was supported by Kruszynska *et al.*[156] who used a thiolate precursor to synthesize $CuInS_2$ NCs with a bullet-like morphology and reported that the formation of Cu_2S−$CuInS_2$ hybrid nanostructures was an essential intermediate step in the growth of $CuInS_2$ nanoparticles. These examples both identified a biphasic growth system, in which $CuInS_2$ domains grew onto a Cu_2S nanostructure. However, Kuzuya *et al.*[162] predicted an additional growth mechanism, in which plate-like WZ $CuInS_2$ NCs are formed by intercalation of In^{3+} into previously formed Cu_2S plates. The intermediates in this mechanism are identified for the first time in this dissertation (Chapter 4).

Phase selection for $CuInS_2$ NCs can be achieved through heat-up, hot-injection or template synthesis methods (Section 2.1). In hot-injection and heat-up techniques, ligand and metal/ sulfur precursor choice can be used to tune the crystal structure of the resultant NCs.[146, 155, 157, 162-167] Typically selection of ligands and precursors that promote the formation of a Cu_2S intermediate result in a WZ NC product. Similarly, template syntheses utilize an intermediate

with similar structure to produce a specific phase: exchange of the appropriate cation into the either β-In_2S_3 (tetragonal, defective spinel)[152, 164] or Cu_2S (hexagonal, wurtzite)[164, 168, 169] results in the formation of CP or WZ $CuInS_2$ respectively.

3.1.4 Optical Properties of $CuInS_2$ NCs

The bond length mismatch in $CuInS_2$ ($R_{Cu-S} \neq R_{In-S}$) leads to a high proportion of intrinsic point defects within the material.[128] Furthermore, the small size of the NCs necessitates a large surface area to volume ratio and a correspondingly high occurrence of surface defects. The defects in $CuInS_2$ NCs are the dominant sources of radiative and non-radiative decay routes as well as plasmonic behavior.

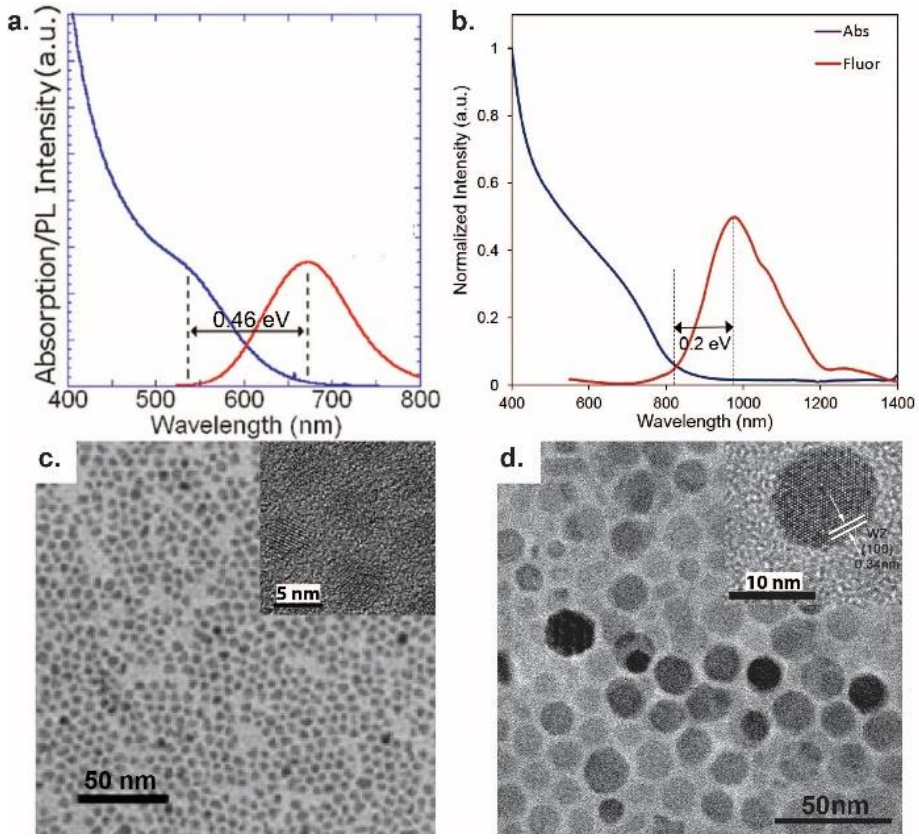

Figure 3.2. Characterization of $CuInS_2$ NCs; The absorbance (blue) and photoluminescence (red) spectra of **a.** Chalcopyrite[133] and **b.** Wurtzite $CuInS_2$ NCs with the Stokes shift for each indicated. Reprinted with permission from reference 133. Copyright 2011 American Chemical Society. TEM images of **c.** Chalcopyrite[131] and **b.** Wurtzite[164] $CuInS_2$ NCs. Inset are HRTEM images showing lattice fringes. Figure 3.2c. is reprinted with permission from reference 131. Copyright 2009 American Chemical Society. Figure 3.2d. is reprinted with permission from reference 164. Copyright 2015 Royal Society of Chemistry.

Plasmonic $CuInS_2$ NCs, with no luminescence, can be synthesized.[170-172] NIR plasmons in Cu chalcogenide NCs typically arise due to Cu deficiency[173] and have been exploited to improve photovoltaic activity.[174] A complete discussion of plasmonic NCs is beyond the scope of this thesis, but is reviewed elsewhere.[172]

As in other luminescent ternary I-III-VI_2 materials,[134, 175] $CuInS_2$ NCs have a lower QY than their II-VI analogues, due to the high proportion of defect-based non-radiative decay paths available. Emission also has a large FWHM (80 – 120 nm), a large Stokes shift from the band gap (200 - 500 meV) (Figure 3.2),[134] and a long decay lifetime of up to approximately 500 ns.[133] All three features are significantly larger than the corresponding values for II-VI NCs, which exhibit band gap emission. It has been shown that these properties are not due to size inhomogeneity, but mainly to the distribution of vibrational states.[144] Photoluminescence (PL) from $CuInS_2$ is thus attributed to defect states.

3.1.5 Origin of Emission from $CuInS_2$ NCs

The exact mechanism behind the radiative decay observed from CP $CuInS_2$ NCs has been the subject of much debate in the literature (Figure 3.3). It is widely accepted that luminescence originates from an intrinsic defect within the NC structure. This was initially suggested by Castro *et al.*,[144] who observed that the nature of the surface ligands did not affect the shape or position of the PL peak for $CuInS_2$ NCs, and confirmed by the work of Li *et al.*,[133] who noted an increase in both QY and fluorescence lifetime on coating $CuInS_2$ NCs with a ZnS layer. The involvement of a two-fold degenerate band edge state, identified by transient absorption spectroscopy, was also reported by Li *et al.*,[133] which was assigned to the electron. Li *et al.* concluded that the luminescent transition was from the conduction band (CB) to a localized intra-gap state. This conclusion was, however, inconsistent with the work of Castro *et al.*[144] and others[149, 176-178] who

identified a donor-acceptor pair (DAP) as the origin of the emissive transition. Further incongruous observations were reported by Omata *et al.*[179] and others,[180] who observed experimental data consistent with a transition between a localized state and the valence band (VB). The observation of size-tunable emission from $CuInS_2$ NCs (Figure 3.4) provides strong support for the argument that luminescence comprises of an optical transition between a quantized level and a defect state. Supporters of DAP theory argue that if a trap state is positioned close to the VB or CB edge, a perturbation in the band energy (*e.g.* confinement) could cause a change in defect energy.[176] Yet a number of ultrafast spectroscopy studies have been undertaken on $CuInS_2$ NCs and results supported assignment of a radiative transition from, or to, a level within the energy bands.[180-182] In particular, Kraatz *et al.*[180] observed that the absorbing excited state was not depopulated by a dump laser and appeared instantly with the excitation laser, implying that it originates in the CB of $CuInS_2$. These data suggest some excited electrons undergo an ultrafast, nonradiative relaxation from the CB into a long-lived, high-lying donor state. Thus the radiative transition was assigned as a donor to VB transition. At this point no consensus has been reached as to the radiative decay mechanism in CP $CuInS_2$ NCs. Additionally, luminescence decay measurements by Li *et al.*[133] identified two different PL signals from CP $CuInS_2$ NCs, associated with two different energy bands at 670 nm and 700 nm. This is supported by numerous steady state fluorescence experiments, which appear to show multiple emission bands from $CuInS_2$ NCs.[144, 177, 183] It was found that coating NCs with CdS eliminated the component with lower energy, suggesting the presence of a second radiative decay path associated with the NC surface.[133] To the author's knowledge the presence of multiple decay paths has not yet been discussed completely in the literature.

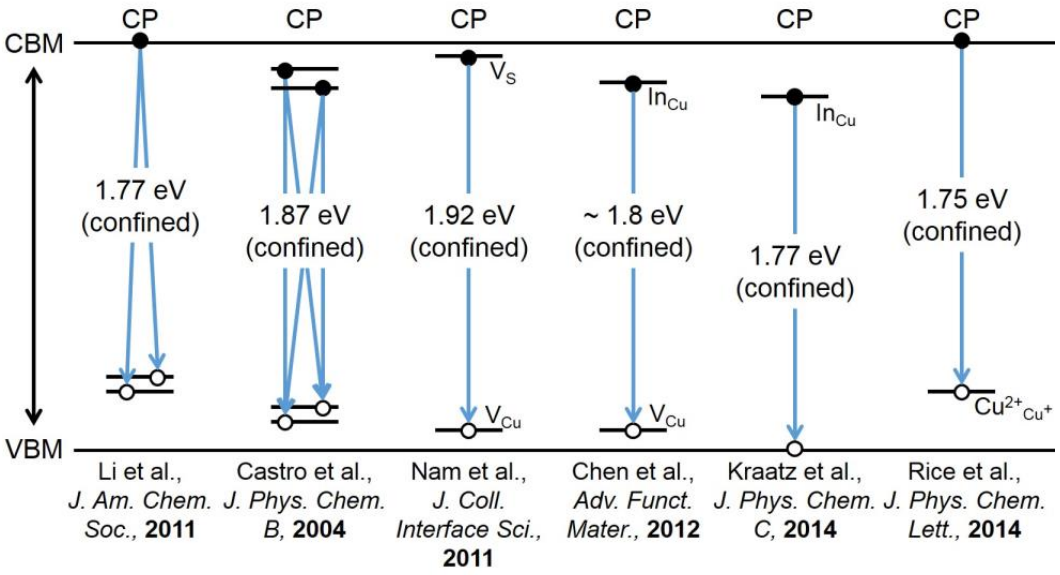

Figure 3.3. Overview of proposed radiative decay mechanisms and their observed energies for CP $CuInS_2$ NCs from references [133], [144], [176], [149], [180], and [184] respectively. Transitions labeled (confined) are for particles at sizes small enough to show the effects of quantum confinement.

In 2012, a first-principles study by Chen *et al.*[185] used density functional theory to calculate the transition energies of various point defects in CP $CuInS_2$. Their work has since been used to identify the possible states responsible for luminescence. The most commonly implicated defect states are In_{Cu}, V_{Cu} or V_S, whose transition energies are in good agreement with experimental observations. However, recently Rice *et al.*[184] used magnetic circular dichroism to identify the presence of Cu^{2+} within $CuInS_2$ NCs, attributing emission to these impurity atoms. The earlier work of Chen *et al.*[185] had omitted this possibility as well as In_i and Cu_i which have been identified as possible sources of luminescent decay in bulk $CuInS_2$.[186, 187] To the author's knowledge the energies of these defects have yet to be calculated. It should also be noted here that cation-disordered ZB $CuInS_2$ NCs have been reported with similar luminescence properties to CP NCs.[132] If assignment of In_{Cu} as the radiative defect state in this system is correct, fluorescence should not be observed from ZB samples, as this defect cannot exist in a cation-disordered system. This assignment cannot be completely discounted, as it is possible that the structure of these samples has been incorrectly identified or ZB samples contain a small

proportion of ordered CP NCs. However, it is the author's opinion that further work is needed here to establish the source of emission from CP and ZB $CuInS_2$ NCs.

The mechanism of fluorescence in WZ $CuInS_2$ NCs has yet to undergo the same level of study. Emission from this structure bears a number of similarities to that of the cubic structure; both materials have a broad PL peak (FWHM = 200 nm) with a large Stokes shift (approximately 200 meV) from the band gap (Figure 3.2a-b) and long lifetime (approximately 270 ns).[164] However, the WZ emission is lower in energy (1.3 eV)[164] than that of CP (1.4 eV).[128] The radiative decay mechanism for WZ $CuInS_2$ NCs is explored in Chapter 5 of this dissertation.

3.1.6 Band Gap Tunability of $CuInS_2$ NCs

The ability to tune the optical band gap of $CuInS_2$ NCs is particularly appealing for photoabsorbing applications. This has been achieved for CP $CuInS_2$ NCs and was reviewed by Zhong *et al.*[134] The author noted that the band gap and correspondingly the luminescence properties could be tuned by adjusting the size, composition and surface chemistry of CP NCs.

The effect of quantum confinement on semiconductor NCs, with size less than the Bohr exciton radius, is well known. Confined NCs, also known as quantum dots, show an increase in the optical band gap with decreasing size. The reported Bohr exciton radius of $CuInS_2$ is 4.1 nm,[140] thus NCs might be expected to show confinement effects up to a diameter of approximately 8 nm. Xie *et al.*[131] reported CP NCs with sizes less than 2 – 20 nm and tunable absorption band edge from 450 – 900 nm (Figure 3.4a). These results were in remarkably good agreement with the calculations of Omata *et al.*,[188] who used the finite-depth-well effective mass approximation to predict the band gap of CP $CuInS_2$ NCs from 2 – 6 nm in size (Figure 3.4b). The molar extinction coefficients for both this material and Zn-Cu-In-S NCs have also been

determined across this size range.[189, 190] Furthermore CP $CuInS_2$ NCs have been prepared with size-tunable emission wavelength ranging from 600 to 900 nm (Figure 3.4c) and luminescence QY up to 18%.[132] Increases in both QY and range of PL peak wavelength can be achieved by alloying or shelling samples with Zn. Confined WZ $CuInS_2$ NCs were reported by van der Stam *et al.*, and extend the tunability of $CuInS_2$ emission deeper into the NIR.[168]

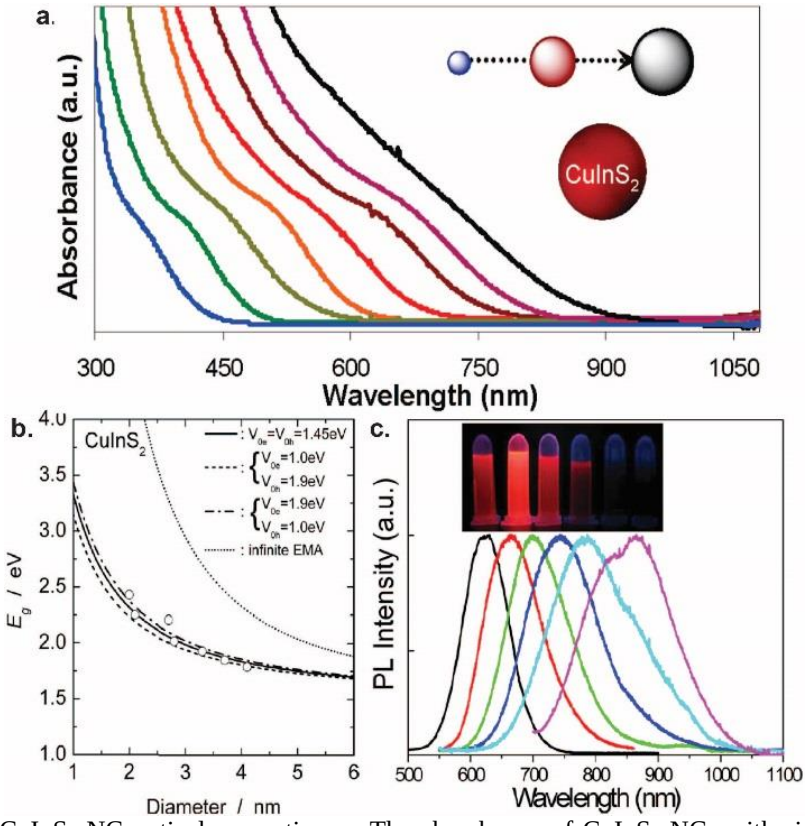

Figure 3.4. Tunable $CuInS_2$ NC optical properties; **a.** The absorbance of $CuInS_2$ NCs with size less than 2 – 20 nm.[131] Reprinted with permission from reference 131. Copyright 2009 American Chemical Society. **b.** Comparison between experimental (open circles) and theoretical size-dependent optical band gap for $CuInS_2$ NCs.[188] Reprinted with permission from reference 188. Copyright 2009 American Institute of Physics. **c.** The size dependent luminescence of $CuInS_2$ NCs.[132] Inset is a digital photograph of the samples taken under a UV lamp. Reprinted with permission from reference 132. Copyright 2012 American Chemical Society.

The ternary nature of $CuInS_2$ allows further control over its band gap via adjustment of the cationic ratio (Figure 3.5a). Control was first demonstrated by Uehara *et al.*,[139] who tuned CP $CuInS_2$ NC composition from $CuInS_2$ to $CuIn_3S_5$ by adjusting the concentration of Cu precursor present in the synthesis. While there was no change in NC size, a decrease in the wavelength of both NC absorption edge and fluorescence peak, corresponding to an increase in the band gap,

was observed with decreasing Cu/In ratio. For bulk $CuInS_2$ the VB results from the hybridization of Cu *d*-orbitals and S *p*-orbitals and has binding energy approximately 2.5 eV.[191, 192] It has been shown for $CuInSe_2$ that a decrease in Cu concentration, with corresponding decrease in Cu *d*-orbital character, results in the reduction of Cu *d*-/Se *p*-interband repulsion, lowering the VB maximum of the material.[193] $CuInS_2$ has analogous band structure, thus the increase in band gap on decreasing Cu/In ratio is attributed to a similar mechanism. However, a comparable study has not been carried out for $CuInS_2$. Uehara *et al.*[139] also observed that the fluorescence intensity increased with Cu deficiency. They attributed the increase to the introduction of a radiative defect related to Cu deficiency. Similar results were reported by Chen *et al.*,[149] who prepared samples with Cu/In = 0.3 – 2.9 and determined that the highest QY was obtained for samples with Cu/In = 0.7. Changes in QY were attributed to changes in defect concentration within the NC. Specifically, they suggested a DAP recombination mechanism, with the transition from V_{Cu} to In_{Cu} responsible for emission, and noted that maximum QY occurred at a defect concentration of one defect pair per three units of $CuInS_2$. It is yet unclear why Cu deficiencies lead to luminescent NCs in some syntheses, still in others, Cu deficiencies lead to plasmonic behavior and no luminescence.

3.1.7 Core-Shell $CuInS_2$ NCs

The shelling of $CuInS_2$ NCs by ZnS and CdS has been very effective at increasing the QY in CP $CuInS_2$ (typically 5 - 10% to 80%, 86%)[132, 133] (Figure 3.5b-c). For WZ $CuInS_2$, improvements in luminescence have been reported when exposure to Zn^{2+} alloys the outermost layers of the NCs.[169] It appears that an alloyed shell is key, as when Zn^{2+} is incorporated throughout the crystal, there is no PL.[169] Shelling WZ NCs with CdS and further study of the results of shelling on their emission are carried out in Chapter 5.

For CP $CuInS_2$, the story is much more complicated. Universally, researchers report that exposure to Zn^{2+} causes a blue shift in fluorescence, with magnitude from approximately 10 – 25 nm[133, 194] up to 130 nm,[195] depending on the extent of Zn incorporation.[177] The blue shift has been attributed to either Zn-alloying increasing the band gap of the material[183, 196] or cation exchange at the surface of the NC yielding a gradient alloy, resulting in a smaller $CuInS_2$ core, thus increasing the band gap through quantum confinement effects.[195] Whilst a blue shift is also observed in the absorbance spectra, its relative magnitude can vary. In some cases, the blue shift in absorbance is of comparable size to that of the luminescence,[177, 183, 194] but in other cases a much less significant change is observed.[177, 197] If the shift in luminescence were merely a feature of the change in band gap energy, similar shifts for both absorbance and luminescence would be expected, therefore the above explanations are too simplistic to explain the electronic changes completely.

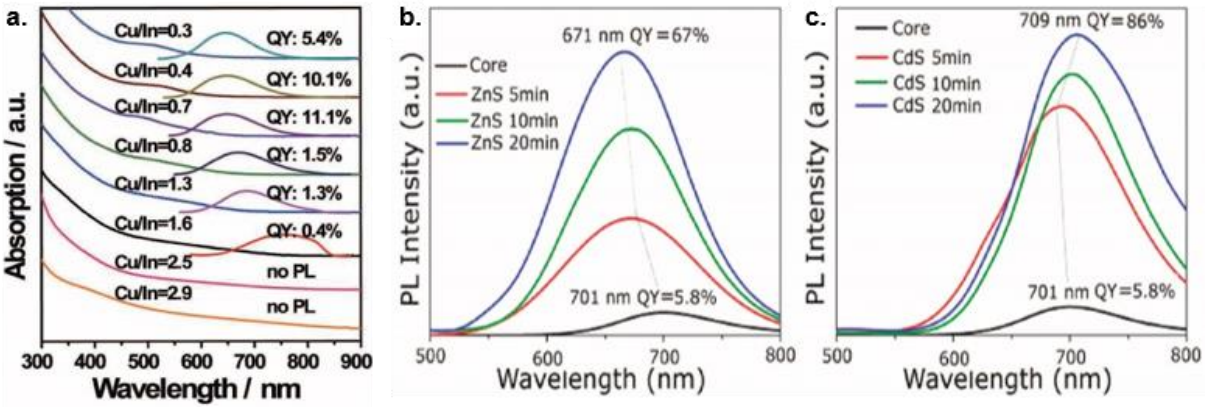

Figure 3.5. Composition dependent optical properties of $CuInS_2$ NCs; **a.** Absorbance and luminescence of $CuInS_2$ NCs with different Cu/In ratios.[149] Reprinted with permission from reference 149. Copyright 2012 Wiley-VCH. The effect of alloying/shelling with **b.** ZnS or **c.** CdS on the fluorescence QY of CP $CuInS_2$.[133] Reprinted with permission from reference 133. Copyright 2011 American Chemical Society.

Beyond the observed blue shift in luminescence, there is little consistency in the literature. The results are highly dependent on the synthetic route taken. For example, in cation exchange procedures De Trizio *et al.*[183] found the Cu^+ was preferentially exchanged for Zn^{2+}, but Park and Kim[195] as well as Wang *et al.*[177] found that it was In^{3+} that was preferentially

exchanged. One would expect Cu^{+} and In^{3+} to be exchanged in equal proportion with Zn^{2+} to maintain S^{2-} valence. Therefore these results speak to a deep complexity in exchange mechanism and likely inhomogeneity of composition and structure of the parent $CuInS_2$ NCs between research groups and preparations. The exact location of Zn in the NCs also appears to be very dependent on the synthetic procedure. Some techniques that include a sulfur precursor provide a formal ZnS shell, indicated by an increase in particle size.[133, 177, 195] Others describe cation exchange behaviors that give alloyed shells,[195] or complete alloying to Zn-Cu-In-S.[177, 183, 198] A combination of these behaviors may also be present,[177] thus distinguishing between shelled or alloyed NCs is difficult. Analysis by XRD is challenging as the reflections of CP $CuInS_2$ and ZnS are very similar and, while shifts towards ZnS are often observed, the broad nature of reflections from NCs prevents resolution of a single alloyed set of reflections from pairs of reflections. Additionally, the resolution of energy dispersive X-ray spectroscopy (EDS) mapping is too poor to show concentration gradients for the 2.5 - 3.5 nm NCs often studied.[183] However, elemental analysis by surface-sensitive X-ray photoelectron spectroscopy (XPS) combined with inductively coupled plasma mass spectrometry (ICP-MS) has confirmed[196] or excluded[183] the existence of shells. High resolution XPS has also been used to identify the incorporation of Zn into the crystal structure through perturbation of the Cu *2p* binding energy.[183]

It is important to note that the proportion of Zn incorporated can be large. For example, De Trizio *et al.*[183] prepared particles with composition $Cu_{0.13}In_{0.74}Zn_{0.59}S_2$ and in the extreme case Zhang *et al.*[199] described the NCs, resulting from a one-pot synthesis, as a Cu dopant in a $ZnInS_2$ host. Elemental ratios in literature examples should be considered with scrutiny; the presence of unreacted cation precursors, sulfur reagents and thiol ligands can result in compositional analysis errors. Additionally, the analysis techniques themselves can be

problematic. For EDS, many TEM sample holders give large Cu background signals even when using low background support grids or sample holders. XPS is highly surface sensitive and the presence of a shell can attenuate the signal of the core. Indeed even 1-1.5 monolayers of a ZnS shell can decrease the apparent core *2p* Cu signal by 50%.[196] For ICP –MS, interference by NO^+ and O^{2+} can be problematic for the sulfur signal.[200] Furthermore, elemental analysis techniques that require acid digestion and oxidation must be performed carefully to avoid the formation of insoluble elemental sulfur.[201]

Exposure to Cd^{2+} is even more effective than Zn^{2+} at increasing the luminescence intensity of CP $CuInS_2$, with a QY of 86% reported.[133] The number of studies including CdS shelling is limited, as it negates the objective of low toxicity NCs, but the few provide an interesting contrast. Unlike ZnS, shelling procedures with Cd^{2+} cause a much smaller blue shift[197] or even a red shift[133] of the luminescence combined with a red shift of the absorption onset.[197] Choi *et al.*[197] suggested that the incorporation of small Zn^{2+} results in the contraction of the lattice, whereas the incorporation of Cd^{2+}, which has an ionic radius approximately one third larger than In^{3+} or Cu^+,[138] causes tensile stress. These stresses cause shifts in the band gap leading to a blue- or red-shifted luminescence, respectively. Again, this explanation alone cannot explain the array of results seen by other groups for Zn shelling, where the magnitude of the blue shift of the absorption does not always match that of the fluorescence.

3.1.8 Applications of $CuInS_2$ NCs

$CuInS_2$ NCs have potential application in a variety of fields including photocatalysis, photovoltaics, biomedicine and light-emitting diodes (LEDs).[56] In applications requiring good charge transport (*e.g.* photovoltaics or photocatalysis), the presence of defects within the NC structure can disrupt the propagation of charge carriers; high quality, defect-free NC samples are

sought, which consequently lack strong defect luminescence.[131] In contrast, for applications requiring a high fluorescence intensity (*e.g.* bioimaging or light emitting devices), the proportion of radiative defects within a sample should be maximized, while non-radiative decay paths should be passivated.[133] For this reason, applications requiring high fluorescence QY frequently use samples alloyed or shelled with Zn. In order to meet the potential of $CuInS_2$ in applications, synthetic efforts are needed to improve these contrasting defect concentration and charge transport properties.

$CuInS_2$ is a particularly promising photocatalyst, due to its high molar absorption coefficient and band gap in the visible region of the solar spectrum. $CuInS_2$ and Zn-Cu-In-S NCs have been shown to catalyze the photo-reduction of H_2 from water.[202, 203] $CuInS_2$ and Zn-Cu-In-S NCs have also been used as a visible photosensitizer for TiO_2 NCs (Figure 3.6a) to drive the degradation of organic pollutants. The band alignment facilitates charge separation with excited electrons transferred from $CuInS_2$ to TiO_2, while holes remain in the $CuInS_2$ domain.[204, 205]

Photocatalytic activity can be further enhanced by fabricating hybrid NCs, which incorporate a metal and semiconductor domain into a single nanostructure (Figure 3.6b). Typically, the Fermi level of the metal component is situated within the band gap of the semiconductor, promoting the transfer of excited electrons from the semiconductor CB into the metal domain. In contrast, holes remain localized in the semiconductor domain, causing separation of the two charges. This results in superior catalytic properties, as the probability of undesirable electron-hole recombination processes occurring is considerably reduced.[101, 106, 206] Hybrid nanostructures have been successfully prepared, using $CuInS_2$, Zn-Cu-In-S, and Cu-In-S-Se NCs with Au, Pt, and Pd_4S domains. These systems show improved catalytic performance with respect to the bare semiconductor NCs.[207, 208] The photostability of $CuInS_2$ hybrid NCs has

not been studied with adequate depth, as it is expected to be one of the great advantages of $CuInS_2$ over CdS.

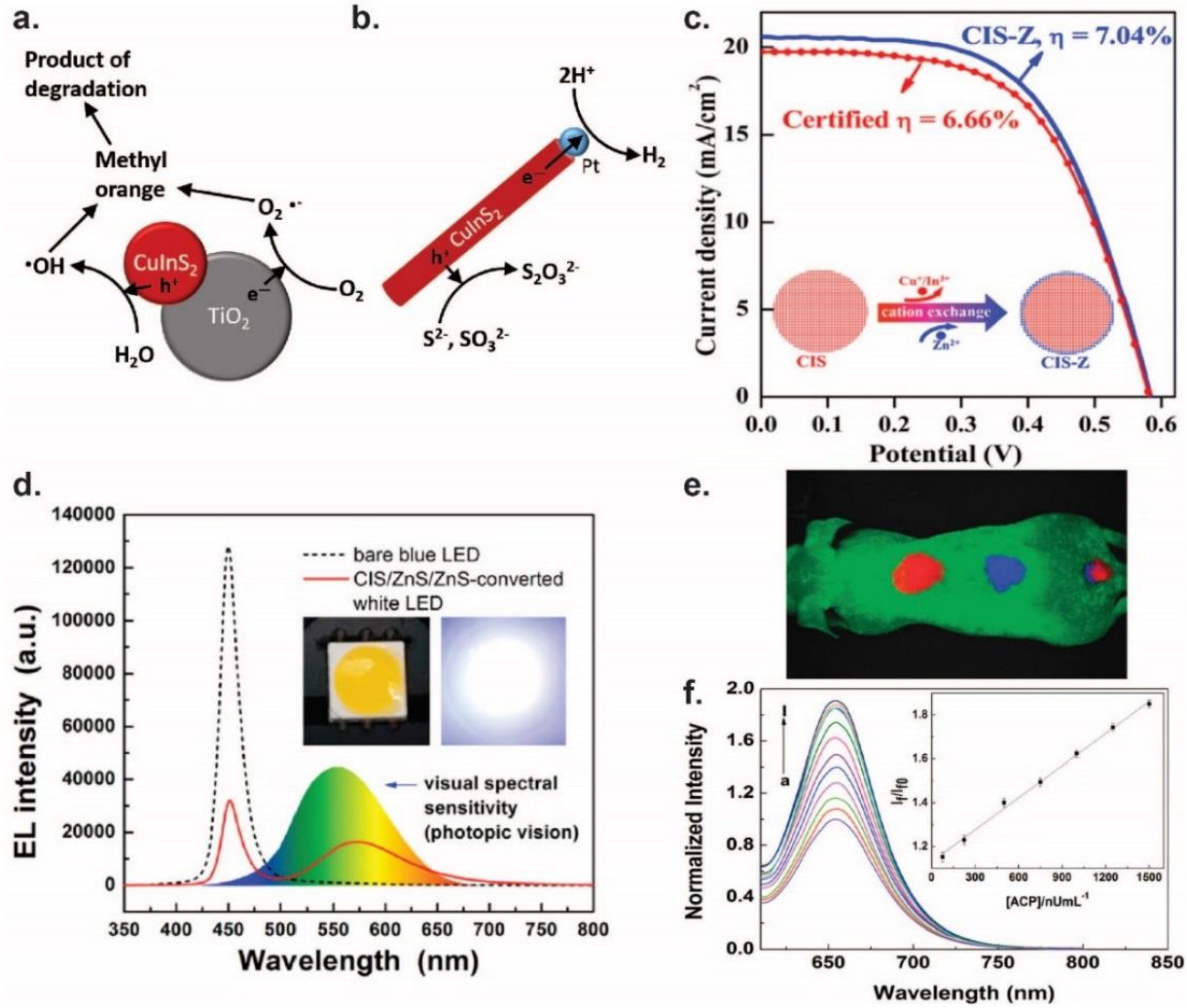

Figure 3.6. Applications of $CuInS_2$ NCs; Schematic diagram of **a.** the photodegradation of methyl orange using $CuInS_2$ and TiO_2 NCs,[205] and **b.** the photocatalytic evolution of H_2 from water.[207] Adapted with permission from references 205 and 207. Copyright 2011 American Chemical Society and 2015 Wiley-VCH. **c.** J−V curves of $CuInS_2$-Zn and $CuInS_2$-based champion quantum dot sensitized solar cells.[194] Reprinted with permission from reference 194. Copyright 2014 American Chemical Society. **d.** Electroluminescence spectra of a blue LED (dotted black line) and a $CuInS_2$/ZnS/ZnS-converted white LED (solid red line).[209] Inset are photographs of the device. Reprinted with permission from reference 209. Copyright 2015 American Chemical Society. **e.** *In vivo* multiplex image of $CuInS_2$/ZnS NCs emitting at 640 nm (red) and 710 nm (blue).[210] Reprinted with permission from reference 210. Copyright 2010 The Royal Society of Chemistry. **f.** The fluorescence spectra of bioconjugated $CuInS_2$ NCs in the presence of different concentrations of acid phosphatase, demonstrating their biosensing capability.[211] Reprinted with permission from reference 211. Copyright 2015 Elsevier.

Quantum dots (QDs) have garnered significant scientific and industrial interest for use in third-generation solar cells, due to their high absorption, low-cost, tunable band gap, and solution

processability.[212, 213] Advances in synthesis and design have enabled the fabrication of photovoltaic devices with efficiencies greater than 10%,[213] however, these 'champion' devices contain toxic Pb or Cd chalcogenide NCs, limiting future commercial application. $CuInS_2$ provides a viable alternative to these materials, however, devices with $CuInS_2$-based photoanodes often suffer from poor power conversion efficiencies of approximately 2.5%,[214] due to the abundance of defects present in the NCs. Defects cause both internal charge carrier recombination inside NCs, and photoexcited electron recombination from the solar cell matrix to the QD sensitizer, lowering efficiency of the resulting device. However, promising results have recently been achieved by Pan *et al.* using Zn-Cu-In-S sensitized devices with a reported power conversion efficiency of 7.04% (Figure 3.6c).[194] In this system, mercaptopropionic acid capped Zn-Cu-In-S NCs were dropcast onto mesoporous TiO_2 film electrode and coated with ZnS. Cells were then constructed using a polysulfide electrolyte and a brass-based Cu_2S counter electrode. The author suggests that this large increase in efficiency is due to the use of $CuInS_2$ QDs with broad light absorption range, the Type I $CuInS_2$-ZnS core-shell structure (Section 2.3.2) of the prepared NCs, and high NC loading in the cell achieved by linker molecule exchange. This work is the first report of a Cd- or Pb-free QD sensitized solar cell with similar efficiency to its heavy metal containing analogues.[213] Alternatively, $CuInS_2$ has been used as a cathode material in dye sensitized solar cells with an I^-/I^{3-} electrolyte.[215] In a polysulfide electrolyte, it is likely that $CuInS_2$ will give high efficiencies but poor chemical stability, similar to Cu_2S.[216, 217]

$CuInS_2$ NCs are very promising as solar concentrators, an application that takes advantage of the large Stokes shift of the luminescence. $CuInS_2$ absorbs sunlight and then emits light, directed into a wave guide ending at a photovoltaic.[218] $CuInS_2$-CdS is predicted to be excellent for this application as it has a large absorption coefficient, a high QY and a large

Stokes shift that prevents reabsorption. For a 2D design, the calculated flux gain was predicted to be three times that of the previously most promising material: defect emissive CdSe, which suffers from low QY.[219]

The use of $CuInS_2$ in LEDs has been carefully considered in the reviews of both Kolny-Olesiak and Zhong.[134, 140] Briefly, electroluminescence from green to deep-red has been observed for devices that sandwich Zn-Cu-In-S/ZnS NCs between ITO and aluminum electrodes with organic electron and hole transport layers.[149, 209, 220-222] The broad emission spectra of $CuInS_2$-based NCs gives inferior color purity with respect to Cd-based devices yet is well suited to the generation of white light. Several examples have been reported of devices incorporating $CuInS_2$ with color rendering indices above 90.[221, 223-225] Further, the large Stokes shift of emission prevents reabsorption in $CuInS_2$-based LEDs, improving efficiency. While early examples of Zn-Cu-In-S-based white LEDs suffered from low stability and brightness,[220] these properties have considerably improved with a recent example showing high luminous efficacy (greater than 80 lm W^{-1}) and high stability (Figure 3.6d).[209]

The use of Zn-Cu-In-S NCs for *in vivo* imaging has been widely demonstrated (Figure **3.6**e).[132, 197, 226-236] Zn-Cu-In-S NCs have some distinct advantages in bioimaging systems, as they possess low toxicity and emission in the tissue transparency window. The long fluorescence decay of $CuInS_2$ allows the use of an increased delay time between photoexcitation and detection, resulting in a decrease of background autofluorescence.[227] Additionally, two-photon absorption has been observed for Zn-Cu-In-S NCs.[237] These NCs can thus be excited by wavelengths in the near-infrared spectral range, which corresponds to the region in which water and biological tissue do not strongly absorb.

For application in biological systems, water soluble NCs must be prepared either via direct synthesis[238-242] or ligand exchange.[226, 227, 229, 234, 243] The rich chemistry of ligand exchange procedures has led not only to water solubility, but also to the design of targeted nanoprobes for the imaging of specific cells.[228, 229, 231, 244] Recently, the use of Zn-Cu-In-S NCs has been expanded to other biomedical areas with applicability demonstrated in both biosensing[211, 245-252] (Figure 3.6f) and the formation of magnetofluorescent nanocomposites.[253] The latter can serve as a multimodal platform for either drug delivery or bioconjugation to targeting biomolecular probes. The wide variety of biological applications currently being reported and the advantageous properties of Zn-Cu-In-S NCs suggest that work in this field will show great progress in the near future.

3.1.9 Conclusion

In summary, a comprehensive discussion of the chemical, optical and structural properties of $CuInS_2$ NCs was presented. The complex chemistry associated with ternary and quaternary systems can lead to challenges in their synthesis, and many compositions and structures are accessible. A high level of synthetic control has now been achieved for $CuInS_2$ NCs, allowing the selection of shape, size, and structure. Furthermore, the ability to tune the optical band gap and luminescence characteristics of $CuInS_2$ NCs has been demonstrated. The relationships between synthesis, structure and optical properties are not always well characterized, and the fluorescence properties of these NCs have yet to be completely understood. Recent reports of $CuInS_2$ NC applications, in particular the observation of high power conversion efficiency from a $CuInS_2$-based photovoltaic device, will renew and increase interest in this ‘green’ material. With this in mind, the author believes that the following

challenges should be addressed, and represent interesting questions to be considered in the field of colloidal semiconductor NCs.

Despite extensive reports on the subject, the mechanism behind radiative decay in $CuInS_2$ NCs has still not been confirmed. Understanding this mechanism will allow synthetic efforts to accurately target the luminescence properties and defect concentrations in $CuInS_2$ NCs, which are indispensable for application. The author suggests that a study of the synthetic mechanism of formation of both WZ and CP NCs in combination with spectroscopic techniques could help to confirm the identity of the fluorescent defect.

The abundance of intrinsic defects in ternary I-III-VI_2 systems leads to a number of advantageous properties, including tunable luminescence with composition, and a high tolerance to doping or alloying. However, it also promotes compositional inhomogeneity within NC samples leading to a variation in optical band gap and broadening of the luminescence peak.[139, 149] Whilst monodispersity is often indicative of uniform composition, characterization of single particle composition is rarely carried out for $CuInS_2$ NC syntheses. This should be carefully considered when reporting novel syntheses, particularly when quaternary systems are presented, such as Zn-Cu-In-S or Cu-In-Ga-S. The distinction between an alloyed quaternary system, a doped ternary system and a shelled system must also be defined. Literature examples, of Zn-Cu-In-S synthesized from $CuInS_2$ NCs, frequently use these terms interchangeably and rarely characterize the resultant NCs completely. In order to apply these systems, the proportion and location of Zn atoms must be well described and their influence on the materials' optical properties must be understood.

Given that $CuInS_2$ is promoted as a low toxicity replacement for heavy metal containing systems, a comprehensive understanding of the toxicity of these NCs must be developed in order

for their potential to be fully realized. The stability of $CuInS_2$ NCs has also been identified as a challenge, and shelling with ZnS,[131, 132] Al_2O_3,[254] $ZnGa_2O_4$[255] or SiO_2[256] can impart greater stability. Whilst work towards determining toxicity and stability for both $CuInS_2$ and Zn-Cu-In-S NCs has begun,[183, 257] there is still considerable work to be done here.

The report of a high efficiency Zn-Cu-In-S solar cell has renewed interest in this material for photovoltaic applications.[194] With further refinement of device design, additional improvements to power conversion efficiency are expected. Therefore, the potential exists for Zn-Cu-In-S NCs to become the preferred sensitizer for quantum dot solar cells. Recent advances in the tuning of NC surface chemistry, have led to numerous possible applications for semiconductor NCs in biomedicine.[56, 258] Implementation of these techniques on $CuInS_2$ NCs could result in significant progress in this field.

3.2 Synthesis & Characterization of $CuFeS_2$ NCs

$CuFeS_2$ is widely known as the naturally occurring mineral chalcopyrite (CP). Despite its terrestrial abundance, laboratory syntheses of this material have proved challenging with early examples requiring solvothermal conditions.[259, 260] More recently, nanostructures of $CuFeS_2$ have come under renewed scrutiny, due to their unique properties. $CuFeS_2$ is an n-type semiconductor with an unusually low band gap (approximately 0.5 eV),[261] as compared to other ternary Cu containing materials (*e.g.* $CuAlS_2$ = 3.5 eV, $CuGaS_2$ = 2.5 eV, $CuInS_2$ = 1.5 eV), resulting in interesting physical phenomena such as thermo- and ferro-electricity. Furthermore, unlike other I-III-VI_2 materials, the flexible valence of Fe means the material can tolerate the partial +2 oxidation state of Cu centers with unusual magneto-optical properties observed as a result.[262, 263] $CuFeS_2$ also possesses a unique composition amongst infrared chromophores as it is composed entirely of earth abundant, low toxicity elements with atomic number less than 30.

Section 3.2 reviews existing knowledge regarding the synthesis and properties of $CuFeS_2$ nanostructures. First, current synthetic strategies for $CuFeS_2$ NCs are described and their crystal structure and mechanism of formation are considered. Then the optoelectronic properties of $CuFeS_2$ NCs and methods to tune these properties are reported. Finally, potential applications of $CuFeS_2$ NCs are discussed.

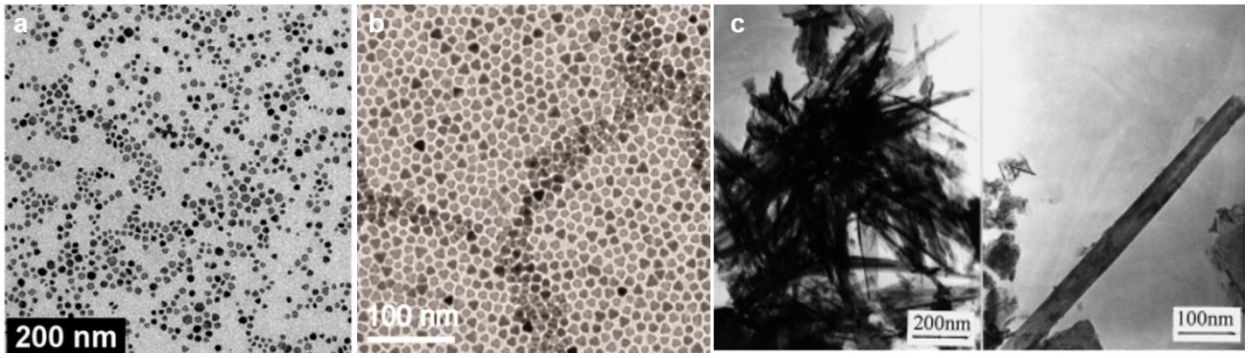

Figure 3.7. TEM images of $CuFeS_2$ NCs; NCs with **a.-b.** spherical and pyramidal morphology synthesized by Bhattacharyya *at al.* and Ghosh *et al*. respectively.[264, 265] Reproduced with permission from reference 264 and 265 respectively. Copyright 2016 American Chemical Society. **c.** $CuFeS_2$ nanorods synthesized by Hu *et al*.[260] Reproduced with permission from reference 260. Copyright 1999 Elsevier Science S.A.

A range of synthetic processes have been used to synthesize colloidal $CuFeS_2$. Early reports of nanostructured $CuFeS_2$ relied on hydrothermal syntheses, resulting in agglomerates of spherical and rod-shaped NCs.[259, 260] Recently, high quality $CuFeS_2$ NCs have been produced with a variety of sizes and morphologies (Figure 3.7) using thermal decomposition,[266-268] hot-injection,[264, 265, 269] and heat-up methods.[270] In all cases, as for the synthesis of $CuInS_2$ NCs, precursors, surfactants, and their concentrations were carefully selected to account for the difference in reactivity between the hard (Fe^{3+}) and soft (Cu^{+}) cations. A good example of this is the synthesis of Bhattacharyya *et al.*, in which CP $CuFeS_2$ NCs with size below the Bohr exciton radius were produced using a hot-injection technique at 180°C.[264] The authors injected both elemental sulfur and dodecanethiol into a solution containing Cu and Fe precursors. Without both S precursors the formation of unwanted Cu and Fe sulfides was observed. Furthermore,

complete dissolution of the cationic precursors was required to avoid the formation of impurity phases.

$CuFeS_2$ commonly exists in the CP structure; in fact, the mineral chalcopyrite ($CuFeS_2$) gave the structure its name. The CP structure has already been described in Section 3.1.3, however, briefly for $CuFeS_2$ the structure is tetragonal belonging to the space group $I_{\bar{4}2d}$ with lattice constants $a = b = 5.24$ Å, and $c = 10.30$ Å.[271] In contrast to $CuInS_2$, the wurtzite (WZ) polymorph of $CuFeS_2$ has been reported only once by Kumar *et al.*, who synthesized micron-size structures of WZ $CuFeS_2$ with a flower like morphology.[268] Refinement of the synthesis of this hexagonal system and complete characterization of its optical properties are of significant interest to the scientific community, due to the strong relationship between crystal structure and properties of the system. Recent work has shown that the WZ structure of $CuInS_2$ NCs contains ordered cations in interlaced crystals.[272] Should WZ $CuFeS_2$ NCs exhibit similar ordering, they hold great potential as a thermoelectric material, due to both the small band gap of the semiconductor in the infrared spectral region (0.5 – 0.6 eV)[261] and its interlaced crystal structure that disrupts thermal conductivity without affecting electron transport.

Few reports exist describing the mechanism of formation for $CuFeS_2$ NCs. Kumar *et al.* theorized that, similar to WZ $CuInS_2$, the formation of WZ $CuFeS_2$ occurred via a hexagonal Cu_2S intermediate, however, that intermediate was not isolated.[268] In the synthesis of CP $CuFeS_2$, both copper and iron sulfide phases are frequently formed as impurity phases. Therefore, it is possible that NCs are produced via cation exchange into nuclei of the binary sulfides. However, given the importance of balancing the reactivity of the cationic precursors in producing $CuFeS_2$, it is likely that CP NCs nucleate as a ternary material. Some controversy exists regarding the chemical valence of Cu and Fe in $CuFeS_2$. Certain reports show monovalent

Cu and trivalent Fe ions,[273] still in others a mixture of $Cu^{+}Fe^{3+}S_2$ and $Cu^{2+}Fe^{2+}S_2$ is observed.[262] Such studies have yet to be conducted on nanostructured $CuFeS_2$, however, the oxidation state of the constituent atoms must be carefully considered when designing a synthesis for $CuFeS_2$ NCs.

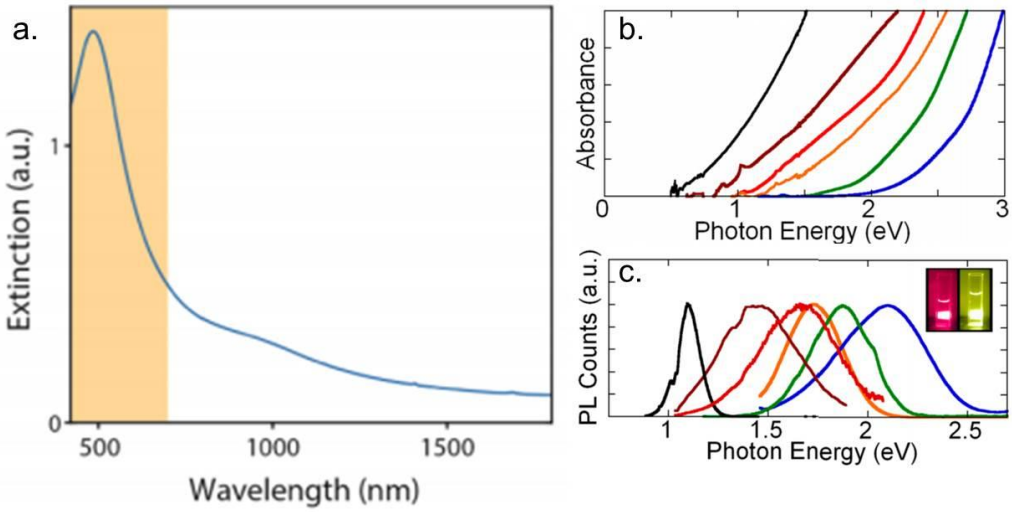

Figure 3.8. Optical properties of $CuFeS_2$ NCs; **a. T**he absorbance spectrum of $CuFeS_2$ the characteristic peak at 480 nm is highlighted.[265] Reproduced with permission form reference 265. Copyright 2016 American Chemical Society. **b.** The absorbance spectra of confined $CuFeS_2$ NCs and **c.** the fluorescence spectra of confined $CuFeS_2$-CdS NCs with size 3 – 15 nm.[264] Reproduced with permission form reference 264. Copyright 2016 American Chemical Society.

The unique optical properties of $CuFeS_2$ NCs stem from the electronic structure of the material. Fe is known to introduce deep trap states in the fundamental band gap of numerous semiconductors.[274, 275] Correspondingly, in $CuFeS_2$, Fe introduces an intermediate band (IB) within the fundamental gap of the material composed predominantly of empty Fe *3d* orbitals. Thus, despite a valence band (VB) to conduction band (CB) transition energy of 3.2 eV, the onset of absorbance is observed from 0.5 – 0.6 eV.[260, 265, 267] The absorbance spectra consists of a peak at around 480 nm accompanied by a broad shoulder centered at around 950 nm (Figure **3.8**a). These features correspond to electronic transitions from the VB to the IB and result in the distinctive purple color of the NCs. Tunable onset of absorption has been reported for $CuFeS_2$ NCs with size less than 15 nm. The observed band gap values spanned the range 0.5 − 2 eV for

quantum dots of diameter 15 – 3 nm (Figure 3.8b). The empirical size-band gap relationship was described as:

$$E = \frac{4.304}{d^2} + 0.515 \qquad (3.1)^{264}$$

Fluorescence has not been observed from bare $CuFeS_2$ NCs. However, on shelling with CdS, bright luminescence centered at approximately 1.1 eV, with QY as high as 87%, was observed. Emission was broad and a significant Stokes shift was reported, suggesting that, as in $CuInS_2$, emission originates from a defect state. Luminescence was tunable across the $0.7 - 2.5$ eV spectral window by tuning the size of the $CuFeS_2$-CdS NCs (Figure 3.8c). The observation of a linear increase in the Stokes shift with increasing quantum dot band gap energy and evidence obtained from transient absorption measurements suggest that the emissive transition involves a delocalized CB electron and a VB hole localized at an internal defect.[264]

The coating of $CuFeS_2$ with CdS has been utilized to passivate non-radiative excitonic decay pathways at NC surfaces, resulting in the observation of fluorescence, as described in the previous paragraph. The composition of these $CuFeS_2$-CdS NCs was characterized using inductively coupled plasma optical emission spectroscopy (ICP-OES). Layer-by-layer digestion of the NCs was performed, yielding a composition profile. This showed that the mole fraction of Fe remained approximately equal throughout the NC, while larger amounts of Cd and smaller amounts of Cu were found at the NC surface. This indicates alloying of the outer layer of the NC in which Cd is substituted for Cu.[264] Changes in the band gap energy of NCs corresponding to changes in their composition were not characterized completely. Another common NC shell material is ZnS. The shelling of $CuFeS_2$ with ZnS has yet to be studied for NCs, however, a recent report indicated that doping $CuFeS_2$ with Zn increased the carrier concentration of the

material resulting in improved thermoelectric properties.[276] A study of the properties of $CuFeS_2$ NCs alloyed or shelled with ZnS could therefore prove valuable.

Due to its band gap in the infrared spectral region (0.5 - 0.6 eV), $CuFeS_2$ has attracted significant interest as a thermoelectric material.[263, 277, 278] NCs have also recently risen to prominence as promising thermoelectric systems, due to the importance of grain boundaries in achieving low thermal conductivity.[56] As such, the thermoelectric properties of $CuFeS_2$ NCs have been the subject of considerable interest. The electrical conductivity, Seebeck coefficient and thermal conductivity of $CuFeS_2$ NCs were measured by Liang *et al.*[269] While the resultant figure of merit $ZT = 0.264$ at 500K was by no means record breaking, the authors observed that ZT was enhanced by 77 times for $CuFeS_2$ NCs with respect to the bulk material, demonstrating significant potential for the nanostructured system.

The properties of $CuFeS_2$ also lend themselves well to use in photothermal tumor therapy. Ghosh *et al.*[265] demonstrated that $CuFeS_2$ NCs coated with an amphiphilic polymer were easily dispersed in aqueous solution and upon laser excitation (808 nm) exhibited a high molar absorption coefficient ($\varepsilon = 5.2 \times 10^6\ M^{-1}cm^{-1}$) and significant heating in water with photothermal transduction efficiency of 49%. Furthermore, viability tests carried out on two different cell lines indicated that the $CuFeS_2$ NCs were not cytotoxic at a therapeutic dose.

Nanostructures of $CuFeS_2$ have also been exploited in both energy storage and energy generation. Ding *et al.* successfully used hexagonal $CuFeS_2$ nanoplates as a cathode material in a lithium ion battery.[279] Moreover, $CuFeS_2$ NCs were utilized as the counter electrode in dye sensitized solar cells fabricated by Wu *et al.*[280] When compared to devices with a Pt counter electrode, those with $CuFeS_2$ as the counter electrode exhibited improved power conversion

efficiency (8.10% *vs.* 7.74%), showing excellent electrocatalytic performance in the reduction of the I^-/I^{3-} redox couple.

In summary, $CuFeS_2$ and its nanostructures are unique among the I-III-VI_2 materials, possessing a remarkably small band gap (approximately 0.5 eV) and low toxicity, earth abundant constituent elements. These properties lend themselves well to thermoelectric and photothermal applications. Promising results have been reported in these areas; however, exquisite synthetic control has yet to be extended to the composition, morphology, or crystal structure of $CuFeS_2$ NCs and a complete understanding of their mechanism of formation has yet to be developed. While the electronic structure of the system is well established and confined NCs have been well characterized, the effect of non-stoichiometric compositions and shelling on the optoelectronic properties of $CuFeS_2$ NCs are not yet understood and would be interesting areas for future study.

3.3 Synthesis & Characterization of $AgFeS_2$ NCs

The silver analogue to $CuFeS_2$, $AgFeS_2$, is unusual in that there is a scarcity of facile synthetic routes to the NC product. One such synthesis exists, reported by Han *et al.* in 2013.[119] The authors used the thermal decomposition of iron(III) diethyldithiocarbamate ($Fe(DDTC)_3$) in the presence of $AgNO_3$ and oleylamine to produce spherical NCs with diameter approximately 15 nm. These NCs exhibited interesting physical properties including superparamagnetism above 8 K and a band gap in the near-infrared (1.21 eV). Continued heating of the particles led to the formation of Ag_2S-Fe_7S_8 heterodimers with thermogravimetric analysis and differential scanning calorimetry measurements indicating that a reversible phase transformation occurred at 176°C. The synthesis did not yield particles with controllable size or morphology; thus confinement effects were not observed. Prior to this, bulk crystals of $AgFeS_2$ had been prepared by Boon from $KFeS_2$ using a cation exchange technique.[271] However, the

physical properties of the material were not explored in depth. More recently, Sciacca *et al.* prepared large nanowires of $AgFeS_2$ (greater than 250 nm in diameter; greater than 10 μm in length) from Ag nanowires using a cation exchange procedure.[281] The authors observed that $AgFeS_2$ formed via a Ag_2S intermediate and measured a direct optical transition from the product nanowires at 0.88 eV. Luminescence has yet to be reported from $AgFeS_2$. Given the measured band gap values for $AgFeS_2$ (1.21 eV and 0.88 eV), its nanostructures hold great promise as light-absorbing materials and could also be used for multiple exciton generation.[119, 281]

$AgFeS_2$, also known by the mineral name lenaite, has a tetragonal CP unit cell similar to that of $CuFeS_2$. It was characterized by Boon in 1944, who assigned the structure to space group $I_{\bar{4}2d}$ with lattice parameters $a = b = 5.66$ Å and $c = 10.30$ Å (Figure 3.9a). Both Ag and Fe atoms are tetrahedrally surrounded by S atoms, with distances Ag–S of 2.47 Å, and Fe–S of 2.25 Å.[282] Natural deposits of lenaite are rare and thus chemical composition has only been analyzed twice with empirical formulae $Ag_{0.96}Fe_{1.01}S_{2.02}$, and $Ag_{0.98}Fe_{0.98}S_{2.04}$ reported.[282] Composition has not been explicitly reported for any man-made $AgFeS_2$. However, EDS mapping has been used to demonstrate the presence of all constituent atoms.[119]

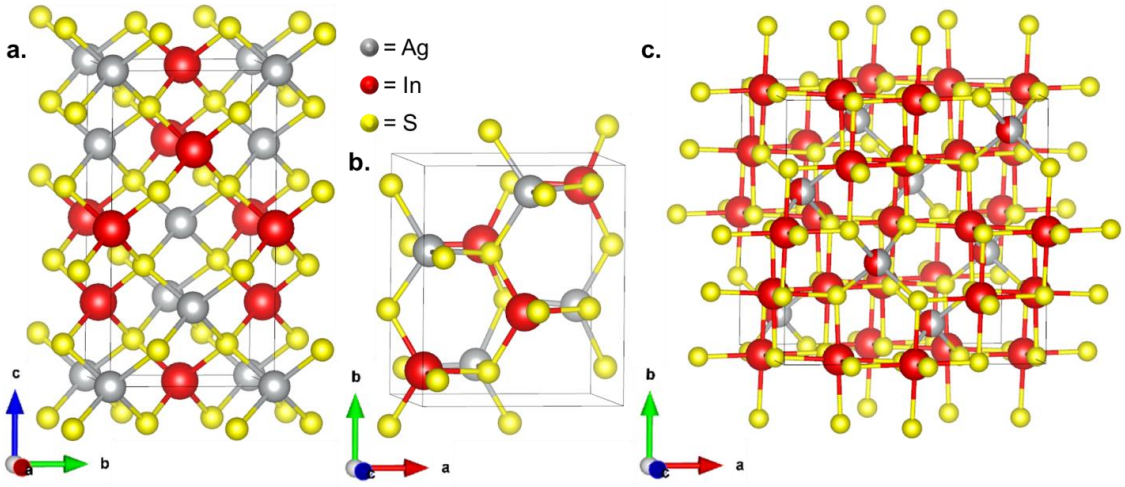

Figure 3.9. Structures of $AgInS_2$; **a.** Tetragonal CP phase; **b.** Orthorhombic pseudo-WZ phase; and **c.** Cubic phase with composition $AgIn_5S_8$.

NCs of the related material $AgInS_2$ are known to crystallize in three distinct structures: tetragonal, orthorhombic, and cubic (Figure 3.9). As in the $CuInS_2$ system described in Section 3.1.3, the thermodynamic crystal structure is the cation-ordered, tetragonal CP phase with a cubic close packed arrangement of S^{2-} anions. However, unlike $CuInS_2$, for $AgInS_2$ a hexagonal close packed arrangement of S^{2-} anions contains formally ordered cations. This results in a doubling of the WZ unit cell, causing the formation of a pseudo-WZ, orthorhombic structure.[283] The reported optical properties of orthorhombic and tetragonal $AgInS_2$ NCs are typically similar,[284] however, calculations indicate that the orthorhombic phase possesses a larger band gap (1.98 eV) than the tetragonal phase (1.87 eV).[283, 285] Defect emission is observed from both phases and bears some resemblance to the luminescence profile of $CuInS_2$ NCs (broad FWHM $\sim$ 85-150 nm; large Stokes shift $\sim$ 0.66 eV). Study of the origin of this emission continues, however, initial evidence suggests a DAP recombination mechanism is responsible for luminescent decay.[286, 287] The cubic material $AgIn_5S_8$ and its copper analogue possess the spinel structure, derived from $CdIn_2S_4$, in which divalent Cd is replaced by monovalent Ag and trivalent In. This structure results in the presence of vacancies in the cation sublattice, thus $AgIn_5S_8$ is a defect semiconductor which exhibits DAP luminescence.[288] The system is also known to possess a smaller band gap in the bulk than the orthorhombic or tetragonal systems (1.80 eV).[284] Nanocrystals of $AgIn_5S_8$ have been synthesized with tunable luminescence across the visible region and QY approximately 25%. They have also been used as fluorescent labels and in photocatalytic systems.[289-291] Ag-Fe-S analogues of the Ag-In-S systems could demonstrate similar desirable structural and optoelectronic properties.

There remains a lot to be learnt about $AgFeS_2$, in particular its structural, optical and electronic properties at the nanoscale. Ternary chalcogenide materials with similar band gaps

have demonstrated great potential in a wide range of applications.[292] It is hoped that $AgFeS_2$ will hold similar promise.

4. PHASE DEPENDENT VISIBLE TO NEAR-INFRARED PHOTOLUMINESCENCE OF $CuInS_2$ NANOCRYSTALS [b]

4.1 Introduction

Semiconductor nanocrystals (NCs) have garnered significant attention from the scientific community due to their tunable, size-dependent optoelectronic properties and large surface area.[293, 294] These properties give rise to many potential applications, including use in photovoltaic devices,[295] biological sensing,[296] as catalysts,[297] and photocatalysts.[298] Amongst the most commonly studied semiconductor NC systems are the II-VI Cd chalcogenides.[299, 300] However, currently these systems are not optimal as the toxicity of Cd leads to concerns about disposal of NC containing devices and limits *in vivo* use.[301] Further they suffer from photoinstability under the conditions used for water splitting, restricting their use as photocatalysts.[302, 303] Therefore NC systems with different constituent elements, but similar optoelectronic properties are sought.

$CuInS_2$ is a particularly promising alternative to the Cd chalcogenide systems, due to the lower toxicity of its constituent elements and its high photostability.[227] Further, the material has a direct band gap approximately 1.5 eV in magnitude,[140] ideally energetically situated for water reduction, and a large optical absorption coefficient ($\alpha > 10^5$ cm^{-1}).[129] NCs of $CuInS_2$ have also shown unexpected phases not observed in the bulk, with nanocrystals reported in three distinct structures: chalcopyrite (CP), zinc blende (ZB), and wurtzite (WZ).[190, 304] CP, the thermodynamic product seen in the bulk phase, is a tetragonal distortion of the cubic ZB phase. It is also the most commonly produced phase and thus has been extensively studied.[141, 170, 198, 305]

[b] Portions of this chapter have been previously published in Leach, A.D.P. et al., *J. Mat. Chem. C*, **2015**, *3*, pp. 3258-3265. Copyright 2015 Royal Society of Chemistry.

The hexagonal WZ structure of $CuInS_2$, only isolable thus far in nanostructures, is particularly interesting as it is anisotropic in the crystallographic *c*-direction.[306] The exploitation of this anisotropy will improve and control electronic, structural and chemical properties in light-absorbing technologies: the anisotropic electronic structure can be used for orthogonal charge propagation in solar cell or photocatalyst design;[81] the hexagonal crystal structure is being used to grow asymmetric nanocrystals,[307, 308] which can act as light absorbing antennae;[309] the anisotropic surface chemistry can be used to enhance epitaxial interactions to an appropriate substrate and has been used to increase charge transfer rates in solar cell design, improving efficiencies.[166]

The WZ phase of $CuInS_2$ NCs was first identified in 2008 by Pan *et al.*[146] Since then, WZ $CuInS_2$ NCs have been synthesized using a variety of methods with a range of accessible morphologies including plates, rods and spheres.[146, 155, 310] Fundamental studies on both cation-ordering within the structure[272] and the electronic band structure of the material[311] have been undertaken. However, the luminescence properties of this material have not yet been completely elucidated, as few examples of luminescent WZ NCs have been reported and none synthesized via direct methods.[168]

The mechanism by which the WZ structure is preferentially formed in colloidal syntheses is not yet fully understood. Several groups have shown evidence of a hexagonal Cu_2S intermediate, possibly achieved through the decomposition of a Cu thiolate complex.[146, 161, 307] Others have evoked the role of stronger metal coordinating agents controlling nucleation kinetics.[130, 157] Without complete understanding of the mechanism, the production of single crystalline, monodisperse, quantum confined WZ $CuInS_2$ remains a considerable challenge.

Colloidal syntheses often instead yield polytypic NCs or hybrid particles composed of Cu_2S—In_2S_3 or Cu_2S—$CuInS_2$.[157, 161, 167, 312-315]

In this chapter, single crystalline NCs of $CuInS_2$ are prepared by a colloidal synthesis through the reaction of In_2S_3 NCs, formed *in situ*, with a Cu thiolate complex (Figure 4.1). By changing the reaction temperature, the crystalline phase, optical properties, and mechanism of formation of the product can be controlled. We propose that at low reaction temperature, cubic $CuInS_2$ is formed by the intercalation of Cu^+ ions into the tetragonal In_2S_3 intermediate. At higher reaction temperatures, the In_2S_3 acts only as an In^{3+} reservoir and WZ $CuInS_2$ NCs are formed by the intercalation of In^{3+} into a hexagonal Cu_2S intermediate. Two distinct regions of emission are observed in the photoluminescence (PL) spectra of these NCs. Emission in the visible region is assigned to ZB $CuInS_2$.[155, 198, 241, 316] A broad peak in the near-infrared (NIR) is also observed and correlates to the presence of WZ $CuInS_2$ NCs in the product.

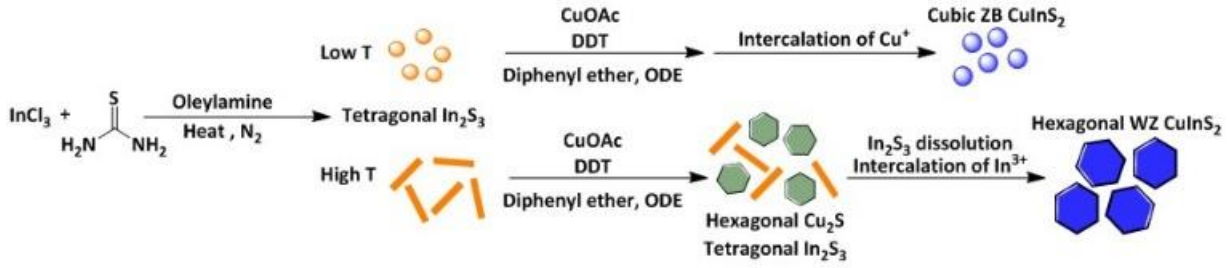

Figure 4.1. Schematic illustration of the synthesis of $CuInS_2$ NCs.

This is the first report of WZ $CuInS_2$, produced using a direct synthesis, with emission in the NIR.[168] This emission will facilitate the study of these NCs through luminescence spectroscopies (Chapter 5).[133, 317, 318] The complete understanding of this material's optical properties is key to the realization of its potential in photovoltaic and photocatalytic applications. Furthermore, the observation of NIR PL within the tissue transparency window, from NCs with non-toxic constituent elements, shows the promise of WZ $CuInS_2$ for use in biological applications.

4.2 Experimental Techniques

4.2.1 Materials

Indium chloride ($InCl_3$, Alfa Aesar, 99.99%), thiourea (Sigma-Aldrich, ≥ 99.0%), oleylamine (OlAm, Aldrich, 70%), copper(I) acetate (CuOAc, Strem Chemicals, 99%), 1-dodecanethiol (DDT, Aldrich, ≥ 98.0%), octadecene (ODE, Aldrich, 90%), diphenyl ether (Sigma-Aldrich, 99%) and tert-dodecylmercaptan (t-DDT, Aldrich, 98.5%) were purchased and used as received. Standard air-free Schlenk techniques were used throughout with N_2 as the inert gas.

4.2.2 Synthesis of $CuInS_2$ NCs

$CuInS_2$ NCs were prepared via the reaction scheme shown in Figure 4.1. Briefly, $InCl_3$ (0.5 mmol) and thiourea (1.0 mmol) were added to oleylamine (10 mL) in a reaction vessel, degased for 1 hr, and heated to the required temperature (115 – 235°C) under a N_2 atmosphere. Separately CuOAc (0.5 mmol) was suspended in ODE (500 μL), diphenyl ether (500 μL) and DDT (1.0 mmol). At the required reaction temperature, 1 mL of the Cu solution was injected quickly (less than 1 s) into the reaction vessel. After 30 min, the heat was removed and the reaction mixture was cooled to room temperature. The obtained $CuInS_2$ NCs were precipitated by addition of methanol/ acetone (v/v, 2:1) and then purified by repeated centrifugation and decantation with addition of methanol/ acetone and hexanes.

4.2.3 Transmission Electron Microscopy

Transmission electron microscopy (TEM) images were collected and energy dispersive X-ray spectroscopy (EDS) was carried out using a FEI Tecnai Osiris™ digital 200 kV S/TEM system. TEM samples were prepared by drop casting a dilute NC solution in hexanes onto a nickel grid with a carbon support and drying in air at room temperature. NCs were sized

manually using ImageJ with number of particles measured, n = 120. Lattice fringes were measured by generating a profile plot of an area of the image using ImageJ, manually counting the cycles, and dividing the length of the profile plot by the number of cycles. The minimum number of cycles used was ten. EDS spectra were collected for 2 min and quantified using the Espirit software. Cu and S were quantified using the K series of peaks, while In was quantified using the L series. All spectra were background subtracted and overlapping Cu sample and Ni grid peaks were deconvoluted before quantification. Drift-corrected EDS maps were collected for 90 s with beam current 1.5 nA.

4.2.4 X-ray Diffraction and Rietveld Refinement

X-ray diffraction (XRD) measurements were performed using a Scintag XGEN-4000 X-ray diffractometer with a CuK_α (λ = 0.154 nm) radiation source. The resulting diffraction patterns were then visually compared to literature data to determine the structure.[167, 319] Rietveld Refinement was performed using the General Structure Analysis System (GSAS) suite of programs and the EXPGUI.[320-322] The GSAS suite of programs allows the refinement of parameters including site occupancy, atomic parameters, lattice parameters, background coefficients, peak profiles, atomic displacements and preferred orientation. The quality of the refinement is monitored by visual comparison of calculated and observed patterns, facilitated by plotting a difference curve below the x-axis, and calculating the goodness-of-fit parameter, χ^2.

4.2.5 Optical Spectroscopy

The absorption spectra of NC samples were collected from 300 – 1400 nm on a ultraviolet-visible spectrophotometer (Jasco V-670). Visible PL spectra were measured from 550 – 900 nm on a spectrofluorometer (Jasco FP-8300). NIR PL spectra were measured from 800 – 1400 nm on a different spectrofluorometer (Jobin Yvon/Horiba Fluorolog-3 FL3-111).

Samples were measured in solution with hexanes as the solvent. Both visible and NIR PL were measured with excitation wavelength 348 nm. Data were then matched at 800 nm and normalized to the quantum yield (QY). The QY was determined for each sample by comparison to a Rh-101 standard.[323] Finally data were analysed by using the Fityk application to fit Gaussian functions to emissive peaks.[324] The goodness of fit parameter, χ^2, was minimized via the Levenberg-Marquardt algorithm.

4.3 Results & Discussion

4.3.1 Morphology of $CuInS_2$ NCs

TEM of the product NCs indicated that a variety of morphologies and NC sizes were accessible via this synthetic route (Figure 4.2). At low temperature (115 – 135°C) small, monodisperse, spherical particles (approximately 1.5 nm in diameter) were observed that showed an increase in size at the higher temperature. When the reaction temperature was above 135°C, rod- and plate-like products were seen in addition to the small spheres. Both these new morphologies showed increased size with increased reaction temperature, though the rods had a consistent width (1.8 nm). Further, the proportion of plates observed increased with reaction temperature.

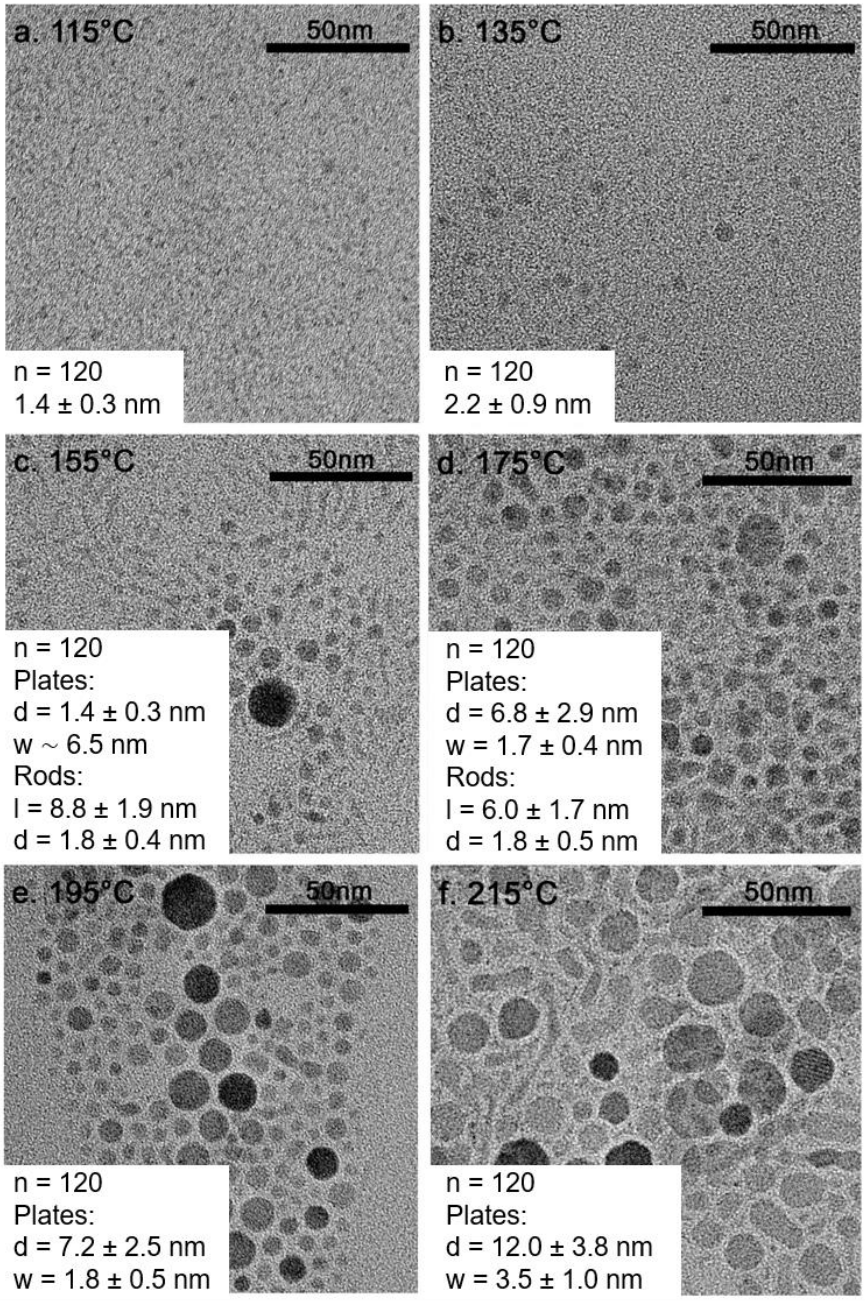

Figure 4.2. TEM images of $CuInS_2$ NCs prepared at reaction temperatures from 115 - 215°C (**a.-f.**).

4.3.2 Structure & Composition of $CuInS_2$ NCs

In order to determine the structure of the prepared NCs XRD data were collected for each sample (Figure 4.3a). For samples prepared at 115°C, reflections characteristic of the ZB phase were observed. As the reaction temperature was increased, however, reflections characteristic of the WZ phase increased in intensity, appearing dominant for samples prepared

at 215°C and 235°C. This structural trend was confirmed by Rietveld Refinement of the resultant XRD patterns for each reaction temperature (Figure 4.3b).

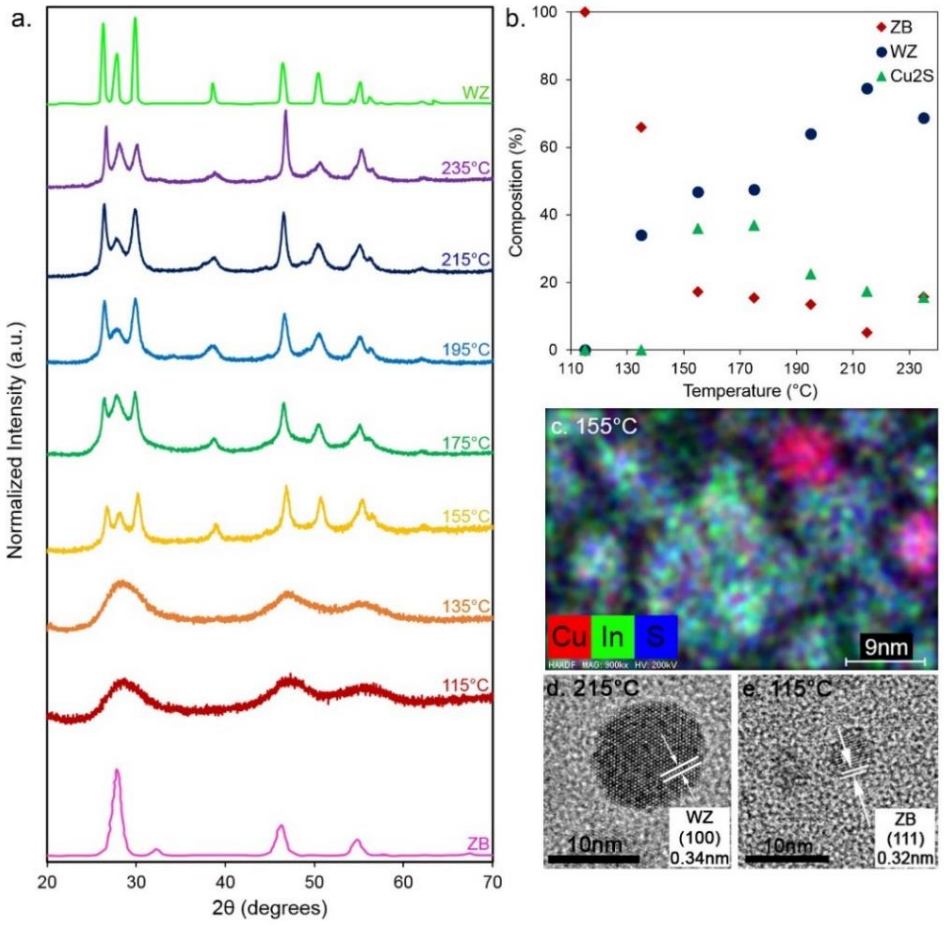

Figure 4.3. Structural characterization of $CuInS_2$ NCs; **a.** XRD of $CuInS_2$ NCs prepared at various temperatures. Pure ZB and WZ spectra are digitized from the work of Chang *et al.*;[167] **b.** Proportion of WZ (blue), ZB (red) and hiCC Cu_2S (green) phases present in each sample plotted as a function of temperature, as determined by Rietveld Refinement of XRD; **c.** EDS map of $CuInS_2$ NCs prepared at 155°C showing the presence of Cu_2S NCs; **d.-e.** High resolution TEM (HRTEM) images of $CuInS_2$ NCs prepared at 215°C (plates) and 115°C (spheres) respectively showing lattice fringes.

An EDS map collected from the sample prepared at 155°C (Figure 4.3c) indicated that some plate-shaped particles seen at intermediate temperatures consisted of only Cu and S. As a result the Rietveld Refinement used to fit a structural model to the experimental data included three phases: the ZB and WZ $CuInS_2$ phases reported by Chang *et al.* and the high chalcocite (hiCC) Cu_2S phase reported by Wuensch *et al.*, (Appendices B.1 and B.2).[167, 319, 322] For samples prepared at 115°C and 135°C, data were fit to within a statistically acceptable tolerance without

the addition of the Cu_2S impurity phase (Appendix B.2).[325] Small amounts of WZ and hiCC Cu_2S may be present at these low reaction temperatures; however, crystallite size broadening of the more intense ZB peaks obscures the reflections from these phases.

Application of the Scherrer equation to the broadened peaks yielded NC domain sizes in good agreement to those of nanoplates (at high temperatures) and spheres (at low temperatures) measured by TEM for samples prepared below 235°C (Appendix B.3). This suggests that the NCs are single crystalline, in contrast to many literature examples, which exhibit polytypism.[314, 315] In order to ensure the prepared NCs were both single phase and single domain HRTEM images of individual NCs were collected. Lattice fringes in HRTEM showed that the nanoplates (Figure 4.3d) were single crystalline with a d-spacing of 0.34 nm indexed to the (100) plane of WZ $CuInS_2$.[155] In contrast, while the smaller spherical NCs (Figure 4.3e) are also single crystalline, they have a d-spacing of 0.32 nm indexed to the (111) plane of ZB $CuInS_2$.[167]

4.3.3 Optical Characterization of $CuInS_2$ NCs

The absorbance spectra for NC samples are shown in Figure 4.4a. At lower reaction temperatures, the absorbance onset increases with increasing temperature, suggesting that the small NCs obtained at low reaction temperature are quantum confined. Above 175°C, there is no significant change in absorbance onset, indicating that NCs have grown larger than the Bohr exciton radius of $CuInS_2$ (approximately 4 nm).[140] This is in good agreement with the average size of NCs, 7 ± 3 nm at 175°C. A Tauc plot (Figure 4.4b) was used to determine the band gap of the sample prepared at 215°C, which consisted of greater than 80% WZ phase NCs.[326, 327] The calculated band gap of 1.56 eV was consistent with the literature value for the WZ phase, 1.55 eV.[272]

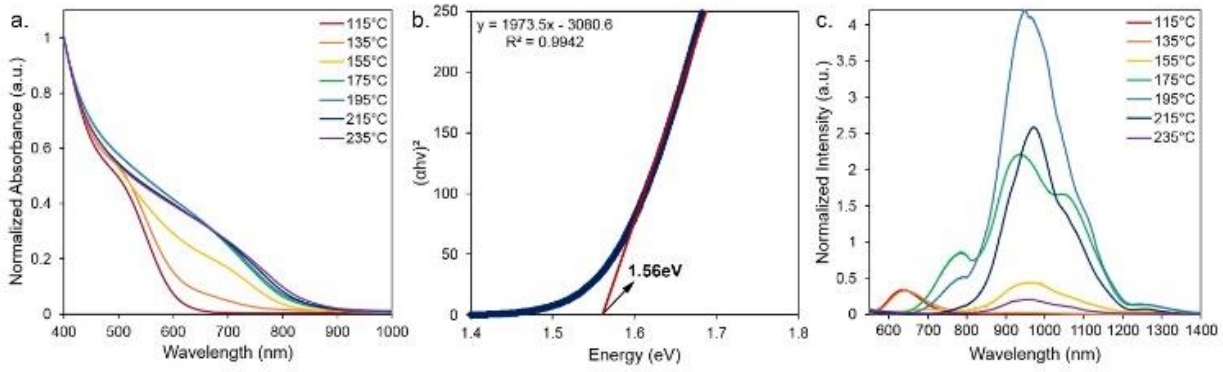

Figure 4.4. Optical characterization of $CuInS_2$ NCs; **a.** Absorbance spectra of $CuInS_2$ NC dispersions in hexanes prepared at different temperatures; **b.** Tauc plot of the predominantly WZ $CuInS_2$ NCs prepared at 215°C; **c.** PL spectra normalized to the QY of $CuInS_2$ NC dispersions in hexanes prepared at different temperatures.

PL spectra were collected for all samples from 550 – 1400 nm and are shown in Figure **4.4**c normalized to the QY. Multiple emissive peaks can be observed in both the visible and NIR spectral regions. At low reaction temperatures, visible emission at approximately 640 nm is dominant, which has been previously reported for ZB $CuInS_2$, and is consistent with both TEM and XRD analysis.[198, 316] At high reaction temperature only NIR emission is observed. It is attributed to WZ $CuInS_2$, the predominant structure formed at these temperatures.[168] The QY was less than 0.8% for all samples (Appendix B.5).

The visible peak, attributed to ZB $CuInS_2$, was fit to a single Gaussian (Appendix B.6), which showed a red shift as reaction temperature increased. This is most likely due to an increase in the size of the NCs and the relaxation of quantum confinement conditions consistent with trends observed in absorbance spectra and reported in literature examples.[131, 132, 226]

The broad, multimodal shape of the NIR PL peak, centered at approximately 950 nm, and the large Stokes shift (0.25 eV) indicate that emission is from several trap states. To identify the energetic location of specific emissive defects, spectra were fit using Fityk, a curve fitting and data analysis application.[324] The data were fit for all samples by four Gaussians centered at

810, 898, 969 and 1069 nm (Appendix B.6). A more detailed study of the origin and properties of this PL is undertaken in Chapter 5.

4.3.4 Mechanism of Formation of $CuInS_2$ NCs

In order to determine the mechanism of formation of the prepared $CuInS_2$ NCs, the In-S precursor solution, into which the Cu complex was injected, was examined. At 115°C, TEM images collected (Figure 4.5c) indicate that small, spherical NCs of In_2S_3 are formed with diameter 1.1 ± 0.4 nm. XRD measurements (Figure 4.5a) indicated a tetragonal β-In_2S_3 phase (JCPDS card no. 25-0390) with considerable line broadening observed due to the small crystallite size.[328] EDS analysis showed that the NCs were S deficient with composition $In_2S_{2.5}$. The ZB $CuInS_2$ product of the complete reaction (Figure 4.2) at 115°C is of comparable size (1.4 ± 0.3 nm) to the β-In_2S_3 precursor and the crystal structures of the two materials are closely related (tetragonal to cubic). It is therefore likely that the ZB $CuInS_2$ product is formed by the intercalation of Cu^+ ions into the previously formed β-In_2S_3 NC host (Figure 4.5c).[329]

At a reaction temperature of 215°C, In_2S_3 NCs with rod-like morphology are observed with length 9.2 ± 5.9 nm and diameter 1.2 ± 0.4 nm (Figure 4.5b). The resulting XRD pattern (Figure 4.5a) was also indexed to the tetragonal phase, β-In_2S_3. The sharp (1 0 9) and (2 2 12) reflections suggest that rods are elongated in the *c*-direction.[330, 331] Since the In_2S_3 is in the same phase at both reaction temperature extremes, it is unlikely that intercalation of Cu^+ into tetragonal β-In_2S_3 is also the mechanism by which the hexagonal WZ $CuInS_2$ is formed. Moreover, the morphology of the In_2S_3 precursor rods is very different than the $CuInS_2$ nanoplates. An alternative mechanism is needed to explain the formation of the distinct product crystal structure (WZ) at higher reaction temperature. Literature examples have shown that at reaction temperatures greater than 200°C decomposition of a Cu thiolate complex can occur

yielding a Cu_2S intermediate.[332-336] It was hypothesized that the formation of WZ $CuInS_2$ proceeds via this mechanism. To confirm the hypothesis, the chemistry of the injected Cu—DDT complex was altered.

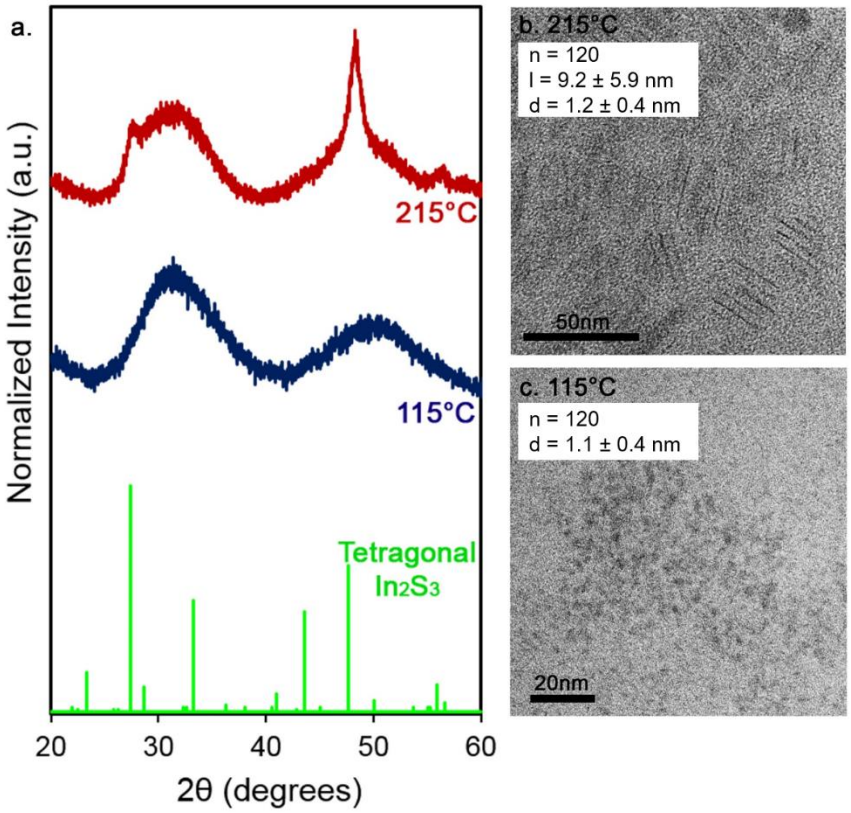

Figure 4.5. Characterization of In_2S_3 NCs; **a.** XRD patterns collected for In_2S_3 NCs prepared at 115°C and 215°C. Data for tetragonal β-In_2S_3 is from JCPDS card no. 25-0390; **b.-c.** TEM images for precursor In_2S_3 NCs prepared at 215°C and 115°C respectively.

At reaction temperature 115°C, the DDT in the Cu solution was replaced by tert-dodecyl mercaptan (t-DDT). The tertiary carbon adjacent to the thiol in t-DDT facilitates the facile decomposition of the Cu thiolate complex.[337] Therefore the injection of a Cu—t-DDT complex was expected to promote the nucleation of Cu_2S, leading to an increase in the proportion of WZ $CuInS_2$ formed at lower temperatures. XRD data of the NCs produced (Figure **4.6**a) indicated that indeed the dominant phase was WZ even at the low reaction temperature of 115°C. TEM images (Figure 4.6b) showed that the sample was polydisperse with plate-like morphology.

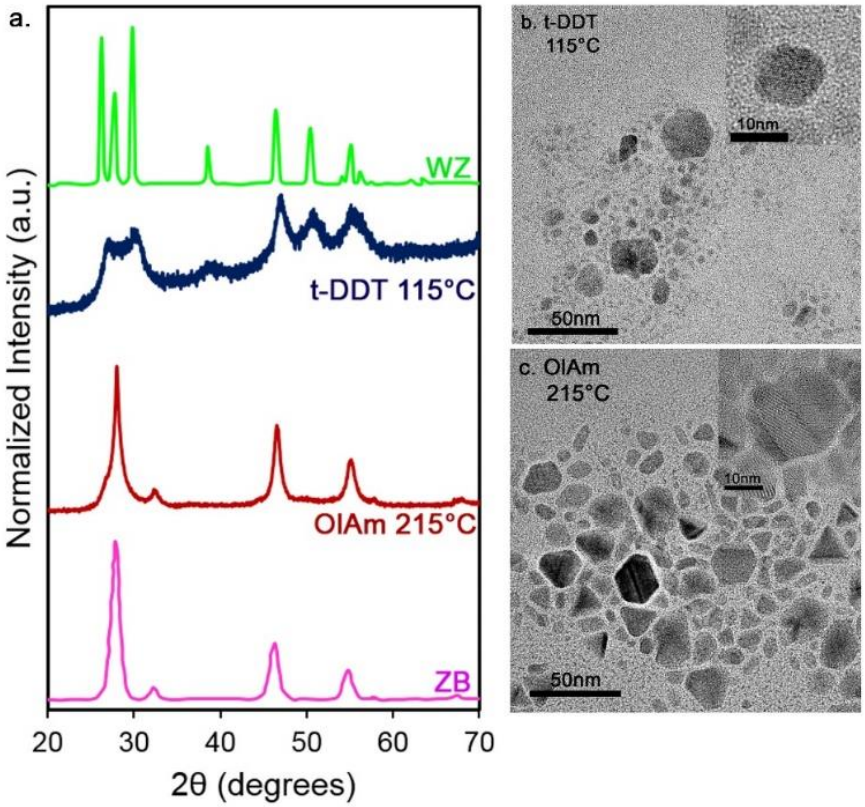

Figure 4.6. Characterization of $CuInS_2$ NCs prepared with different Cu complexes; **a.** XRD patterns collected for $CuInS_2$ NCs prepared with OlAm as the injection solvent at 215°C and t-DDT as the injection solvent at 115°C. Pure ZB and WZ spectra are digitized from the work of Chang et al.;[167] **b.-c.** TEM images collected for samples prepared with t-DDT injection at 115°C and with OlAm injection at 215°C respectively.

In an additional study, the DDT in the Cu solution was replaced by an equimolar amount of oleylamine (OlAm) at reaction temperature 215°C. If the decomposition of the Cu—DDT complex causes the nucleation of hexagonal Cu_2S, allowing the growth of hexagonal WZ $CuInS_2$, the use of a Cu amine complex should give only the ZB phase. The XRD pattern of the resulting NCs (Figure 4.6a) was, as expected, indexed to the ZB phase of $CuInS_2$. TEM images (Figure 4.6c) showed that these NCs had a mixture of morphologies with hexagonal and triangular shapes observed. Lattice fringe spacing indicated that these morphologies were not characteristic of a hexagonal phase, but of twinning of the cubic ZB phase. It is therefore clear that the mechanism of WZ formation proceeds via the decomposition of the Cu thiolate complex.

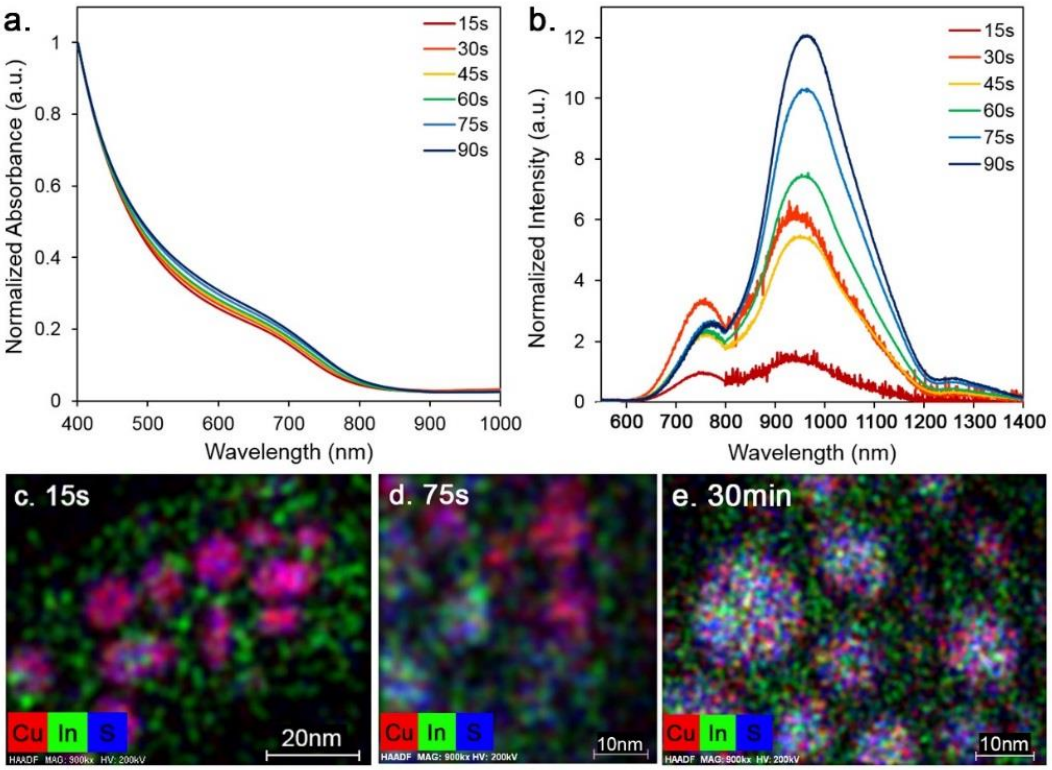

Figure 4.7. Aliquot study of $CuInS_2$ NC synthesis; **a.** Absorbance and **b.** PL spectra of aliquots taken from the synthesis of $CuInS_2$ NCs at 215°C; **c.-d.** EDS maps of the 15s and 75s aliquots taken from the synthesis of $CuInS_2$ NCs at 215°C; **e.** EDS map of the resultant $CuInS_2$ NCs produced by the synthesis for 30 min at 215°C.

To add further support to our mechanistic hypothesis, a detailed aliquot study of the reaction at 215°C was undertaken. Six aliquots of the reaction mixture were taken every 15s from injection of the Cu—DDT complex. The absorbance spectra of the aliquots (Figure 4.7a) showed a steady increase in both onset and intensity with temperature at larger wavelength. This is indicative of both the size and proportion of WZ $CuInS_2$ increasing with time. PL measurements were also performed on each aliquot (Figure 4.7b). Little fluorescence was observed at 15s, suggesting that NCs are not yet completely crystalline, highly defective, or are in the non-fluorescent intermediate phases Cu_2S and In_2S_3.[313, 338] As the reaction progressed a peak in the visible region was observed to grow over the first 30s and then decayed completely by 30 min (Figure 4.4). We have assigned PL in this region to ZB $CuInS_2$ and it is thought that this emission is due to some intercalation of Cu into previously formed β-In_2S_3. This observation

suggests that the ZB $CuInS_2$ NCs are a reversible, kinetic product and WZ NCs are more stable at high reaction temperature. Continued heating caused the ZB NCs to dissolve in order for the growth of WZ particles to progress. This hypothesis is supported by the steady increase in intensity of PL in the NIR, which was assigned to WZ $CuInS_2$.

Figure 4.7c-e show EDS mapping data from aliquots taken at 15s, 75s, and 30 min. Bright field, dark field and elemental analysis images can be found in Appendices B.8 and B.9. After 15 s two distinct types of NC were present: nanoplates (diameter 7.4 ± 2.6 nm, depth 3.4 ± 0.5 nm), and nanorods (length 10.0 ± 4.7 nm, diameter 1.5 ± 0.4 nm). EDS mapping showed that the nanoplates were largely composed of Cu and S with some showing small amounts of In present. Lattice fringe spacing in HRTEM indicated that the nanoplates were single crystalline and had the hiCC Cu_2S structure (Appendix B.8).[312] Literature precedent suggests that the formation of these Cu_2S NCs was due to the decomposition of the Cu thiolate complex into a Cu_2S intermediate.[332-336] The smaller rods were composed of In and S and were similar in size to the β-In_2S_3 rods (length 9.3 ± 1.2 nm, diameter 1.2 ± 0.4 nm) observed before injection.

As the reaction progressed, the nanoplates showed a small increase in size (diameter 7.4 ± 2.6 nm, depth 3.4 ± 0.5 nm at 15s; and diameter 8.6 ± 2.7 nm, depth 3.6 ± 1.1 nm at 75s). Further, EDS mapping indicated that the proportion of In in the plates also increased with time (Figure 4.7c-e). This suggests that the hiCC Cu_2S nanoplates are the most stable structure and early stage growth proceeds primarily through the intercalation of In into these NCs. The small β-In_2S_3 rods decreased in size with time and acted as a reservoir of In^{3+} ions. The large increase in WZ $CuInS_2$ nanoplate size between 75s (Appendix B.8) and 30 min (Figure 4.2) indicates that

beyond the initial intercalation step, there is further growth through the addition of more reactant ions and/or Ostwald ripening processes.

In summary, the proposed mechanism of WZ $CuInS_2$ formation (Figure 4.1) is as follows: on injection of the Cu—DDT complex, decomposition of the thiol causes the nucleation of hiCC Cu_2S. Then, as the reaction progresses, the dissolution of the precursor β-In_2S_3 rods occurs. Excess In in the reaction mixture exchanges into the hiCC Cu_2S nanoplates forming WZ $CuInS_2$. Growth then proceeds until the reaction is quenched. This mechanism is in agreement with a number of literature examples, which report that the formation of WZ $CuInS_2$ occurs via a Cu_2S intermediate.[146, 161, 307] While not always explicitly implicated, in all of these examples a thiol is present in the reaction mixture and the reaction temperature is high enough ($\geq$ 200°C) for the decomposition of the Cu thiolate precursor to occur. Other studies suggest that WZ formation is dependent on the additional presence of a chelating amine ligand that coordinates strongly to the metallic precursors, manipulating the nucleation kinetics.[130, 157] Reinterpretation with our experiments in mind, suggests that the amine chelates the In^{3+} and allows the formation of the Cu_2S intermediate necessary for WZ $CuInS_2$ formation.

4.4 Conclusions

A new synthetic method has been developed that produces WZ $CuInS_2$ nanoplates with broad emission in the NIR. Samples were multiphase (WZ and ZB) and the presence of both β-In_2S_3 and hiCC Cu_2S impurities was observed, however, by tuning the reaction temperature the relative proportion of these phases can be controlled. It was further found that the mechanism of WZ $CuInS_2$ NC formation proceeded via exchange of In^{3+} into a hexagonal Cu_2S intermediate, while ZB $CuInS_2$ NCs were formed via exchange of Cu^+ into a tetragonal β-In_2S_3 precursor. Finally, it was determined that, in order to form the WZ structure, the decomposition of a Cu

thiolate precursor complex was necessary. The mechanistic insight into the formation of this structure will inform future syntheses, advancing progress towards the production of WZ $CuInS_2$ for use in applications.

This chapter describes the first example of WZ $CuInS_2$ NCs, produced using a direct synthesis, with emission in the NIR that the author is aware of. The observation of PL within the tissue transparency window, from NCs with non-toxic constituent elements, shows the exciting potential of WZ $CuInS_2$ for use in biological applications. Additionally, the observation of PL provides a strong foundation for further study of the optical properties of WZ $CuInS_2$ via luminescence spectroscopies (Chapter 5). An understanding of these properties is indispensable in advancing work towards the use of WZ $CuInS_2$ in both photocatalytic and photovoltaic applications.

5. DEFECT LUMINESCENCE FROM WURTZITE $CuInS_2$ NANOCRYSTALS: COMBINED EXPERIMENTAL AND THEORETICAL ANALYSIS [c]

5.1 Introduction

Semiconductor nanocrystals (NCs) of ternary and quaternary Cu chalcogenides have recently garnered considerable interest in a wide range of applications.[339] $CuInS_2$ shows particular promise due to its high molar absorption coefficient and wide band gap (1.5 eV), well situated for utilization in both photovoltaics and photocatalysis.[129, 140] $CuInS_2$ is also appealing for use in biological systems due to its low toxicity with respect to Cd- and Pb-based systems.[169]

$CuInS_2$ NCs typically have the zinc blende (ZB) or chalcopyrite (CP) structure.[198, 332] The CP structure is analogous to ZB, but the cation sublattice is shared by two species, which are ordered, resulting in a tetragonal distortion. NCs with both of these structures have been extensively studied and a variety of synthetic methodologies have been reported.[142, 170, 198, 305] Relevant to lighting and display applications, the emission of CP NCs can be tuned across the visible spectrum.[198] The emission results from a defect inside the NC. A number of different species have been implicated, including sulfur vacancies (V_S),[179, 340] indium at a copper site (In_{Cu}), [179, 340] and Cu^{2+} impurity atoms;[184, 341] yet at this time there is no consensus as to the identity of the defect that is responsible for the observed emission.

In 2008 Pan *et al.*[146] identified a different crystal structure, isolable in $CuInS_2$ NCs. The hexagonal analogue to the ZB structure, wurtzite (WZ), is distinct from both CP and ZB due to its ABAB layered anionic lattice, and is of particular interest as it is anisotropic in the crystallographic *c*-direction. By exploiting this anisotropy it is possible to control the electronic,[81] structural,[307, 309] and chemical[166] properties of the system in light absorbing

[c] Portions of this chapter have been previously published in Leach, A.D.P. et al., *J. Phys. Chem. C*, **2016**, *120* (9), pp 5207–5212. Copyright 2016 American Chemical Society.

technologies. Since 2008, considerable synthetic progress has been made with the isolation of single crystalline WZ NCs of $CuInS_2$ being achieved[157] and the mechanism of their formation being elucidated.[164] Fundamental studies on both cation-ordering within the NC[272] and the electronic band structure of the material[311] have also been undertaken; however, the optical properties of WZ $CuInS_2$ have yet to be completely explained. In particular, the recent observation of photoluminescence (PL) in the near-infrared (NIR) from this material is not fully understood.[164, 168, 169] The NIR PL generated significant interest due to its position within the tissue transparency window. In order to harness the potential of WZ $CuInS_2$, a more comprehensive understanding of the optoelectronic properties is necessary.

Emission from the WZ structure does bear some similarity to that of CP: both peaks are broad and show a large Stokes shift from the band gap of the material. However, the few examples of fluorescent WZ $CuInS_2$ NCs[164, 168] exhibit much lower PL than ZB $CuInS_2$ NCs.[142] Furthermore, a key difference leads the author to question if these two luminescence mechanisms are analogous; while the band gaps are similar (approximately 1.5 eV), the WZ fluorescence (1.3 eV) is lower in energy than that of CP (1.4 eV).[128]

In this chapter, the preparation of luminescent WZ $CuInS_2$ NCs is reported. The dependence of PL intensity on both reaction time and different surface passivation layers are observed. Additionally, time-resolved PL (TRPL) data are collected for these samples and their Zn and Cd alloys, which allow the radiative defect to be identified as an internal point defect. The characteristics of the PL are then compared to defect energy levels calculated using density functional theory (DFT) with the hybrid exchange-correlation functional. This comparison enables the identification of possible candidates for the luminescent defect state.

5.2 Results & Discussion

5.2.1 Synthesis & Characterization of WZ $CuInS_2$ NCs

Luminescent WZ $CuInS_2$ NCs were prepared using a previously reported hot-injection method at 215°C. In this synthesis, Cu_2S forms *in situ*, followed by In exchange.[164] The resulting WZ $CuInS_2$ NCs had plate-like morphology and were approximately 8 nm in diameter. The hexagonal crystal structure was confirmed by both XRD and lattice fringe spacing from high resolution TEM images (Figure 5.1a-b).[164]

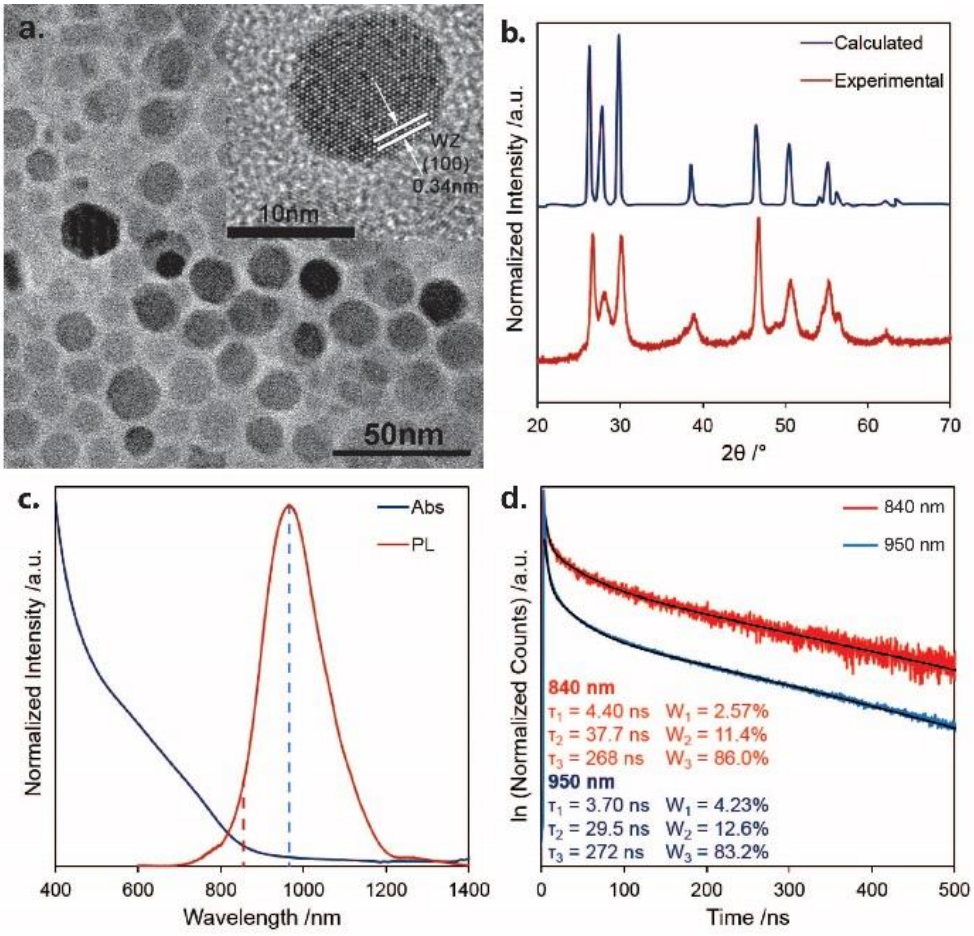

Figure 5.1. Characterization of WZ $CuInS_2$ NCs; **a.** TEM image of WZ $CuInS_2$ NCs (inset: HRTEM image showing lattice fringe spacing characteristic of the WZ (100) plane); **b.** XRD of WZ $CuInS_2$ NCs, the calculated WZ pattern is digitized from the work of Chang *et al.*;[167] **c.** Absorbance (blue) and PL (red) spectra normalized to the QY of $CuInS_2$ NCs in hexanes. Dashed lines indicate wavelengths at which luminescence decay curves were collected (840 nm – red, 950 nm – blue); **d.** Luminescence decay curves of WZ $CuInS_2$ NCs (λ_{ex} = 532 nm, measured at 840 nm (red) and 950 nm (blue)). Curves are best fit with three exponentials (shown in black) where τ_x represents the decay time of the PL emission and W_x represents the relative weights of the decay components.

The NCs exhibited a broad PL peak in the NIR centered at approximately 950 nm, 1.31 eV (Figure **5.1**c.),[164, 168, 169] with a quantum yield of emission (QY) approximately 0.5%. The large peak width (0.25 eV) and Stokes shift (0.20 eV), indicate the emission likely originates from a luminescent defect state.[133, 144, 149, 198, 342] While NCs are polydisperse and emission could originate from a particular size fraction within each sample, it has been reported that QY increases with increasing WZ proportion and thus emission is attributed to this phase.[164]

5.2.2 Time-Resolved Photoluminescence Measurements

TRPL measurements were collected for the fluorescent NCs (Figure 5.1d.) and the decay profiles were best fit with three exponentials with time constants of approximately 4, 30 and 270 ns. The 4 ns decay was assigned to the intrinsic recombination of initially populated core states, as typically assigned to lifetimes of the order of 1 - 5 ns.[318] The 30 ns lifetime was assigned to surface traps as surface-related trap states are usually shallow and therefore show faster decay lifetime compared to the intrinsic defect-related trap states.[316] Lifetimes approximately 15 ns in length have been observed for CP $CuInS_2$ NCs and ascribed to surface trap states.[142, 316] Finally, the longest lifetime ($\tau_3 \sim 270$ ns) was attributed to an internal defect-related state. Longer decay times (greater than 100 ns) have also been reported for CP NCs and assigned to similar states.[142, 179, 316, 318] greater than 80% of the radiative transitions occur with this long decay time, suggesting that this is the most efficient radiative recombination channel.

5.2.3 Luminescence Stability of WZ $CuInS_2$ NCs

To determine the stability of the luminescence, a study of PL intensity with reaction time was performed (Figure 5.2a.). Aliquots of the reaction, collected at 215°C, show that the QY of the NCs increases until the 15 min time point and then decreases significantly over the following 15 min (Figure 5.2b.). This trend was consistent across all samples studied (n = 6). This indicates

that, initially, there is an increase in the proportion of excitons decaying radiatively or, correspondingly, a decrease in non-radiative decay. After 15 min, however, either annealing of the material decreases the proportion of radiative defects within the structure or the efficiency of non-radiative decay paths increases. Typically, no luminescence is reported for $CuInS_2$ samples prepared with the WZ structure. However, reported reaction times are often in excess of 30 min.[157, 166, 307] Thus, it is possible that these samples exhibit PL at earlier stages during their synthesis.

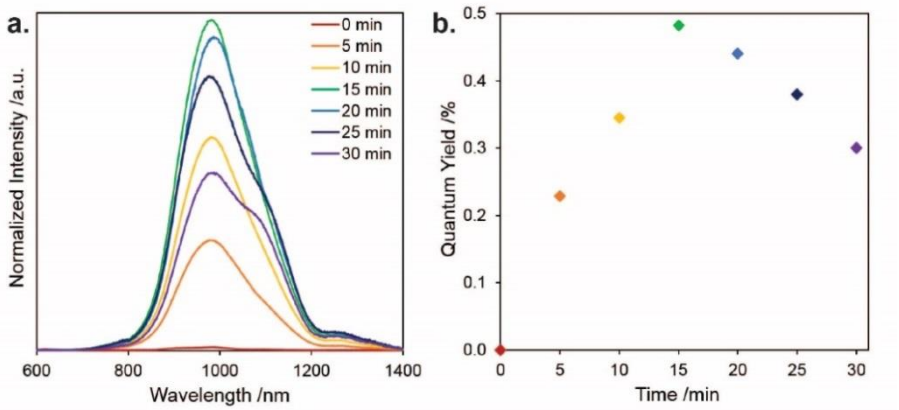

Figure 5.2. Time-dependent luminescence properties of aliquots of WZ $CuInS_2$ NCs; **a.** PL spectra normalized to the QY of $CuInS_2$ NCs in hexanes at different time points during the reaction; **b.** Calculated QY for each time point.

5.2.4 Surface Passivation of WZ $CuInS_2$ NCs

To improve PL efficiency, inorganic surface passivation was undertaken with CdS and ZnS. Literature procedures were used, which were reported to result in alloying of the outer layer of the NCs.[133, 183] Reflections in the powder XRD pattern of the resultant NCs (Appendix C.9) show small shifts to larger (Zn-Cu-In-S) and smaller (Cd-Cu-In-S) angle. This is indicative of alloying rather than the formation of distinct domains of ZnS or CdS, which would result in the formation of additional peaks.[343] No significant increase in particle size was observed on alloying. However, EDS analyses confirmed the presence of Cd/Zn within the NCs (Appendices C.10, C.11, and C.12).

Both alloying procedures resulted in a large increase in the QY: approximately a two-fold increase for Zn-Cu-In-S, and 16-fold increase for Cd-Cu-In-S (Figure 5.3a.). No substantial change in the spectral position or shape of the emission was observed.[144] To try and understand these changes in QY, the PL dynamics of NCs were explored before and after alloying (Figure **5.3**b.). The effective lifetime of the alloyed samples increased with the same order as the QY: $\tau_{eff}(CuInS_2) < \tau_{eff}(Zn\text{-}Cu\text{-}In\text{-}S) < \tau_{eff}(Cd\text{-}Cu\text{-}In\text{-}S)$. Decay profiles were again best fit with three exponentials (Appendix C.8). For both Cd-Cu-In-S and Zn-Cu-In-S, there was a significant increase in the proportion (W_3) of the crystalline defect decay (τ_3) and a corresponding decrease in proportion (W_2) of the surface trap decay time (τ_2). It is likely, therefore, that recombination through surface defects is a major path for non-radiative decay.[133, 180]

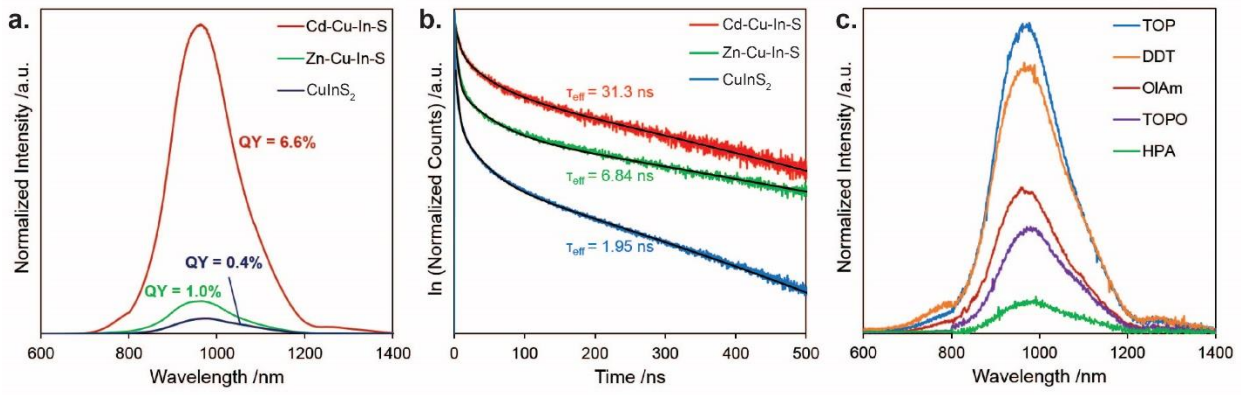

Figure 5.3. Luminescence properties of WZ $CuInS_2$ NCs with different surface passivation; **a.** PL spectra normalized to the QY of $CuInS_2$ NCs prepared with different inorganic passivation layers; **b.** Luminescence decay curves collected at 950 nm, shown with calculated effective lifetimes τ_{eff}, of WZ $CuInS_2$ NCs prepared with different inorganic passivation layers (λ_{ex} = 532 nm). Curves of best fit are shown for each sample in black. Fit parameters can be found in Appendix C.3; **c.** PL spectra normalized to the QY of $CuInS_2$ NCs prepared with different organic passivation layers.

The effect of organic surface passivation on the PL of WZ $CuInS_2$ NCs was also examined. NCs were subjected to ligand exchange with dodecanethiol (DDT), hexylphosphonic acid (HPA), trioctylphosphine (TOP), and trioctylphosphine oxide (TOPO) (Figure 5.3c.). NMR was used to determine that ligand exchange had occurred (Appendix C.13) and identified that

30% or less of the original ligand oleylamine (OlAm) remained in each sample.[344] No substantial change in shape or wavelength of PL was observed, supporting our hypothesis that emission originates from an internal defect. In contrast, significant changes in QY were noted. The soft ligands TOP and DDT, which bind preferentially to soft species (Cu^+ and S^{2-}), resulted in higher QYs than the hard ligands OlAm and TOPO, which bind to hard species (In^{3+}). Samples treated with HPA showed a considerable decrease in QY, and a NIR plasmon concomitantly appeared in the absorbance spectrum (Appendix C.6). It can be concluded that HPA is oxidizing and caused the formation of V_{Cu} within the NCs.[170] These observations suggest that non-radiative decay paths on the NC surface are passivated by soft ligands and are therefore likely Cu- or S-based. This conclusion is in good agreement with previous work on CP $CuInS_2$ NCs, in which coupling between V_{Cu} and V_S at the NC surface was implicated as the major non-radiative decay path.[180]

5.2.5 Density Functional Theory Calculations

Given strong experimental support for the presence of a radiative internal defect within these samples, DFT calculations were carried out for a number of possible species (Appendix C.15). Structures, optical levels (energy eigenvalues), and wavefunctions (eigenstates) of vacancies (V_{Cu}, V_{In}, V_S), interstitial atoms (Cu_i, In_i) and substitutional impurities (In_{Cu}, Cu_{In}, O_S, $Cu^{2+}{}_{Cu^+}$) in WZ $CuInS_2$ were investigated using a 128-atom supercell. Other probable charge states were also considered for each defect. The calculations were based on hybrid density functional theory with the Heyd–Scuseria–Ernzerhof 06 (HSE06) version of the exchange-correlation functional.[345, 346] This method has been shown to accurately describe the properties of CP $CuInS_2$.[347] The proportion of Hartree-Fock exchange used (15.4%) allowed replication of the experimental band gap of the NCs (Appendix C.17). Projector augmented wave (PAW) potentials[348] and a plane-wave basis were used as implemented in the VASP code.[349] A

plane-wave energy cutoff of 295 eV was used. The ionic relaxations are converged to 10^{-3} eV for the total energy difference between two steps. A single *k*-point at $(1/4, 1/4, 1/4)$ was used for Brillouin zone sampling during ionic relaxation.[350]

5.2.6 Mechanism of Defect Luminescence for WZ $CuInS_2$ NCs

Among the candidate defects that were studied, the transition energies associated with the optical levels of In (In_i, Cu_{In}, and V_{In}) agree best with experimental data, E_{exp} = 1.31 eV (950 nm).[351] None of the other candidate defects have transition energies within 0.3 eV of the experimental value (Appendix C.15). The calculated optical levels and squared wave functions of the defect states In_i^{3+}, Cu_{In}^{0} and V_{In}^{3-} are shown in Figure 5.4. In the case of In_i, the transition corresponds to one electron dropping from an occupied In_i defect level to the valence band maximum of $CuInS_2$. In the case of both Cu_{In} and V_{In}, the transitions correspond to one electron dropping from the conduction band minimum of $CuInS_2$ to an unoccupied Cu_{In}/V_{In} defect level. The corresponding calculated photon energies are 1.16, 1.12 and 1.07 eV, respectively. As WZ $CuInS_2$ does not have inversion symmetry, the transitions are not prohibited by parity. In addition, for all cases the initial and final state electron wave functions have spatial overlap (Appendix C.16). CP $CuInS_2$ NCs have been reported to show two different PL signals that overlap in energy,[133, 144, 183] the emission observed here is similarly broad and multimodal (Figure 5.2a). While the measured luminescence decay times were similar at 840 nm and 950 nm (Figure 5.1d) indicating a single radiative pathway at these two wavelengths, the limitations of the detectors prevented TRPL measurements on the red side of the emission. It is therefore possible that more than one of the transitions identified here are radiative. It should be noted that the calculated transition energy for In_i^{2+} (1.32 eV) is in extremely good agreement with the peak experimental transition energy (1.31 eV). This charge state represents an intermediate species of

the In_i^{3+} defect, which accepts an electron under optical excitation, before decaying by emitting a photon. The author therefore suggests that In_i is most likely the dominant source of PL.

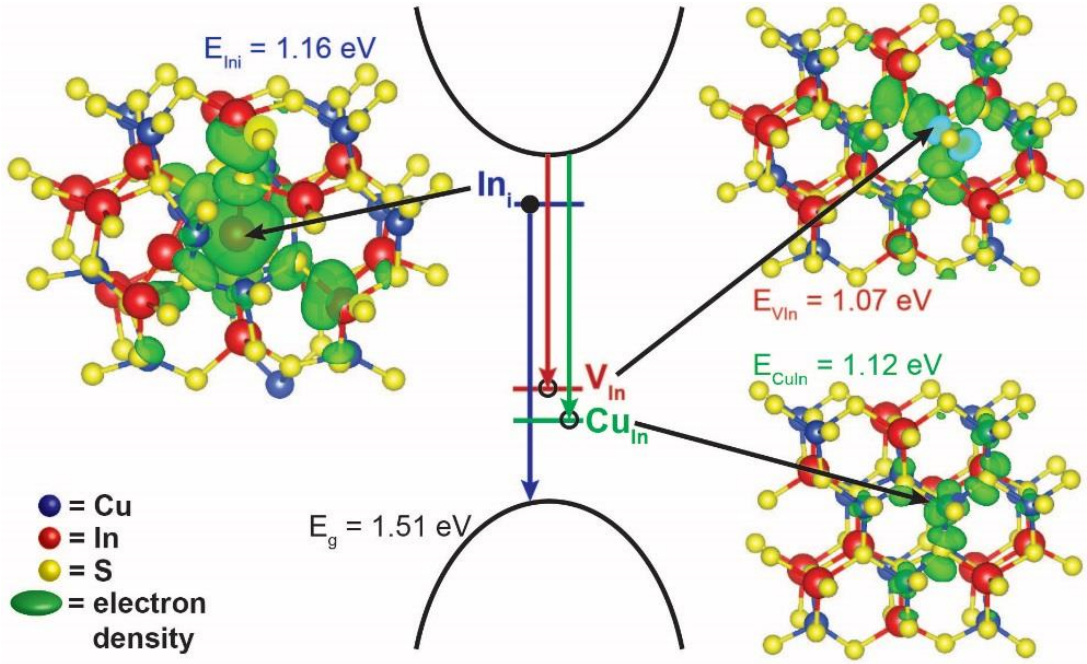

Figure 5.4. Calculated energy levels for In-based point defects. The wave functions (squared) and the optical levels of defect species In_i^{3+}, Cu_{In}^{0} and V_{In}^{3-} shown within the band gap of WZ $CuInS_2$.

The identification of In_i, Cu_{In} and V_{In} as best candidates for the radiative defect is supported by the mechanism of formation for fluorescent WZ NCs. In all reported cases, slow exchange of In^{3+} into Cu_2S has resulted in the production of fluorescent WZ $CuInS_2$.[164, 168, 169] Given that In^{3+} is the peripatetic cation, it is likely that some In will sit in interstitial positions on the crystalline lattice as exchange occurs. At the same time, a fraction of would-be In sites could remain unfilled as V_{In}, or occupied by Cu as Cu_{In}, because of the low diffusivity of In_i at the moderate synthesis temperature of 215°C. As the NCs are heated further we would expect In_i to move to a cation site in the structure, Cu at Cu_{In} to be replaced by In, or any V_{In} present to be filled resulting in the decrease in QY observed in Figure 5.2.

Notably, in all cases the luminescent transition involves either the valence (In_i) or conduction (Cu_{In}, V_{In}) band. If NCs are quantum confined, the band energies should change.

Consequently, the radiative decay mechanism reported here is in good agreement with the size-dependent emission observed for WZ $CuInS_2$ NCs reported by van der Stam *et al*.[168]

The optical properties of WZ $CuInS_2$ do bear some resemblance to those of CP $CuInS_2$, but there are some key differences. Both have PL which originates from an intrinsic defect within the NC, have radiative decay lifetimes of the order of 100 ns, and exhibit Cu-/S-based non-radiative decay paths at the NC surface.[133, 142, 180, 316] However, the assignment of the radiative defect as Cu_{In}, V_{In} or In_i differs from assignments made for the tetragonal structure (In_{Cu}, V_S, *etc.*).[179, 340] The calculations described here showed that none of the analogous defects have suitable optical levels in WZ $CuInS_2$ (Appendix C.15). While no consensus exists as to the origin of the radiative transition for CP $CuInS_2$, it is often attributed to a donor-acceptor pair recombination mechanism.[142, 316, 318] In this study, no donor-acceptor transitions between calculated optical levels have energies in good agreement with the experimentally observed emission.

PL in the NIR has also been observed recently for $CuInSe_2$ and $CuInS_2$/$CuInSe_2$ dot-core/rod-shell NCs with the WZ structure.[352] The origin of this PL has not yet been investigated completely. However, emission is similarly broad, has a large Stokes shift and a long lifetime. Thus, the radiative decay mechanism proposed here may also be applicable to $CuInSe_2$. Furthermore, similarities exist between this system and NCs of $AgInS_2$, which also have a broad PL band with long lifetime and large Stokes shift.[286, 353] Analogous improvements in QY were observed on coating $AgInS_2$ NCs with ZnS, indicating the presence of non-radiative recombination sites at the NC surface.[354] Emission has been attributed to both donor-acceptor pair and VB/CB to a localized defect state recombination mechanisms.[355] NIR PL has also been observed from Ag_2S NCs.[356] Ag_2S NCs are prone to form lattice defects, resulting in mid-gap

optical levels, which broaden and quench excitonic emission.[357] Thus a similar study of both $AgInS_2$ and Ag_2S NCs may lead to advances in the understanding of their optical properties.

5.3 Conclusion

In summary, there is strong experimental evidence that PL recently observed from WZ $CuInS_2$ originates from an intrinsic point defect. TRPL measurements indicate that the decay profile is dominated by a long lifetime ($\tau_3 \sim 300$ ns) with a high weight ($W_3 > 80\%$), suggesting a large number of point defects are present in the structure. Using inorganic surface passivation with either CdS or ZnS, non-radiative transitions associated with surface states were obstructed. The QY of the samples was increased and an increase in the fluorescence lifetime of the NCs was observed. This allowed definitive assignment of the PL to a radiative point defect within the NC. Of the possible intrinsic defects within WZ $CuInS_2$, DFT calculations suggest that In_i has energy levels that are closest to the observed emission. This designation was supported by both the previously reported mechanism of formation[164] and an aliquot study, in which a decrease in QY with extended reaction time indicates the defect species can be annealed from the structure. Finally, by carrying out ligand exchange on the NCs, non-radiative decay paths at the NC surface were identified as Cu- or S-based.

This work is of particular significance as not only has the defect most likely responsible for the NIR PL from WZ $CuInS_2$ been identified, but also a template has been provided for study of NCs that exhibit defect luminescence. As PL is assigned to a transition between the In_i defect state and the valence band, further work on these NCs could focus on producing quantum confined samples with tunable emission across the visible and NIR spectral region. Additionally, by adjusting a synthetic procedure to tune the proportion of In_i within the structure, control over the QY of WZ $CuInS_2$ NCs could now be achieved. This will allow the optimization of the NIR

PL for biological imaging applications. Furthermore, the elucidation of the electronic defect structure within WZ $CuInS_2$ is of potential importance with respect to charge extraction for photovoltaic applications.

6. A SYNTHETIC EXPLORATION OF METAL–SEMICONDUCTOR HYBRID PARTICLES OF $CuInS_2$ [d]

6.1 Introduction

Over the past two decades research efforts in the field of nanocrystal (NC) synthesis have led to the development of synthetic pathways that allow precise control of NC size, shape, and composition. Recently, considerable effort has been focused on the synthesis of hybrid nanostructures which requires an even greater level of control. Hybrid nanostructures combine distinct and often disparate material components into a single particle, which can lead to bifunctionality and synergistic properties. In particular, semiconductor-based hybrids have garnered much interest as promising architectures for applications such as sensing, bioimaging, photovoltaics, and photocatalysis.[101, 102, 154, 358] Building on knowledge from single component NCs, most of the semiconductor hybrid systems synthesized and studied have been based on II-VI semiconductors. While these semiconductors have been the cornerstones for the development of hybrid structures, the high toxicity of Cd and Pb is a major drawback for many applications.

Cu-based semiconductors have attracted considerable attention as alternatives to the II-VI materials in hybrid structures due to their optical properties, low toxicity, and high elemental abundance.[359] A key feature is the localized surface plasmon resonance exhibited by these semiconductors due to the oscillations of holes in Cu-deficient off-stoichiometries, which has been shown to enhance the photovoltaic[174] and electrocatalytic[360] properties. The synthesis of Cu-based semiconductor hybrids has been achieved following diverse strategies.[101, 207, 229, 361-364] For example, Au-Cu_2S dimers have been synthesized by phase segregation of AuCu alloy nanoparticles upon addition of sulfur.[361] The synthesis of core-shell Au-Cu_2S and Au-$Cu_{2-x}Se$

[d] Portions of this chapter have been previously published in Hernández-Pagán, E.A. et al., *Chem. Mater.*, **2015**, *27* (23), pp 7969–7976. Copyright 2015 American Chemical Society.

dimers was achieved by nucleation of the semiconductor phase on Au nanoparticles;[229] while Ru-caged Cu_2S hybrids were obtained through selective growth of Ru on the edges of the facets of the Cu_2S seeds.[362] Recently, both Yu *et al.*[101] and Dilsaver *et al.*[363] reported the syntheses of hybrids of the quaternary semiconductor Cu_2ZnSnS_4 with Pt and Au. The hybrids were formed using Cu_2ZnSnS_4 as seeds for the growth of the metal phase. As with other systems,[229, 309, 365-368] the hybrids showed enhanced photocatalytic properties with respect to hydrogen evolution and dye degradation relative to the pristine nanoparticles.

One of the most studied semiconductors of the Cu family is $CuInS_2$. $CuInS_2$ has a direct band gap of 1.5 eV, high photostability, high tolerance to off-stoichiometries, and can also exhibit the localized surface plasmon resonances observed in other members of the family.[140] These properties make $CuInS_2$ an ideal component for a semiconductor-metal hybrid photocatalyst system. To date, only $CuInS_2$-Au hybrid nanostructures have been synthesized.[208] Au possesses a strong surface plasmon resonance and high photothermal conversion efficiency that make these hybrids ideal candidates for biological applications.[369, 370] However, they are not as suitable for photocatalysis as Au is not as catalytically active as Pt.

In addition to catalytic activity, control of the metal catalyst loading on the semiconductor is of critical importance. Excess loading can prevent efficient light absorption[366] and hinder effective separation of the photogenerated charge carriers. The large amount of metal present can also impact the ability to modify the semiconductor surface with ligands that can render the hybrids water-soluble.

In Chapter 6, work towards synthetic control of the placement and loading of Pt domains on wurtzite (WZ) $CuInS_2$ with the ultimate goal of photocatalytic application is reported. The WZ structure was selected over both the chalcopyrite and zinc blende structures due to its

anisotropic nature, which allows for the possibility of orthogonal charge propagation within the material.[81, 306] Single or multiple metal domains could be obtained based on the seeding material and by controlling the reactivity of the Pt precursor through choice of organic reducing agent and coordinating ligands. This strategy was further extended to synthesize $CuInS_2$-Pd_xS hybrid nanostructures. Synthetic development, initial characterization, and solvent studies were carried out by Dr. Emil Hernández-Pagán. Synthetic refinement, additional particle characterization, and synthetic development for Pd hybrids were performed by Alice Leach. Dr. Suresh Sarkar assisted with photoelectrical measurements. Chapter 6 was written in collaboration with Dr. Emil Hernández-Pagán.

6.2 Experimental Techniques

6.2.1 Synthesis of Pt NCs

A synthesis was developed based on the work of Sun *et al.*[47] Standard Schlenk line techniques were used throughout with N_2 as the inert gas. Oleylamine (OlAm, 0.2 mL), oleic acid (OlAc, 0.2 mL), 1,2-hexadecanediol (0.16 mmol), and diphenyl ether (10.0 mL) were added to a 3-neck flask and degassed under vacuum at 80°C for 30 min. The temperature was then increased to 210°C under N_2. $Pt(acac)_2$ (0.04 mmol) dissolved in diphenyl ether (1.0 mL) was swiftly injected and the color changed from yellow to black within 30 s. The reaction was heated for 10 min, then cooled to room temperature. The product NCs were precipitated with methanol followed by removal of the supernatant and resuspension in hexanes. This process was repeated three times. The product NCs were stored as a stable black solution in hexanes.

6.2.2 Synthesis of $CuInS_2$ NCs

$CuInS_2$ NCs were synthesized following a procedure reported by Korgel *et al.*[314] CuCl (0.5 mmol), $InCl_3$ (0.5 mmol), thiourea (1.0 mmol), and oleylamine (10.0 mL) were loaded into a

25 mL 3-neck flask. The mixture was placed under vacuum at 60°C for 30 min, then heated to 245°C under N_2 and held at this temperature for 1 hr. After cooling to room temperature, NCs were precipitated with ethanol followed by removal of the supernatant. Three cycles were performed of suspension in hexanes: OlAm (20:1, by volume) followed by precipitation with excess ethanol and removal of the supernatant. Finally, the NCs were stored in hexanes: OlAm.

6.2.3 Synthesis of Pt-$CuInS_2$ Hybrids

Pt NCs in hexanes were transferred to a 25 mL 3-neck flask containing CuCl (0.5 mmol), $InCl_3$ (0.5 mmol), and OlAm (10.0 mL). The mixture was placed under vacuum at room temperature to remove the hexanes. Then the mixture was degassed at 60°C for 30 min. In a single neck flask, thiourea (1.0 mmol) was dissolved in OlAm (1.2 mL) by heating to 175°C under N_2. Once the thiourea was dissolved the temperature was decreased to 50°C. The flask containing the metal precursors was heated to 200°C under N_2. At this temperature, thiourea was injected and the growth of hybrid nanoparticles proceeded for 1 hr. The flask was cooled to room temperature and the NCs were precipitated with ethanol. Three cycles were performed of suspension in hexanes: oleylamine (20:1, by volume) followed by precipitation with excess ethanol and removal of the supernatant. Finally, NCs were stored in hexanes: OlAm.

6.2.4 Synthesis of $CuInS_2$-Pt Hybrids with 1,2-Hexadecanediol

OlAm (0.2 mL), OlAc (0.2 mL), 1,2-hexadecanediol (0.16 mmol), and diphenyl ether (10.0 mL) were loaded into a 25 mL 3-neck flask. The mixture was placed under vacuum at 80°C for 30 min. In a vial, $Pt(acac)_2$ (0.04 mmol) was dissolved in diphenyl ether (1.0 mL) with addition of 1.0 mL of the $CuInS_2$ NC stock solution. The flask containing 1,2-hexadecanediol was heated to 210°C under N_2 and the $Pt(acac)_2$-NC mixture was swiftly injected. After 10 min, the heating mantle was removed and the flask was allowed to cool to room temperature. The

product NCs were precipitated with ethanol. Three cycles were performed of suspension in hexanes: OlAm (20:1, by volume) followed by precipitation with excess ethanol and removal of the supernatant. Finally, the product NCs were stored in hexanes: OlAm.

6.2.5 Synthesis of $CuInS_2$-Pt Hybrids with Trioctylphosphine

$CuInS_2$ NC stock solution (2.0 mL), OlAc (0.2 mL), and OlAm (10.0 mL) were loaded into a 25 mL 3-neck flask. The mixture was placed under vacuum at 80°C for 30 min. In a vial, $Pt(acac)_2$ (0.04 mmol) was dissolved in a mixture of trioctylphosphine (TOP, 17.0 µL) and diphenyl ether (1.0 mL). Under N_2, the temperature of the flask containing the $CuInS_2$ NCs was increased to 210°C. At this temperature, the Pt solution was swiftly injected. After 5 min, the heating mantle was removed and the flask was cooled to room temperature. The particles were precipitated with ethanol followed by removal of the supernatant. Three cycles were performed of suspension in hexanes: OlAm (20:1, by volume) followed by precipitation with excess ethanol and removal of the supernatant. Finally, the nanocrystals were stored in hexanes: OlAm.

6.2.6 Characterization

Transmission electron microscopy (TEM) and energy dispersive X-ray spectroscopy (EDS) were performed on a Phillips CM20 microscope operating at 200kV. High resolution TEM (HRTEM) and EDS mapping data were collected using a FEI Tecnai Osiris™ digital 200 kV S/TEM system equipped with ChemiSTEM EDS. TEM samples were prepared by drop casting a dilute NC solution in hexanes onto a nickel grid with a carbon support and drying in air at room temperature. Lattice fringes were measured by generating a profile plot of an area of the image using ImageJ, manually counting the cycles, and dividing the length of the profile plot by the number of cycles. The minimum number of cycles used was ten. EDS spectra were collected for 2 min and quantified using the Espirit software. Cu and S were quantified using the K series

of peaks, while In, Pd and Pt were quantified using the L series. All spectra were background subtracted and overlapping Cu sample and Ni grid peaks were deconvoluted before quantification. Drift-corrected EDS maps were collected for 90 s with beam current 1.5 nA. XRD measurements were performed using a Scintag XGEN-4000 X-ray diffractometer with a CuK_{α} ($\lambda = 0.154$ nm) radiation source. The resulting diffraction patterns were then visually compared to data from the ICDD database and literature examples to determine the structure.[167] The absorption spectra of NC samples were collected from 300 – 1200 nm on a UV-visible (UV-Vis) spectrophotometer (Jasco V-670). Samples were measured in solution with hexanes as the solvent.

6.2.7 Photoelectrical Measurements.

Measurements were carried out using a Gamry Series G-300 potentiostat with the PHE200 software package in the linear sweep voltammetry and chronoamperometry modes. A simple device was fabricated, based on the work of Wang *et al.*,[371] by drop-casting a concentrated solution of the NCs on a glass substrate with ITO film on either edge as conductive electrodes. The current was then measured using linear sweep voltammetry from -0.5 - 0.5 V with a scan rate of 0.01 Vs^{-1} and a 1 mV voltage step. This measurement was performed both in the dark and under illumination by a 500 W Xe lamp with the solar spectrum. Chronoamperometry measurements were then taken using a fixed voltage of 0.5 V and a light on-off cycle with 20 s intervals.

6.3 Results & Discussion

6.3.1 Pt-$CuInS_2$ Hybrids

The first route taken to synthesize hybrid nanostructures was based on Pt seeds serving as nucleation sites for the semiconductor, denoted as Pt-$CuInS_2$ (Figure 6.1a). The Pt seeds were

prepared by the reduction of $Pt(acac)_2$ with 1,2-hexadecanediol in a mixture of OlAm and OlAc (Appendix D.2).[47] The Pt seeds were transferred to a flask containing the CuCl and $InCl_3$ precursors in OlAm. To initiate the hybrid growth, thiourea dissolved in OlAm was swiftly injected at 210°C.

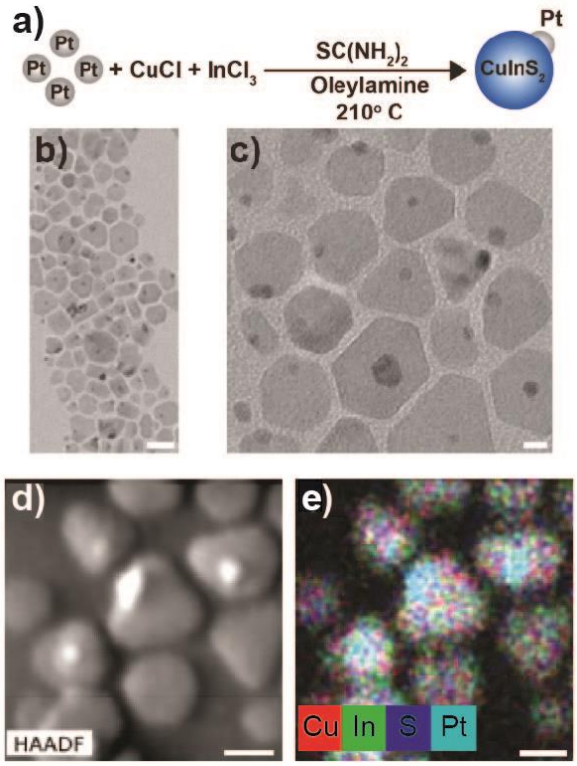

Figure 6.1. Characterization of Pt-$CuInS_2$ hybrids; **a.** Schematic showing the synthesis of Pt-$CuInS_2$ from Pt nanoparticles; **b., c.** TEM images of the Pt-$CuInS_2$ hybrids. Scale bars are 20 nm and 5 nm, respectively; **d.** High angle annular dark field STEM image and **e.** EDS mapping of the hybrids. Scale bars are 10 nm.

TEM images of the Pt-$CuInS_2$ hybrid nanostructures (Figure 6.1b-c) indicated that this synthetic path yielded hybrid dimers with $CuInS_2$ domains of 5-20 nm in size and plate-like morphology. The formation of more complex structures, such as trimers, was not observed. For approximately 2 % of the Pt particles, growth of a $CuInS_2$ domain was not observed. An aliquot of the reaction taken 30 s after the injection of thiourea suggested that the hybrid growth proceeded via heterogeneous nucleation (Appendix D.2). The UV-Vis spectrum of the heterostructured nanoparticles showed an optical transition analogous to that of bare $CuInS_2$ NCs

(Appendix D.2). A high angle annular dark field (HAADF) STEM image showed distinct metal and semiconductor domains (Figure 6.1d). EDS mapping indicated the presence of Cu, In, S, and Pt at the expected locations (Figure 6.1e). Furthermore, XRD of the hybrids revealed the crystal structure of the $CuInS_2$ domains to be WZ (Appendix D.2). The WZ structure is of particular interest for photocatalysis as its anisotropy allows for orthogonal charge propagation.[81]

This scheme was extended to synthesize Pt-$CuInS_2$ hybrids with bullet-like $CuInS_2$ morphologies by replacing the metal chlorides with metal acetates and thiourea with a mixture of dodecanethiol and tert-dodecylmercaptan (Appendix D.3).[140] While the study described above yielded Pt-$CuInS_2$ hybrids, the polydispersity of the resultant nanostructures motivated us to investigate a different approach.

6.3.2 $CuInS_2$-Pt Hybrids with 1,2-Hexadecanediol

In an alternate and complementary route to Pt-$CuInS_2$ (Figure 6.2a), hybrid nanostructures were synthesized by nucleation of Pt domains onto $CuInS_2$ seeds, denoted as $CuInS_2$-Pt. $CuInS_2$ seeds were synthesized in a single pot reaction using CuCl, $InCl_3$, and thiourea in OlAm (Figure 6.2b).[314] These seeds had the WZ structure (Appendix D.4) and were again plate-like in morphology, but more uniform in size (approximately 18 nm). The growth of the Pt domains was carried out by injecting a mixture of $Pt(acac)_2$ and $CuInS_2$ NCs into a flask that contained OlAm, OlAc, and 1,2-hexadecanediol, in diphenyl ether at 210°C. Here, 1,2-hexadecanediol acted as a reducing agent, while OlAm and OlAc were stabilizing ligands.

A TEM image of the product hybrids (Figure 6.2c) showed that the plate-shaped $CuInS_2$ seeds were decorated with multiple Pt domains on the edges. EDS was employed to confirm the presence of Pt (Appendix D.5). A similar result was obtained when bullet-shaped $CuInS_2$ NCs were used as seeds (Appendix D.6). It should be noted that under these reaction conditions

homogenous nucleation of Pt NCs was also observed, but these could be removed using size-selective precipitation. The hybrids also formed at shorter reaction times, as well as at injection temperatures up to 20°C lower (Appendix D.7). Upon further examination of the $CuInS_2$-Pt hybrids it was noticed that in addition to the Pt domains there appeared to be a Pt shell surrounding the $CuInS_2$ seeds.

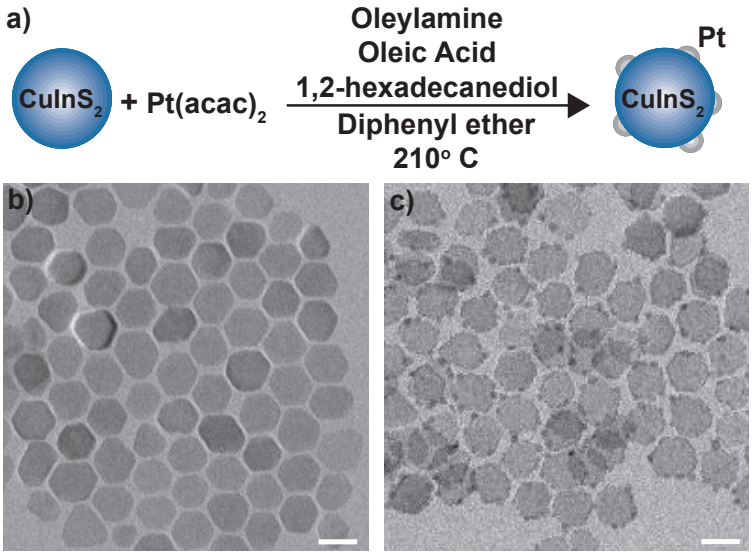

Figure 6.2. Characterization of $CuInS_2$-Pt hybrids with 1,2-hexadecanediol; **a.** Schematic of the synthesis of $CuInS_2$-Pt from $CuInS_2$ NCs/1,2-hexadecanediol; TEM images of **b.** the $CuInS_2$ seeds and **c.** the $CuInS_2$-Pt hybrids. Scale bars are 20 nm for both images**.**

To elucidate if the $CuInS_2$ seeds were covered with a Pt shell, aliquots taken during the reaction at 1, 5, and 10 minutes were analyzed by HAADF-STEM and EDS mapping. HAADF allows us to exploit the high imaging contrast of Pt relative to $CuInS_2$ since the technique is sensitive to Z^2. After 1 min, HAADF and EDS mapping (Figure 6.3a, d) indicated the presence of a patchy Pt shell covering the $CuInS_2$ seeds. After 5 min, the shell coverage increased, however, Pt domains were not observed protruding from the particle (Figure 6.3b, e). The shell had a ring-like appearance in EDS, as the shelling plane was parallel to the plane of observation at the NC edges. At 10 min, the $CuInS_2$ NCs were decorated with a Pt shell and between three and five discrete, protruding domains (Figure 6.3c, f) reminiscent of the Stranski-Krastinov

growth mode.[154] The UV-Vis spectra (Figure 6.3g) of the aliquots were in agreement with these observations. The spectrum obtained for the 1 min aliquot showed a defined optical transition resembling that of the $CuInS_2$ seeds, consistent with low Pt coverage. The 5 and 10 min aliquots showed a washed out band gap absorption onset due to higher Pt coverage.

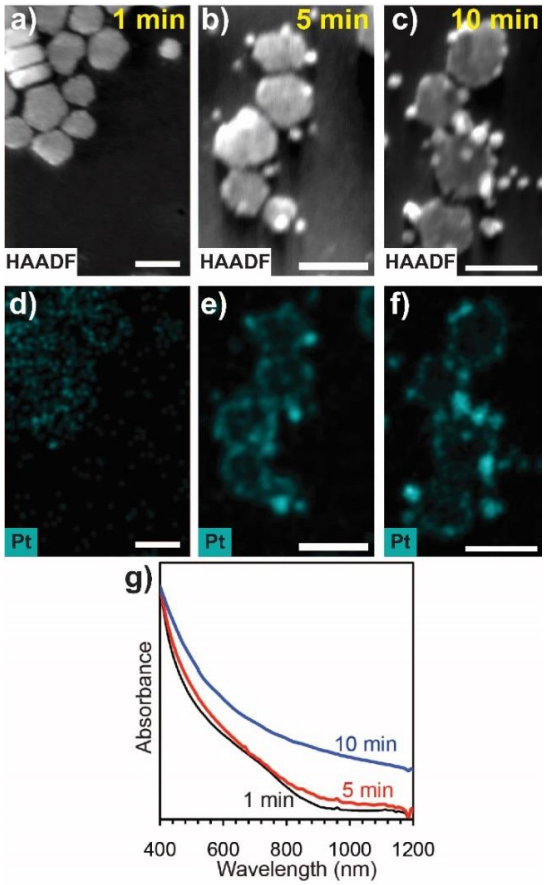

Figure 6.3. Aliquots of of $CuInS_2$-Pt hybrids with 1,2-hexadecanediol; **a.-c.** HAADF images and **d.-f.** Corresponding EDS mapping for aliquots taken after 1, 5, and 10 minutes. Scale bars are 20 nm; **g.** UV-Vis spectra of the hybrids at the different time points.

6.3.3 Morphology of the Hybrid NCs

While some applications may require the chemical robustness imparted to the $CuInS_2$ NCs by a complete Pt shell, a photocatalyst would require exposure of both the Pt and $CuInS_2$ domains to solution for electron and hole charge transfer respectively. To determine if the Pt shell was complete or patchy, an aliquot of the final hybrid nanostructures was suspended in chloroform and stirred with an excess of neocuproine. It has been shown that neocuproine can

preferentially bind to and leach Cu^+ from copper sulfides.[362] TEM images of the hybrid nanostructures after reaction with neocuproine (Figure 6.4) indicated that leaching of Cu^+ left behind a Pt shell forming a rattle-like structure. Analysis of the core lattice fringes gave lattice spacing in the range of 0.33 - 0.34 nm, close to that of the (100) plane for WZ $CuInS_2$ and the (109) plane for tetragonal β-In_2S_3. Given that the neocuproine treatment was carried out at room temperature, it is unlikely that a transformation from the original hexagonal $CuInS_2$ crystal structure to a tetragonal In_2S_3 crystal structure would occur with retention of crystallinity. From the standpoint of a photocatalyst, the observed rattle-like structures indicated that the Pt coverage was patchy and that $CuInS_2$ was exposed to the solution. Although the Pt shell was patchy, its presence could still decrease light absorption due to scattering of photons limiting the efficiency of a photocatalytic system.[366] Thus additional routes were sought that would limit the Pt growth on the surface of the $CuInS_2$ to create discrete domains of Pt rather than a shell.

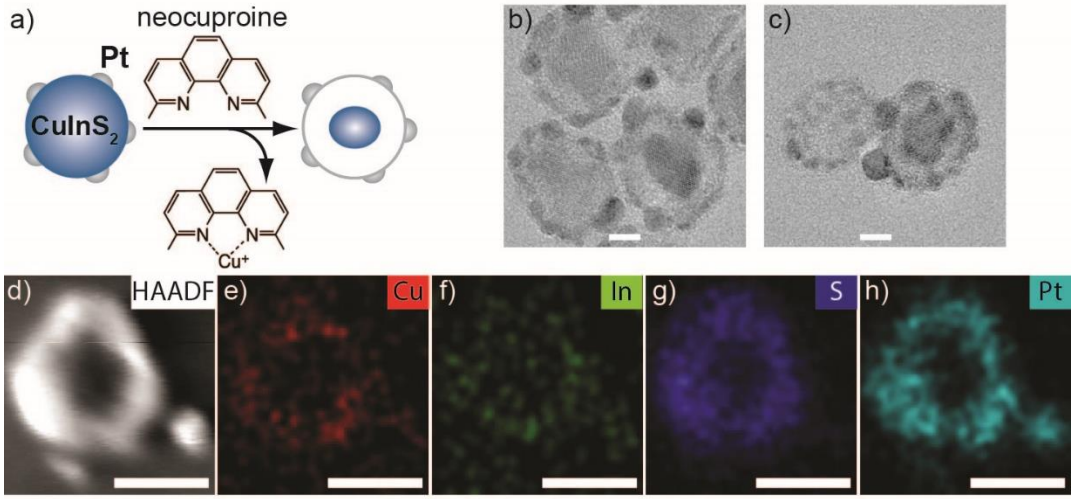

Figure 6.4. Treatment of hybrids with neocuproine; **a.** Schematic diagram showing treatment of hybrids with neocuproine; **b.-c.** TEM images showing Pt shell left behind after the hybrids were reacted with neocuproine. Scale bars are 5 nm; **d.-h.** EDS mapping of the Pt shell. Scale bars are 10 nm.

The morphology of hybrid structures can be tuned by the ligands present in their synthesis, as well as the ratio thereof. For instance, in the synthesis of FePt-PbS hybrids reported

by Lee *et al.* the product nanostructures exhibited a core-shell morphology in the presence of OlAc/ OlAm.[372] In contrast, a dumbbell morphology was obtained when only OlAc was present in the reaction. Another example is the work reported by Baaziz *et al.* for Co-Fe based nanoparticles.[373] Here, the reaction of a combination of Fe- and Co-stearate in the presence of OlAm led to $Co_xFe_{1-x}O@Co_yFe_{3-y}O_4$ core-shell nanoparticles. When the authors replaced OlAm with OlAc, $CoFe_2O_4$ NCs were produced.

With this in mind, a systematic study was carried out to determine the influence of the ligands on the synthesis of $CuInS_2$-Pt hybrids. In this study, hybrids were synthesized in the presence of only one or two of the three surfactants (1,2-hexadecanediol, OlAm, and OlAc) under otherwise identical conditions to those described in Section 6.2.4.

In the three cases for which OlAm was present: OlAm/ OlAc, OlAm/ 1,2-hexadecanediol, and OlAm (Figure 6.5a, b, f respectively); Pt growth was indiscriminate and agglomeration of the NCs was observed. In contrast, in the presence of OlAc/ 1,2-hexadecanediol or OlAc only (Figure 6.5c, e), the Pt growth was attenuated and aggregates were not observed. When the reaction was done with only 1,2-hexadecanediol present, single Pt domain growth was predominately observed with significant particle aggregation (Figure 6.5d). These results suggested that OlAm served as a co-reducing agent to 1,2-hexadecanediol in addition to being a ligand.[374] Furthermore, OlAc seemed to bind more strongly to the NCs than OlAm providing colloidal stability. Therefore, it was established that under the experimental conditions reported here the presence of all three components was essential for the synthesis of high quality hybrids with colloidal stability. A similar result was reported by Shevchenko *et al.* for the synthesis of $CoPt_3$ nanocrystals with 1,2-hexadecanediol, where the combination of 1-

adamantenecarboxilic acid and hexadecylamine yielded narrow size distribution and stability against aggregates.[375]

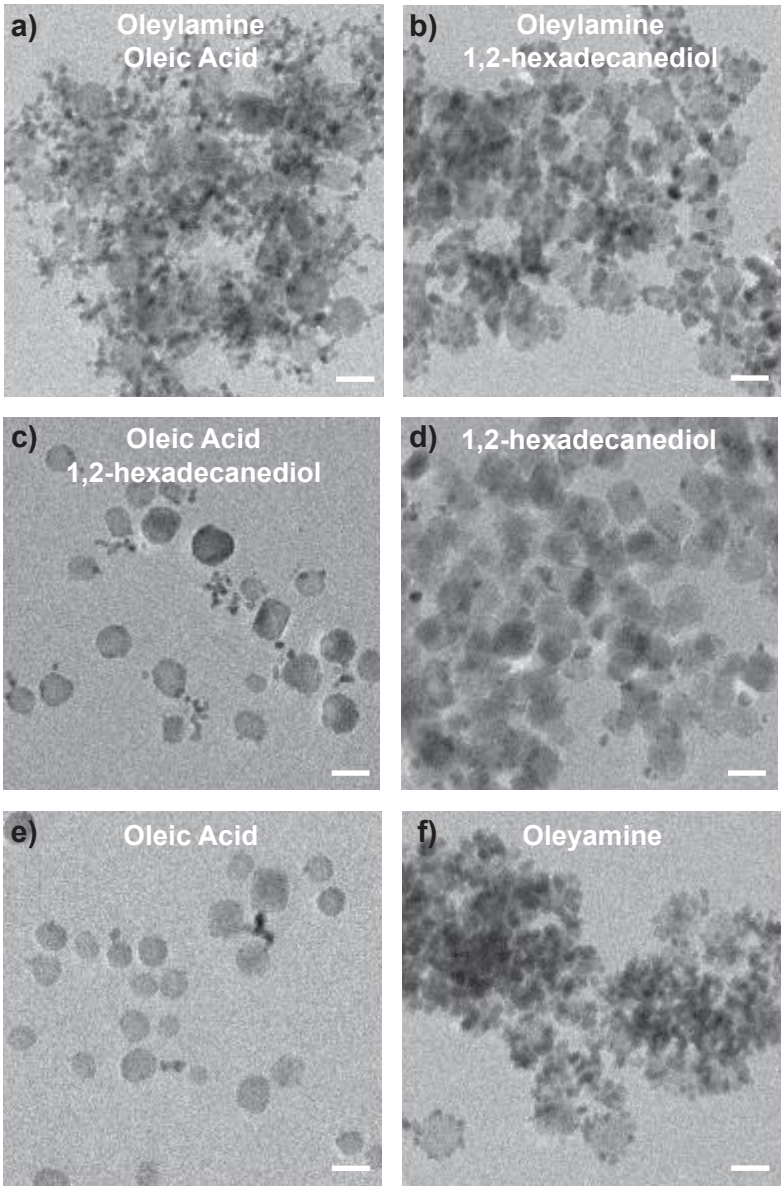

Figure 6.5. $CuInS_2$-Pt hybrids synthesized with different ligand combinations; **a.** OlAm/OlAc; **b.** OlAm/1,2-hexadecanediol; **c.** OlAc/1,2-hexadecanediol; **d.** 1,2-Hexadecanediol; **e.** OlAc; and **f.** OlAm. All scale bars are 20 nm.

In seeded hybrid growth under ideal conditions, only heterogeneous nucleation of the second material should occur. To explore this in the system described here, a reaction containing the three components was executed in the absence of $CuInS_2$ seeds. Nucleation of Pt NCs was observed 30 s after injection of the $Pt(acac)_2$. Consequently, it was clear that attenuation of the Pt

precursor reactivity was required to obtain dimeric hybrids with discrete Pt domains rather than a shell. To slow down the nucleation of Pt, the Pt species formed *in situ* was altered. Pt^{2+} is a soft Lewis acid, therefore it can bind more tightly to a soft Lewis base than the OlAm or OlAc (hard Lewis bases) present in the original synthesis. With this in mind, a soft species trioctylphosphine (TOP) was utilized as the coordinating ligand for the Pt precursor solution. In an additional measure to limit the Pt reactivity, 1,2-hexadecanediol was eliminated from the synthesis leaving only the weaker reducing agent OlAm. As a control, the reaction was carried out without $CuInS_2$ NCs. The TOP: Pt^{2+} precursor solution was injected into a flask containing OlAc and OlAm at 210°C. After 10 minutes, the reaction mixture remained colorless. The temperature was slowly increased and at 225°C the mixture turned black indicating nucleation of Pt NCs. The higher temperature required for nucleation, relative to the original reaction, confirmed that the reactivity of the Pt had been suppressed. This was in good agreement with reports from Yang *et al*.[376] and Ortiz *et al*.,[377] in which TOP-based precursors were employed to control the nucleation of Pd and Pt nanoparticles.

6.3.4 $CuInS_2$-Pt Hybrids with Trioctylphosphine

A hybrid synthesis carried out with TOP: Pt^{2+} as the precursor (Figure 6.6a). When the TOP: Pt^{2+} molar ratio was 1:6, Pt growth did not occur. However, when the molar ratio was 1:1, the reaction yielded $CuInS_2$-Pt hybrids. Given the results of the control experiment described above, it was evident that the $CuInS_2$ NCs served as nucleation sites lowering the temperature required for nucleation from 225°C to 210°C.

TEM images indicated that the $CuInS_2$ NCs were decorated with a single Pt domain (Figure **6.6**b-c), resembling an island or Volmer-Weber like growth mode.[154] The presence of Pt was confirmed by EDS (Appendix D.5). The UV-Vis spectrum of these hybrids (Appendix D.8)

was comparable to that of the bare $CuInS_2$ NCs. In the surfactant study described above, a reaction containing $Pt(acac)_2$ and OlAm/OlAc without 1,2-hexadecanediol yielded agglomerated hybrids with multiple Pt domains (Figure 6.5a). Therefore, although 1,2-hexadecanediol was excluded from this synthesis as well, it is apparent that the presence of TOP was the key to obtaining colloidally stable dimers.

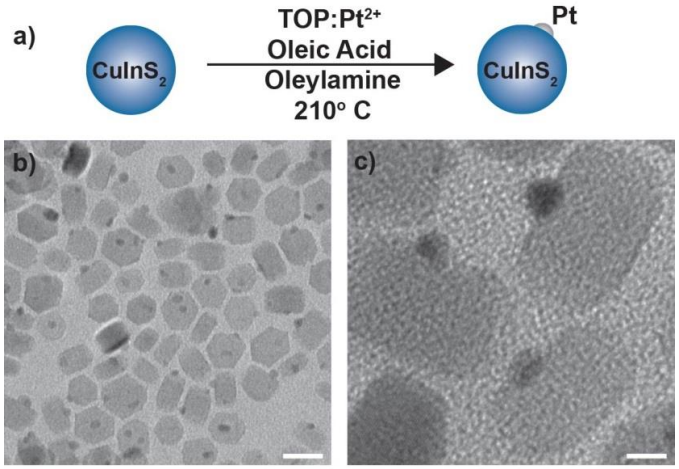

Figure 6.6. Synthesis of $CuInS_2$-Pt hybrids with trioctylphosphine; **a.** Schematic showing the synthesis of $CuInS_2$-Pt from $CuInS_2$ NCs with the complex TOP:Pt^{2+} as the precursor; TEM images of the resulting $CuInS_2$-Pt. Scale bars are **b.** 20nm and **c.** 5 nm.

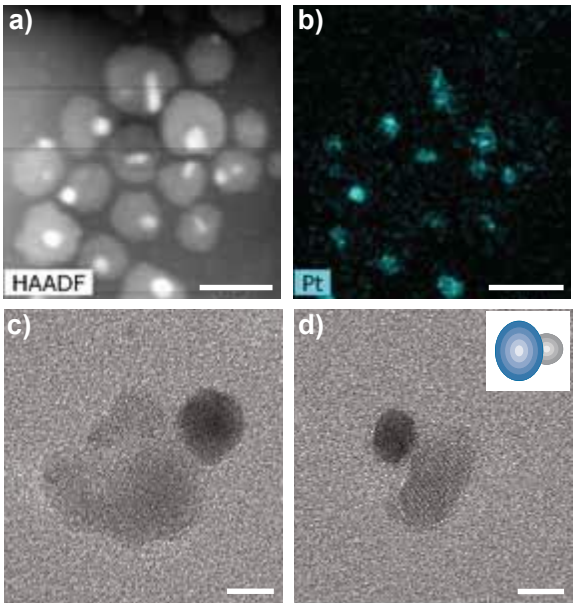

Figure 6.7. Characterization of $CuInS_2$-Pt hybrids with trioctylphosphine; **a.** HAADF image and **b.** corresponding EDS mapping of the hybrids synthesized with the complex TOP: Pt^{2+} as the precursor. Scale bars are 20 nm; **c.-d.** TEM images of the hybrid nanostructures after being stirred with neocuproine. Scale bars are 5 nm.

To determine if the controlled Pt nucleation had prevented the formation of a Pt shell, the $CuInS_2$-Pt hybrids were analyzed with HAADF and EDS mapping. The images (Figure 6.7a-b) clearly showed discrete Pt domains and no shell formation. Additionally, TEM images (Figure **6.7**c-d) of the hybrids stirred with neocuproine indicated that leaching of Cu^+ led to a dimer morphology, instead of the rattles observed for more reactive Pt conditions. This supported the evidence obtained from EDS mapping that the hybrids were shell-free.

6.3.5 $CuInS_2$-PdS Hybrids

$CuInS_2$-Pd hybrid nanostructures were also synthesized by replacing the Pt precursor with TOP: Pd^{2+} (1:1) under otherwise similar conditions. Contrary to the Pt hybrids, TEM images showed the formation of between three and five Pd domains (Figure 6.8a-b). Further when the Pd hybrids were examined using EDS mapping, it was apparent that some smaller nanoparticles had undergone cation exchange (Appendices D.9 and D.10), as S regions overlapped with the Pd regions. The distinct behavior of these two $CuInS_2$-metal hybrids is attributed to the lower reduction potential of Pd^{2+} complexes ($E^{\theta} = 0.07$ V), when compared to those of Pt^{2+} ($E^{\theta} = 0.14$ V). Similar reactivity and cation exchange has been observed for Pd in the CdS-PdX family of hybrid nanoparticles and by Ye *et al.* for ZnS-$CuInS_2$.[207, 309] In these cases, the Pd-S species was identified as Pd_4S. It is possible that this species also exists in the $CuInS_2$-Pd samples prepared here, however, Pd-S reflections were not of high enough intensity to confirm this via XRD (Appendix D.11). A low angle reflection at $2\theta \sim 22°$ was observed in good agreement with a reflection seen for the $Pd_{2.8}S$ phase. However, higher angle peaks matching this pattern were not observed so definitive phase identification is not possible.

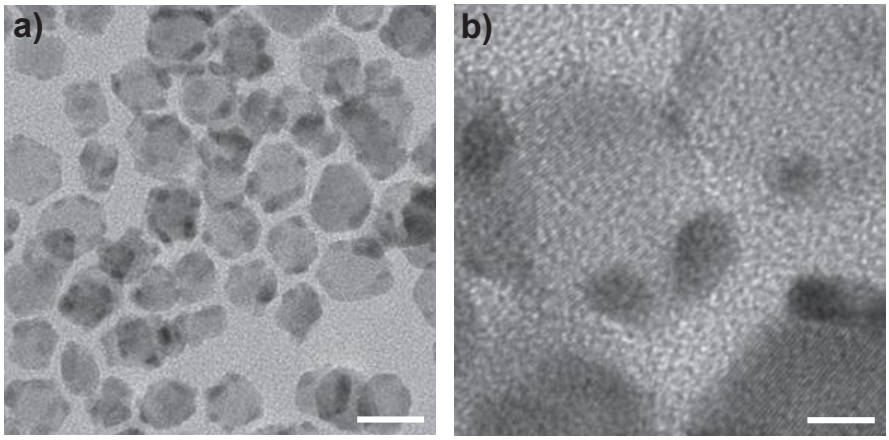

Figure 6.8. TEM images of $CuInS_2$-PdS. Scale bars are **a.** 20nm and **b.** 5 nm.

6.3.6 Ligand Exchange for Hybrids

For applications such as bioimaging and photocatalysis, it is important that the nanostructures are able to undergo ligand exchange processes to modify the surface with a particular functional group or to impart water solubility. In order to make the hybrid nanostructures water soluble, ligand exchange using 11-mercaptoundecanoic acid (MUA) was attempted. Briefly, an aliquot of the hybrids was precipitated with ethanol followed by removal of the supernatant. The hybrids were redispersed in chloroform with excess MUA followed by the addition of water with pH 11. After vigorous agitation, the phases were allowed to separate (Appendix D.12). When this process was carried out with the shell-free $CuInS_2$-Pt hybrids synthesized with a TOP:Pt^{2+} precursor, the hybrids transferred from the organic to the aqueous layer. Phase transfer to the aqueous layer indicated that the hybrids underwent a successful ligand exchange. The same result was observed for bare $CuInS_2$ NCs and Pt-$CuInS_2$ hybrids. In contrast, the $CuInS_2$-Pt hybrids synthesized with $Pt(acac)_2$/ 1,2-hexadecandiol remained in the chloroform layer (Appendix D.12). This result suggests that the Pt shell present on these hybrids alters the surface chemistry sufficiently to prevent ligand exchange, perhaps requiring a more aggressive ligand exchange methodology based on Pt surface chemistry.

6.3.7 Photoelectrical Properties

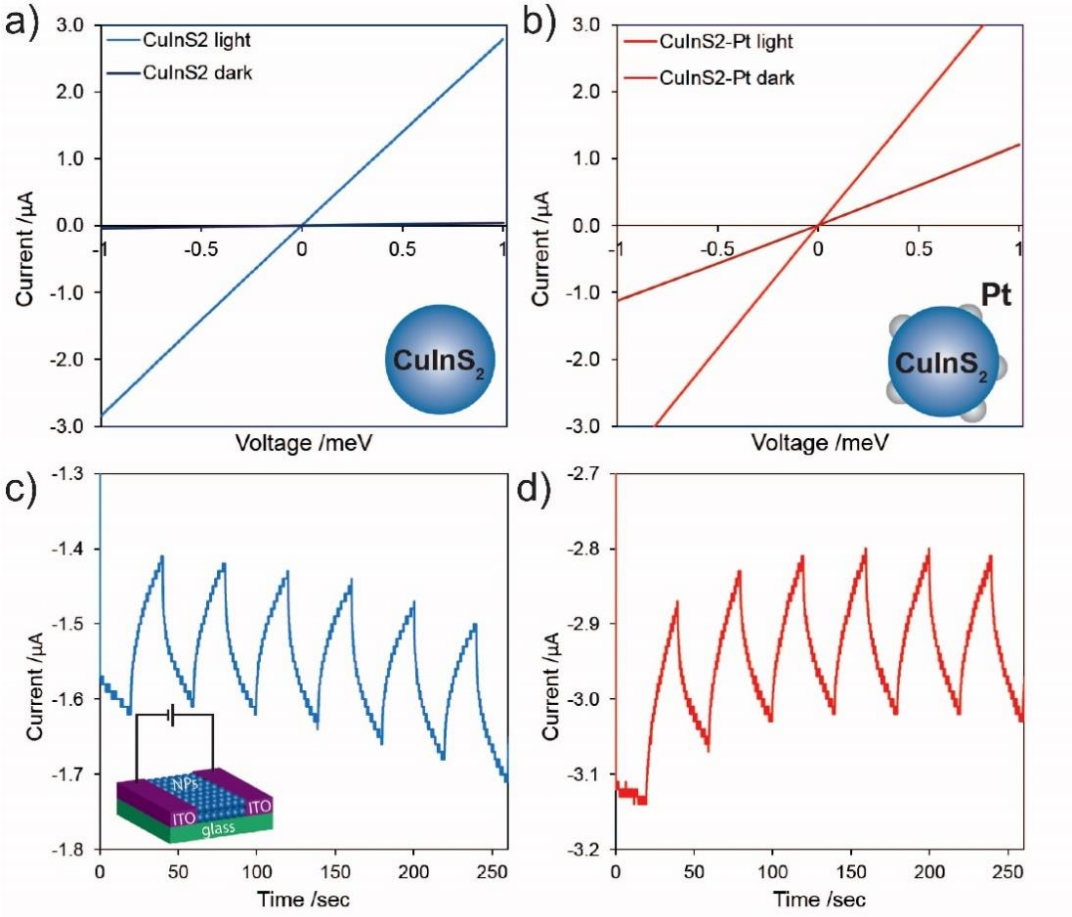

Figure 6.9. Photoelectrical measurements for $CuInS_2$-Pt hybrids; **a., b.** Current versus voltage plots of $CuInS_2$ and $CuInS_2$ nanostructures. Inset: Schematic diagrams of the corresponding NCs; **c., d.** Current against time for On-Off cycles for $CuInS_2$ and $CuInS_2$-Pt nanostructures, respectively. Inset **c.**: Schematic diagram of the device.

To determine the efficacy of using these nanostructures in photocatalytic and photovoltaic application, a photoelectrical study was carried out on $CuInS_2$-Pt hybrids prepared with HDD and bare $CuInS_2$ NCs (Figure 6.9).[378] A simple device was fabricated, based on the work of Wang et al.,[371] by drop-casting a concentrated solution of the NCs on a glass substrate with ITO films on either edge as the conductive electrodes (Figure 6.9c inset). Chronoamperometry measurements (Figure 6.9c-d) indicated that the hybrid nanoparticles had higher stability with no decrease in observed current over 260 s, while bare nanoparticles showed a significant decrease. Hybrid NCs also displayed higher photocurrent than the corresponding

bare nanoparticles. While this difference was not large, it is believed that the hybrid device had a smaller number of NCs deposited on it, as the concentration of the dropcast solutions were set to be of equal absorbance at 400 nm and additional scattering from the Pt is anticipated. This suggests that hybrid NCs exhibit superior carrier transport and stability with respect to bare $CuInS_2$ NCs, demonstrating their potential for use in both photovoltaic and photocatalytic applications.

6.4 Conclusion

Several schemes for the synthesis of $CuInS_2$-Pt hybrid NCs were presented. When Pt NCs were employed as seeds for the growth of $CuInS_2$, the hybrids obtained had a dimer configuration. Alternatively, hybrids were synthesized from $CuInS_2$ NCs with 1,2-hexadecanediol as the reducing agent, and OlAm/ OlAc as stabilizing ligands. A systematic study revealed that the presence of all three components was important to obtain stable hybrids. Furthermore, this reaction pathway yielded hybrids consisting of a Pt shell with additional growth of distinct Pt domains. The presence of the Pt shell altered the surface chemistry of the hybrids, preventing them from undergoing ligand exchange. The behavior of the Pt was controlled by rational selection of the Pt precursor. Utilization of TOP: Pt^{2+} as the precursor, attenuated the Pt reactivity and allowed for single domain growth, resulting in dimeric hybrid nanostructures that could be rendered water soluble through ligand exchange. Additionally, the same synthetic routes were employed to produce hybrids with bullet-shaped $CuInS_2$ domains and extended to the synthesis of $CuInS_2$-Pd hybrids. Hybrids were synthesized with Pt domains on both the basal and perpendicular edge planes. It has been determined that the mass of the hole and electron are different for WZ $CuInS_2$ in the *a*-/*b*- and *c*-directions,[379] thus the position of these domains should facilitate the advanced design of nanostructures for photocatalytic

function. A complete investigation of this phenomenon and detailed characterization of the optical and photocatalytic properties of the reported hybrid nanostructures is currently in progress.

7. PROGRESS TOWARDS THE SYNTHESIS OF WURTZITE $CuFeS_2$ NANOCRYSTALS

7.1 Introduction

Over the last thirty years, colloidal semiconductor nanocrystals (NCs) have become one of the most useful systems for the study of nanoscale semiconductor properties and their applications.[56, 293, 294] The nature of colloidal synthesis allows the formation of NCs with exquisite control over size, shape, composition, and crystal structure unencumbered by a substrate.[42] As such, the dependence of NC properties on such parameters can be studied and NCs can easily be integrated into matrices or deposited onto surfaces for application.[10, 212, 296, 380] In order to realize the full potential of these systems, a library of well-understood NC materials with controlled syntheses and properties tailored to specific uses must be developed. Currently only a few of the II-VI metal chalcogenides (PbS, PbSe, CdS, CdSe, CdTe) have been the subject of intense study.[121, 300, 381-383] While these systems are well suited for a range of applications including solar energy capture, light emission, and biomedicine, they contain toxic constituent elements and thus concerns remain regarding their commercial use and disposal.[126, 301] Correspondingly, significant effort is focused on the development of alternative semiconductor NC systems with promising properties.

Amongst the semiconductor materials, nanostructures of $CuFeS_2$ have recently attracted considerable interest due to their unusually low band gap (approximately 0.5 eV) and highly abundant, low-cost, low toxicity constituent elements. The small band gap of $CuFeS_2$, caused by the presence of an intermediate band made up primarily of Fe *3d* orbitals within the band gap,[265, 274] lends itself well to application of the material as a thermoelectric[263, 269, 277, 278] or photothermal therapeutic agent.[265] Furthermore its abundant constituent elements will allow for the low-cost

synthesis of this system at the commercial scale.[384] Synthetic efforts thus far have focused on tuning the size and shape of $CuFeS_2$ NCs,[264, 267] however, as of yet a complete understanding of $CuFeS_2$ NC crystal structure has not been developed.

Ternary I-III-VI_2 NCs are known to crystallize in three distinct structures: chalcopyrite (CP), zinc blende (ZB), and wurtzite (WZ).[292] CP is the thermodynamic product, while the WZ and ZB phases are only isolable in nanostructures. The CP and ZB structures are closely related: a CP unit cell consists of two stacked ZB unit cells with ordered cations. WZ is the hexagonal analogue of ZB, which possesses a unit cell that is anisotropic in the crystalline *c*-direction. This anisotropy can be exploited to produce asymmetric NC morphologies and promote orthogonal charge propagation, both of which are useful in applications requiring charge extraction.[81] Furthermore, Shen *et al.* recently observed cation-ordering in WZ $CuInS_2$ resulting in interlaced crystals.[272] The interlaced crystal structure disrupts thermal conductivity without affecting electron transport. Therefore, if WZ $CuFeS_2$ exhibits similar ordering, it will be an exceptional thermoelectric material.

The synthesis of other I-III-VI_2 WZ nanomaterials (*e.g.* $CuInS_2$) has been explored extensively and a great deal regarding their optical properties is now known;[134, 292] however, WZ $CuFeS_2$ has only been prepared once. Kumar *et al.* used the thermal decomposition of a Cu-thiourea complex in the presence of an Fe precursor to produce microstructures of $CuFeS_2$.[268] By tuning the Fe precursor, the authors were able to isolate WZ $CuFeS_2$ 'microflowers'. However, these structures were microns in size and complete characterization of their optical properties was not undertaken.

In this chapter, three potential synthetic routes to nanostructures of WZ $CuFeS_2$ are described. The morphology, structure and composition of the resulting NCs are discussed. The

mechanism behind their formation is suggested and comparisons to the WZ $CuInS_2$ system are drawn. Finally the optical properties of the resultant NCs are detailed and density functional theory (DFT) calculations are used to explore their origin.

7.2 Results & Discussion

7.2.1 Synthesis of WZ $CuFeS_2$ via Cation Exchange

Cation exchange has emerged as a versatile route for the synthesis of NCs with diverse structures. In particular, the metal chalcogenide systems are known to possess a high cationic mobility which, coupled with their high surface area to volume ratio at the nanoscale, means they are a good template for cation exchange. NCs of Cu_2S are known to crystallize in the hexagonal chalcocite structure and thus present a useful intermediate to NCs with the WZ phase. Cation exchange of Cu_2S NCs has been used successfully to produce NCs of both CdS and $CuInS_2$ with the WZ structure.[63, 168, 352] Therefore, initial efforts to synthesize WZ $CuFeS_2$ utilized this synthetic method.

The procedure used was based on the work of van der Stam *et al*. and is described in detail in Appendix E.1.[168] Briefly, dodecanethiol-capped Cu_2S NCs approximately 13 nm in diameter were prepared by Evan Robinson of the Macdonald group using a method modified from the literature,[385] and suspended in toluene. A solution of $FeCl_3.6H_2O$ in methanol was added as the Fe^{3+} precursor and neocuproine was added as a Cu-extracting agent. The mixture was then sonicated for 90 min, as Cu_2S NCs are susceptible to superlattice formation, then stirred for a week at room temperature in a N_2 filled glove box.

The resultant particles were similar in morphology to the parent NCs, however, a slight decrease in size was measured (11.1 ± 1.3 nm, n = 100; Cu_2S = 13.0 ± 0.7 nm, n = 150, Figure 7.1a). Decreases in size of this magnitude are frequently reported in cation exchange

reactions and have been attributed to both lattice contraction of the host due to the incorporation of guest cations (in agreement with Vegard's law) or a contraction effect due to the surface strain field.[386] A second population of nanostructures significantly smaller in size (approximately 1 nm) was also observed. EDS mapping (Figure 7.1b) indicated that these species consisted largely of Fe thus it is likely that this is unreacted Fe^{3+} precursor.

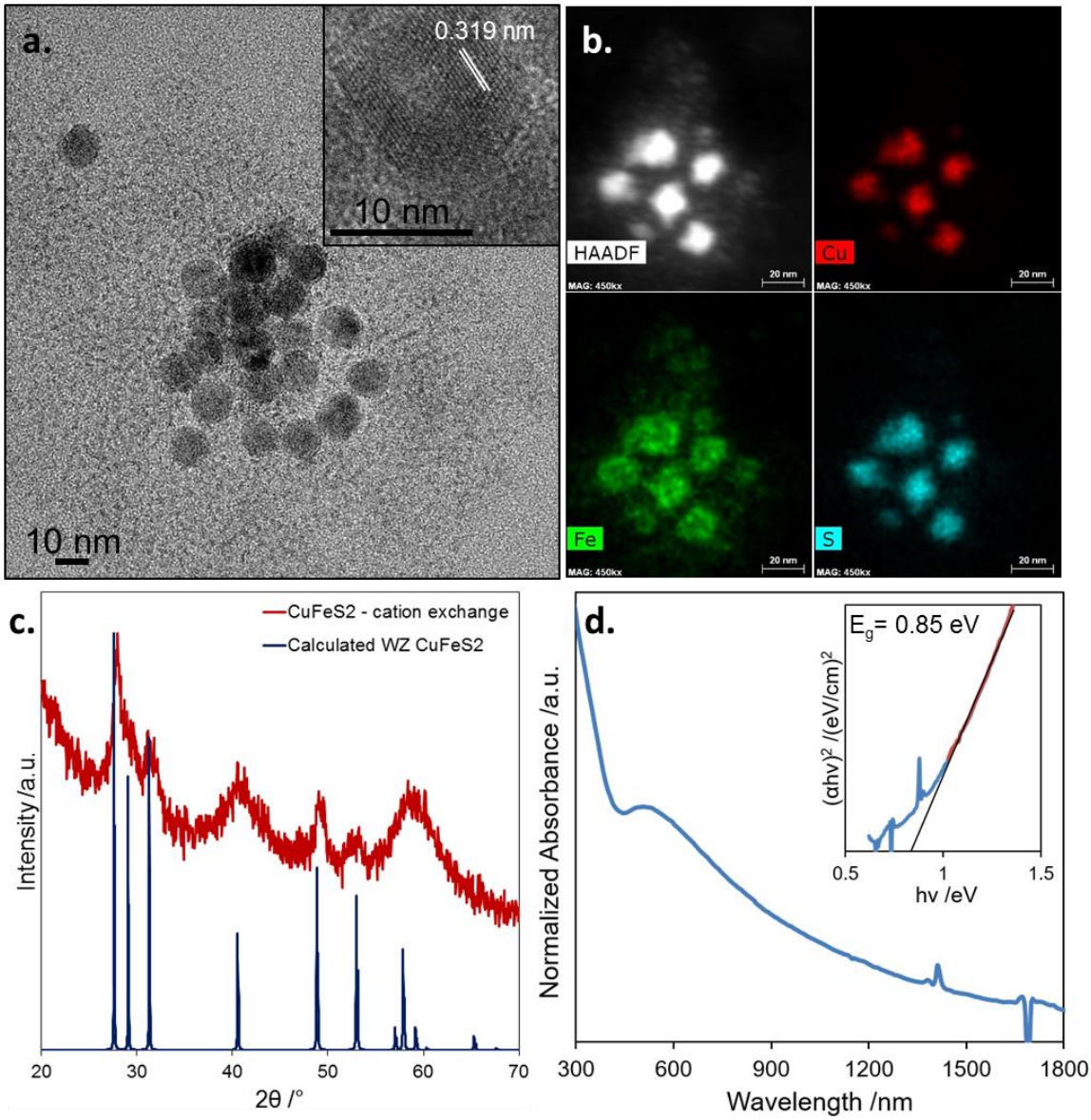

Figure 7.1. Characterization of WZ $CuFeS_2$ NCs synthesized via cation exchange; **a.** TEM image (inset: HRTEM with lattice fringes denoted); **b.** EDS mapping data; **c.** XRD pattern with the calculated pattern for WZ $CuFeS_2$ shown; **d.** UV-Vis absorbance spectrum (inset: Tauc plot used to estimate the experimental band gap (0.85 eV)).

The diffraction pattern of the resultant NCs (Figure 7.1c) showed reflections characteristic of the WZ structure; however, reflections were broad and had low intensity indicating that the product had poor crystallinity. This observation was supported by high resolution transmission electron microscopy (HRTEM) images, in which few lattice fringes were observed. For some particles, lattice fringes were observed with d-spacing 0.319 nm (Figure 7.1a inset), in good agreement with the most intense (100) reflection in the diffraction pattern ($2\theta = 28.0°$; d = 0.319 nm). EDS indicated that NCs had the stoichiometry $CuFe_{1.0}S_{1.4}$.

The absorbance of the product NCs is shown in Figure 7.1d. A peak is observed at 530 nm, reminiscent of that measured for CP NCs (480 nm, Section 3.2), but longer in wavelength. A Tauc plot (Figure 7.1d inset) was used to estimate the band gap at 0.85 eV, considerably larger than the band gap reported for the CP structure (approximately 0.5 eV).

7.2.2 Synthesis of WZ $CuFeS_2$ via Hot-Injection Method

While synthesis of WZ $CuFeS_2$ NCs via cation exchange was successful, limitations to this procedure exist including inconsistent product and issues regarding scalability. Thus a direct synthesis to the WZ product was sought. The reaction described in Chapter 4 was known to proceed via a hexagonal Cu_2S intermediate,[164] therefore it was theorized that a similar procedure might produce WZ $CuFeS_2$. Briefly, $FeCl_3.6H_2O$, thiourea and OlAm were added to a flask and degased for 1 hour. The flask was placed under N_2, heated to 120°C, and a Cu-thiol complex was injected into the mixture. After heating for 30 min, the product NCs has no specific morphology and had diameter 2.7 ± 0.6 nm (Figure 7.2a). The diffraction pattern of the resultant NCs (Figure 7.2c) contained the three reflections characteristic of the WZ structure, however, they were shifted to higher angle ((100) reflection, $2\theta = 28.4°$, d = 0.314 nm). In reasonable

agreement with this, lattice fringes were observed in HRTEM with d-spacing 0.316 nm (Figure 7.2a inset). EDS and EDS mapping (Figure 7.2b) indicated that the NCs were S poor with stoichiometry $CuFe_{0.6}S_{1.2}$. Therefore, the decrease in d-spacing, the distance between lattice planes, is likely due to the low proportion of S^{2-} anions within the material, causing a slight lattice contraction. In this case, the low intensity and broad nature of the powder diffraction reflections are likely due to the poor crystallinity and small size of the NCs.

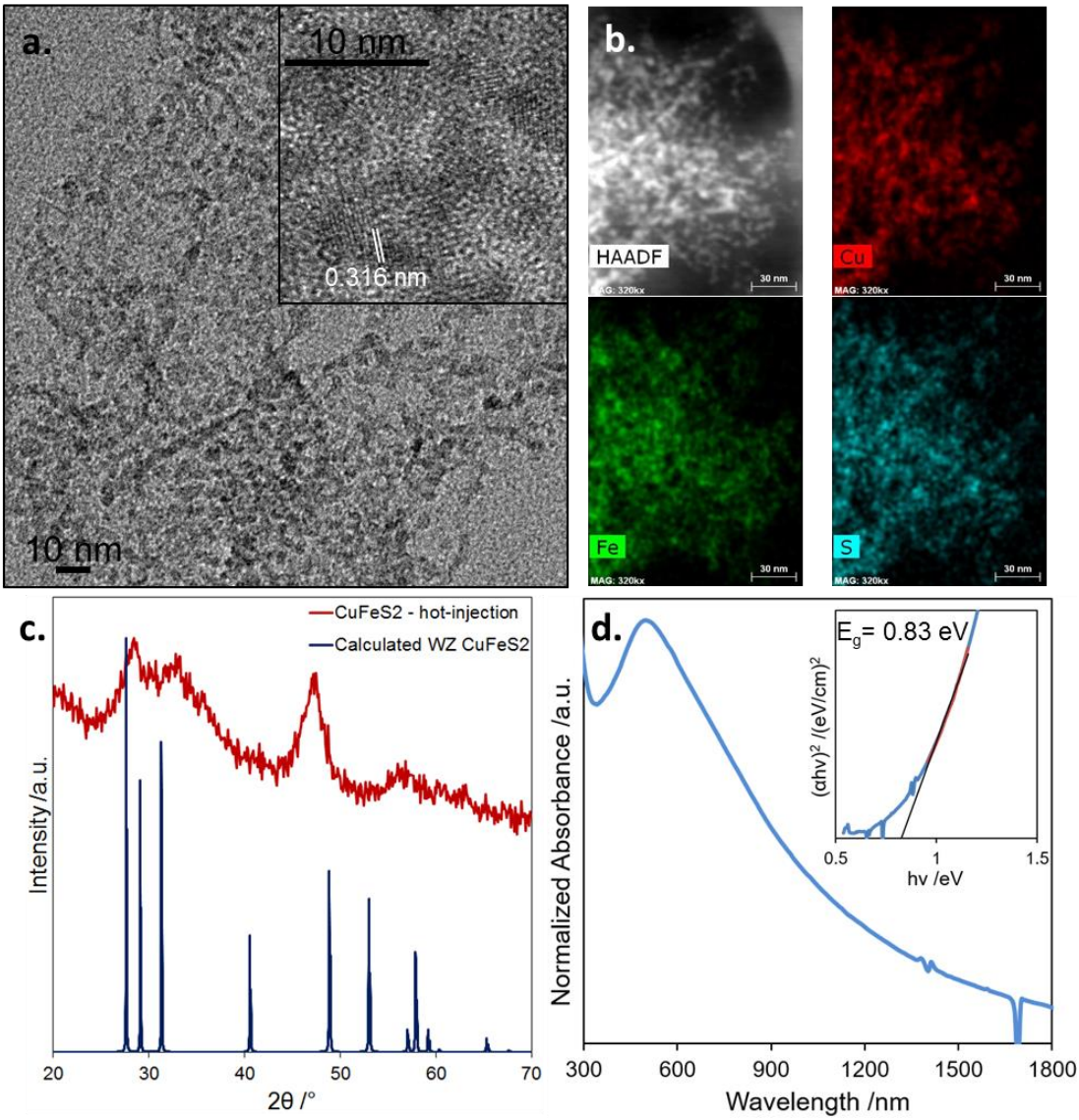

Figure 7.2. Characterization of WZ $CuFeS_2$ NCs synthesized via a hot-injection method; **a.** TEM image (inset: HRTEM with lattice fringes denoted); **b.** EDS mapping data; **c.** XRD pattern with the calculated pattern for WZ $CuFeS_2$ shown; **d.** UV-Vis absorbance spectrum (inset: Tauc plot used to estimate the experimental band gap (0.83 eV)).

A peak in the absorbance of the product NCs (Figure 7.2d) is observed at 500 nm, significantly lower in wavelength than the peak observed for WZ $CuFeS_2$ synthesized using cation exchange, but similar to the peak observed for CP $CuFeS_2$ NCs (Figure 3.8). A Tauc plot (Figure 7.2d inset) was used to estimate the band gap at 0.83 eV, which was in good agreement with WZ $CuFeS_2$ synthesized using cation exchange. This is surprising as NCs of size (approximately 3 nm) are typically confined and in the case of CP have band gap, approximately 1.6 eV.[264] Three possible explanations exist for this; either the Bohr exciton radius of WZ $CuFeS_2$ NCs is less than 1.5 nm; the NC agglomerates observed via TEM are actually attached and the crystallite size is larger than the measured NC size; or the crystallite size of cation exchanged NCs is smaller than the measured NC size. Scherrer line broadening analyses of the (100) reflection were used to estimate the crystallite size for each sample. NCs synthesized using cation exchange had calculated crystallite size 12.8 nm (TEM size 11.1 nm), while NCs produced using a hot-injection method had calculated crystallite size 4.0 nm (TEM size 2.7 nm), in reasonable agreement with the NC size measured using TEM. Therefore, it is most likely that WZ $CuFeS_2$ has a small Bohr exciton radius (less than 1.5 nm).

7.2.3 Synthesis of WZ $CuFeS_2$ via Heat-Up Method

In the synthesis of I-III-VI_2 materials, the distinct reactivity of the constituent ions must be considered.[140, 304] In the case of $CuFeS_2$, Cu^+ and S^{2-} are 'soft' ions, while Fe^{3+} is 'hard'. Therefore, the formation of Cu-S bonds is more favorable than Fe-S. By utilizing a single source precursor containing Cu and S, this reactivity can be exploited and a Cu_2S intermediate can be formed in the synthesis. In this case, a Cu-S complex, copper(II) diethyldithiocarbamate ($Cu(DDTC)_2$) was prepared and added to a flask with $Fe(acac)_3$ and OlAm. The mixture was degased, placed under N_2, and then heated at 120°C for 30 min. The resultant nanostructures

consisted of thin nanosheets, which were observed lying flat on the TEM grid and clustered into hexagonal plates approximately 500 nm in diameter (Figure 7.3a). These large shapes were reminiscent of the 'microflowers' reported by Kumar *et al*.[268] Small clusters of amorphous dark nanoparticles were also observed within the nanostructures (Figure 7.3b). EDS mapping (Appendix E.2) indicated that Cu, Fe, and S were distributed throughout all structures. Lattice fringes were observed with d-spacing consistent with the (100) plane of WZ $CuFeS_2$ and the (112) plane of CP $CuFeS_2$ from different areas of the structure (Figure 7.3a-b inset). These observations were in good agreement with the powder diffraction pattern, which showed strong CP (112) and WZ (100) reflections (Figure 7.3c). Interestingly, all reflections characteristic of CP $CuFeS_2$ were present, however, only the WZ (100) reflection was observed. A possible explanation of this phenomenon is that the product nanosheets are truncated in the crystalline *c*-direction. If this is the case, the intensity of reflections from planes with *c*-indices will be low. Hence, only the (100) and (110) reflections should be observed. In this case, the (100) reflection is observed, while the (110) reflection overlaps with the observed (220)/(204) reflections from the CP phase. No strong indicators for preferred orientation were observed for reflections from the CP structure.

When the $Cu(DDTC)_2$ precursor was heated alone in OlAm, the primary product was the cubic phase digenite ($Cu_{1.8}S$), however, reflections characteristic of the hexagonal covellite structure were also observed (Figure 7.3c). It is possible that the CP and WZ product nanomaterials result from exchange of Fe^{3+} into the cubic and hexagonal Cu-S structures respectively, however, attempts to isolate digenite and covellite intermediates during the reaction were unsuccessful.

The composition of the product nanostructures, measured using EDS, was $CuFe_{0.9}S_{1.8}$. The characteristic broad $CuFeS_2$ peak in the absorbance was centered at approximately 660 nm for this product (Figure 7.3d). The band gap of the product NCs was estimated to be 0.60 eV (Figure **7.3**d inset) lower than the estimated values for WZ synthesized via cation exchange or hot-injection methods; however, this value is consistent with literature values for the band gap of CP, a constituent product.[264, 265]

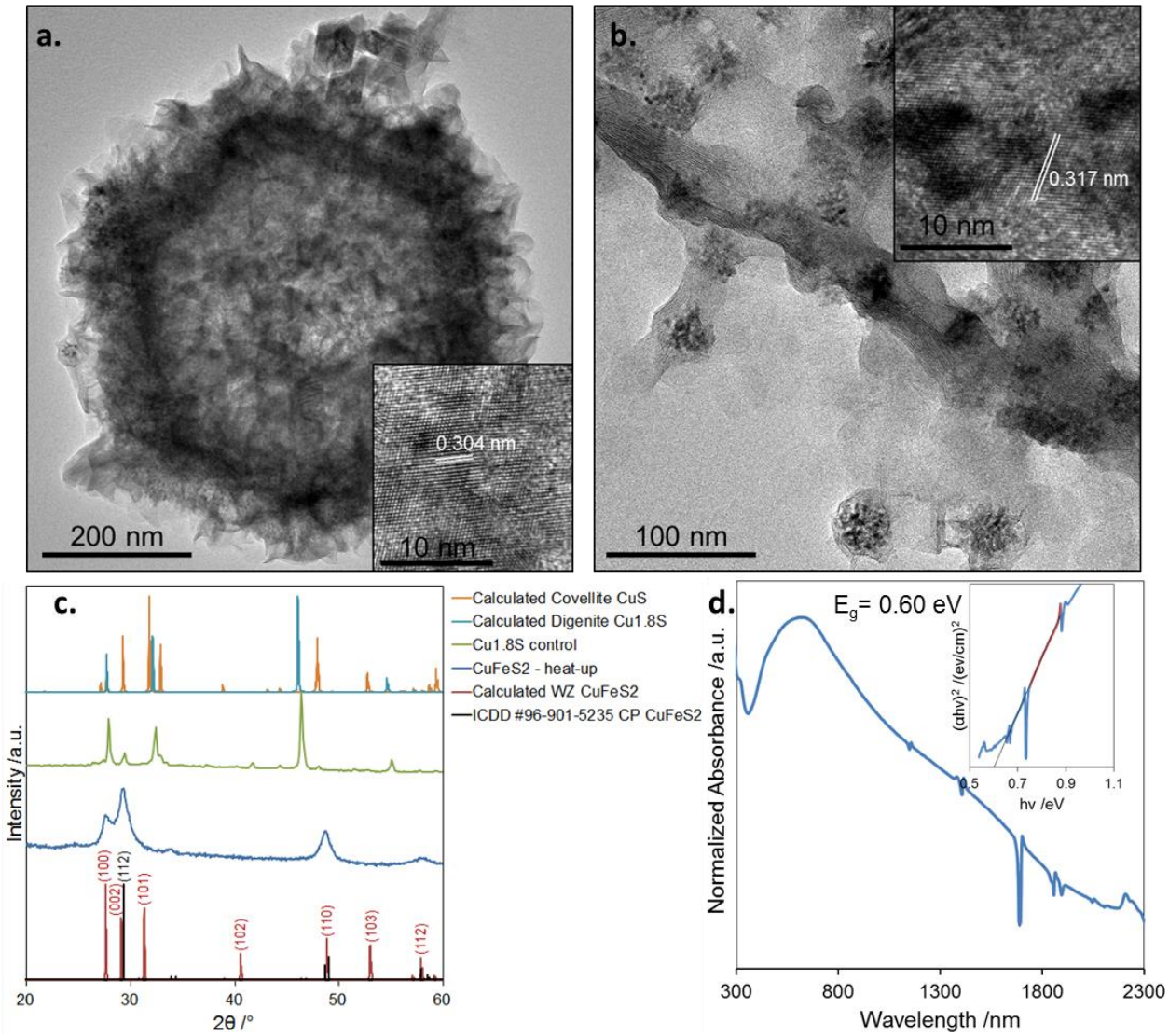

Figure 7.3. Characterization of $CuFeS_2$ nanostructures synthesized via a heat-up method; **a.- b.** TEM images (inset: HRTEM with lattice fringes denoted for CP (**a.)** and WZ (**b.**) phases); **c.** XRD patterns for $CuFeS_2$ nanostructures and the product of the Cu-S control reaction with the calculated patterns for WZ $CuFeS_2$, $Cu_{1.8}S$, CuS and the ICDD card for CP $CuFeS_2$ shown; **d.** UV-Vis absorbance spectrum (inset: Tauc plot used to estimate the experimental band gap (0.60 eV)).

7.2.4 Optical Properties of $CuFeS_2$

Across all three synthetic techniques the shape and position of the absorbance peak changed (Figure 7.4a). For CP NCs, this peak is known to correspond to a transition from the valence band edge, consisting of S *3p* and Cu *3d* orbitals, to empty Fe *3d* orbitals (Section 3.2).[264, 274] In fact, molecular orbital calculations by Kambara indicated that the intermediate band Fe *3d* orbitals were also hybridized with S *3p* orbitals.[387] Thus the authors expect that differences in the concentration of both Fe and S atoms within the NCs will lead to differences in the shape and position of the absorbance peak. Compositional analysis indicates that NCs synthesized via hot-injection have a stoichiometric 1:2 Fe:S ratio, while NCs synthesized via cation exchange had a 1:1.4 Fe:S ratio. In contrast for nanostructures synthesized via heat-up methods, compositional analysis indicated that the system was close to stoichiometric in composition ($CuFe_{0.9}S_{1.8}$); however, given a variety of nanostructure phases (CP and WZ) and morphologies (sheets, clusters, and particles) were observed, it is likely that a range of compositions also exist, leading to the broad multimodal shape of the absorbance.

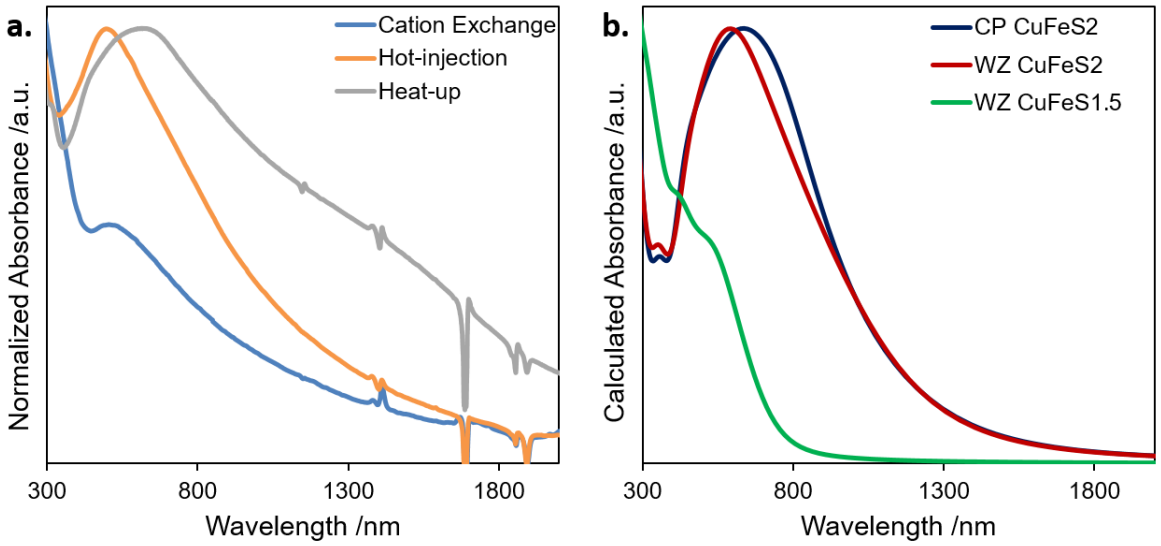

Figure 7.4. Experimental and calculated optical properties for $CuFeS_2$ NCs; **a.** Experimental UV-Vis absorbance spectra for $CuFeS_2$ nanostructures synthesized using three distinct synthetic methods; **b.** Calculated UV-Vis absorbance spectra for CP, WZ and S-deficient WZ $CuFeS_2$.

To further understand the role of structure and S-deficiency on the optical properties of $CuFeS_2$, DFT calculations were performed by Dr. Andrew O'Hara using the Vienna Ab initio Simulation Package (VASP)[349] with exchange correlation described by the Perdew-Burke-Ernzerhof form of the Generalized Gradient Approximation.[388] A plane-wave basis was used with a cutoff of 450 eV and projector augment wave (PAW) pseudopotentials[348, 389] to describe the interaction between valence and core elections. Reciprocal space was sampled using Γ-centered Monkhorst-Pack grids[390] of $8 \times 8 \times 4$ and $6 \times 6 \times 6$ for the CP and cation-ordered, pseudo-WZ, orthorhombic phase respectively. The orthorhombic phase with G-type antiferromagnetic Fe^{3+} ordering was used in all relevant calculations. The localized nature of the Fe *d*-orbitals were described using an on-site Hubbard-like U correction[391] of 4.3 eV. All atomic coordinates and lattice vectors were optimized so that the residual forces were less than 1 meV/Å.

The calculated UV-Vis absorbance spectra (Figure 7.4b) indicated that there were no significant changes in the absorbance of the system for the two different structures. However, when the composition of the system was altered to $CuFeS_{1.5}$, a significant change in the calculated density of states was noted (Appendix E.3), which resulted in a significant depression of the broad absorbance peak centered at approximately 600 nm calculated for stoichiometric $CuFeS_2$. This was similar in character to the depression in absorbance peak measured experimentally for S-deficient NCs synthesized via cation exchange (Figure 7.4a), supporting our hypotheses that changes in NC composition resulted in changes in the NC optical properties. Calculations are currently underway to explore the effect of other non-stoichiometric compositions on NC optical properties.

7.2.5 Comparisons between WZ $CuInS_2$ and $CuFeS_2$ Formation.

Given the similarities between WZ $CuFeS_2$ and WZ $CuInS_2$, a number of comparisons can be drawn in their synthesis. In all of the methods described above, a synthesis for WZ $CuInS_2$ was altered to form the Fe analogue.[164, 168, 304] As such, it is likely that the mechanism of formation for the two materials is similar and proceeds via a hexagonal copper sulfide intermediate. However, significantly lower temperatures were required for WZ $CuFeS_2$ formation. Reactions carried out at higher temperature resulted in the formation of the CP structure. For example, the hot-injection procedure carried out at 140°C resulted in the formation of the CP product (Appendix E.4), whereas for analogous reactions to $CuInS_2$, the WZ product was observed even at far higher reaction temperatures (215°C).[164] A similar trend was noted by Gusain *et al.* who observed a change in phase from WZ to CP on doping $CuInS_2$ NCs with Fe.[392]

The observed differences indicate that WZ $CuFeS_2$ is significantly less stable than its In-analogue. This may well be due to the cation-disorder or interlaced crystal ordering, which contains low symmetry cation-ordering, reported for the WZ system. High spin Fe^{3+} cations have a large magnetic moment and therefore exhibit a strong energetic preference for highly cation-ordered systems. Furthermore, cation-disordered systems tend to be more stable when the constituent cations are similar in size. There is a greater size difference between Cu^+ (r = 77pm) and Fe^{3+} (r = 60 pm), than Cu^+ and In^{3+} (r = 80 pm), which likely contributes to the poor relative stability of WZ $CuFeS_2$. In the related phase, $AgInS_2$ a pseudo-wurtzite, cation-ordered orthorhombic structure is observed. Further synthetic efforts will be focused on obtaining this anisotropic phase for $CuFeS_2$.

7.3 Conclusion

In this report, $CuFeS_2$ nanostructures with the WZ structure were synthesized using three distinct methods. The methods were carefully selected to ensure that each reaction proceeded via a hexagonal copper sulfide intermediate to reach the hexagonal $CuFeS_2$ product. While products were not highly crystalline, in the case of cation exchange and hot-injection techniques WZ was identified as the primary product by XRD and lattice fringes observed using HRTEM. The estimated band gaps of these two systems were in good agreement (approximately 0.85 eV), higher in energy than the reported band gap value for CP (0.5 – 0.6 eV). Crystallite size measured via TEM and Scherrer line broadening analysis were distinct (13 nm and 3 nm), therefore, there is evidence that the system is not confined. The third synthetic method, a heat-up synthesis resulted in a mixed CP/ WZ product. Nanostructures were sheet-like in morphology and a corresponding reduction in intensity was observed via XRD for WZ reflections with non-zero indices along the *c*-axis. A control reaction indicated that the $Cu(DDTC)_2$ precursor decomposed into cubic and hexagonal copper sulfide intermediates under these synthetic conditions. This was likely the origin of the mixed CP/ WZ phase in the product nanostructures. UV-Vis absorbance spectra collected for the product nanostructures of all three syntheses showed variation in the shape and peak position of a broad absorption feature at approximately 500 nm. In CP $CuFeS_2$, this transition is known to correspond to a transition from the valence band to an intermediate band made up of Fe *3d* and S *3p* orbitals. The composition of the product NCs, measured via EDS, varied from $CuFe_{0.6}S_{1.2}$ to $CuFe_{0.9}S_{1.8}$. Thus it is likely that changes in this absorption feature were caused by changes in the concentration of Fe and S atoms within the NCs. This hypothesis was supported by DFT calculations carried out by Dr. Andrew O'Hara, which showed that S-deficient NCs have a markedly different electronic structure,

resulting in a suppression of the broad UV-Vis absorbance peak typically observed for $CuFeS_2$ NCs.

Currently, work is focused on ensuring syntheses to WZ $CuFeS_2$ are robust and repeatable. Further refinement of reaction parameters including surfactant type, precursor type, and temperature will be used to improve the monodispersity, crystallinity and colloidal stability of product nanostructures and, in the case of the heat-up method promote the formation of the WZ structure.

After robust synthetic procedures to monodisperse NCs have been isolated, further investigation of the structural and optical properties of WZ $CuFeS_2$ can be undertaken. Z-contrast STEM images of product NCs can be collected to detect the presence of cation-ordering within NCs. Additionally, monodisperse WZ $CuFeS_2$ NCs in a range of sizes can be synthesized with a view to exploring confinement effects within this system. Moreover, it has been shown that CP $CuFeS_2$ NCs are fluorescent when alloyed and shelled with CdS.[264] Therefore, shelled WZ NCs will be prepared and their luminescence properties studied. Ultimately, the thermoelectric properties of WZ $CuFeS_2$ will be tested to determine the efficacy of this material in application.

8. AN INVESTIGATION OF THE FLEXIBLE STRUCTURE AND COMPOSITION OF $AgFeS_2$ NANOCRYSTALS

8.1 Introduction

Colloidal semiconductor nanocrystals (NCs) have become an important class of nanomaterials with a variety of established applications from biomedicine to optoelectronic devices.[212, 296, 380] As the field has grown, the library of studied NC materials has expanded from the model II-VI metal chalcogenide systems to numerous semiconductors with properties tailored to specific applications. Ternary I-III-VI_2 semiconductors represent a particularly promising material system with a wide range of accessible band gaps from 0.5 eV ($CuFeS_2$) – 3.5 eV ($CuAlS_2$), low toxicity components, and favorable optoelectronic properties.[134, 339, 393] Over the last ten years, significant progress has been made in the understanding of these materials and their efficacy in application has been demonstrated. In particular, $CuFeS_2$ has been identified as a strong candidate for use as a thermoelectric or photothermal therapeutic agent due to its unusually low band gap energy (0.5 eV) and low toxicity constituent elements.[263-265, 269, 278] Additionally, $AgInS_2$ has been investigated for use in solar energy capture and display technology due its band gap at the edge of the visible spectral region (1.8 eV).[134, 286, 287, 353, 394] Interestingly, NCs of the related material $AgFeS_2$ have yet to be characterized completely. Given the potential demonstrated by its analogues, it is likely that NCs of $AgFeS_2$ will also possess valuable properties.

To the author's knowledge, two reports exist describing syntheses to $AgFeS_2$ nanostructures. In the first, Han *et al.* prepared spherical NCs with diameter approximately 15 nm.[119] The estimated band gap of the material was 1.21 eV, well suited for solar energy capture. The authors also noted a reversible phase transition at 176°C in which Ag_2S-Fe_7S_8

hetero-nanostructures were formed. In the second report, Sciacca *et al.* used cation exchange to convert Ag nanowires to Ag_2S, then $AgFeS_2$.[281] The authors estimated the band gap of the $AgFeS_2$ nanowires to be 0.88 eV, suggesting that the discrepancy between the band gap value for $AgFeS_2$ wires and NCs was due to confinement of the spherical particles. In both cases a tetragonal phase (lenaite) was observed.

Ag-based I-III-VI_2 NCs have been reported to crystallize in three distinct structures: tetragonal, cubic, and orthorhombic.[284, 395] The tetragonal phase is similar to the chalcopyrite phase of $CuFeS_2$ and is the thermodynamic product. The cubic spinel phase has composition $AgIn_5S_8$, is metastable, and has proven difficult to isolate in nanostructures.[284] NCs with the orthorhombic phase are also metastable, but are more frequently reported.[284, 353, 395, 396] The orthorhombic structure, which has been observed for $AgInS_2$ and $AgGaSe_2$, is pseudo-wurtzite with cation-ordering resulting in a doubling of the wurtzite unit cell.[283, 396, 397] As such, the phase is also anisotropic which can lead to advantageous material properties such as asymmetric morphology and orthogonal charge transport.[80, 398] To the author's knowledge, no reports of an orthorhombic structure for $AgFeS_2$ exist.

Fe-containing and Fe-doped I-III-VI_2 semiconductor materials are known to possess an unusually low band gap, due to the presence of Fe *3d* orbitals within the expected band gap.[264, 265, 274, 392, 399] In a recent review, it was noted that amongst the most promising applications of colloidal NCs are thermoelectrics, and infrared photodetectors.[56] Here, it is key that NCs possess a band gap in the infrared spectral region; thus ternary systems containing Fe are generating significant interest in the NC community.

In this chapter, $AgFeS_2$ NCs are prepared with spherical and bullet-like morphology. With elemental S in octadecene (ODE) as the S precursor, NCs with the metastable

orthorhombic phase of $AgFeS_2$ (o-$AgFeS_2$) are produced. With elemental S in oleylamine (OlAm) as the S precursor, the product NCs have the stable tetragonal structure (t-$AgFeS_2$). By altering the concentration of elemental S used in the synthesis with a S-ODE precursor, the composition of the NCs can be tuned with a greater amount of S correlating to an Fe-rich product. As the proportion of Fe in the NCs increases, an additional broad absorbance feature at approximately 1050 nm and a corresponding decrease in the estimated band gap of the NCs is observed. To the author's knowledge, this is the first time that an orthorhombic phase and composition-dependent optical properties have been reported for $AgFeS_2$ NCs. The observation of these unique properties demonstrates that $AgFeS_2$ is a fascinating material for further study at the nanoscale. Moreover, NCs with similar optoelectronic properties have proven invaluable in application,[265, 269, 394] thus $AgFeS_2$ nanostructures can now be considered for utilization in a variety of research areas.

8.2 Results & Discussion

8.2.1 Synthesis of $AgFeS_2$ NCs

A procedure based on the synthesis of $AgInS_2$ quantum dots reported by Xie *et al.* was used to produce $AgFeS_2$ NCs.[131] Complete experimental methods can be found in Appendix F.1. Briefly, $AgNO_3$ (0.03 mmol), $Fe(acac)_3$ (0.04 mmol), dioctyl ether (DiOE, 10 mL), oleylamine (OlAm, 0.4 mmol) and oleic acid (OlAc, 0.4 mmol) were degased at 90°C for 1 hr. At this stage, the mixture was placed under N_2 and heated to 180°C. When the reaction mixture reached 180°C, elemental S (0.08 mmol) dissolved in octadecene (ODE, 0.16 M solution) or OlAm (0.16 M solution) was injected and the mixture was heated for 30 min. The resultant NCs were imaged using transmission electron microscopy (TEM, Figure 8.1a-b). NCs prepared with S-OlAm were spherical in morphology with diameter 7.7 ± 2.1 nm (n = 150). In contrast, NCs

prepared with S-ODE had bullet-like morphology with length 24.1 ± 5.5 nm and width 12.9 ± 2.6 nm, n = 150.

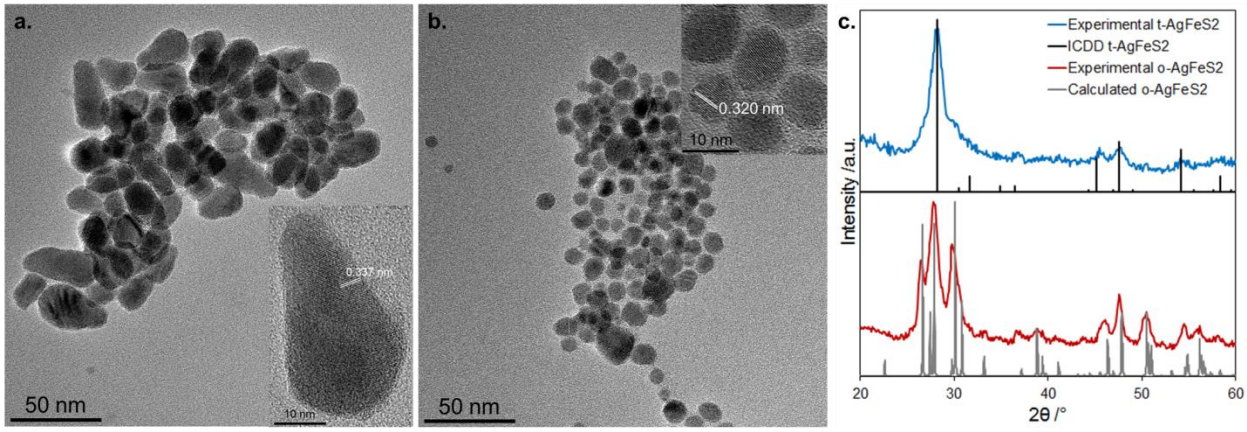

Figure 8.1. Characterization of $AgFeS_2$ NCs; **a.** TEM image of $AgFeS_2$ NCs synthesized using S-ODE (inset: HRTEM with lattice fringes denoted); **b.** TEM image of $AgFeS_2$ NCs synthesized with S-OlAm (inset: HRTEM with lattice fringes denoted); **c.** XRD for $AgFeS_2$ synthesized with S-ODE (red) and S-OlAm (blue) precursors. Calculated reflections for o-$AgFeS_2$ and a literature pattern for t-$AgFeS_2$ JCPDS No. 65-2736 are also shown.

In syntheses to I-III-VI_2 NCs, reaction conditions must be carefully selected to prevent the formation of unwanted binary sulfides. In this case, the introduction of a 'soft' ligand species (dodecanethiol, DDT) resulted in the formation of Ag_2S as a secondary product (Appendix F.2). This phase was also observed as the primary product when the reaction temperature was lowered to 150°C without DDT (Appendix F.3). In contrast, at higher reaction temperature (210°C and 240°C) the $AgFeS_2$ product was observed, but the agglomeration of product NCs occurred (Appendices F.4 and F.5). When a more reactive Fe^{3+} precursor (iron(III) stearate) was used at 210°C, the formation of greigite Fe_3S_4 was observed (Appendix F.6).

8.2.2 Structure & Composition of $AgFeS_2$ NCs

The powder X-ray diffraction (XRD) pattern of NCs prepared with S-OlAm (Figure 8.1c, blue) was a good match to reported reflections for t-$AgFeS_2$. Lattice fringes with d = 0.320 nm (Figure 8.1b, inset) were observed using high resolution transmission electron microscopy (HRTEM) and were consistent with the (112) plane of t-$AgFeS_2$ (2θ = 28.2°, d = 0.317 nm).

The observed tetragonal structure was in good agreement with the work of Han *et al.* in which spherical, t-$AgFeS_2$ NCs were synthesized using a heat-up method.[119]

In contrast, the XRD pattern of NCs prepared with S-ODE (Figure 8.1c, red) showed three sharp peaks at centered at $2\theta = 26.4°$, 28.2°, and 29.8°. The central reflection (28.2°) was indexed to the (112) plane of t-$AgFeS_2$, however, adjacent reflections at $2\theta = 26.4°$, and 29.8° were not a good match to this pattern and do not correspond to the reflections of binary silver or iron sulfide structures.[119, 400, 401] A two phase Rietveld refinement (Figure 8.2a, $\chi^2 = 2.598$)[325] of the experimental diffraction pattern with the unit cell of orthorhombic $AgInS_2$,[402] and t-$AgFeS_2$[282] (Figure 8.2c) was carried out using the General Structure Analysis System (GSAS) with EXPGUI, a graphical user interface (GUI) editor for GSAS experiment files (.EXP).[321, 322] This showed that an o-$AgFeS_2$ structure with space group $P_{n\,a\,2_1}$ and lattice parameters $a = 6.56$ Å, $b = 7.87$ Å, and $c = 6.43$ Å (Figure 8.2b) was a good match to the reflections at $2\theta = 26.4°$, and 29.8°, the pronounced shoulder on the low angle side of the tetragonal (112) reflection, and additional high angle reflections at $2\theta = 50°$, and 56°. The calculated unit cell of o-$AgFeS_2$ was smaller in size than that reported for o-$AgInS_2$ ($a = 6.95$ Å, $b = 8.26$ Å, and $c = 6.68$ Å).[283] This reduction in size is expected given the smaller size of Fe^{3+} (r = 60 pm) with respect to In^{3+} (r = 80 pm). Lattice fringes observed from the bullet-shaped NCs (Figure 8.1a, inset) were also consistent with o-$AgFeS_2$, with measured d-spacing of 0.337 nm in good agreement with the $(120)/(200)$ planes of o-$AgFeS_2$ ($2\theta = 26.4°$, d = 0.338 nm). Furthermore, similar bullet-like NC morphologies have been observed for orthorhombic $AgInS_2$ and wurtzite $CuInS_2$, providing additional support for the assignment of these reflections to o-$AgFeS_2$.[156, 396]

The two phase Rietveld refinement indicated that the product consisted of approximately 40% t-$AgFeS_2$ and 60% o-$AgFeS_2$. Rietveld refinement that included only the orthorhombic

structure did not fit data to within a statistically acceptable tolerance ($\chi^2 = 8.413$). Closer inspection of the product NCs showed small spherical particles with lattice fringe spacing, d = 0.320 nm (Appendix F.7), consistent with the (112) plane of t-$AgFeS_2$ (2θ = 28.2°, d = 0.317 nm). Fine-tuning of the reported synthesis will be required to isolate phase pure o-$AgFeS_2$.

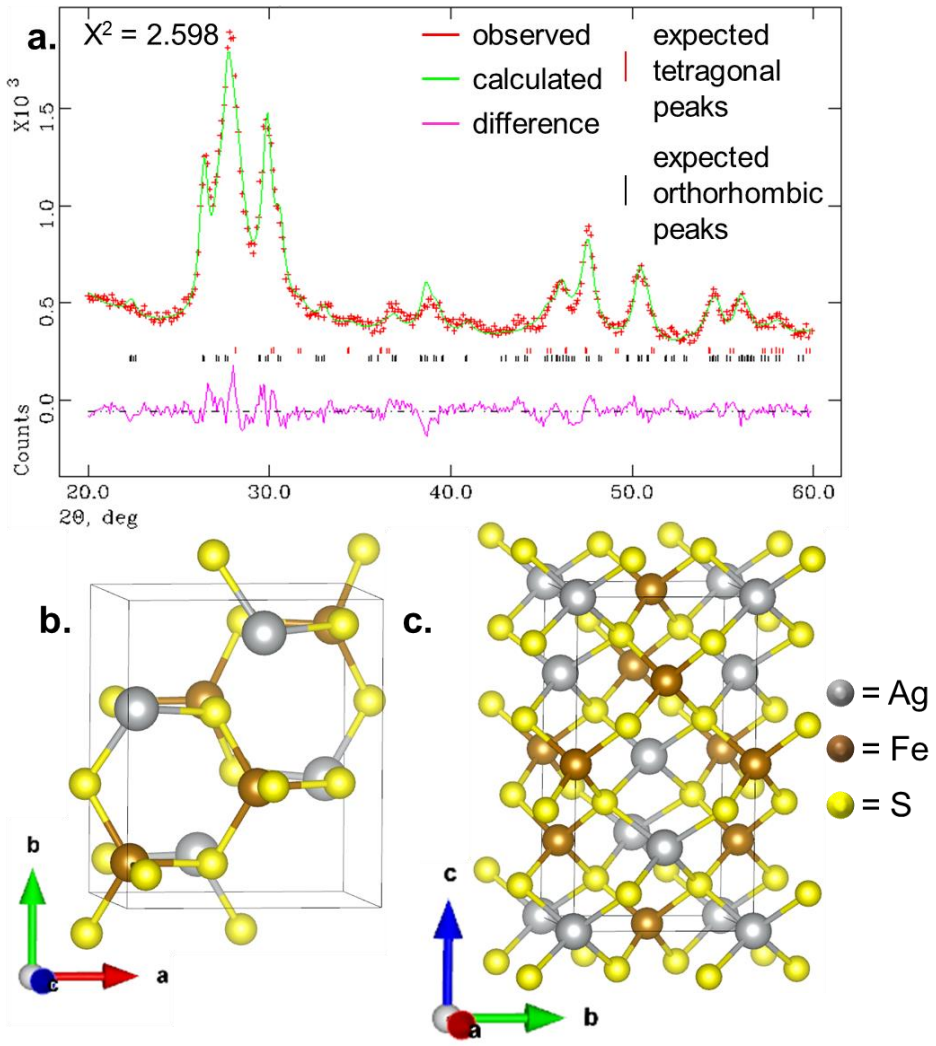

Figure 8.2. Structural analysis for $AgFeS_2$ NCs; **a.** Rietveld refinement of the observed XRD pattern for o-$AgFeS_2$ NCs; **b.** Diagram of the unit cell for o-$AgFeS_2$; **c.** Diagram of the unit cell for t-$AgFeS_2$.

Literature precedent suggests that the orthorhombic phase of Ag-III-Se_2 materials can be stabilized by increasing the concentration of amine ligand, which reduces the surface energy of NCs with the orthorhombic structure;[397, 403] however, here additional OlAm in the synthesis

resulted in the formation of t-$AgFeS_2$ (Figure 8.1c). These contradictory synthetic trends can be attributed the use of the S-OlAm precursor. Elemental S produces alkylammonium polysulfide species when dissolved in OlAm.[404] Thus, in this synthesis, OlAm not only acts as a stabilizing ligand, but also forms a reactive S precursor. The presence of this S complex results in the formation of the thermodynamic product t-$AgFeS_2$. Polysulfide ions have shown greater reactivity than S_8 rings, which are the S species present in S-ODE.[405] Therefore, it was thought that by attenuating the S reactivity the orthorhombic phase was stabilized. To test this hypothesis, a less reactive S precursor, thiourea, was used in ODE under otherwise similar synthetic conditions; however, this resulted in the formation of the binary impurity phase Ag_2S. Increasing or decreasing the concentration of OlAm within the reaction vessel before the addition of S resulted in no significant change in NC structure or morphology.

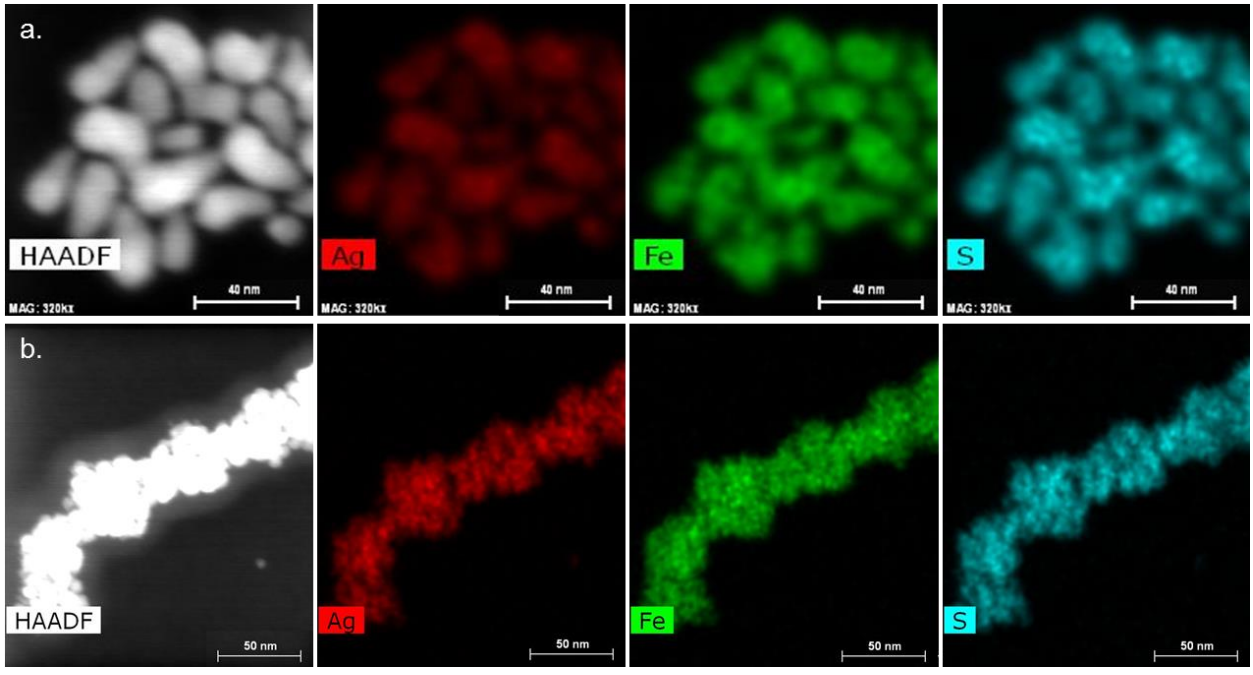

Figure 8.3. EDS mapping for $AgFeS_2$ NCs; **a.** o-$AgFeS_2$ and **b.** t-$AgFeS_2$.

Energy dispersive X-ray spectroscopy (EDS) mapping of nanostructures prepared with S-OlAm and S-ODE showed that all particles were composed of Ag, Fe, and S (Figure 8.3a-b)

indicating that binary sulfide impurity phases were not formed. Measured stoichiometry was $AgFe_{0.97}S_{1.85}$ for o-$AgFeS_2$ and $AgFe_{1.20}S_{1.78}$ for t-$AgFeS_2$ (n = 5).While there was some variability in the measured Ag:Fe ratio, samples were consistently S deficient.

8.2.3 Optical Properties of $AgFeS_2$ NCs

The ultraviolet-visible (UV-Vis) absorbance spectrum of both o-$AgFeS_2$ and t-$AgFeS_2$ NCs (Figure 8.4a) had similar absorbance features to previously published results. Band gap values were estimated to be 1.06 eV for t-$AgFeS_2$ and 1.20 eV for o-$AgFeS_2$ (Appendix F.8) between the values reported by Han *et al.*[119] (1.21 eV) and Sciacca *et al.*[281] (0.88 eV).

The band gap of NCs can be size-, structure-, and composition-dependent. If NCs are small enough in size to be confined, as proposed by Sciacca *et al.*,[281] a decrease in band gap energy with increasing NC size is expected. o-$AgFeS_2$ NCs were significantly larger in size than t-$AgFeS_2$ NCs, yet had a larger band gap energy so confinement is unlikely the origin of the changes in the band gap energy observed here.

If the band gap is structure-dependent, in a mixed phase product the lower energy band gap is consistently observed, but changes in absorbance intensity can occur. Here, the mixed phase o-$AgFeS_2$ product had a higher energy band gap so structural origin of the changes in the band gap energy can also be discounted.

If the band gap is composition dependent, when atomic states which contribute to the valence and conduction band of the material are removed or added the band gap will change. In order to obtain $AgFeS_2$ NCs with a range of composition, syntheses were carried out with different concentrations of elemental S. When the concentration of the S-OlAm precursor was increased, no change in the measured absorbance of the product NCs was observed, but the

presence of low intensity reflections characteristic of o-$AgFeS_2$ was detected (Appendix F.9). In contrast, when the concentration of the S-ODE precursor was increased, an additional absorbance feature at approximately 1050 nm was observed (Figure 8.4b). This correlated to a decrease in the estimated band gap for the product NCs from 1.20 eV (1:2 Fe:S precursor ratio) to 0.59 eV (1:3 Fe:S precursor ratio) (Appendix F.8). XRD of the product NCs (Appendix F.9) showed that all three products were mixed phase with no binary impurity phases observed. The size of the product NCs was measured via TEM (Appendix F.10). No significant change in product size was observed when the S precursor concentration was altered, thus size-dependent absorbance features due to quantum confinement were ruled out.

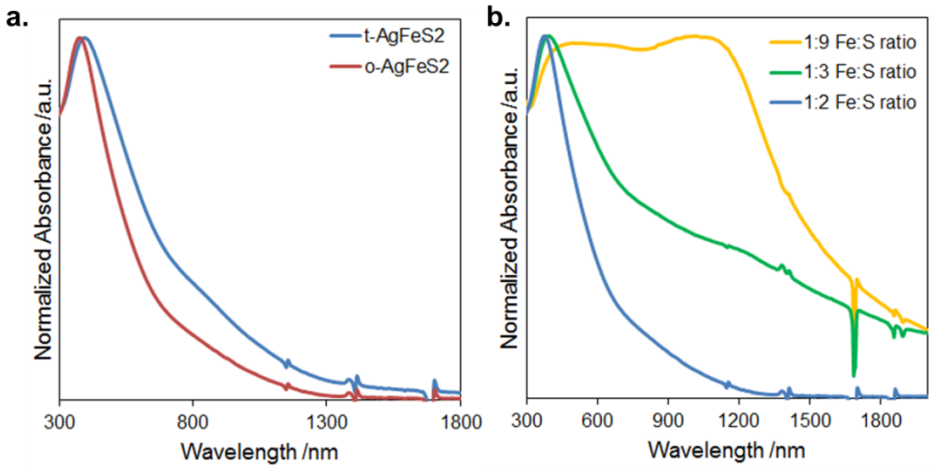

Figure 8.4. Optical properties of $AgFeS_2$ NCs; **a.** UV-Vis absorbance spectra for $AgFeS_2$ NCs synthesized with S-OlAm (t-$AgFeS_2$, blue) and S-ODE (o-$AgFeS_2$, red) precursors; **b.** UV-Vis absorbance of $AgFeS_2$ NCs synthesized with S-ODE with concentration 0.16 M, 0.24 M and 0.72 M, resulting in Fe:S precursor ratio 1:2, 1:3, and 1:9 respectively.

EDS was used to measure the composition of the product NCs and an increase in the proportion of Fe within the NCs was observed corresponding to an increase in the intensity of the absorbance feature at approximately 1050 nm (Table 8.1). Given the correlation between Fe-rich NC composition and the absorbance feature at approximately 1050 nm, it is suggested that this feature is caused by the presence of additional Fe *3d* orbitals within the band gap of the stoichiometric material. This is in good agreement with existing knowledge of the Cu-based, Fe-

containing, I-III-VI_2 materials which show broad absorbance features in the near-infrared and visible spectral regions.[264, 265, 274, 392, 399] Literature calculations have demonstrated that these features correspond to the energetic transition between a valence band made up of Cu *3d* and S *3p* orbitals and an intermediate band consisting of Fe *3d* orbitals.[265, 274, 387] DFT calculations performed by Dr. Andrew O'Hara for $CuFeS_2$ (Chapter 7) suggest that the electronic structure is in fact more complex than initial calculations suggest, with S *3p* orbitals making a significant contribution to the valence and conduction bands. Therefore, while it is clear that the absorbance features observed here are dependent on NC composition, the true origin of these properties must be investigated further. Additional DFT calculations for $AgFeS_2$ are currently underway.

Synthetic conditions	EDS atomic %			Stoichiometry
	Ag /%	Fe /%	S /%	
1:2 Fe:S ratio	26.2	25.4	48.4	$AgFe_{0.97}S_{1.85}$
1:3 Fe:S ratio	25.2	27.1	47.8	$AgFe_{1.08}S_{1.90}$
1:9 Fe:S ratio	24.8	29.7	45.5	$AgFe_{1.20}S_{1.83}$
XS $Fe(acac)_3$	27.4	26.7	45.9	$AgFe_{0.97}S_{1.68}$
$Fe(stear)_3$	26.0	28.3	45.7	$AgFe_{1.09}S_{1.76}$

Table 8.1. Composition of $AgFeS_2$ NCs synthesized under different synthetic conditions.

Interestingly, when a reaction was carried out with excess Fe^{3+} there was no increase in the proportion of Fe in the product NCs measured using EDS (Table 8.1), rather a large amount of unreacted Fe^{3+} was observed in the background of an EDS map (Appendix F.11). Correspondingly no absorbance feature was observed at approximately 1050 nm, as the product $AgFeS_2$ NCs were not Fe-rich. In contrast, when a more reactive Fe^{3+} precursor was used (iron(III) stearate), a strong absorbance feature at approximately 1050 nm was observed (Appendix F.12) along with an increase in measured Fe proportion within the NCs (Table 8.1).

However, the formation of unwanted binary impurity phases (Ag_2S and Fe_3S_4) was also observed.

8.3 Conclusion

A colloidal hot-injection synthesis was developed to obtain $AgFeS_2$ NCs. When S-OlAm was used as a precursor, spherical t-$AgFeS_2$ NCs were produced as the primary product. When S-ODE was used as a precursor, bullet-shaped o-$AgFeS_2$ NCs were produced as the primary product. The difference in phase of the product NCs was attributed to the formation of a reactive alkylammonium polysulfide intermediate in the S-OlAm mixture, which promoted the formation of t-$AgFeS_2$. The less reactive S precursor, S_8 suspended in ODE, promoted the formation of o-$AgFeS_2$. This is the first report of the metastable orthorhombic phase, therefore Rietveld refinement was used to determine lattice parameters for the unit cell (a = 6.56 Å, b = 7.87 Å, and c = 6.43 Å). A broad absorbance feature centered at approximately 1050 nm was also observed for $AgFeS_2$ NCs for the first time. The intensity of this feature correlated to the proportion of Fe within the product NCs. The low energy absorbance was therefore attributed to the introduction of Fe *3d* orbitals within the band gap of stoichiometric $AgFeS_2$, a phenomenon observed in Cu-based I-III-VI_2 materials. NCs with lower Fe concentration exhibited a single absorbance feature with a shoulder at approximately 900 nm in good agreement with literature data. As a result, the band gap of the system was tuned from 0.59 – 1.20 eV.

Currently, efforts are focused on refining the NC synthesis to isolate o-$AgFeS_2$. The work presented here and literature syntheses for other orthorhombic I-III-VI_2 NCs suggest that the selection of surfactants and their concentrations are key in promoting the growth of orthorhombic NCs. For example, Bai *et al.* reported that increasing OlAm concentration in the synthesis of $AgGaSe_2$ NCs resulted in an increase in the proportion of o-$AgGaSe_2$ and a

corresponding decrease in the proportion of t-$AgGaSe_2$ formed.[397] Similarly, Ng *et al.* reported that both DDT and OlAm were required for the formation of o-$AgInSe_2$ NCs, with t-$AgInSe_2$ or binary impurity phases observed when using only one of the two surfactants.[403] As such, work towards the isolation of phase pure $AgFeS_2$ NCs will begin by tuning the surfactant type and surfactant concentration in their synthesis.

When NCs of each phase have been isolated, syntheses to monodisperse o- and t-$AgFeS_2$ NCs with controlled compositions and a range of sizes will be developed. Given the strong dependence of NC phase on surfactant type and concentration, these parameters will be fixed. Therefore, efforts to tune the size of NCs will initially be focused on altering the reaction time and temperature, while efforts to tune NC composition will be focused on altering the type and concentration of precursor materials. The synthesis of NCs with a variety of size and composition will facilitate additional study of the optical properties of the material, allowing their dependence on size, structure, and composition to be understood more completely. In support of this study, density functional theory calculations will be performed to investigate the origin of changes in the optical properties. While the NCs reported here are not luminescent, it is hoped that by shelling or alloying with ZnS fluorescent NCs will be obtained. This will enable additional spectroscopic techniques, such as time-resolved photoluminescence spectroscopy, to be utilized to further understand this material and allow the integration of these NCs into applications requiring luminescence.

$AgFeS_2$ is uniquely positioned for a low toxicity material as the biological effects of the constituent atoms are already well understood.[136] NCs of this material with a small band gap energy (Fe-rich) can thus be utilized as a photothermal therapeutic agent. Furthermore, NCs with an anisotropic crystal structure (o-$AgFeS_2$) and a low band gap energy (Fe-rich) hold great

promise for use in applications requiring infrared absorbance and charge transport, such as thermoelectricity or infrared photodetection. Ultimately, the synthesis of $AgFeS_2$ will be tuned to produce NCs well suited for each application and their performance tested.

9. SUMMARY & FUTURE DIRECTIONS

It is well known that the crystal structure of a material dictates several of its properties. In a semiconductor, this is particularly important as the electronic structure and correspondingly the band gap of a material are dictated by the arrangement of ions in the crystal lattice. At the nanoscale, metastable crystal structures can be isolated which cannot be accessed in the bulk. Such systems can possess unique optoelectronic properties and demonstrate superior performance in application. Despite this potential, the correlation between the structure and optical properties of nanoscale materials is not well understood, which makes prediction of properties from structure difficult. The overarching theme of this dissertation is to develop a more complete understanding of the properties of metastable, anisotropic I-III-VI_2 nanostructures so that improved predictions can be made for similar materials. In the following chapter, a brief summary of the conclusions drawn from the conducted research is presented. Recommended future work applicable to all projects is then described. Finally, the impact of this research on the wider field of colloidal semiconductor nanocrystals (NCs) is reviewed, and the author's opinions on the outlook of this research area are detailed.

9.1 Summary

Over the last 25 years, the study of colloidal NCs has resulted in the elucidation of countless fundamental properties for nanoscale materials. Amongst these, the properties of semiconductor NCs, such as their large catalytic surface area, high fluorescence quantum yield, and size-tunable band gap, hold great potential for a huge range of applications. Commercially, quantum dots are being utilized in displays and solid state lighting. Their use has also been explored in a range of other fields, including biomedicine, solar energy capture, and catalysis.

Exquisite control has been demonstrated over the synthesis of NCs, allowing the selection of particle size, morphology, phase, and functionality. The nano-size of these semiconductors can allow the isolation of structures not seen in the bulk. The dependence of a material's optoelectronic properties on structure means such nanostructures exhibit unique characteristics, which can be exploited in application. The ternary I-III-VI_2 semiconductors, $CuInS_2$ and $CuFeS_2$, are a good example of this. Both materials possess the chalcopyrite structure in the bulk, but the hexagonal structure, wurtzite, can be formed under certain synthetic conditions. Similarly, for $AgInS_2$ and $AgFeS_2$ a pseudo-wurtzite, orthorhombic structure can be accessed at the nanoscale. In this dissertation, syntheses were developed to form wurtzite $CuInS_2$, wurtzite $CuFeS_2$, and orthorhombic $AgFeS_2$ NCs and their properties were investigated.

In the Cu-containing materials, wurtzite NCs are formed via a Cu_2S intermediate. The high and low chalcocite phases of Cu_2S have a hexagonal anionic lattice, thus cation exchange processes yield a hexagonal product. As chalcopyrite is the thermodynamic product, the reaction conditions must be carefully selected to ensure the hexagonal product is retained. In the case of $CuFeS_2$ (Chapter 7), the wurtzite structure was difficult to isolate with reaction conditions that yield the wurtzite structure for $CuInS_2$ found to yield chalcopyrite $CuFeS_2$. This is likely due to both the large magnetic moment of Fe^{3+} and the large difference in ionic radius between Fe^{3+} and Cu^{+}, resulting in a large energetic preference for cation-ordering. In contrast, In^{3+} and Cu^{+} are similar in size, thus cation-disordered wurtzite $CuInS_2$ is more stable. In Chapter 4, a direct synthesis to wurtzite $CuInS_2$ NCs was developed. The product NCs exhibited photoluminescence in the near-infrared (1.3 eV) with low quantum yield (approximately 0.5%). In Chapter 5, the quantum yield was increased to 1.0% or 6.6% by coating the NCs with ZnS or CdS respectively. Given the large Stokes shift and long radiative lifetime of the luminescence, it was assigned to a

radiative point defect within the NC. Density functional theory was used to calculate the optical levels of candidate point defects. Of the calculated levels, the transition energies associated with In-defects (In_i, Cu_{In}, and V_{In}) agreed best with experimental data. Therefore photoluminescence was assigned to an In-based defect within the NC, in good agreement with the cation exchange mechanism of NC formation.

The anisotropy of the wurtzite crystal structure can allow for orthogonal charge propagation within the material. This is particularly desirable for photocatalytic applications, in which charge extraction is required. Metal-semiconductor hybrid particles also enhance charge separation, as the metallic domain can act as an electron sink. Therefore, in Chapter 6, the synthesis of a range of wurtzite $CuInS_2$-metal hybrid NCs was developed. Pt-$CuInS_2$ hybrids could be synthesized with dimeric or core-shell morphologies. The presence of a Pt shell prevented the hybrids from undergoing ligand exchange, however, these hybrids showed improved photocurrent and photostability with respect to the bare $CuInS_2$ NCs, demonstrating the efficacy of these NCs in solar energy capture applications. Replacing Pt^{2+} with Pd^{2+} in a synthetic scheme resulted in the formation of $CuInS_2$-Pd_xS NCs.

The optical properties of $CuFeS_2$ and other Fe-containing semiconductors have proven unique with the introduction of Fe atoms into a system resulting in unusually low band gap materials such as chalcopyrite $CuFeS_2$ (E_g = 0.5 eV). In Chapter 7, the band gap of wurtzite $CuFeS_2$ was estimated to be slightly larger than this (E_g = 0.8 eV); however, broad absorbance features consistent with those of chalcopyrite $CuFeS_2$ were observed for the wurtzite structure across the visible spectral region. Therefore a similar band structure to the chalcopyrite was proposed for the hexagonal material with energetic transitions to a band composed of Fe *3d* orbitals and S *3p* orbitals suggested. Density functional theory calculations of the density of

states for WZ $CuFeS_2$ were in good agreement with this. Interestingly, an analogous broad absorbance feature at approximately 1050 nm was also observed for Fe-rich $AgFeS_2$ NCs (Chapter 8). This is the first time broad, multimodal absorbance has been observed for $AgFeS_2$. It was determined to be size and structure independent, and correlated to changes in the composition of the NCs measured using EDS. Specifically, NCs which contained more Fe had a more intense absorbance peak at approximately 1050 nm. Therefore, it is likely that this absorbance is caused by the introduction of Fe *3d* states within the band gap of the stoichiometric material. The presence of this feature allowed the tuning of the $AgFeS_2$ band gap energy from 0.6 – 1.1 eV.

Furthermore, NCs of $AgFeS_2$ with an orthorhombic structure were synthesized in Chapter 8. This is the first report of orthorhombic $AgFeS_2$ NCs. While phase pure samples could not be isolated, the identification of this anisotropic structure represents a significant leap forward in our understanding of this material.

9.2 Future Directions

While a road map for each project has been outlined in the conclusion of each chapter, here the author considers valuable future studies that are applicable to all three of the materials explored in this dissertation.

Anisotropic crystal structures have been identified as materials that can exhibit superior charge transport. More specifically, differences in the mass of the hole and electron along lattice axes can cause them to move preferentially in a certain direction. If the preferred direction for the hole and electron are orthogonal, recombination is prevented. Calculations carried out by Dr. Xiao Shen have indicated that for WZ $CuInS_2$ the mass of the hole and electron differ by an order of magnitude ($\mu_{e^-} = 0.15$; $\mu_{h^+} = 1.5$) in the lattice *c*-direction.[379] Similar discrepancy is

expected in the mass of charge carriers for $CuFeS_2$ and $AgFeS_2$. With careful design, it should be possible to create a NC system that exhibits measurable orthogonal charge transport. Direct measurements of anisotropic charge transport have been carried out for thin film and single crystal materials,[406, 407] however, for NCs the inherently small size of the component material presents an added level of experimental complexity. To perform a direct measurement, a film of NCs can be deposited and tested in the same manner as a thin film.[406] Preferred orientation of NCs within the films can be achieved using electrophoretic deposition,[408] which exploits the polarity intrinsic to the wurtzite crystal structure. It is likely that annealing of the NC films to remove insulating organic surfactant molecules or a ligand exchange procedure to replace long chain molecules with molecules conducive to charge transfer will also need to be performed to enhance conductivity of the NC film. If direct measurements are successful, this study can be used to inform the design of efficient NC photocatalysts and NC-based electronics.

The unusual optical properties of Fe-containing, Cu-based semiconductors are well known, and it is clear from this work that Ag-based nanoscale systems can exhibit similar properties. Further examination of the literature reveals that while these properties are well known, a fundamental understanding of their origin has not been developed. Initial calculations performed in support of this dissertation show that the position and intensity of NC absorbance are not only reliant on the presence of Fe within the material, but also highly dependent on the NC composition with changes in S concentration resulting in significant changes in the electronic structure of the material. A combined experimental and theoretical study of the effect of composition on the optical properties of Fe-containing, I-III-VI_2 NCs is proposed, in which $CuFeS_2$ and $AgFeS_2$ NCs with a range of compositions are prepared and characterized, then the results compared to the calculated electronic structure for materials of similar composition. This

will allow the elucidation of the origin of the unusual optical characteristics observed for Fe-containing semiconductor NCs. This knowledge will inform future synthetic efforts towards the production of these promising infrared absorbers.

Due to their low band gap energies, potential for superior charge transport, and in some cases interlaced crystal structure, the wurtzite NCs synthesized here are well-suited to application as a NC thermoelectric. Therefore, an important area for future study will be the testing of their thermoelectric properties. A widely applicable method for testing NC thermoelectrics has been developed by the Cabot group,[409] NC powders are annealed to remove the organic ligands then pressed into a pellet. Thermoelectric characterization is carried out using a standard four-probe method to determine the electrical properties of the system and a combination of xenon flash apparatus and differential scanning calorimetry to determine its thermal properties. It is hoped that similar measurements can be carried out on the NC materials described in this dissertation to determine their efficacy as a thermoelectric material.

9.3 Outlook

The elucidation of the structural properties for a family of ternary NCs may seem to be an incremental step; however, when considered in the broader context of NC research, I believe a number of lessons can be learnt. Firstly, amongst the surfeit of tunable parameters for colloidal NCs, crystal structure can be easily overlooked. While anisotropic structures have frequently been exploited to grow NCs with asymmetric morphology, their effect on the optoelectronic properties of a system are often not considered. In this work, I have highlighted the importance of structure in NC systems and significantly improved the understanding of the wurtzite structure, a common phase in nanoscale II-VI and I-III-VI_2 materials. This knowledge and the

methods used to obtain it can now be utilized either to improve material performance in application or inform the synthesis and study of related NC systems.

Over the course of my research, my experiences at the interface of experiment and calculation have been incredibly impactful. The most significant lesson that I have learnt is the exceptional value of combining experimental and theoretical study in the elucidation of the fundamental properties of nanoscale materials. Without calculations, hypotheses regarding the origin of trends observed experimentally are difficult to support. The inverse is also true. I believe here strong evidence for the origin of NC optical properties is provided using a balance of experiment and theory. This work could act as a template for the elucidation of the fundamental properties of other semiconductor systems at the nanoscale and beyond.

I believe the final key lesson to be learnt from this work is that, as the library of NC materials is expanded, there remains a need for fundamental research. Over the last fifteen years, the selection of materials for exploration in NC form has been predominantly driven by application. Early applications for colloidal NCs included photovoltaics, bioimaging, light-emitting diodes, and display technology. Thus, semiconductors with band gaps in the visible or near-infrared spectral regions dominated the field. At this stage, materials such as $CuFeS_2$ were discounted as useless or uninteresting. As the scope of NC application has widened it has become apparent that such materials are well suited for promising technologies. In work driven by curiosity, previously unobserved material properties for $AgFeS_2$ have been discovered, which identify the system as a good candidate material for a number of applications. Therefore, as researchers expand and develop our library of NC materials, it is important that no proverbial stone is left unturned.

This final lesson can perhaps be extended to the colloidal semiconductor NC field as a whole. Current political climate aside, application driven research is often the result of a well-understood system, which is certainly the case for the model II-VI NC materials. Given the versatility and promise of colloidal semiconductor NCs, I have no doubt that they will find use commercially in a range of applications. However, at present I believe the relentless drive towards devices is to the detriment of developing a complete understanding of NC systems for a wider scope of materials. Without this understanding, NCs cannot meet their full potential in application. As more mature NC technologies such as quantum dot sensitized solar cells and quantum dot displays reach their apex, they have faced significant competition from other materials (*e.g.* perovskite photovoltaics and organic light emitting diodes). These challenges have thus far limited their commercial use, but perhaps will encourage a greater proportion of fundamental studies as researchers work to improve the performance of NCs in application.

The array of reported uses for NCs continues to expand rapidly. Ultimately, the most lucrative and/ or most practical application for colloidal NCs may well not yet exist. In the short term, I believe commercial applications for NCs will continue to be limited to their integration into well-established technologies (*e.g.* quantum dot displays). In particular, NCs have recently been integrated into infrared cameras, which can be operated at wavelengths not accessible to silicon devices,[56] and into security inks, which are invisible under ambient lighting conditions, but are readable using a near-infrared laser.[410]

In the longer term, I believe that research will focus on three key areas. The first is driven by market opportunity. Commercially available infrared photodetectors are based on bulk semiconductors or epitaxially grown materials. The high material and processing cost per unit area of this technology, in excess of $50,000 for an infrared camera,[56] prevents large scale

deployment. Therefore, opportunity exists for novel disruptive technologies to enter the market. Colloidal NCs of low band gap materials can sustain infrared electronic transitions and afford low-cost liquid processing at moderate temperature; thus, they may well turn out to be a disruptive technology in this market. The development of colloidal NCs with infrared transitions is ongoing and this work has been extended to focus on NCs as a thermoelectric material. The second application in which I believe NCs will play a significant role is biomedicine. While NCs are already widely used as fluorescent markers, recent research progress has indicated that the focus of NC bio-research will expand to include theranostics and photothermal therapy. The biggest challenge remains their translation from lab to industry with regulatory approval a major obstacle here. In the immediate future, it is more likely that NCs will find biomedical application outside the body. A good example of this is the work of the Giorgio group at Vanderbilt University who have developed an extracorporeal microfluidic device that utilizes gold nanoparticles to capture and separate bacteria from blood. Arguably the most significant property of NCs is their high surface area to volume ratio. Eventually, I suspect that NCs will find application in a field that utilizes this unique attribute, catalysis. Recently, a great deal of research in the Macdonald group and beyond has focused on developing a fundamental understanding of NC surfaces and charge transfer at NC interfaces. This work is now being utilized to develop efficient NC catalysts for a diverse range of reactions including water-splitting, the degradation of organic pollutants, and the synthesis of organic molecules. While challenges remain in this field, I believe that the low-cost and high surface area of colloidal NCs will ultimately allow for their commercial application in this area.

As researchers strive to develop a more complete understanding of NC systems, they are often limited by the characterization tools available to them. Therefore, within the area of

fundamental NC research I predict that the development of new characterization tools will be an area of significant growth. In particular, the advent of *in situ* characterization techniques will allow the study of formation mechanisms for the complete library of NC materials. The elucidation of the role of surfactants in NC nucleation, the role of clusters in NC formation, and the dynamics of NC growth will enhance researchers' control over NC parameters and lead to the synthesis of even more unique nanostructures with unimaginable properties.

As a scientist, I am primarily driven by my own curiosity and a need to answer the question, why. This is the premise of fundamental research, which seeks to broaden our knowledge of the world around us. While its value has been the subject of some debate, there is no doubt that such work provides the foundation upon which applied research is built. The research presented in this dissertation is by nature fundamental, but represents a significant step forward in the understanding of structure within the field of colloidal semiconductor NCs. Over the last 10 years, NCs have emerged as an important class of materials with great potential in a wide range of applications. It is my hope that the work described here will act as a stepping stone in the realization of some of this potential.

APPENDICES

A. Quantum mechanical description of bulk semiconductors

A free electron in a vacuum can be described by only a plane wave ($\Psi(x) = e^{ikx}$) and has a continuum of energy levels (Figure A.1a). Solution of the Schrödinger equation results in the dispersion relation:

$$E(k) = \frac{\hbar^2 k^2}{2m_0} \tag{A1}$$

In contrast, electrons in a semiconductor experience a potential caused by the Coulombic attraction of positively charged atomic cores. Given the repeating nature of bulk crystal structures, this can be modeled by a periodic potential originating from the crystal lattice. The Hamiltonian to describe the system (in one dimension) is:

$$H = H^0 + V(x) = -\frac{\hbar}{2m}\frac{\partial^2}{\partial x^2} + V(x) \tag{A2}$$

where $V(x)$ describes the potential set by the crystal lattice and is periodic over the lattice constant, a, such that $V(x) = V(x + a)$. The corresponding wavefunctions should have similar periodicity, so they possess the same eigenvalue, E, after translation over the distance a. A solution of the Schrödinger equation that displays these properties is known as a Bloch wavefunction and has the form:

$$\Psi_k(x) = e^{ikx}.u_k(x) \tag{A3}$$

where k is the wavevector ($k = \frac{2\pi}{\lambda}$) and $u_k(x)$ is a function that is periodic with the lattice constant ($u_k(x) = u_k(x + a)$). Physically, the plane wave (e^{ikx}) represents the phase of the wavefunction, and $u_k(x)$ describes the response of the valence electrons to the crystal lattice.

Electrons with $\lambda \gg a$ or $\lambda \ll a$ feel little or no effect from the periodic potential and thus their energy is similar to that of free electrons. However, when $\lambda \sim 2a$ (or $k = \frac{\pi}{a}$) electrons are reflected by the periodic potential. The reflection of electrons results in the formation of standing waves, consisting of a linear combination of the plane waves with $k = \frac{\pi}{a}$ and $k = -\frac{\pi}{a}$. The two standing waves Ψ^{+}_{Bloch} and Ψ^{-}_{Bloch} are displaced by $\frac{a}{2}$. Therefore, the first concentrates the probability of finding an electron at the ions (lowering the potential energy), while the second concentrates the probability between the ions (increasing the potential energy). The difference in energy between the two waves creates a gap in the dispersion relation for free electrons (equation A1) at $k = \frac{n\pi}{a}$, where n is an integer (Figure A.1). This gap known as the band gap, E_g^0.

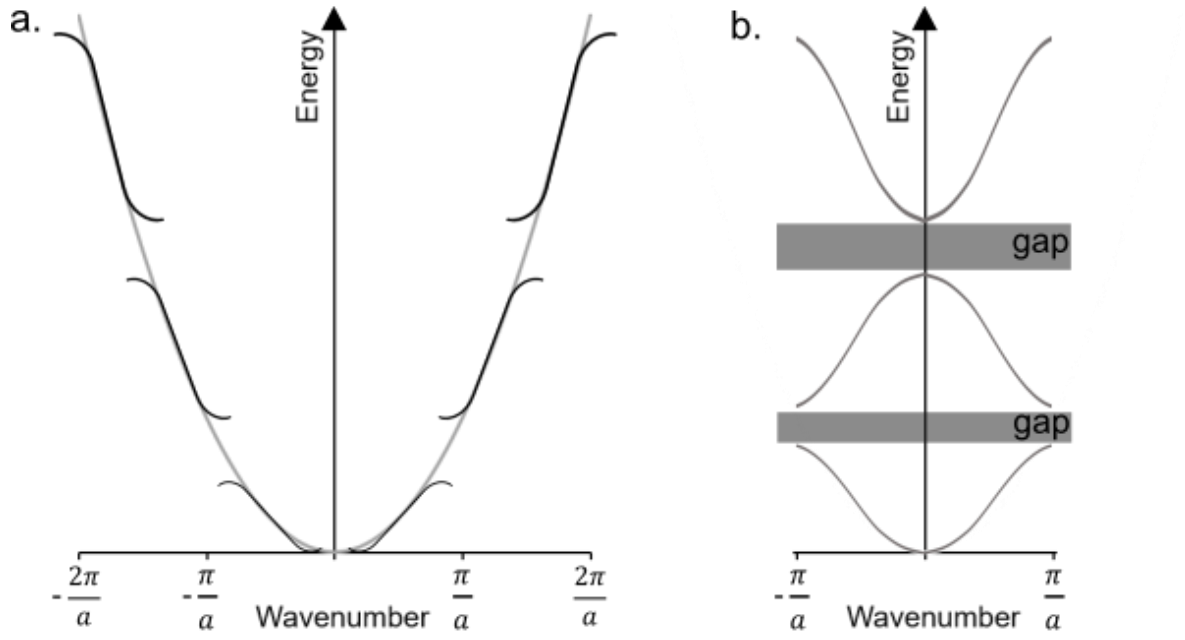

Figure A.1. Dispersion relation for electrons in a periodic potential. **a.** Dispersion relation of free electrons in vacuum (gray line), and of electrons in the periodic potential of an infinite crystal with lattice constant, *a* (black line); **b.** Reduced zone representation of the dispersion relation for electrons in a periodic potential in **a.**

When the effects of quantum confinement are considered, the Bloch wavefunctions describing the bulk properties of the semiconductor are multiplied by an envelope function to correct for the size of the structure:

$$\Psi_{total}(x) = \Psi_{Bloch}(x).\phi_{env} \quad \text{(A4)}$$

The envelope function (ϕ_{env}) is the product of spherical harmonics ($Y_l^m(\theta,\phi)$) and a radial Bessel function ($R(r)$). It is also a solution of the Schrödinger equation for the particle-in-a-sphere problem, the best representation for a quantum dot. Inserting ϕ_{env} into the Schrödinger equation gives the discrete energy-levels of a confined electron in a spherical box:

$$E_{n,l}^{conf}(r) = \frac{\hbar^2 \chi_{n,l}^2}{2m^* r^2} \quad \text{(A5)}$$

where m^* is the effective mass of electrons (or holes), and $\chi_{n,l}$ are the roots of the Bessel function. These roots are absolute values dependent on the principal ($n = 1,2,3$ ...) and azimuthal ($l = 0,1,2,$ ...) quantum numbers.

The band gap of a quantum dot is therefore the sum of the fundamental band gap (E_g^0) and the confinement energy, E^{conf}, of both electrons and holes (Equation A5):

$$E_g^{tot}(r) = E_g^0 + E_{n,l}^{conf}(r) = E_g^0 + \frac{\hbar^2 \chi_{n,l}^2}{2m_e^* r^2} + \frac{\hbar^2 \chi_{n,l}^2}{2m_h^* r^2} \quad \text{(A6)}$$

Addition of a term describing the Coulomb interaction between electrons and holes and appropriate substitution of the Bessel function[411] results in the Brus equation:

$$E_g(r) = E_g^0 + \frac{\hbar^2 \pi^2}{2r^2}\left(\frac{1}{m_e^*} + \frac{1}{m_h^*}\right) - \frac{1.786 e^2}{4\pi\varepsilon_0 \varepsilon_r r} \quad \text{(A7)}^6$$

B. Supplementary material for Chapter 4

B.1. Rietveld refinement for $CuInS_2$ prepared at 215°C

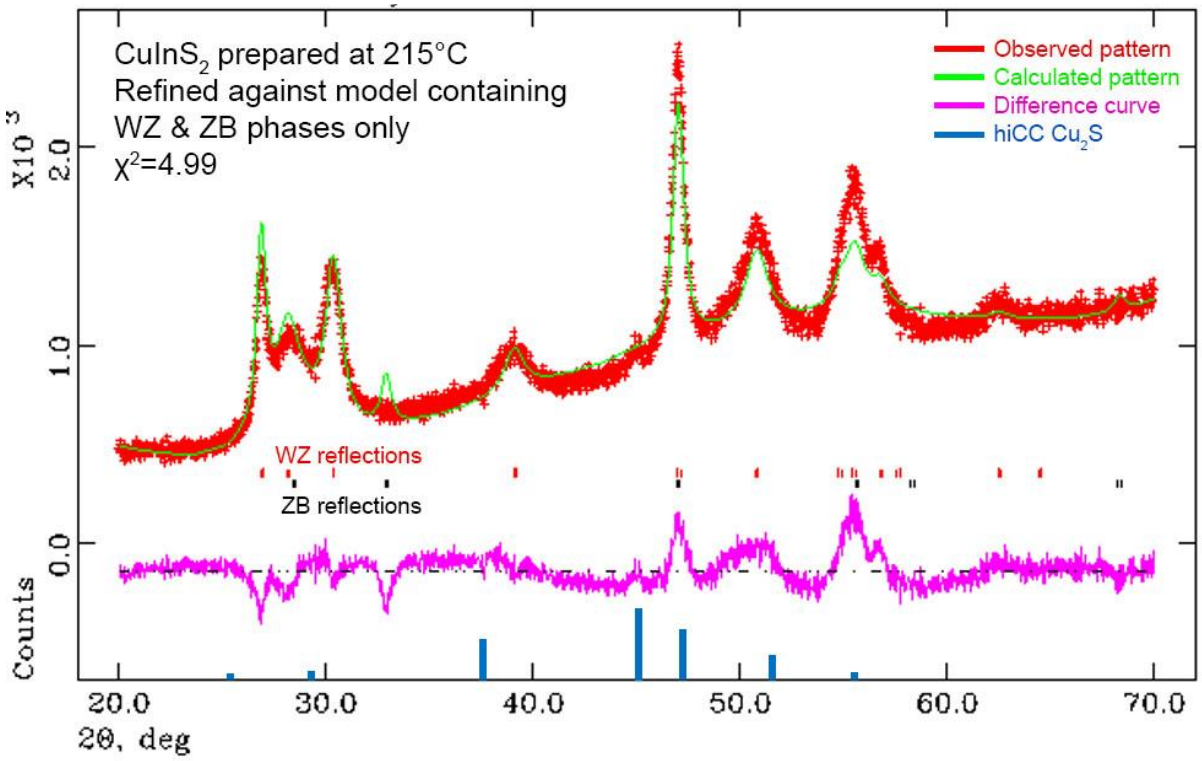

Figure B.1. Rietveld refinement for $CuInS_2$ sample prepared at 215°C using a model of the $CuInS_2$ ZB & WZ structures only. The reflections for hiCC Cu_2S (JCPDS card no. 46-1195) are shown below (blue) and are in good agreement with large peaks in the difference curve (pink).

B.2. Rietveld refinement for $CuInS_2$ samples

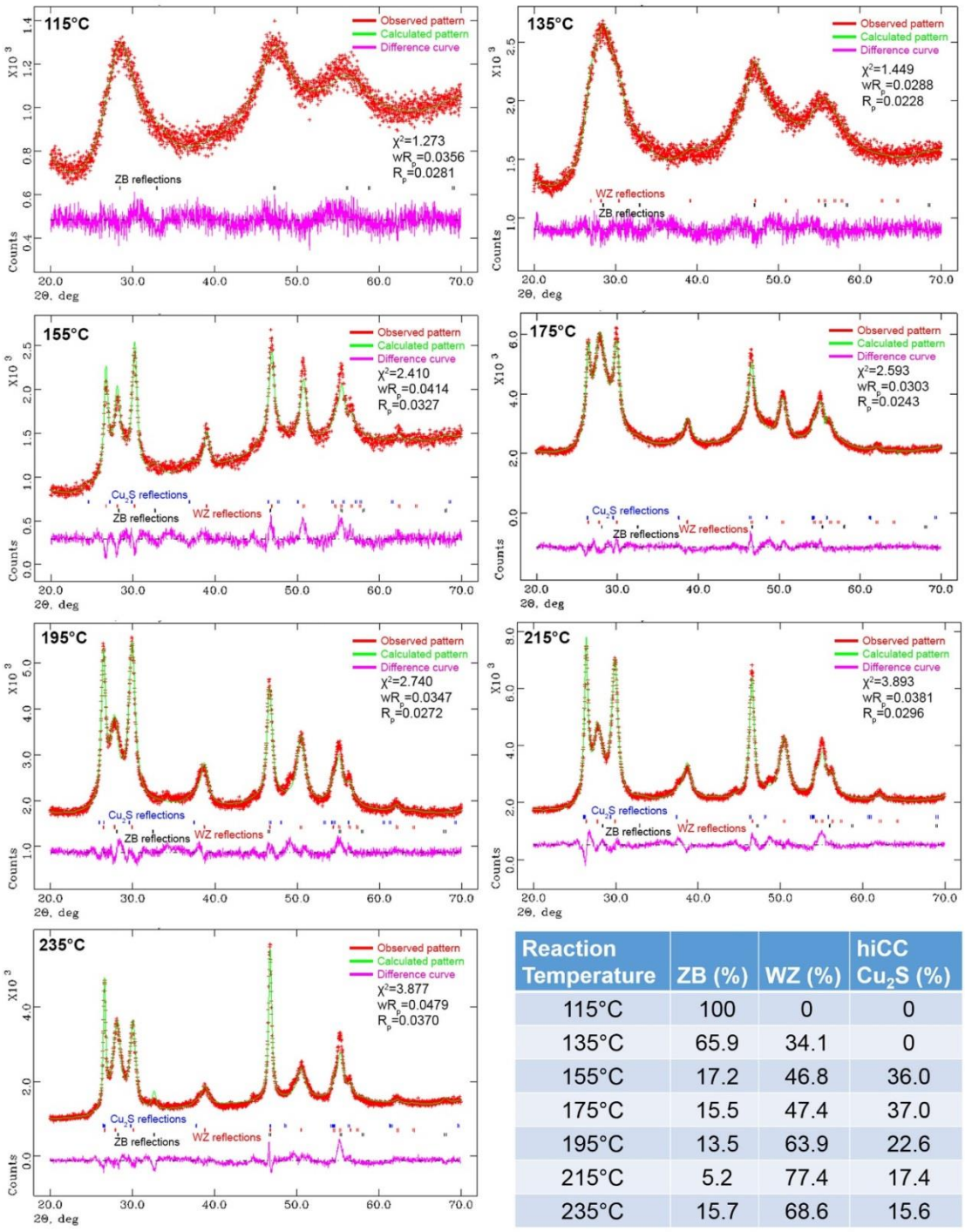

Reaction Temperature	ZB (%)	WZ (%)	hiCC Cu_2S (%)
115°C	100	0	0
135°C	65.9	34.1	0
155°C	17.2	46.8	36.0
175°C	15.5	47.4	37.0
195°C	13.5	63.9	22.6
215°C	5.2	77.4	17.4
235°C	15.7	68.6	15.6

Figure B.2. Rietveld refinements for samples prepared from 115 - 235°C. Reflections for each phase in the model are shown between the experimental and difference curves. *Note*: at 115°C the model only contains the ZB $CuInS_2$ phase; at 135°C the model contains only the ZB & WZ $CuInS_2$ phases. Phase content values (%) are shown at the bottom right.

B.3. Nanocrystal diameter

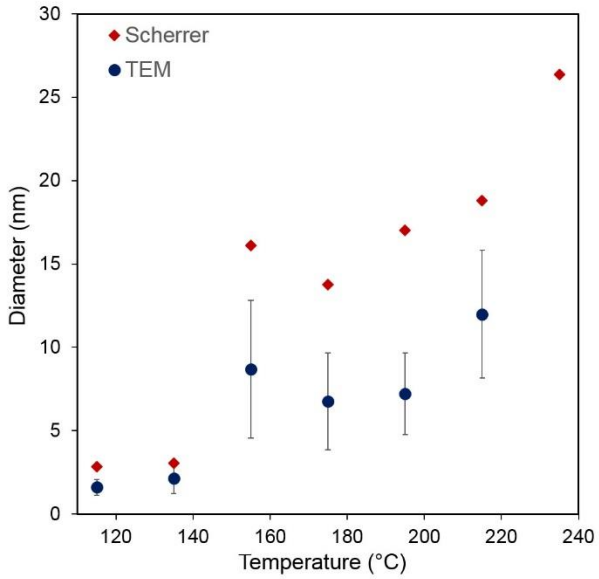

Figure B.3. Variation in spherical/plate-like NC diameter calculated from TEM images (blue) and the Scherrer line broadening equation *via* XRD (red) plotted as a function of temperature. Error bars show the standard deviation. The diameter of rod shaped NCs measured from TEM images is not plotted.

B.4. EDS data for $CuInS_2$ samples

Reaction Temperature	Cu : In : S Ratio
115°C	1.4 : 1 : 19.3
135°C	5.3 : 1 :15.0
155°C	1.0 : 1 : 3.1
175°C	1.4 : 1 : 3.7
195°C	1 : 1.0 : 3.8
215°C	2.7 : 1 : 2.0
235°C	1.1 : 1 : 1.93

Table B.1. EDS data collected from $CuInS_2$ samples prepared from 115 - 235°C.

This indicates the ensemble elemental composition of each sample. This data is of limited significance given the multitude of phases identified in the final product as well as the potential for unreacted reagents in the product at lower temperatures. However, in general, as the reaction temperature increases, samples become closer in stoichiometry to $CuInS_2$.

B.5. Quantum yield measurements

Reaction Temperature	QY (%)
115°C	0.05
135°C	0.06
155°C	0.11
175°C	0.45
195°C	0.76
215°C	0.42
235°C	0.04

Table B.2. The quantum yield (QY) as a percentage value for $CuInS_2$ samples.

QY was calculated using the photoluminescence spectra shown in Figure 4.4b. The QY was determined for each sample by comparison to a Rh-101 standard. All samples have QY less than 1%.

B.6. Photoluminescence peak fitting

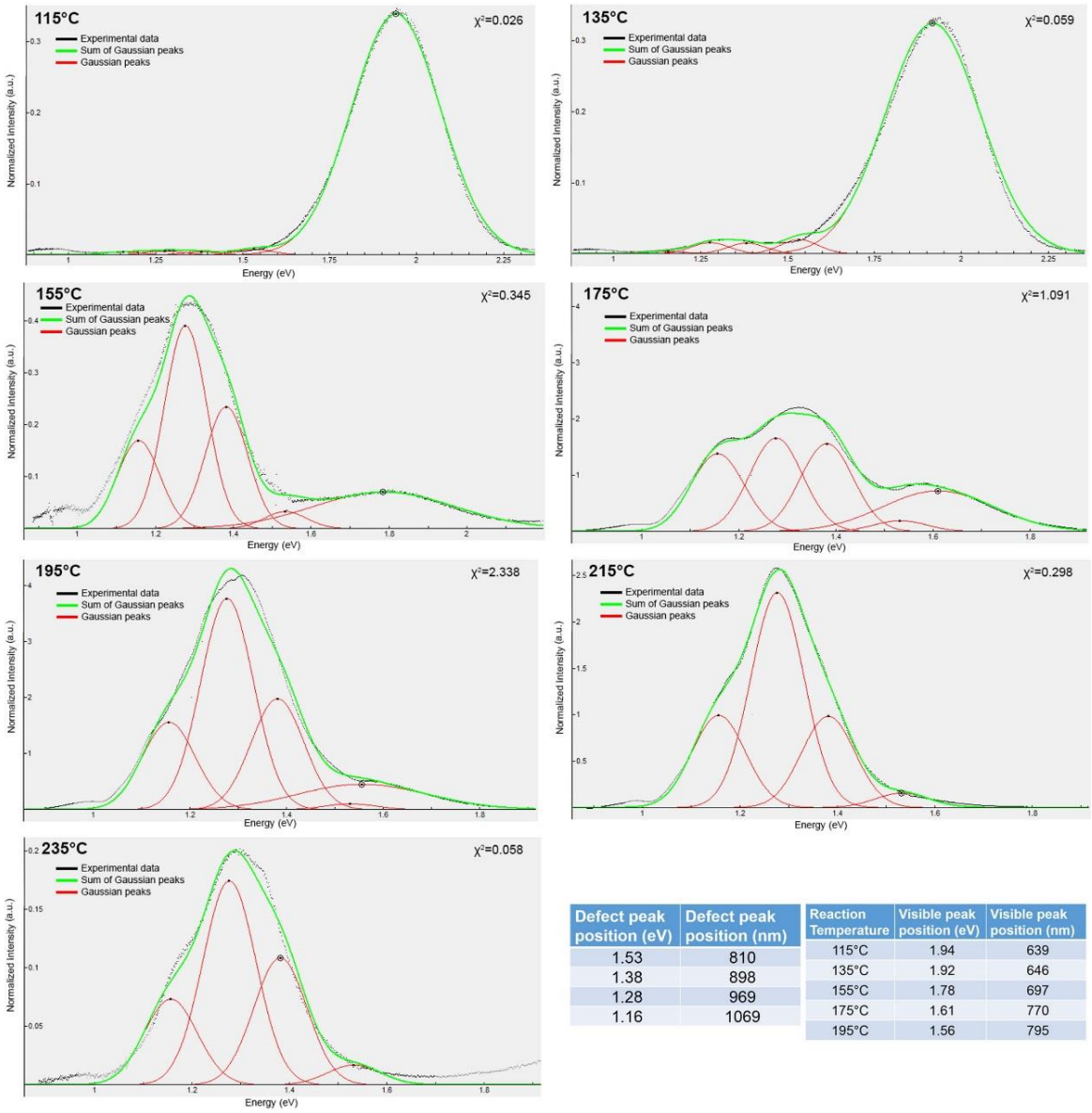

Defect peak position (eV)	Defect peak position (nm)
1.53	810
1.38	898
1.28	969
1.16	1069

Reaction Temperature	Visible peak position (eV)	Visible peak position (nm)
115°C	1.94	639
135°C	1.92	646
155°C	1.78	697
175°C	1.61	770
195°C	1.56	795

Figure B.4. Photoluminescence data fit with Gaussian peaks. Photoluminescence data (black) for samples prepared at reaction temperature (115-235°C) were fit with Gaussian peaks (red) using Fityk, a curve fitting and data analysis application. Data were fit to within a statistically acceptable tolerance ($\chi 2 \leq 2.4$) with four peaks in the NIR region and one peak in the visible region. The sum of the fitted peaks is shown (green). Fit was initially performed on data obtained for reaction at 215°C, as no peak in the visible was observed here allowing only WZ emission to be considered. The spectral position of the NIR peaks (in eV and nm) is shown at the bottom right (left hand side). FWHM (0.12 eV) and peak positions of the Gaussians were then fixed and these curves were fit to PL data at each reaction temperature. At reaction temperatures ≤ 195°C a further Gaussian peak in the visible region was added to account for the emission of the ZB phase. The position of this peak increased in wavelength with temperature and is shown in the table at the bottom right (right hand side).

B.7. Absorbance spectra of hexanes

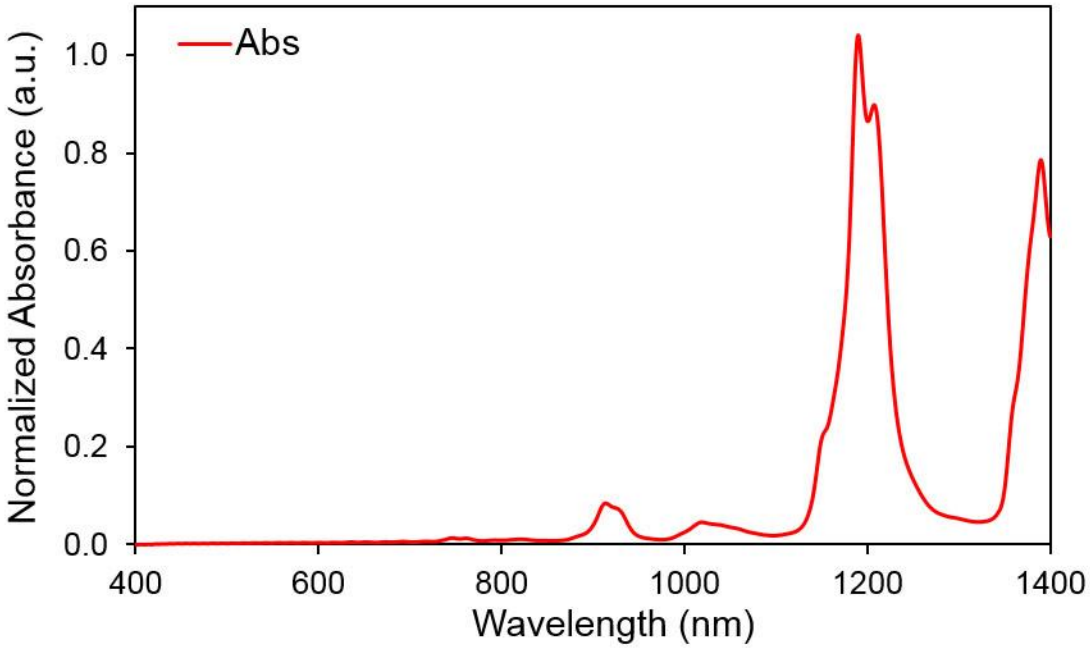

Figure B.5. Absorbance spectra of hexanes. The intense peak at 1200 nm causes the re-absorbance of emitted light from $CuInS_2$ samples that fluoresce in this region. It should be therefore be noted that the decrease in PL intensity observed at approximately 1200 nm in all samples is due to the re-absorbance of emitted light by the solvent hexanes.[412] Given the nature of this absorbance, PL data is fit excluding the region from 1130 – 1290 nm.

B.8. TEM images of $CuInS_2$ aliquots

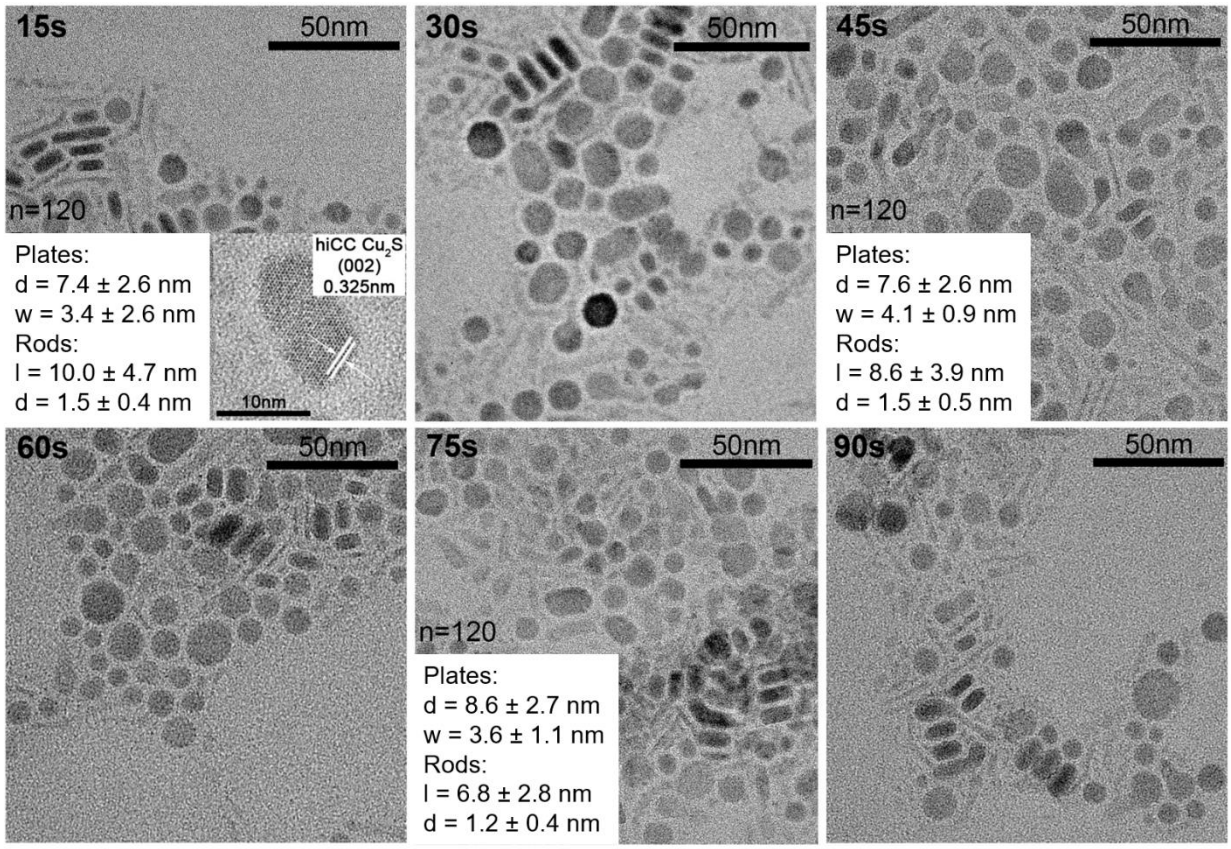

Figure B.6. TEM images of $CuInS_2$ aliquots taken 15s, 30s, 45s, 60s, 75s and 90s after injection of the Cu—thiolate complex at reaction temperature 215°C. Inset in the 15s image is an HRTEM image showing lattice fringes characteristic of hiCC Cu_2S.[312] Images were sized every 30s.

B.9. EDS mapping of $CuInS_2$ aliquots

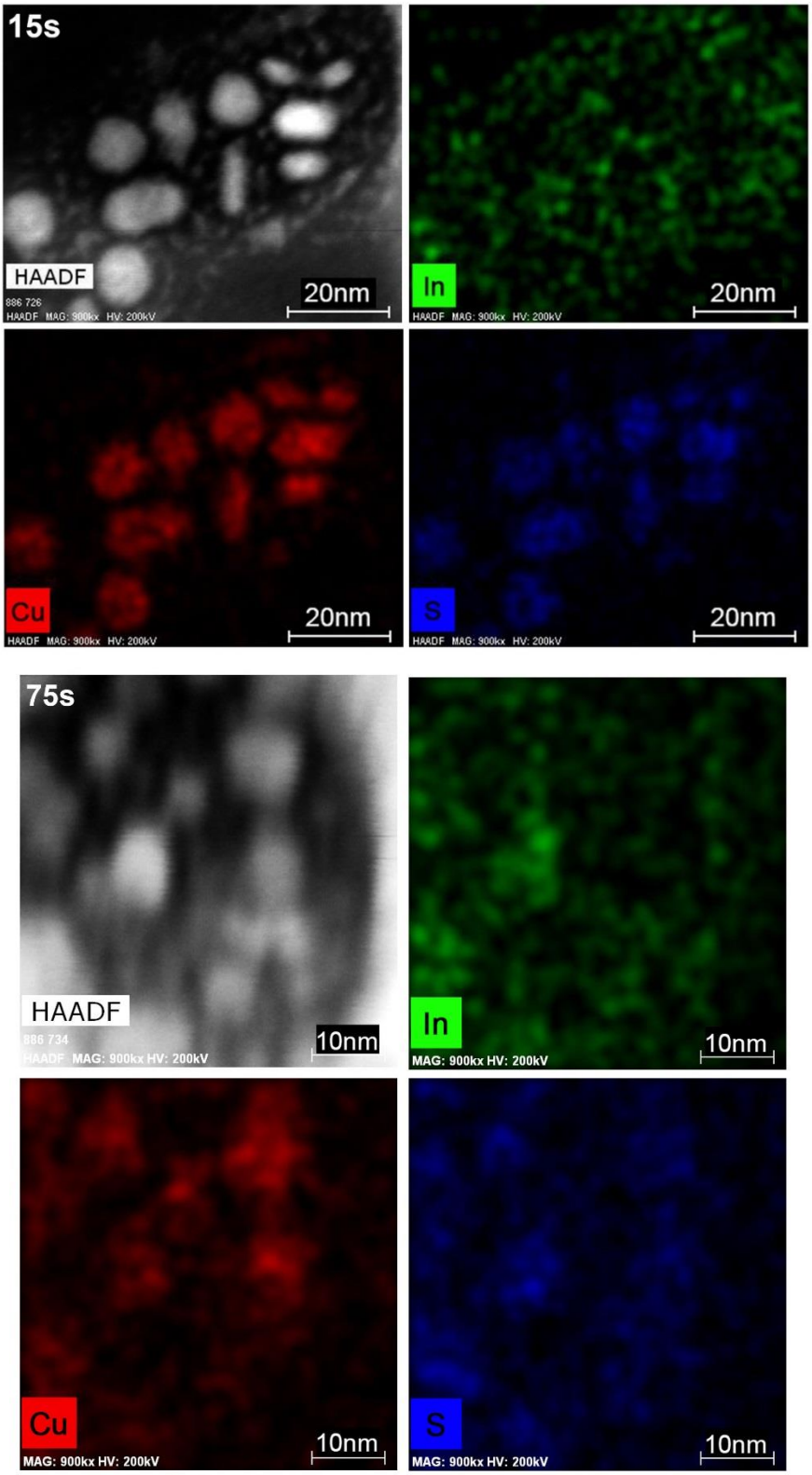

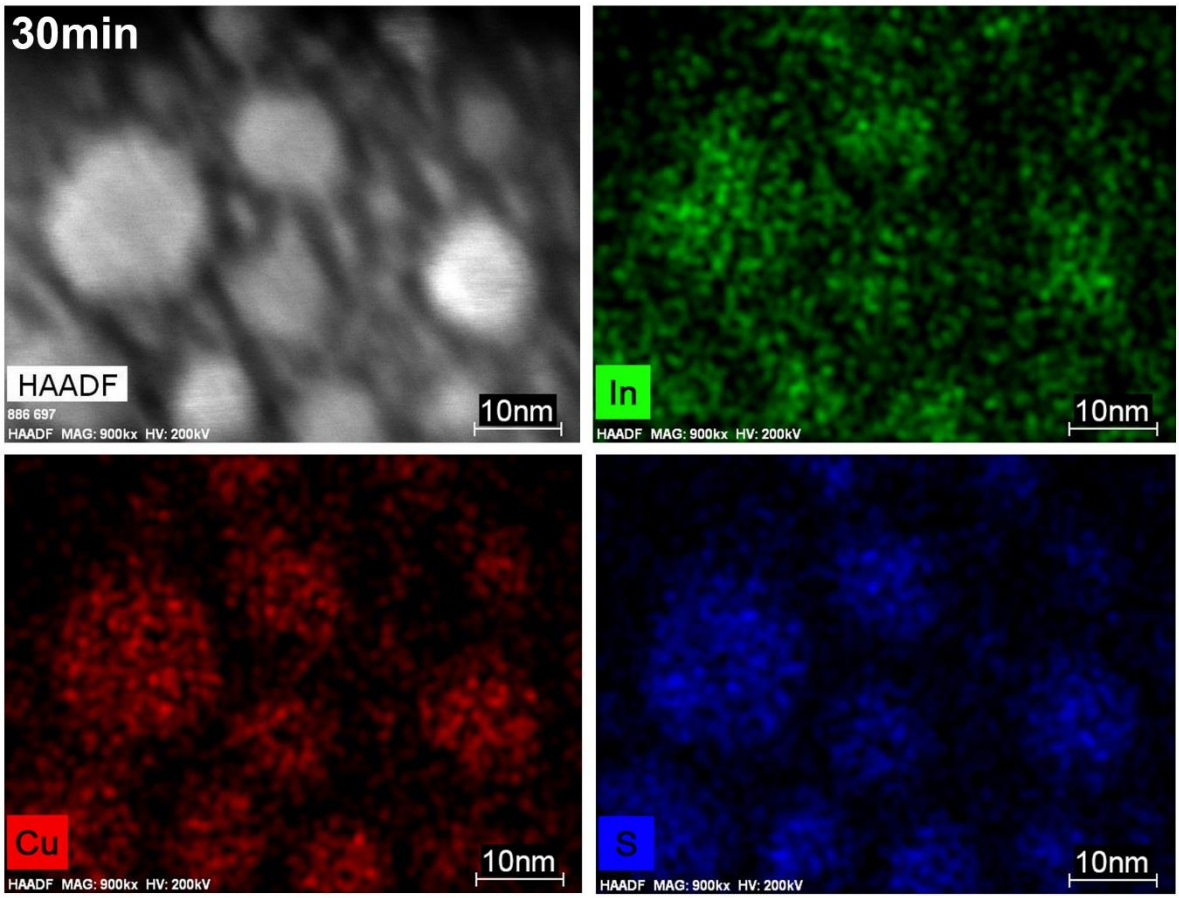

Figure B.7. Complete EDS mapping data for $CuInS_2$ NCs. HAADF (high-angle annular dark field) images and single elemental analyses of the EDS maps shown in Figure 4.7**.**

C. Supplementary material for Chapter 5

C.1. Experimental techniques

Materials. Indium chloride ($InCl_3$, Alfa Aesar, 99.99%), thiourea (Sigma-Aldrich, ≥ 99.0%), oleylamine (OlAm, Aldrich, 70%), copper (I) acetate (CuOAc, Strem Chemicals, 99%), 1-dodecanethiol (DDT, Aldrich, ≥ 98.0%), octadecene (ODE, Aldrich, 90%), diphenyl ether (Sigma-Aldrich, 99%), cadmium oxide (CdO, Strem Chemicals, 99.999%), oleic acid (Aldrich, 90%), zinc stearate (ACROS Organics), sulfur (Sigma-Aldrich), n-hexylphosphonic acid (HPA, PCI synthesis, > 99%), trioctylphosphine (TOP, Aldrich, 90%), and trioctylphosphine oxide (TOPO, Aldrich, 99%) were purchased and used as received. Standard air-free Schlenk techniques were used throughout with N_2 as the inert gas.

Synthesis of WZ $CuInS_2$. $InCl_3$ (111.5 mg, 0.5 mmol) and thiourea (77.5 mg, 1.0 mmol) were added to OlAm (10 mL) in the reaction vessel, degassed for 1 h, and heated to 215°C under an N_2 atmosphere. Separately CuOAc (65.0 mg, 0.5 mmol) was suspended in ODE (500 μL), diphenyl ether (500 μL) and DDT (240 μL, 1.0 mmol). At 215°C, 1 mL of the Cu solution was injected quickly (less than 1 s) into the reaction vessel. After 15 min, the heat was removed and the reaction mixture was cooled to room temperature. The obtained $CuInS_2$ NCs were precipitated by addition of ethanol and then purified by repeated centrifugation and decantation with addition of ethanol and hexanes.

Alloying procedure. Inorganic surface passivation was carried out using syntheses based on literature procedures.[133, 183] For growth of a CdS (ZnS) outer layer, 0.4 mmol of cadmium oleate (zinc stearate) and 0.4 mmol of sulfur dissolved in 0.5 mL TOP was added to 8.5 mL of ODE. $CuInS_2$ NCs were prepared as described above, however, after 15 min the temperature was lowered to 210°C and the Cd (Zn) solution was added dropwise to the reaction mixture over 12 min. The reaction vessel was then heated for a further 75 min. The obtained Cd (Zn)-Cu-In-S NCs were again precipitated by addition of ethanol and then purified by repeated centrifugation and decantation with addition of ethanol and hexanes. Cadmium oleate was prepared by adding CdO (65 mg, 0.5 mmol) and oleic acid (0.4 mL, 1.26 mmol) to ODE (10 mL). This mixture was degassed for 45 min, then heated for 30 min at 250°C under N_2.

Ligand exchange. $CuInS_2$ NCs were cleaned and suspended in 10 mL hexanes. 1 mL of the resulting solution was added to a 2 dram vial containing a further 1 mL of hexanes and 0.25 mmol of OlAm (as a control), DDT, HPA, TOP or TOPO. The vials were then shaken for 30 min. The resultant particles were precipitated with the addition of methanol/ ethanol (v/v, 1:1) and then purified by repeated centrifugation and decantation with addition of methanol/ ethanol and hexanes.

Optical characterization. The absorption spectra of NC samples were collected from 300 – 1400 nm on a UV-visible spectrophotometer (Jasco V-670). Visible PL spectra were measured from 600 – 900 nm on a spectrofluorometer (Jasco FP-8300). NIR PL spectra were measured from 800 - 1400 nm on a different spectrofluorometer (Jobin Yvon/Horiba Fluorolog-3 FL3-111). A 610 nm longpass filter was used for PL measurements. Samples were measured in solution with hexanes as the solvent. Both visible and NIR PL were measured with excitation wavelength

348 nm. Data were then matched at 800 nm and normalized to the QY. The QY was determined for each sample by comparison to a Rh-101 standard.[323] The time resolved fluorescence measurements were carried out in a time-correlated single-photon counting (TCSPC) approach using an Edinburgh Instruments FLS920 fluorescence spectrometer with a TCC900 TCSPC card. Samples were excited using a Fianium WL-SC400-4-PP super continuum pulsed laser monochromatized at 532 nm. The emission from the samples was collected at a right angle, through a double-monochromator to suppress the scattering from excitation source, and collected using a Hamamatsu H10330A-75 NIR-PMT or a Hamamatsu R2658P Extended-red-PMT detector.

Further characterization. Transmission electron microscopy (TEM) and energy dispersive X-ray spectroscopy (EDS) were carried out using a FEI Tecnai Osiris™ digital 200 kV S/TEM system equipped with ChemiSTEM EDS. TEM samples were prepared by drop casting a dilute NC solution in hexanes onto a nickel grid with a carbon support and drying in air at room temperature. NCs were sized manually using ImageJ with number of particles measured, n = 300. Lattice fringes were measured by generating a profile plot of an area of the image using ImageJ, manually counting the cycles, and dividing the length of the profile plot by the number of cycles. The minimum number of cycles used was ten. EDS spectra were collected for 2 min and quantified using the Espirit software. Cu and S were quantified using the K series of peaks, while In was quantified using the L series. All spectra were background subtracted and overlapping Cu sample and Ni grid peaks were deconvoluted before quantification. Drift-corrected EDS maps were collected for 90 s with beam current 1.5 nA. XRD measurements were performed using a Scintag XGEN-4000 X-ray diffractometer with a CuK_{α} (λ = 0.154 nm) radiation source. The resulting diffraction patterns were then visually compared to literature data to determine the structure.[167] ^{1}H NMR spectra of the NC solutions were acquired using a 11.7 T magnet equipped with a Bruker DRX console operating at 400 MHz. Chemical shifts were referenced internally to $CDCl_3$ (7.26 ppm), which also served as the ^{2}H lock solvent. The extent of ligand exchange was determined by comparing the integrations of the methylene hydrogen peak of OlAm at 5.5 ppm to those of the terminal —CH_3 group of the ligands at 0.88 ppm.

C.2. Photoluminescence excitation spectra

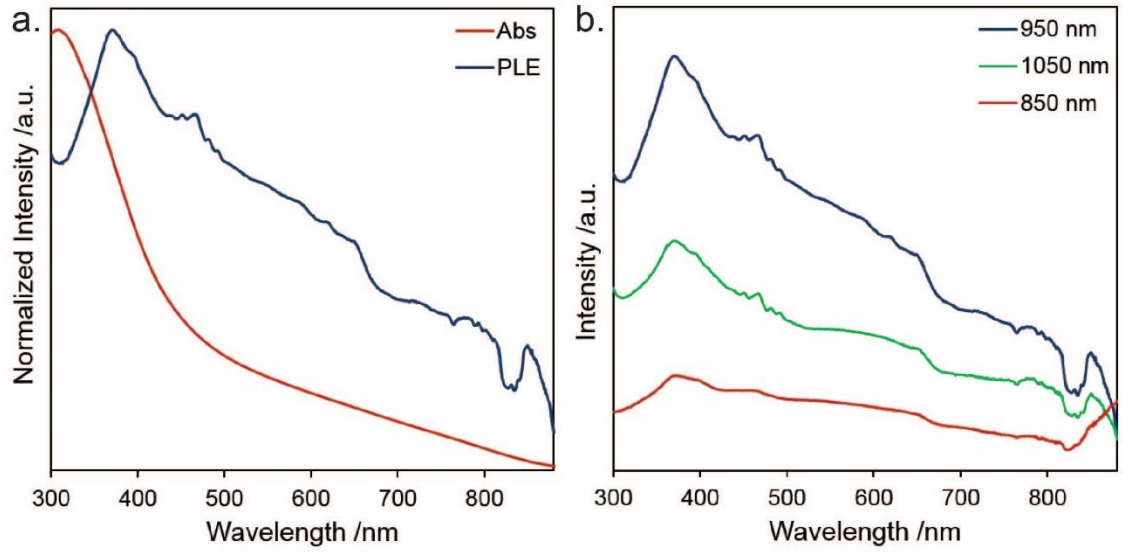

Figure C.1. Photoluminescence excitation spectra for $CuInS_2$ NCs. Normalized absorbance (red) and photoluminescence excitation (PLE) spectra for as prepared WZ $CuInS_2$ NCs; b) PLE spectra for WZ $CuInS_2$ NCs collected at 850, 950 and 1050 nm.

C.3. Tri-exponential fit parameters

Sample	Detection wavelength (nm)	χ^2	τ_1 (s)	A_1 (%)	τ_2 (s)	A_2 (%)	τ_3 (s)	A_3 (%)
$CuInS_2$ - 1	840	1.47	4.40	2.57	37.7	11.4	268	86.0
$CuInS_2$ - 1	950	5.40	3.70	4.23	29.5	12.6	272	83.2
$CuInS_2$ - 2	840	1.86	4.12	7.45	24.7	15.4	279	77.1
$CuInS_2$ - 2	950	1.17	3.73	14.6	22.4	26.3	232	59.1
$CuInS_2$ - 3	845	4.10	2.87	4.49	20.1	7.88	241	87.6
$CuInS_2$ - 3	990	5.55	4.43	5.69	23.9	18.3	229	76.1

Table C.1. Tri-exponential fit parameters for luminescent decay curves of $CuInS_2$ NCs.

τ_x represents the decay time of the PL emission and A_x represents the relative weights of the decay components.

C.4. Absorbance spectra of $CuInS_2$ aliquots

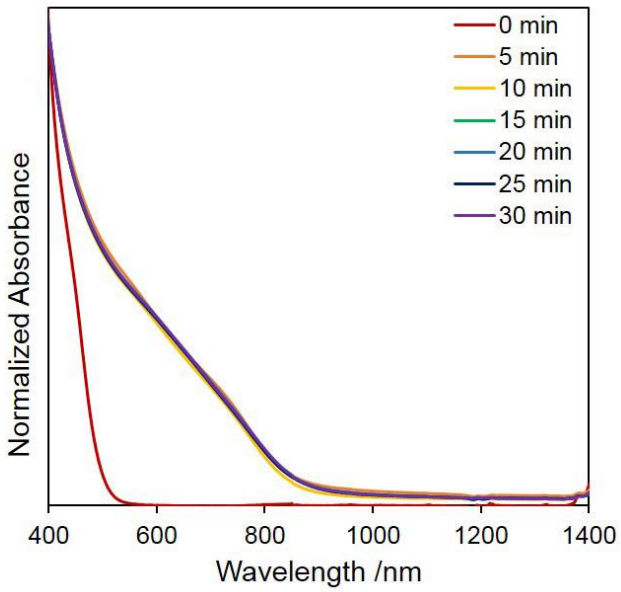

Figure C.2. Absorbance spectra of $CuInS_2$ aliquots in hexanes at different time points during the reaction.

C.5. Absorbance spectra of $CuInS_2$ with different inorganic passivation

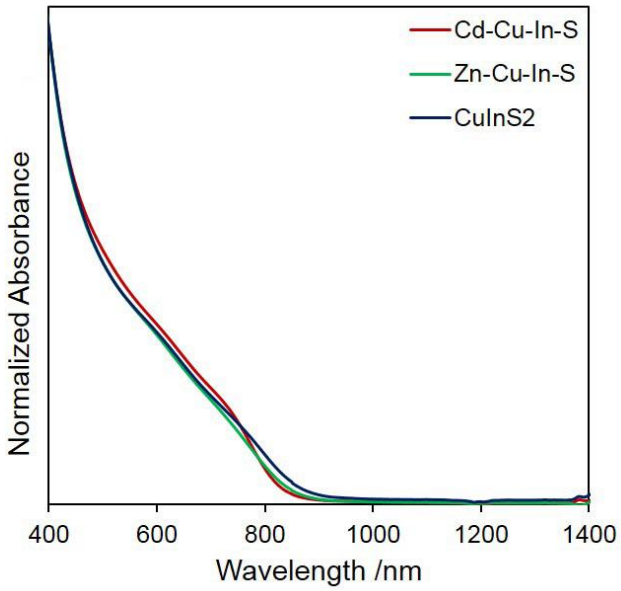

Figure C.3. Absorbance spectra of alloyed $CuInS_2$ NCs prepared with different inorganic passivation layers.

C.6. Absorbance spectra of $CuInS_2$ with different organic passivation

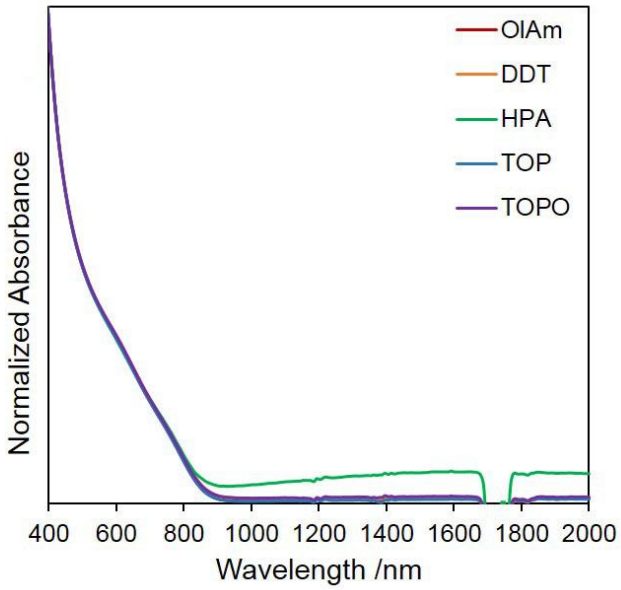

Figure C.4. Absorbance spectra of $CuInS_2$ NCs with different organic passivation layers. A small plasmon can be observed in the HPA spectra with a peak at approximately 1700 nm. The feature in the spectra between 1650 – 1750 nm is due to the absorption of the solvent.

C.7. TEM images & EDS compositional analyses for $CuInS_2$ aliquots

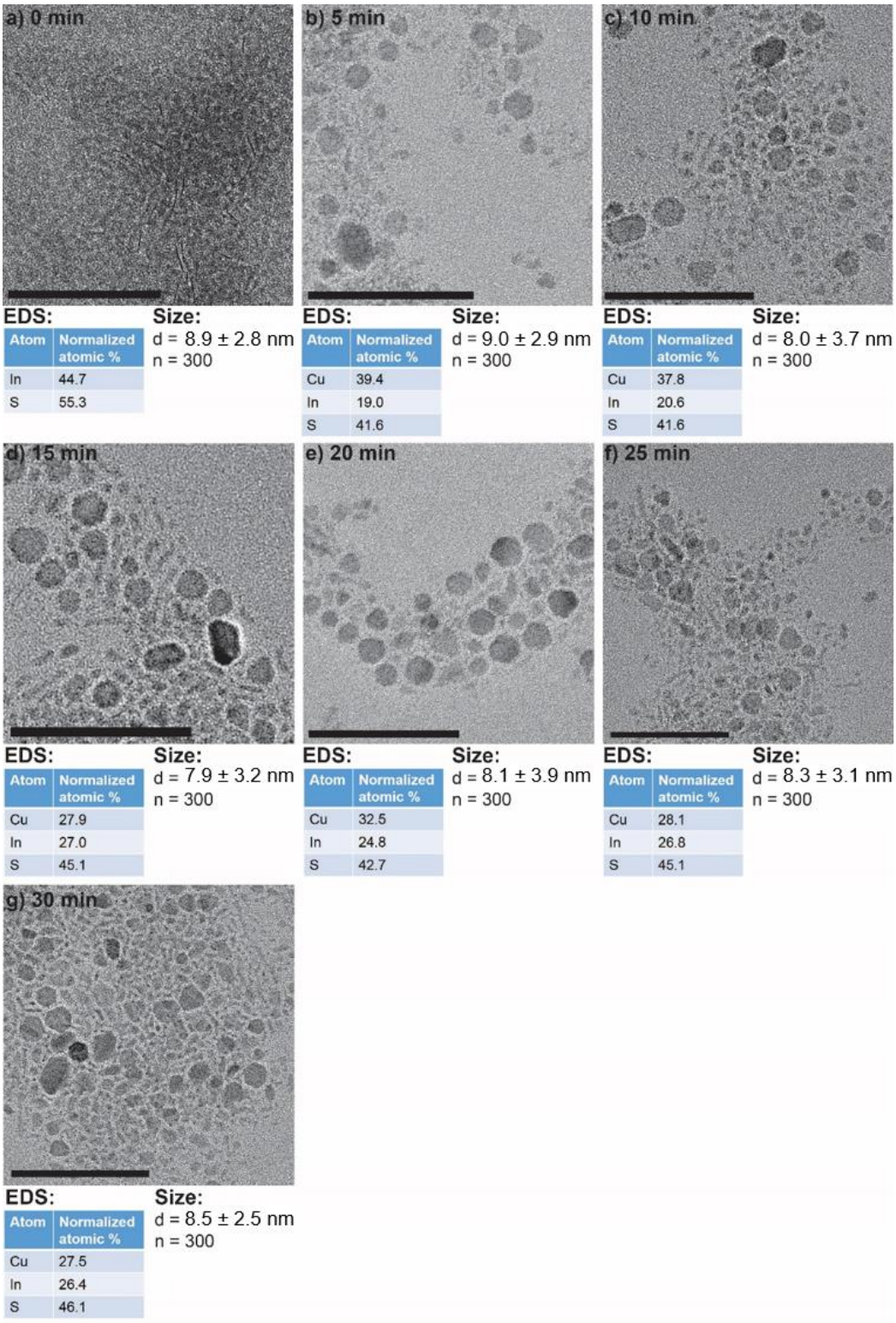

Figure C.5. TEM images, EDS compositional analyses and sizes for $CuInS_2$ aliquots prepared at 215°C removed from the reaction at a) 0 min, b) 5 min, c) 10 min, d) 15 min, e) 20 min, f) 25 min, and g) 30 min. Scale bars: 100 nm.

C.8. Luminescence decay curves of alloyed WZ $CuInS_2$ NCs

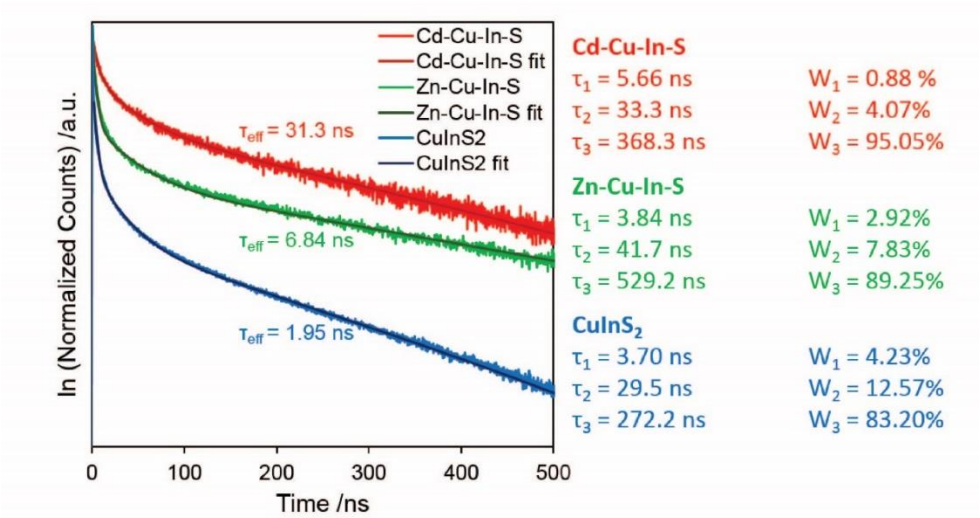

Figure C.6. Luminescence decay curves of alloyed WZ $CuInS_2$ NCs, shown with calculated effective lifetimes, τ_{eff}, prepared with different inorganic passivation layers (λ_{ex} = 532 nm). Natural log of counts is plotted against time. Curves are best fit with three exponentials (black line) where τ_x represents the decay time of the PL emission and W_x represents the relative weights of the decay components.

C.9. Powder XRD patterns for alloyed WZ $CuInS_2$ NCs

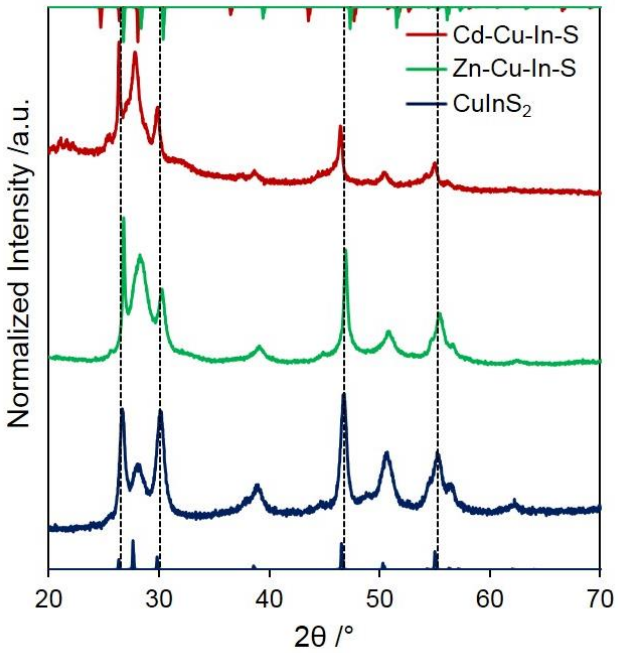

Figure C.7. Powder XRD patterns of alloyed WZ $CuInS_2$ NCs, Cd-Cu-In-S (red), Zn-Cu-In-S (green), and WZ $CuInS_2$ (blue). The calculated reflections for WZ CdS (red), WZ ZnS (green), and WZ $CuInS_2$ (blue) are shown along the top (CdS and ZnS) and bottom ($CuInS_2$) horizontal axes.

C.10. TEM images & EDS compositional analyses for alloyed $CuInS_2$ NCs

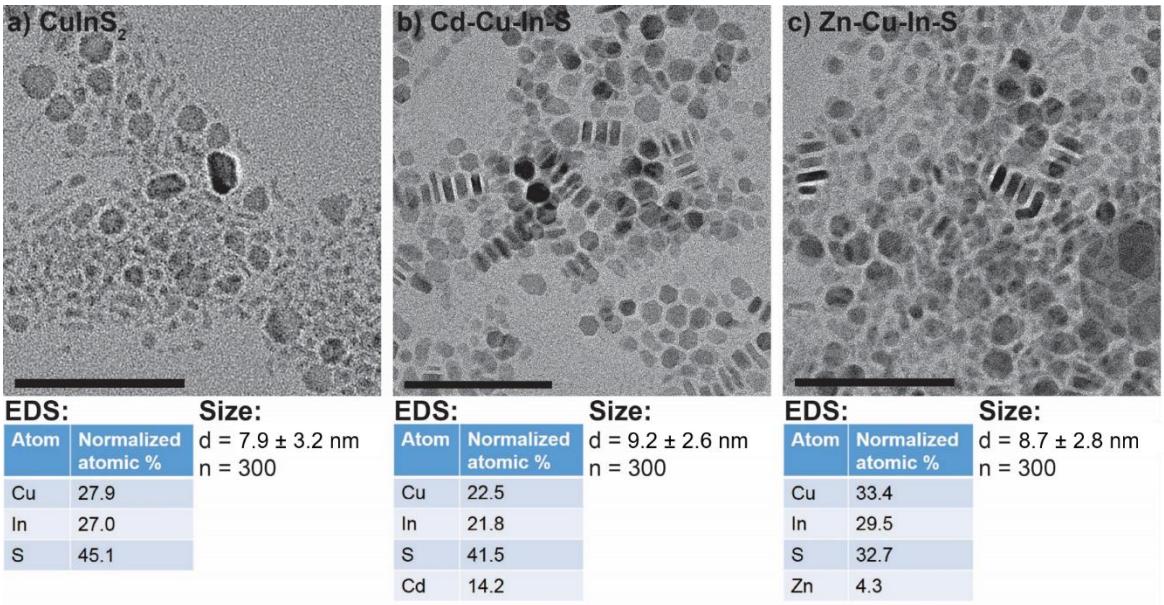

EDS:

Atom	Normalized atomic %
Cu	27.9
In	27.0
S	45.1

Size: d = 7.9 ± 3.2 nm, n = 300

EDS:

Atom	Normalized atomic %
Cu	22.5
In	21.8
S	41.5
Cd	14.2

Size: d = 9.2 ± 2.6 nm, n = 300

EDS:

Atom	Normalized atomic %
Cu	33.4
In	29.5
S	32.7
Zn	4.3

Size: d = 8.7 ± 2.8 nm, n = 300

Figure C.8. TEM images, EDS compositional analyses and sizes for alloyed $CuInS_2$ NCs, a) $CuInS_2$, b) Cd-Cu-In-S, and c) Zn-Cu-In-S NCs. Scale bars: 100 nm.

C.11. EDS mapping for alloyed Zn-Cu-In-S NCs

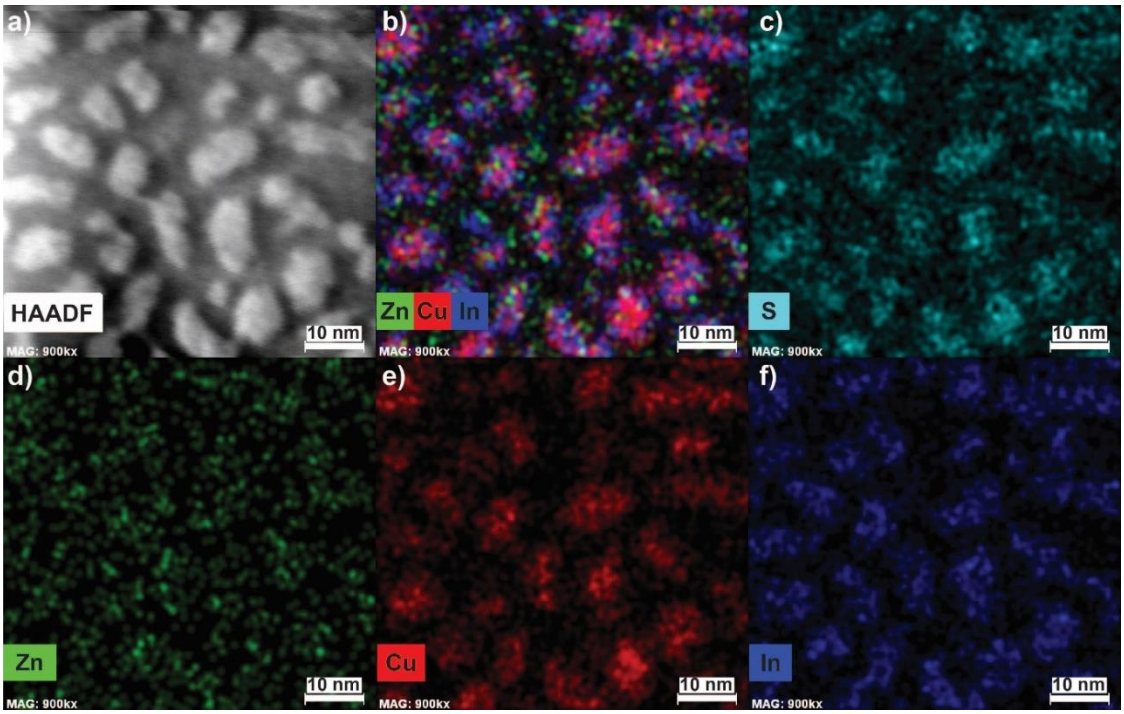

Figure C.9. EDS mapping for alloyed Zn-Cu-In-S NCs; a) High angle annular dark field STEM image; EDS mapping showing b) Zn, Cu, In; c) S; d) Zn; e) Cu; and f) In. Scale bars: 10 nm. The integrated pixel spectrum from this image indicates composition: Zn = 4.4%; Cu = 32.4%; In = 28.5%; S = 34.7%.

C.12. EDS mapping for alloyed Cd-Cu-In-S NCs

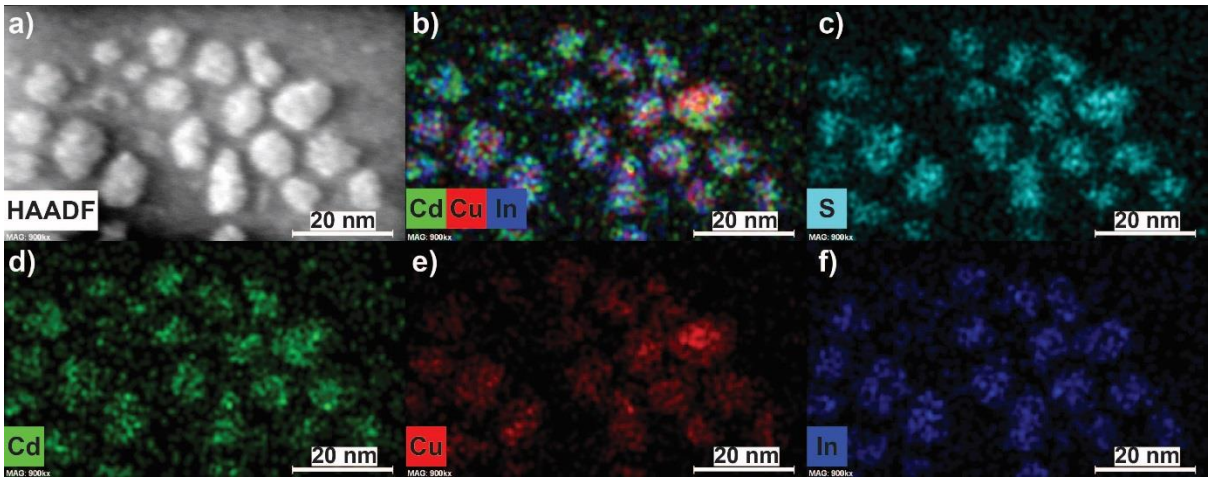

Figure C.10. EDS mapping for alloyed Cd-Cu-In-S NCs; a) High angle annular dark field STEM image; EDS mapping showing b) Cd, Cu, In; c) S; d) Cd; e) Cu; and f) In. Scale bars: 20 nm. The integrated pixel spectrum from this image indicates composition: Cd = 15.1%; Cu = 22.3%; In = 19.7%; S = 42.9%.

C.13. NMR spectra for WZ $CuInS_2$ NCs with different organic passivation layers

a)

Ligand	Ratio	Proportion of OlAm remaining (%)
OlAm	0.86 : 3	—
HPA	0.14 : 3	16.2
DDT	0.26 : 3	30.2
TOP	0.04 : 3	4.7
TOPO	0.26 : 3	30.2

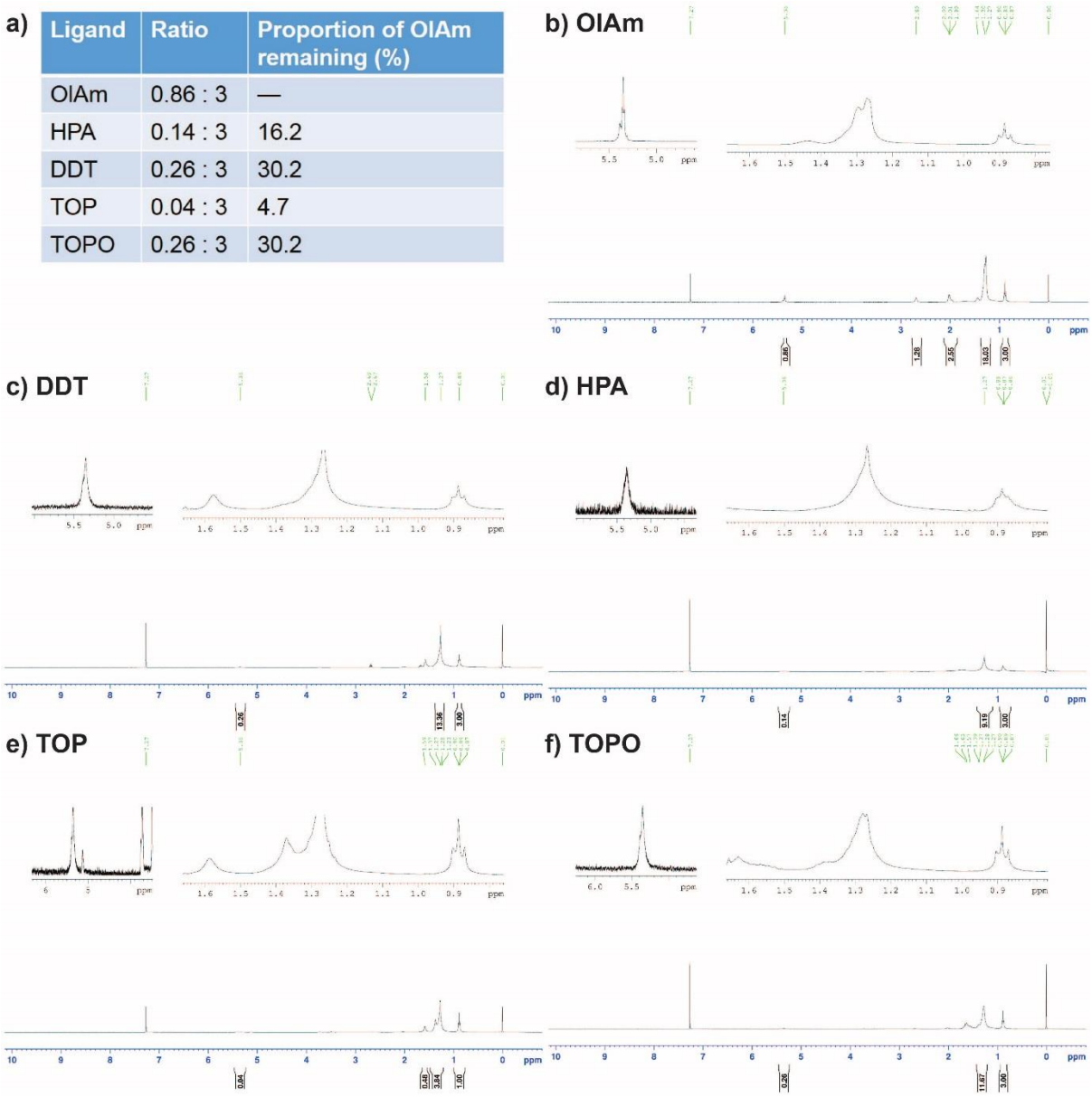

Figure C.11. NMR spectra for WZ $CuInS_2$ NCs; a) Table showing the ratio of integrations between the methylene hydrogen peak of oleylamine (OlAm) at 5.5 ppm and the terminal —CH_3 group of the ligands at 0.88 ppm, and the calculated proportion of OlAm remaining after ligand exchange. The low ratio (0.86:3) for the methylene peak of OlAm in the control is due to an ODE impurity that remains from the reaction; Raw NMR data for NCs that have undergone the ligand exchange procedure with b) OlAm, c) DDT, d) HPA, e) TOP, and f) TOPO.

C.14. TEM images and EDS compositional analyses for ligand exchanged NCs

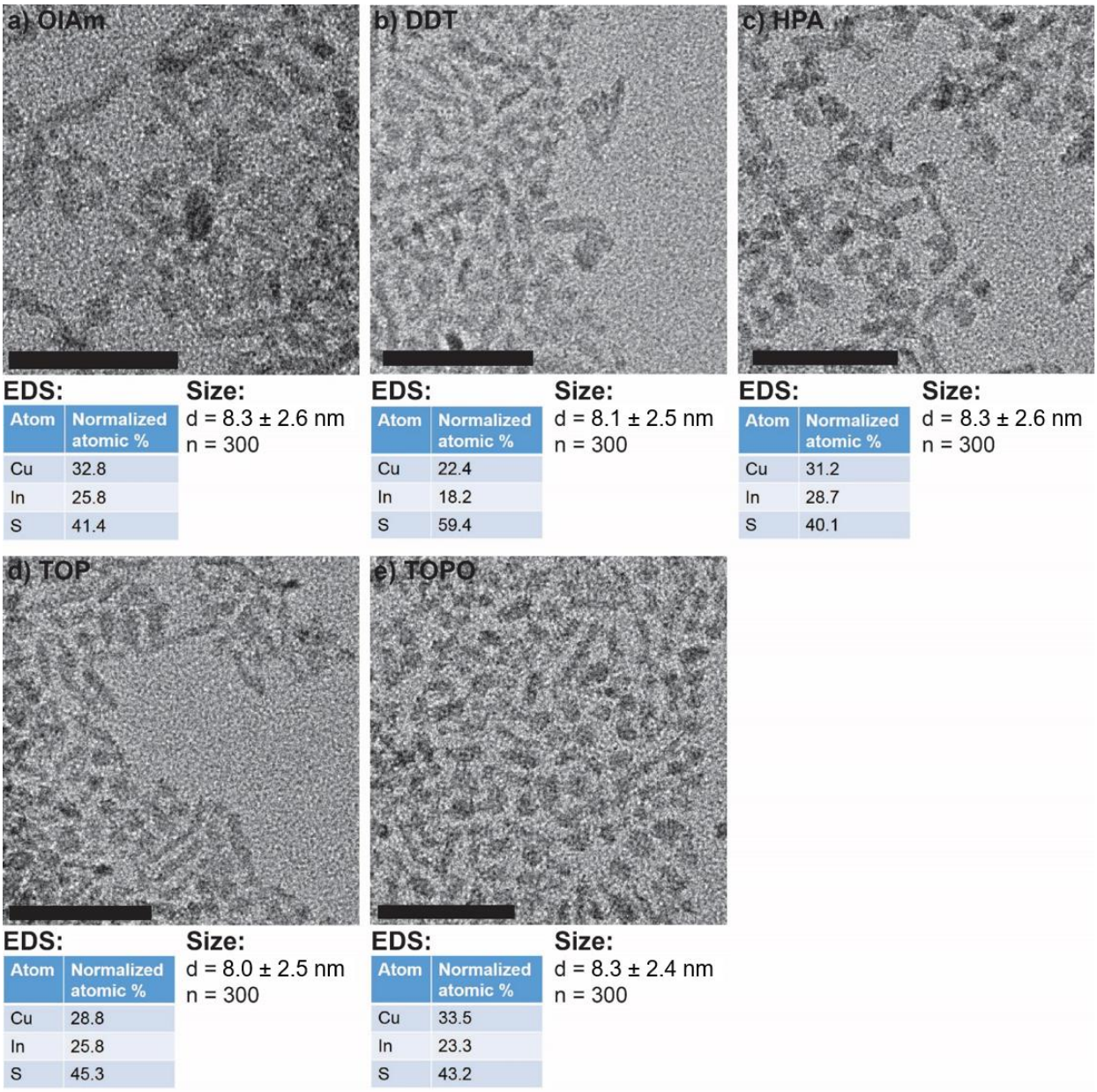

Figure C.12. TEM images, EDS compositional analyses and sizes for ligand exchanged NCs with a) OlAm, b) DDT, c) HPA, d) TOP, and e) TOPO. Scale bars: 50 nm.

C.15. Calculated optical transition energies

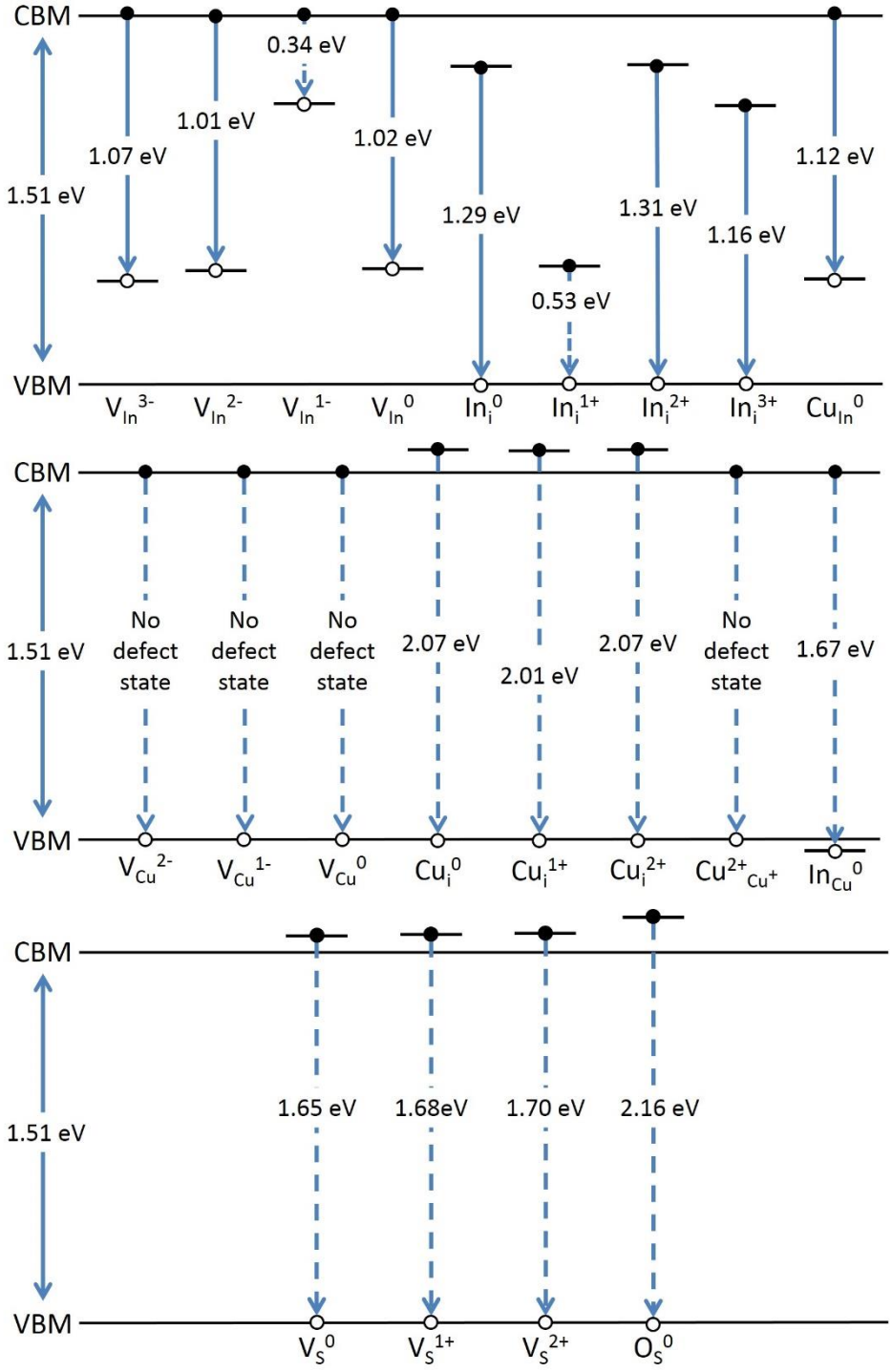

Figure C.13. Calculated optical transition energies for $V_{In,}$ In_i, Cu_{In}, V_{Cu}, Cu_i, $Cu^{2+}{}_{Cu}+$, In_{Cu}, V_S, and O_S. Dashed lines indicate transitions that are not in agreement with experimental evidence. For Cu_i, In_{Cu} and V_S the calculated defect levels exist above/ below the conduction band maximum/ valence band minimum. For V_{Cu} and $Cu^{2+}{}_{Cu}+$ no defect levels were found within 10 eigenstates of the band gap. For V_{In}^{1-} and In_i^{1+} the transition energies are greater than 0.5 eV smaller than the transition energy observed experimentally.

C.16. 2D cross section plots of the defect state squared wavefunction

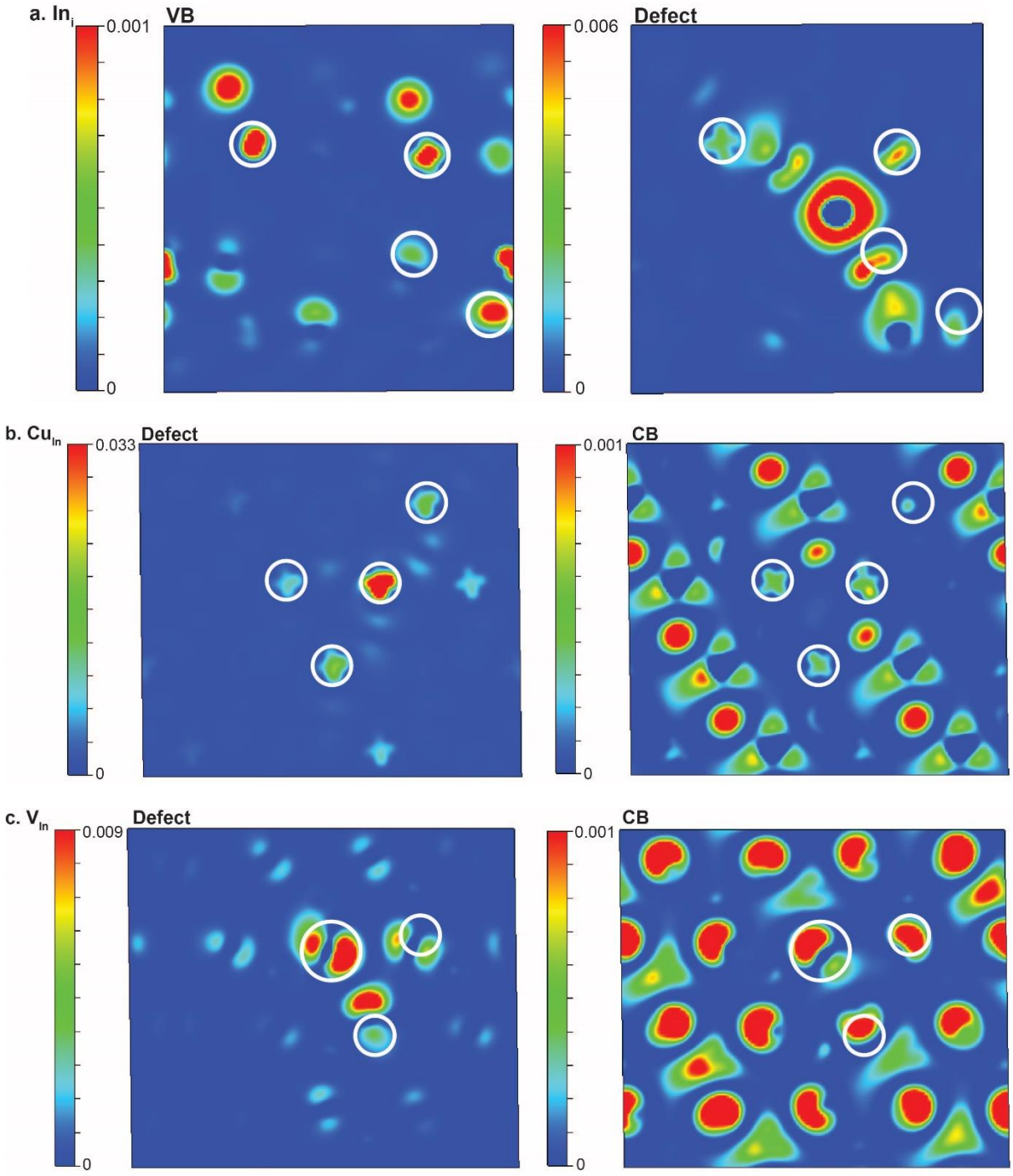

Figure C.14. 2D cross-section plots showing the squared wave functions of the defect state and corresponding energy band maximum/minimum for **a.** In_i^{2+} – valence band (left) and defect state (right); **b.** Cu_{In} – defect state (left) and conduction band (right); **c.** V_{In}^{2-} – defect state (left) and conduction band (right). All plots show the (001) plane with slices taken through the center of the defect. White circles show areas of overlap.

C.17. Tauc plot for WZ $CuInS_2$ NCs

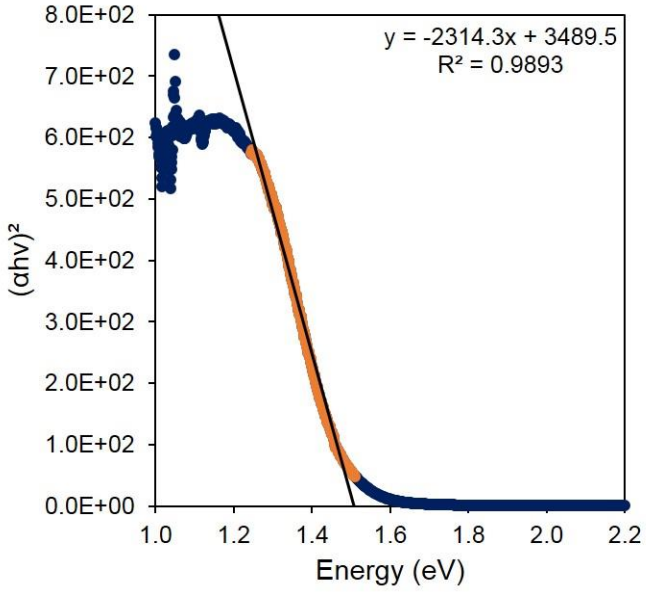

Figure C.15. Tauc plot used to calculate the experimental band gap of the NCs. The equation of the best fit line (black) for the fitted data (orange) is shown and used to calculate the band gap, E_g = 1.51 eV. The absorption coefficient of wurtzite $CuInS_2$ is not known definitively, so an approximation of the Tauc relationship[326] was used:

$$[\alpha \times hv]^2 = \left[\frac{(1 - Abs)^2}{2(Abs)} \times hv\right]^2$$

D. Supplementary material for Chapter 6

D.1. Additional experimental techniques

Synthesis of Pt-$CuInS_2$ with "bullet" morphology. The synthesis of $CuInS_2$ with bullet morphology was adapted from a literature procedure.[140] Pt nanoparticles in hexanes were transferred to a 25 mL 3-neck flask containing CuOAc (1.0 mmol), $InOAc_3$ (1.0 mmol), TOPO (3.5 mmol), oleylamine (9.0 mL), and a stir bar. The mixture was placed under vacuum at room temperature to remove the hexanes. The flask containing the metal precursors was heated to 150°C under nitrogen. At this temperature, a 0.313 mL/2.20 mL mixture of dodecanethiol/tert-dodecanethiol, respectively, was injected and the temperature was further increased to 280°C. The growth of hybrid nanoparticles proceeded for 1 hr. The flask was cooled to room temperature by removing the heating mantle and the particles were precipitated with ethanol followed by centrifugation and removal of the supernatant. Three cycles were performed of suspension in hexanes: oleylamine (20:1, by volume) followed by precipitation by excess ethanol, centrifugation and removal of the supernatant. Finally, the nanocrystals were stored in hexanes: oleylamine.

Synthesis of $CuInS_2$-Pt with "bullet" morphology. First, the $CuInS_2$ seeds with bullet morphology were synthesized as described above. A 25 mL 3-neck flask containing CuOAc (1.0 mmol), $InOAc_3$ (1.0 mmol), TOPO (3.5 mmol), oleylamine (10.0 mL), and a stir bar was placed under vacuum. The temperature was increased to 60°C and held there for 30 minutes. Under nitrogen, the temperature was increased to 150°C and at this point a mixture of dodecanethiol /tert-dodecanethiol (0.313 mL/2.20 mL, respectively) was injected. The temperature was rapidly increased to 280°C and held there for 30 min. The flask was cooled to room temperature by removing the heating mantle and the particles were precipitated with ethanol followed by centrifugation and removal of the supernatant. Three cycles were performed of suspension in hexanes: oleylamine (20:1, by volume) followed by precipitation by excess ethanol, centrifugation and removal of the supernatant. The nanocrystals were stored in 10.0 mL of hexanes: oleylamine.

For the hybrid synthesis oleylamine (0.2 mL), oleic acid (0.2 mL), 1,2-hexadecanediol (0.16 mmol), and diphenyl ether (10.0 mL) were loaded into a 25 mL 3-neck flask containing a stir bar. The mixture was placed under vacuum at 80°C for 30 min. In a vial, $Pt(acac)_2$ (0.043 mmol) was dissolved in diphenyl ether (1.0 mL) with addition of 1.0 mL of the $CuInS_2$ nanoparticles stock solution. The flask containing 1,2-hexadecanediol was heated to 210°C under nitrogen and the $Pt(acac)_2$-nanoparticle mixture was swiftly injected. After 10 min the heating mantle was removed and the flask was allowed to cool down to room temperature. The particles were precipitated with ethanol followed by centrifugation and removal of the supernatant. Three cycles were performed of suspension in hexanes: oleylamine (20:1, by volume) followed by precipitation by excess ethanol, centrifugation and removal of the supernatant. Finally, the nanocrystals were stored in hexanes: oleylamine.

D.2. Additional characterization of Pt-$CuInS_2$ hybrids

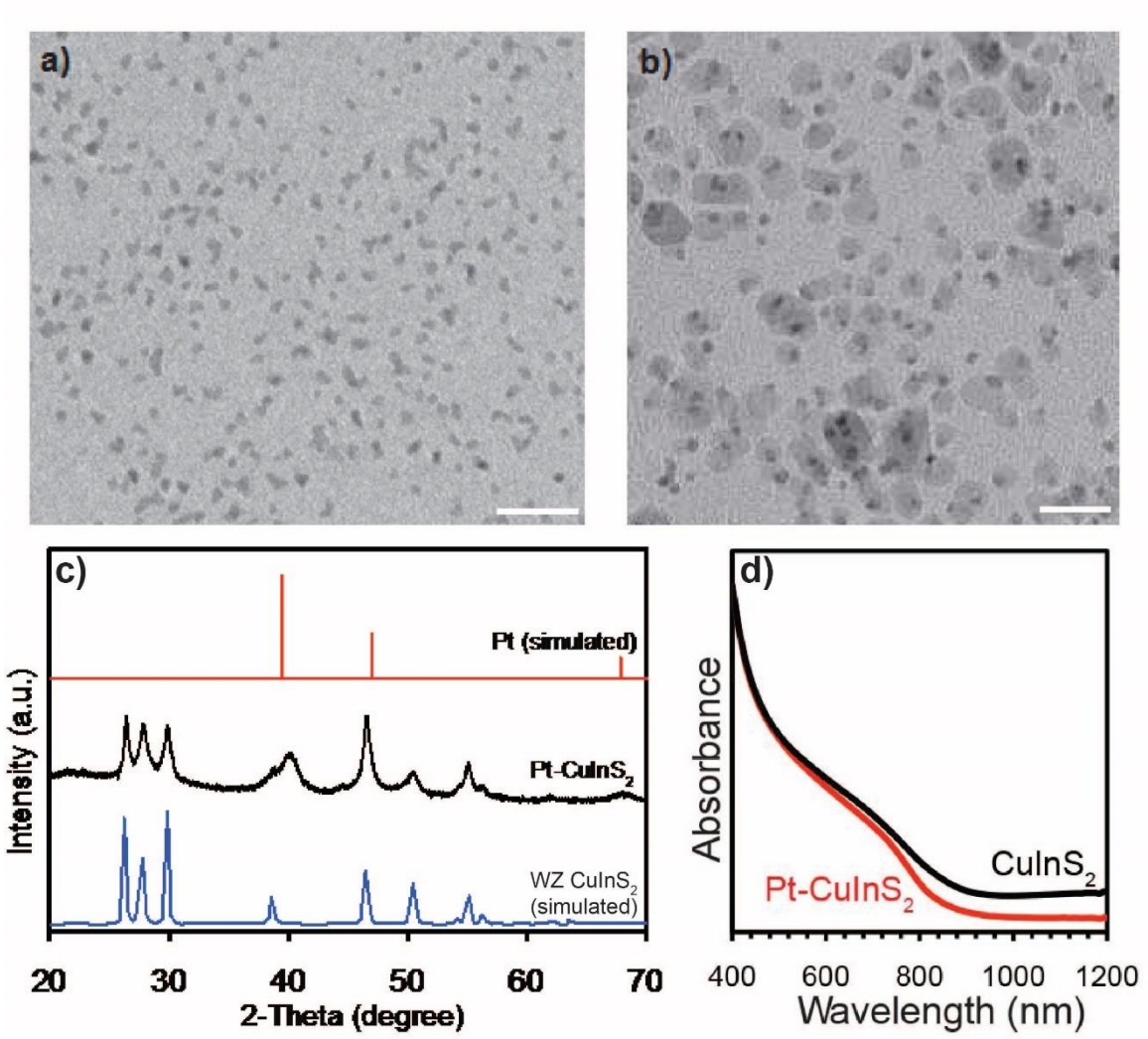

Figure D.1. Additional characterization of Pt-$CuInS_2$ hybrids; TEM images of: a) the Pt seeds used in the growth of Pt-$CuInS_2$ hybrids, b) an aliquot taken 30 s after injection of thiourea in the synthesis of Pt-$CuInS_2$ hybrids with the chloride metal precursors (Scale bars in a, b: 20 nm), c) Comparison of the XRD patterns shows the $CuInS_2$ domains in the hybrid structures have the wurtzite crystal structure. Pure wurtzite $CuInS_2$ spectra are digitized from the work of Chang *et al.*[167] Data for Pt is from JCPDS card no. 04-0802. d) UV-Vis spectra of the hybrids and $CuInS_2$ particles.

D.3. Additional characterization of bullet Pt-$CuInS_2$ hybrids

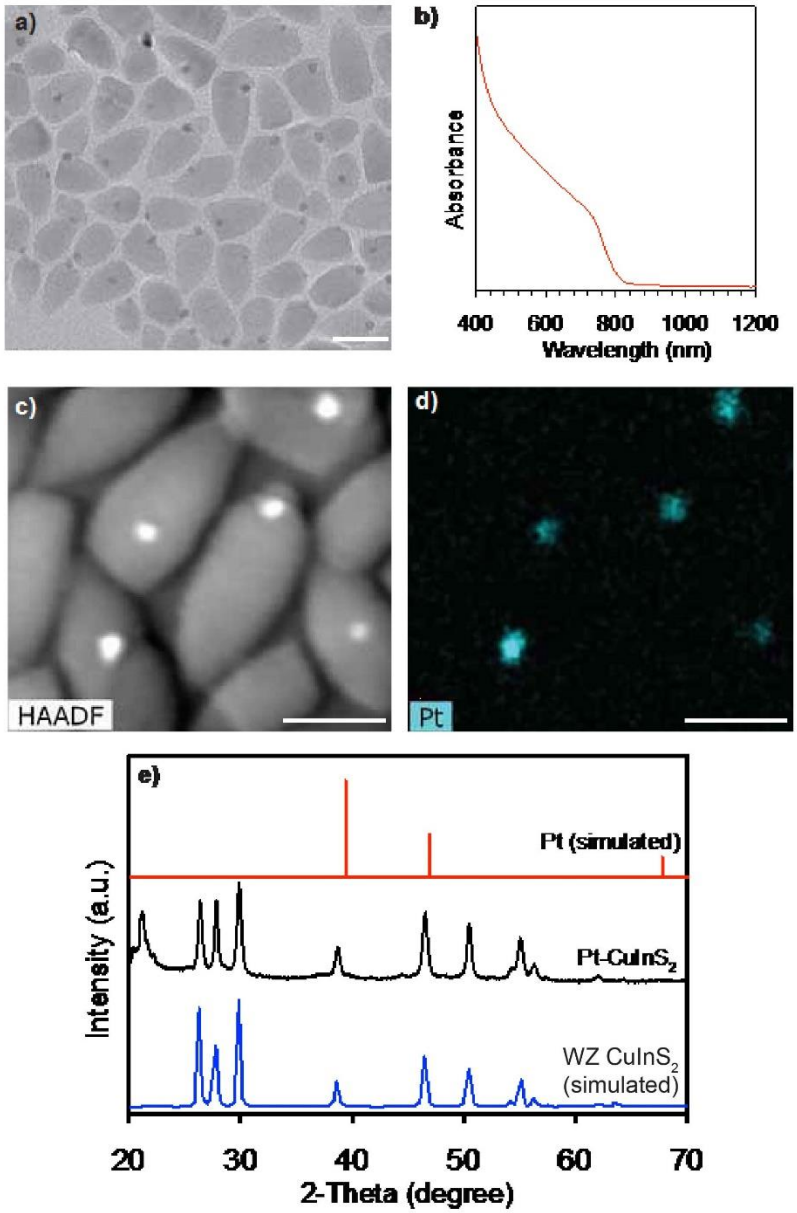

Figure D.2. Additional characterization of bullet Pt-$CuInS_2$ hybrids; a) TEM image of bullet Pt-$CuInS_2$ hybrids synthesized with metal acetate precursors and dodecanethiol/tert-dodecylmercaptan (Scale bar: 20 nm), b) UV-Vis spectrum of bullet Pt-$CuInS_2$ hybrids, c) high angle annular dark field STEM image and d) EDS mapping of the hybrids (Scale bars in c,d; 20 nm), e) Comparison of the XRD patterns. Pure wurtzite $CuInS_2$ spectra are digitized from the work of Chang *et al.*[167] Data for Pt is from JCPDS card no. 04-0802.

D.4. XRD of $CuInS_2$ seeds

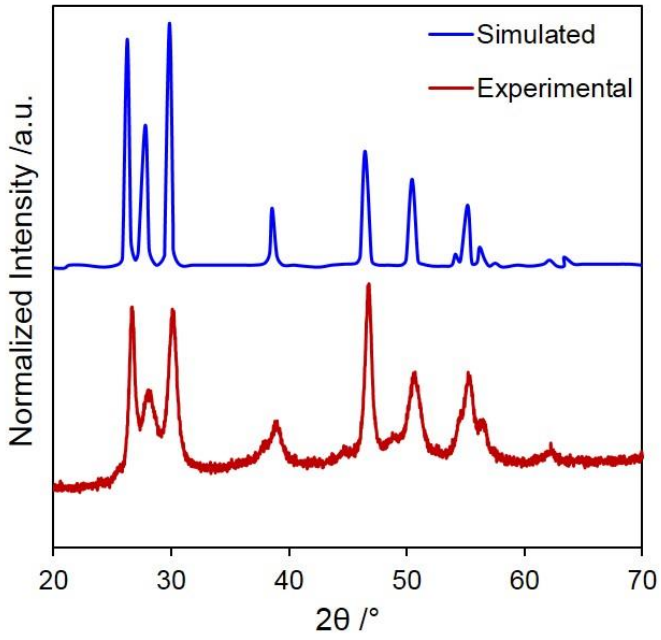

Figure D.3. XRD of $CuInS_2$ seeds. Pure wurtzite $CuInS_2$ spectra are digitized from the work of Chang *et al*.[167]

D.5. Compositional analyses of $CuInS_2$-Pt hybrids

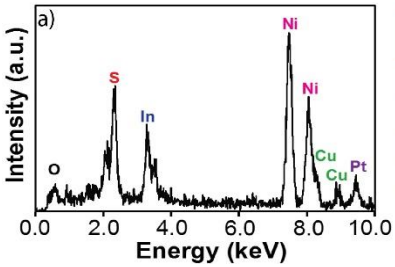

b) $CuInS_2$-Pt : HDD	Atomic %
Cu	19.8
In	14.7
S	37.8
Pt	27.7
Composition: $CuIn_{0.75}S_{1.9}Pt_{1.4}$	

c) $CuInS_2$-Pt : TOP	Atomic %
Cu	26.6
In	22.3
S	44.7
Pt	5.4
Composition: $CuIn_{0.84}S_{1.7}Pt_{0.2}$	

d) Pt-$CuInS_2$	Atomic %
Cu	27.6
In	25.7
S	44.7
Pt	2.0
Composition: $CuIn_{0.93}S_{1.6}Pt_{0.1}$	

Figure D.4. Compositional analyses of $CuInS_2$-Pt hybrids; a) Example EDS spectrum of the $CuInS_2$-Pt hybrids synthesized with $Pt(acac)_2$ and 1,2-hexadecanediol as reducing agent at 210°C. b) - d) Quantized EDS spectrum for $CuInS_2$-Pt hybrids showing nanoparticle composition.

D.6. Additional characterization of bullet $CuInS_2$-Pt hybrids

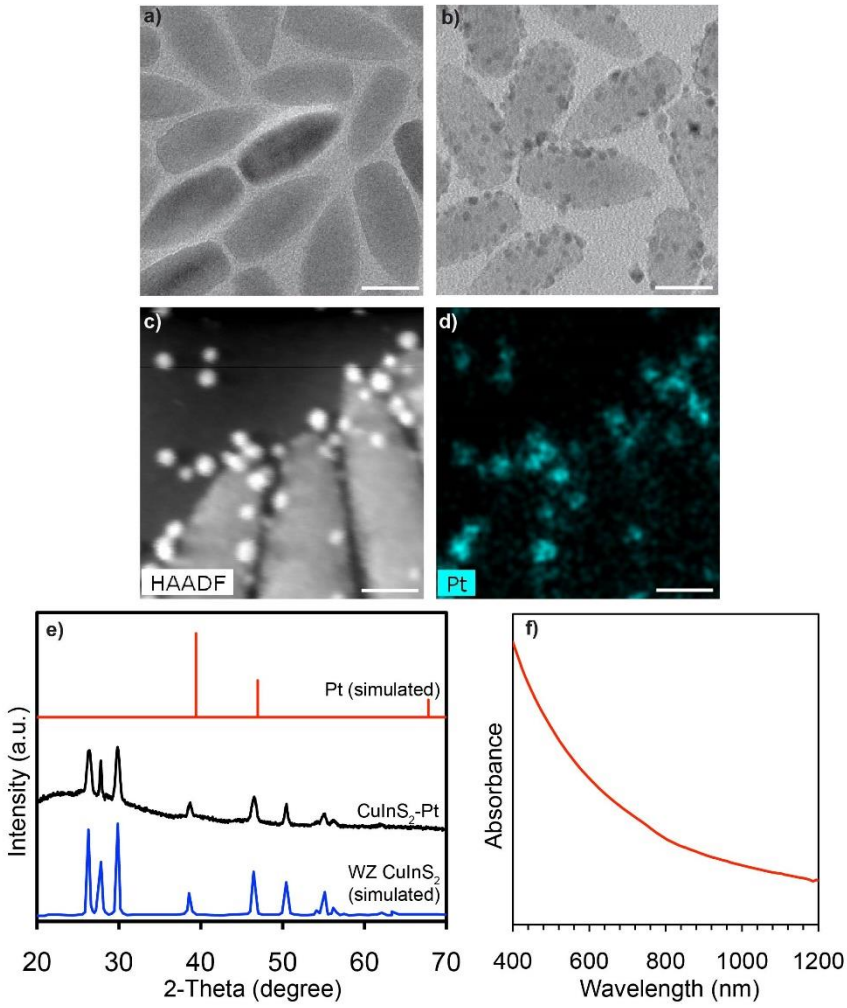

Figure D.5. Additional characterization of bullet $CuInS_2$-Pt hybrids; TEM images of a) $CuInS_2$ seeds with bullet morphology and b) $CuInS_2$-Pt synthesized with $Pt(acac)_2$, 1,2-hexadecanediol as reducing agent, and bullet $CuInS_2$ seeds (Scale bars in a,b: 20 nm), c) High angle annular dark field STEM image and d) EDS mapping of the hybrids (Scale bars in c,d; 10 nm), e) Comparison of the XRD patterns. Pure wurtzite $CuInS_2$ spectra are digitized from the work of Chang *et al.*[167] Data for Pt is from JCPDS card no. 04-0802; f) UV-Vis spectrum.

D.7. TEM images of additional hybrid syntheses

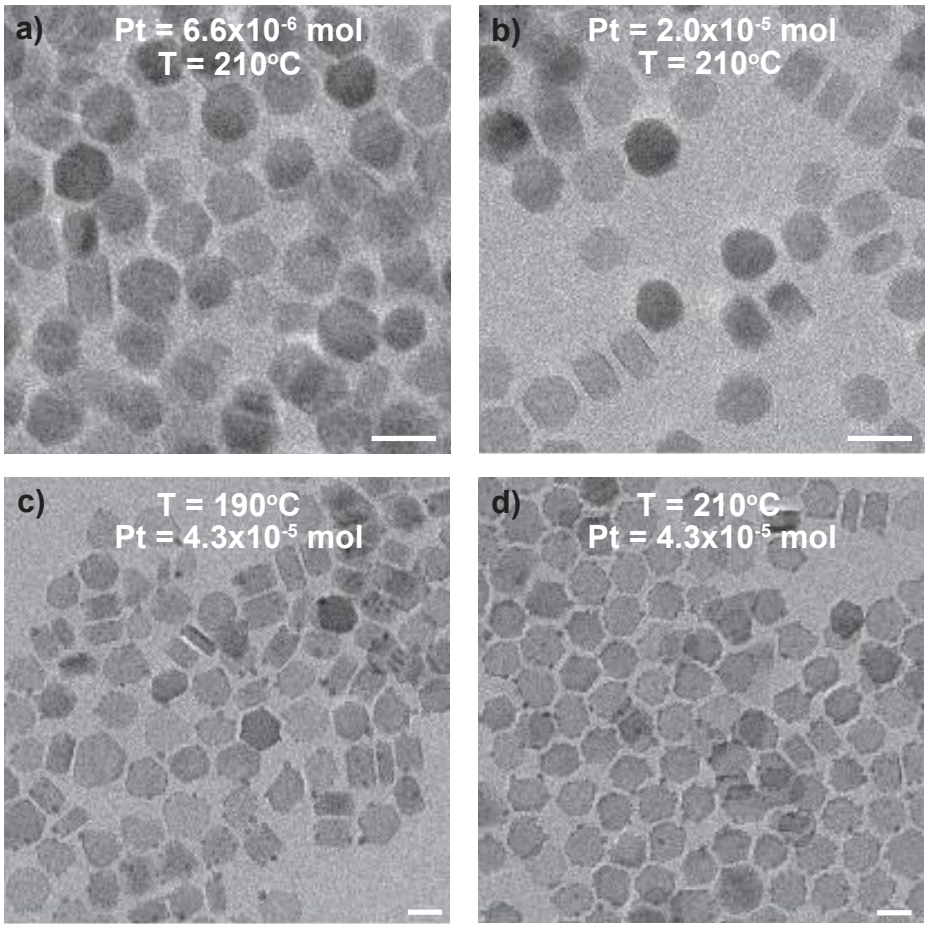

Figure D.6. TEM images of additional hybrid syntheses; TEM images of $CuInS_2$-Pt synthesized with $Pt(acac)_2$ and 1,2-hexadecanediol as reducing agent a,b) using different amounts of $Pt(acac)_2$ at the normal reaction temperature, and c,d) at lower temperatures with the normal amount of $Pt(acac)_2$. Scale bars in a-d: 20 nm.

D.8. Absorbance spectrum of $CuInS_2$-Pt:TOP hybrids

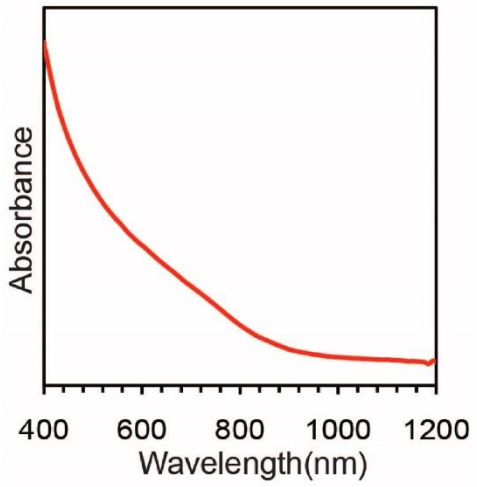

Figure D.7. Absorbance spectrum of $CuInS_2$-Pt:TOP hybrids.

D.9. Compositional analyses of $CuInS_2$-Pd hybrids

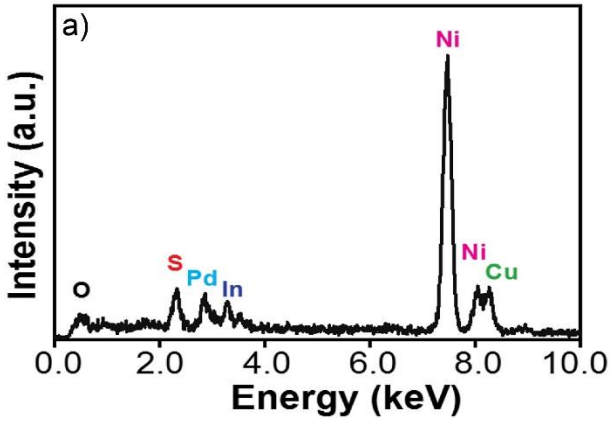

b) $CuInS_2$-Pd	Atomic %
Cu	31.2
In	10.0
S	32.2
Pd	26.6

Composition: $CuIn_{0.3}S_{1.0}Pd_{0.9}$

Figure D.8. Compositional analyses of $CuInS_2$-Pd hybrids; a) EDS spectrum of the $CuInS_2$-Pd hybrids synthesized with TOP:Pd^{2+} and oleylamine as reducing agent at 210°C. b) Quantized EDS data showing hybrid composition.

D.10. EDS mapping for $CuInS_2$-Pd hybrids

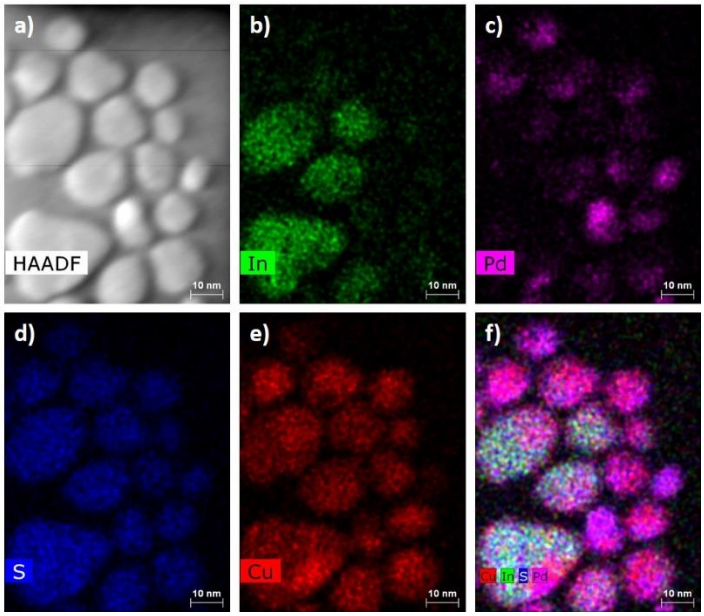

Figure D.9. EDS mapping for $CuInS_2$-Pd hybrids. a) High angle annular dark field STEM image, b) EDS mapping showing In, c) EDS mapping showing Pd, d) EDS mapping showing S, e) EDS mapping showing Cu, and f) Cu, In, S, Pd. Scale bars: 10 nm. Data indicate Pd ions have replaced In ions via cation exchange.

D.11. XRD of $CuInS_2$-Pd hybrids

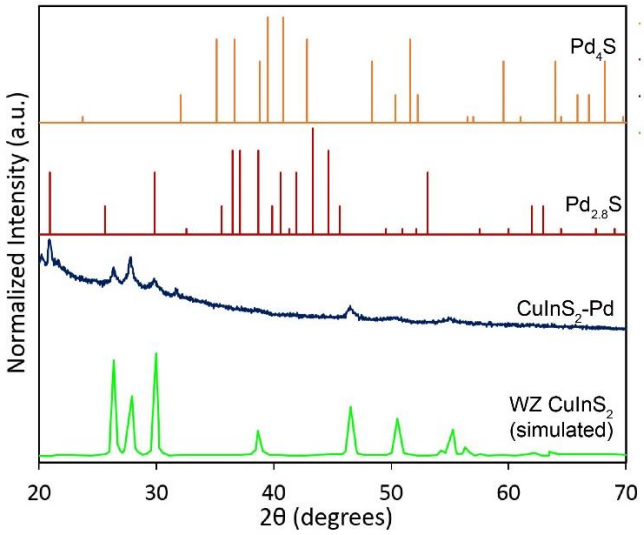

Figure D.10. XRD of $CuInS_2$-Pd hybrids. Pure wurtzite $CuInS_2$ spectra are digitized from the work of Chang *et al.*[167] Data for Pd_4S is from JCPDS card no. 10-0335. Data for $Pd_{2.8}S$ is from JCPDS card no. 10-0334.

D.12. Results after ligand exchange

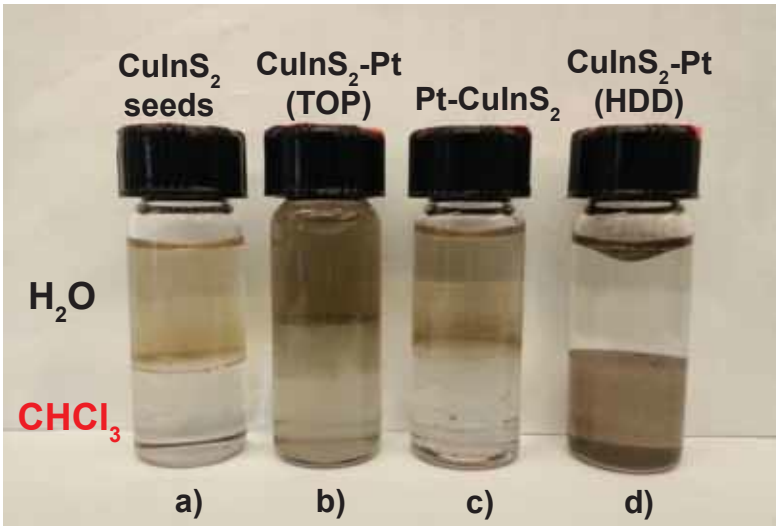

Figure D.11. Results after ligand exchange with 11-mercaptoundecanoic acid; a) pristine $CuInS_2$ seeds b) $CuInS_2$-Pt hybrids synthesized from with TOP:Pt^{2+} c) Pt-$CuInS_2$ synthesized using Pt seeds, and d) $CuInS_2$-Pt hybrids synthesized from $CuInS_2$ with $Pt(acac)_2$ and 1,2-hexadecanediol.

E. Supplementary material for Chapter 7

E.1. Experimental techniques

Materials. Copper(II) acetylacetonate ($Cu(acac)_2$, Strem Chemicals, 98%), copper(II) chloride ($CuCl_2$, Alfa Aesar, 98%), copper(I) acetate (CuOAc, Strem Chemicals, 99%), iron(III) acetylacetonate ($Fe(acac)_3$, Aldrich, 97%), iron(III) chloride hexahydrate ($FeCl_3.6H_2O$, Sigma-Aldrich, 97%), thiourea (Sigma-Aldrich, ≥ 99.0%), 1-dodecanethiol (DDT, Aldrich, ≥ 98.0%), tert-dodecylmercaptan (t-DDT, Aldrich, 98.5%), dioctyl ether (DiOE, Sigma-Aldrich, 99%), oleylamine (OlAm, Aldrich, 70%), octadecene (ODE, Aldrich, 90%), diphenyl ether (Sigma-Aldrich, 99%), octadecylamine (ODA, Aldrich, 90%), methanol (MeOH, Fisher Scientific), toluene (Fisher Scientific, HPLC grade), sodium diethyldithiocarbamate trihydrate ($Na(DDTC).3H_2O$, Alfa Aesar, 98%) and neocuproine (Aldrich, ≥ 98%) were purchased and used as received. Standard air-free Schlenk techniques were used throughout with N_2 as the inert gas.

Synthesis of Cu_2S NCs. Cu_2S NCs were prepared by Evan Robinson using a modified literature synthesis.[413] Briefly, $Cu(acac)_2$ (2.0 mmol), DDT (8.0 mL) and DiOE (2.0 mL), a non-coordinating solvent, were degased at 60°C, then heated under inert atmosphere at 215°C for 1 hr. The 12-14 nm seeds were transferred into a glovebox and precipitated in polar and non-polar solvents to remove unreacted precursors and side products.

Cation exchange method. A cation exchange procedure modified from the report of van der Stam *et al.* was used.[168] All steps were carried out in a N_2 filled glove box. A solution of Cu_2S NCs in toluene (20 mM, 0.8 mL) was added to a vial with ODA (10 mg), neocuproine in toluene (20 mM, 0.8 mL), and $FeCl_3.6H_2O$ in MeOH (10 mM, 1.2 mL). The mixture was sonicated for 90 min to remove any Cu2S superlattices, and then stirred at room temperature for one week. Samples were then dried under vacuum to remove the solvent, re-suspended in anhydrous isopropanol and centrifuged to remove unreacted precursor. The product was then cleaned by repeated centrifugation and decantation with chloroform and isopropanol before characterization.

Hot-injection method. A hot-injection method modified from the synthesis of $CuInS_2$ NCs detailed in Chapter 4 was used.[164] $FeCl_3.6H_2O$ (0.5 mmol), thiourea (1.0 mmol), and OlAm (10 mL) were added to a reaction vessel and degased at 85°C for 1 hr. Concomitantly, CuOAc (0.5 mmol) was suspended in ODE (500 μL), diphenyl ether (500 μL) and t-DDT (1.0 mmol). At 120°C, 1 mL of the Cu solution was injected quickly (less than 1 s) into the reaction vessel. After 30 min, the heat was removed and the reaction mixture was cooled to room temperature. The obtained $CuFeS_2$ product was precipitated by addition of methanol/ isopropanol (v/v, 2:1) and then purified by repeated centrifugation and decantation with addition of methanol/ isopropanol and chloroform.

Preparation of copper(II) diethyldithiocarbamate precursor. The preparation method used was based on work by Han *et al.*[119] Briefly, $Na(DDTC).3H_2O$ (1.0 mmol) was dissolved in 10 mL deionized water (DI H_2O) via sonication and shaking over a 1 hr period. Concomitantly, $CuCl_2$ (0.5 mmol) was dissolved in 5 mL DI H_2O. The two solutions were then mixed in a 50 mL beaker, 10 mL additional DI H_2O was added and the mixture was stirred for 1 hr. The mixture was filtered and the resultant brown precipitate was washed five times with DI H_2O. The solid $Cu(DDTC)_2$ was then dried overnight under vacuum.

Heat-up method. $CuFeS_2$ nanostructures were prepared using a modified literature procedure.[119] $Cu(DDTC)_2$ (0.10 mmol) and $Fe(acac)_3$ (0.10 mmol) were added to a reaction vessel containing OlAm (5 mL). The reaction mixture was degased at 65°C for 1 hr, then placed under N_2 and heated to 120°C. The reaction mixture was kept at 120°C for 30 min, then cooled to room temperature. The obtained $CuFeS_2$ nanostructures were precipitated by addition of methanol/ isopropanol (v/v, 2:1) and then purified by repeated centrifugation and decantation with addition of methanol/ isopropanol and chloroform.

Optical characterization. The absorption spectra of NC samples were collected from 300 – 2300 nm on a UV-visible spectrophotometer (Jasco V-670). Samples were measured in solution with chloroform as the solvent.

Further characterization. Transmission electron microscopy (TEM) and energy dispersive X-ray spectroscopy (EDS) were carried out using a FEI Tecnai Osiris™ digital 200 kV S/TEM system equipped with ChemiSTEM EDS. TEM samples were prepared by drop casting a dilute NC solution in chloroform onto a nickel grid with a carbon support and drying in air at room temperature. NCs were sized manually using ImageJ with number of particles measured, $n \geq 100$. Lattice fringes were measured by generating a profile plot of an area of the image using ImageJ, manually counting the cycles, and dividing the length of the profile plot by the number of cycles. The minimum number of cycles used was ten. EDS spectra were collected for 2 min and quantified using the Espirit software. Cu, Fe and S were quantified using the K series of peaks. All spectra were background subtracted and overlapping Cu sample and Ni grid peaks were deconvoluted before quantification. Drift-corrected EDS maps were collected for 90 s with beam current 1.5 nA. XRD measurements were performed using a Scintag XGEN-4000 X-ray diffractometer with a CuK_α (λ = 0.154 nm) radiation source. The resulting diffraction patterns were then visually compared to literature data to determine the structure.

E.2. EDS mapping for $CuFeS_2$ nanostructures synthesized via heat-up method

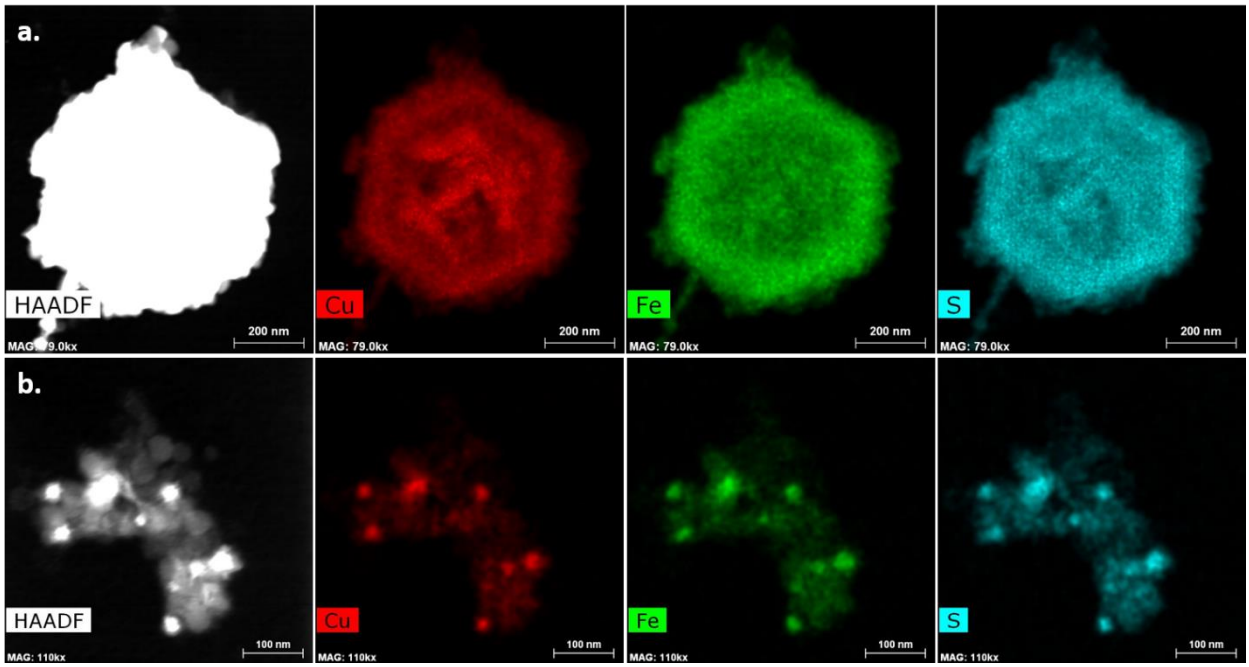

Figure E.1. EDS mapping for $CuFeS_2$ nanostructures synthesized via heat-up method; **a.** Hexagonal clusters of $CuFeS_2$, **b.** $CuFeS_2$ nanosheets with associated nanoparticle clusters.

E.3. Calculated density of states for CP, WZ and S- deficient WZ $CuFeS_2$

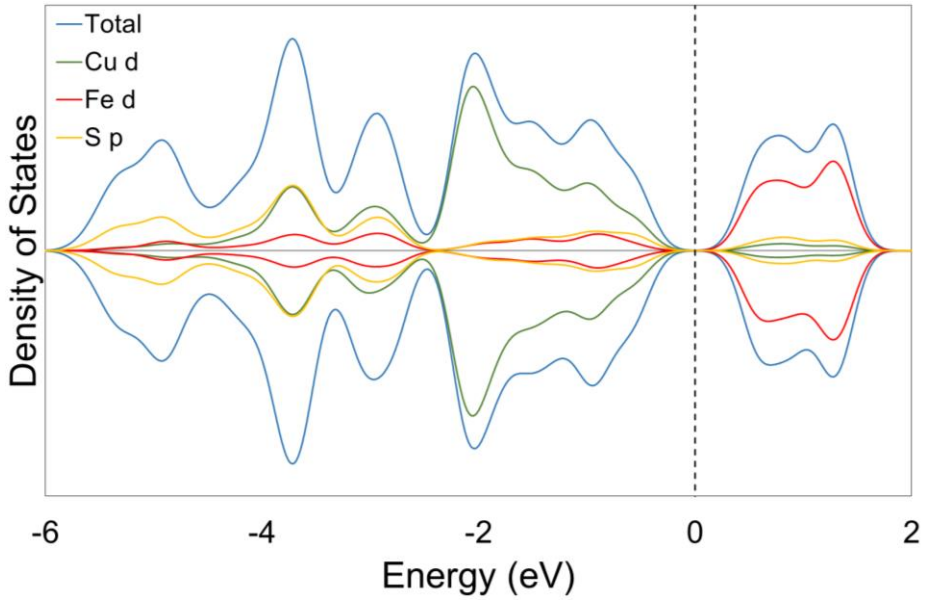

Figure E.2. Calculated density of states for CP $CuFeS_2$.

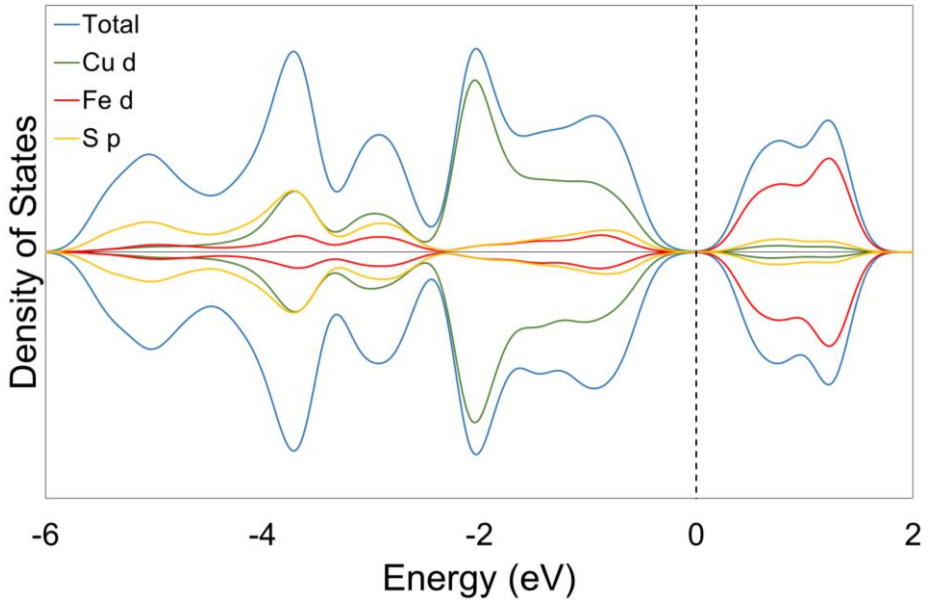

Figure E.3. Calculated density of states for WZ $CuFeS_2$.

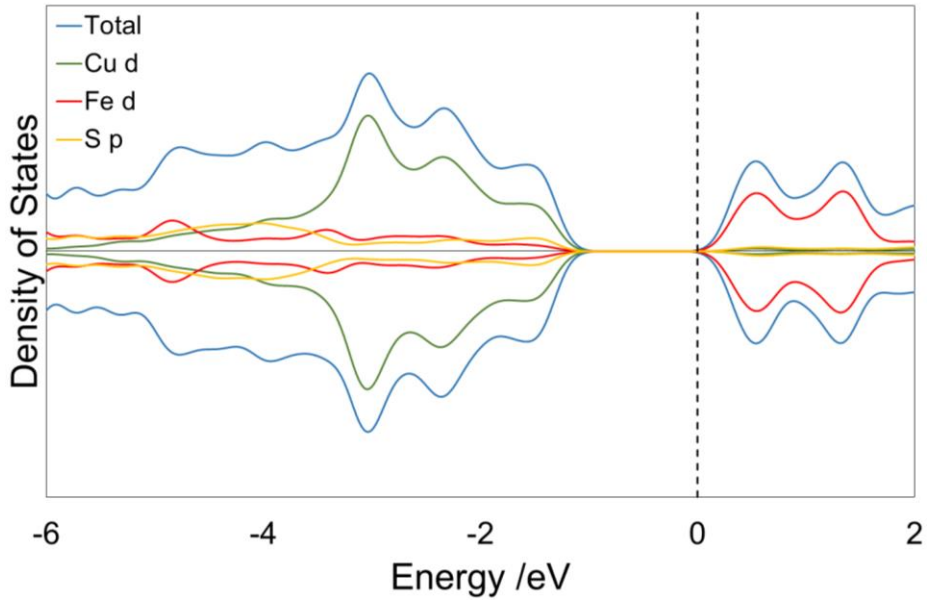

Figure E.4. Calculated density of states for S-deficient WZ $CuFeS_2$.

E.4. Characterization of $CuFeS_2$ NCs synthesized at 140°C

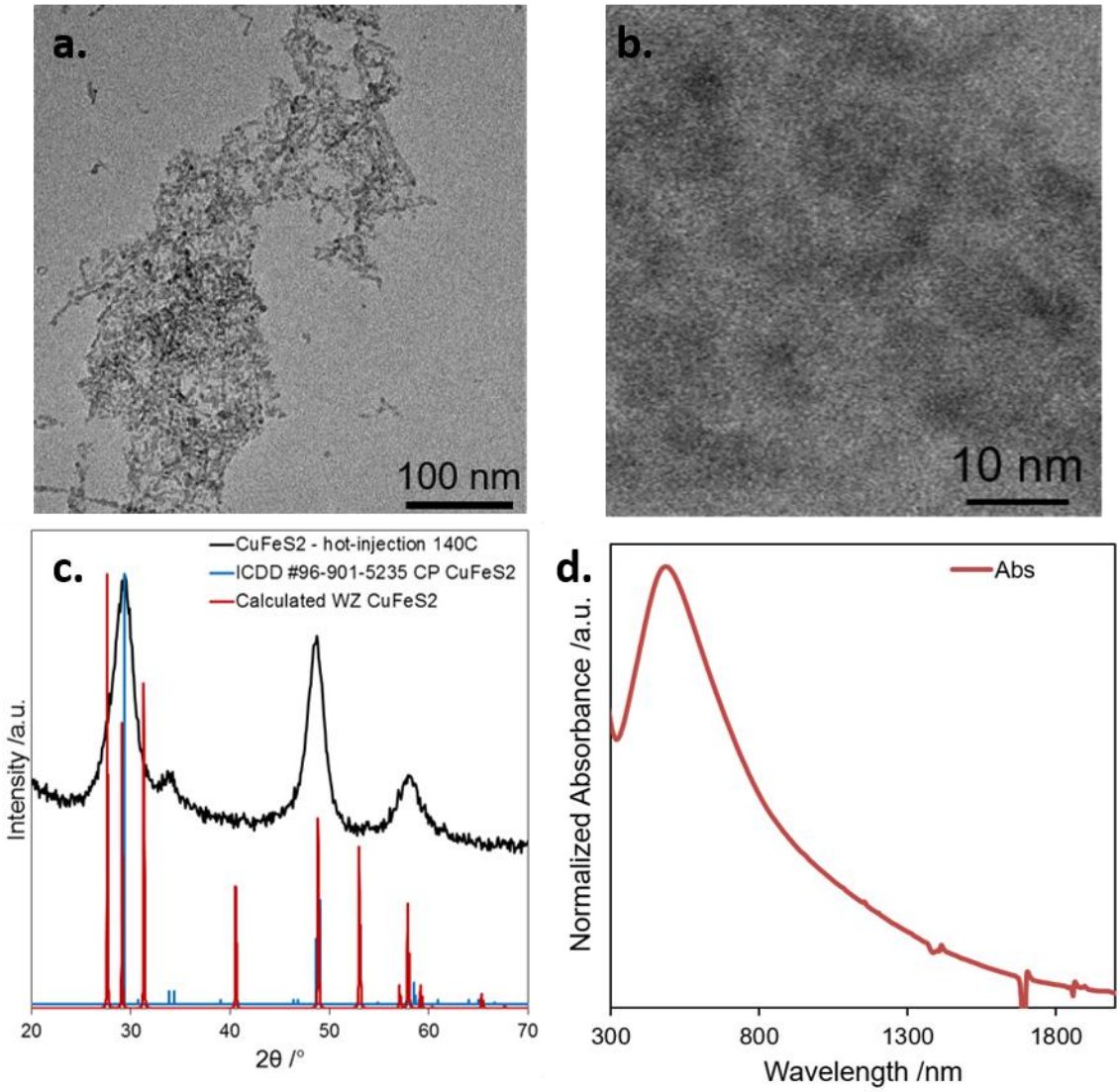

Figure E.5. Characterization of $CuFeS_2$ NCs synthesized via hot-injection method at 140°C; **a.-b.** TEM images, **c.** Experimental XRD pattern (black) with calculated WZ (red) and ICDD CP (blue) $CuFeS_2$ reflections shown, and **d.** UV-Vis absorbance spectrum.

F. Supplementary material for Chapter 8

F.1. Experimental techniques.

Materials. Silver nitrate ($AgNO_3$, Sigma-Aldrich, ≥ 99.0%), iron(III) acetylacetonate ($Fe(acac)_3$, Aldrich, 97%), elemental sulfur (S, Sigma-Aldrich, 99.98%), oleylamine (OlAm, Aldrich, 70%), oleic acid (OlAc, Aldrich, 90%) dioctyl ether (DiOE, Sigma-Aldrich, 99%), methanol (MeOH, Fisher Scientific) toluene (Fisher Scientific, HPLC grade), octadecene (ODE, Aldrich, 90%), 1-dodecanethiol (DDT, Aldrich, ≥ 98.0%), iron(III) chloride hexahydrate ($FeCl_3.6H_2O$, Sigma-Aldrich, 97%), and sodium stearate (Na(stear), Sigma, > 88%) were purchased and used as received. Standard air-free Schlenk techniques were used throughout with N_2 as the inert gas.

Synthesis of $AgFeS_2$ NCs. The synthesis of $AgFeS_2$was based on the synthesis of Xie *at al.* for $AgInS_2$.[131] $AgNO_3$ (0.40 mmol), $Fe(acac)_3$ (0.40 mmol), and S (0.80 mmol) were dissolved in MeOH (5 mL), toluene (5 mL), and ODE (5 mL) or OlAm (5 mL) respectively. DiOE (10 mL), OlAm (0.40 mmol), OlAc (0.40 mmol), $AgNO_3$ solution (375 µL), and $Fe(acac)_3$ solution (500 µL) were added to a reaction vessel, and degased for 1 hr at 90°C. The mixture was then placed under N_2 and heated to 180°C. At 180°C, S solution (0.5 mL) was injected. The reaction mixture was heated for 30 min, and then cooled to room temperature. The obtained $AgFeS_2$ NCs were precipitated by addition of methanol/ isopropanol (v/v, 2:1) and then purified by repeated centrifugation and decantation with addition of methanol/ isopropanol and chloroform.

For reactions carried out with different S precursor concentration, S solutions were prepared with concentration 0.16 M, 0.24 M, and 0.72 M in both ODE and OlAm. 0.5 mL of each was injected. In additional studies, DDT (0.08 mmol) was added to the original reaction mixture, excess $Fe(acac)_3$ (0.1 mmol in 500 µL toluene) was used, and iron(III) stearate ($Fe(stear)_3$) was used as a substitute for $Fe(acac)_3$ in the same molar amounts as described above.

Synthesis of iron(III) stearate. The synthesis of iron(III) stearate was based on the work of Bai *et al.*[414] Na(stear) was dissolved in 200 mL deionized water (DI H_2O) at 50°C. Concomitantly, $FeCl_3.6H_2O$ was dissolved in 10 mL DI H_2O. The Fe^{3+} solution was added dropwise to the Na solution at 50°C with stirring. Then the mixture was held at 50°C and stirred for 1 hr. The mixture was filtered and the resultant pink precipitate was washed five times with hot DI H_2O. The solid $Fe(stear)_3$ was then dried overnight under vacuum.

Optical characterization. The absorption spectra of NC samples were collected from 300 – 2300 nm on a UV-visible spectrophotometer (Jasco V-670). Samples were measured in solution with chloroform as the solvent.

Further characterization. Transmission electron microscopy (TEM) and energy dispersive X-ray spectroscopy (EDS) were carried out using a FEI Tecnai Osiris™ digital 200 kV S/TEM system equipped with ChemiSTEM EDS. TEM samples were prepared by drop casting a dilute NC solution in chloroform onto a copper grid with a carbon support and drying in air at room temperature. NCs were sized manually using ImageJ with number of particles measured, n = 150. Lattice fringes were measured by generating a profile plot of an area of the image using ImageJ, manually counting the cycles, and dividing the length of the profile plot by the number of cycles. The minimum number of cycles used was ten. EDS spectra were collected for 2 min and quantified using the Espirit software. Fe and S were quantified using the K series of peaks,

while Ag was quantified using the L series. All spectra were background subtracted and overlapping peaks were deconvoluted before quantification. Drift-corrected EDS maps were collected for 90 s with beam current 1.5 nA. XRD measurements were performed using a Scintag XGEN-4000 X-ray diffractometer with a CuK_{α} (λ = 0.154 nm) radiation source. The resulting diffraction patterns were then visually compared to literature data to determine the structure.

Rietveld refinement. Rietveld refinement was performed using the General Structure and Analysis System (GSAS) suite of programs and the EXPGUI.[320-322] The GSAS suite of programs allows the refinement of parameters including site occupancy, atomic parameters, lattice parameters, background coefficients, peak profiles, atomic displacements and preferred orientation. The quality of the refinement is monitored by visual comparison of calculated and observed patterns, facilitated by plotting a difference curve below the x-axis, and calculating the goodness-of-fit parameter, χ^2.

F.2. Characterization of $AgFeS_2$ NCs synthesized with dodecanethiol

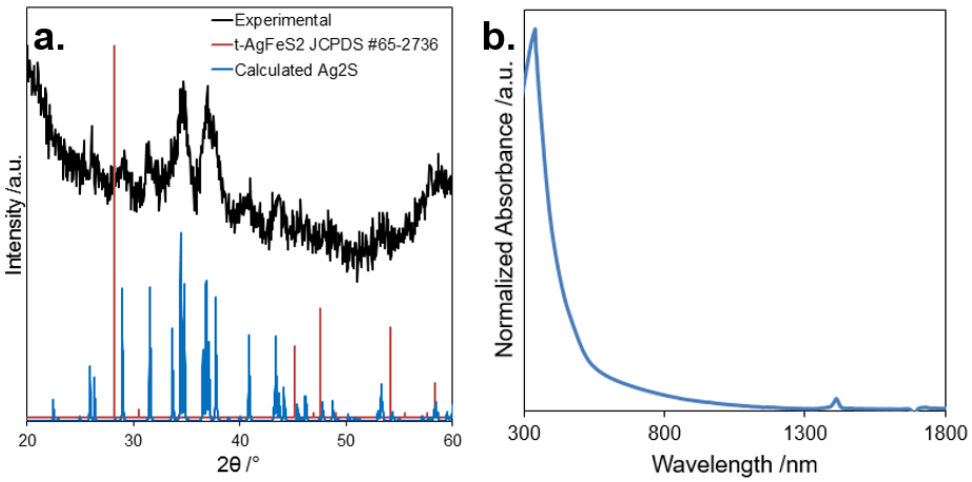

Figure F.1. Characterization of $AgFeS_2$ NCs synthesized with dodecanethiol; **a.** XRD and **b.** UV-Vis absorbance.

F.3. Characterization of $AgFeS_2$ NCs synthesized at 150°C

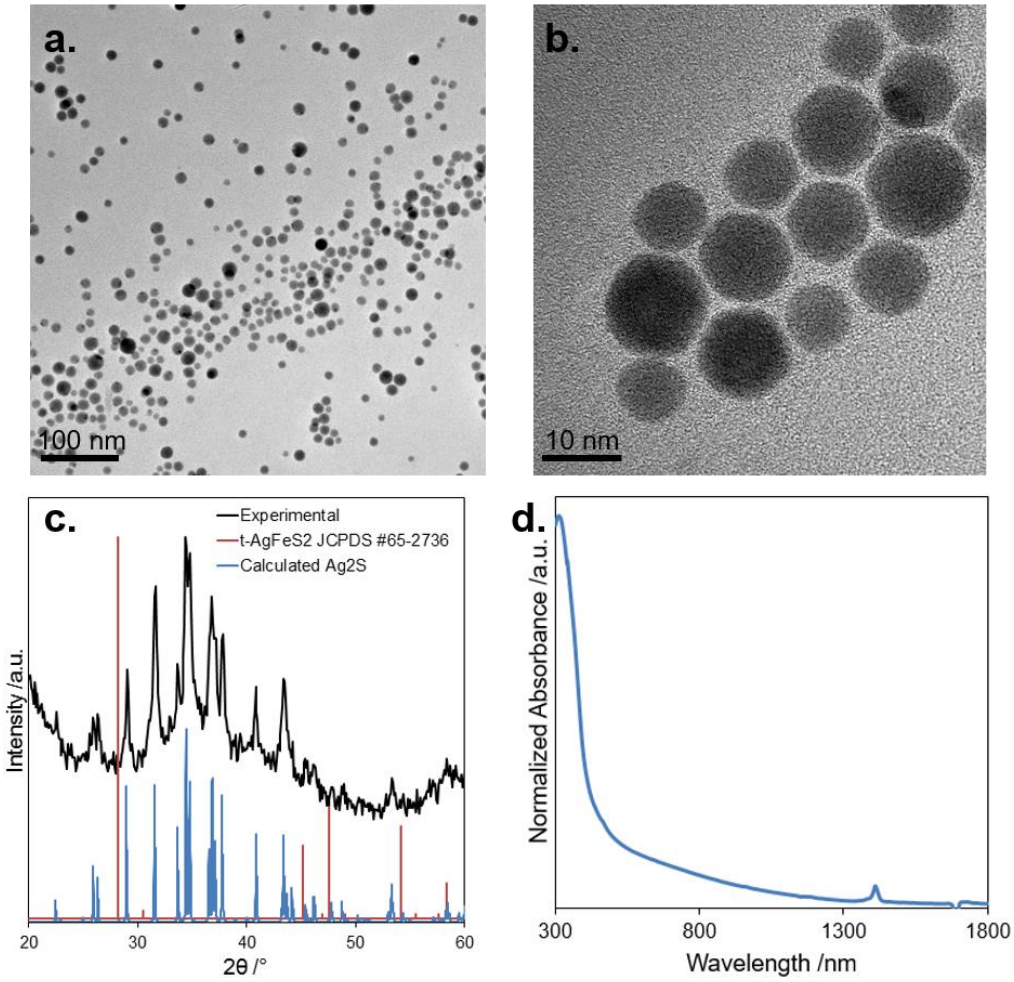

Figure F.2. Characterization of $AgFeS_2$ NCs synthesized at 150°C; **a.-b.** TEM images, **c.** XRD and **d.** UV-Vis absorbance.

F.4. Characterization of $AgFeS_2$ NCs synthesized at 210°C

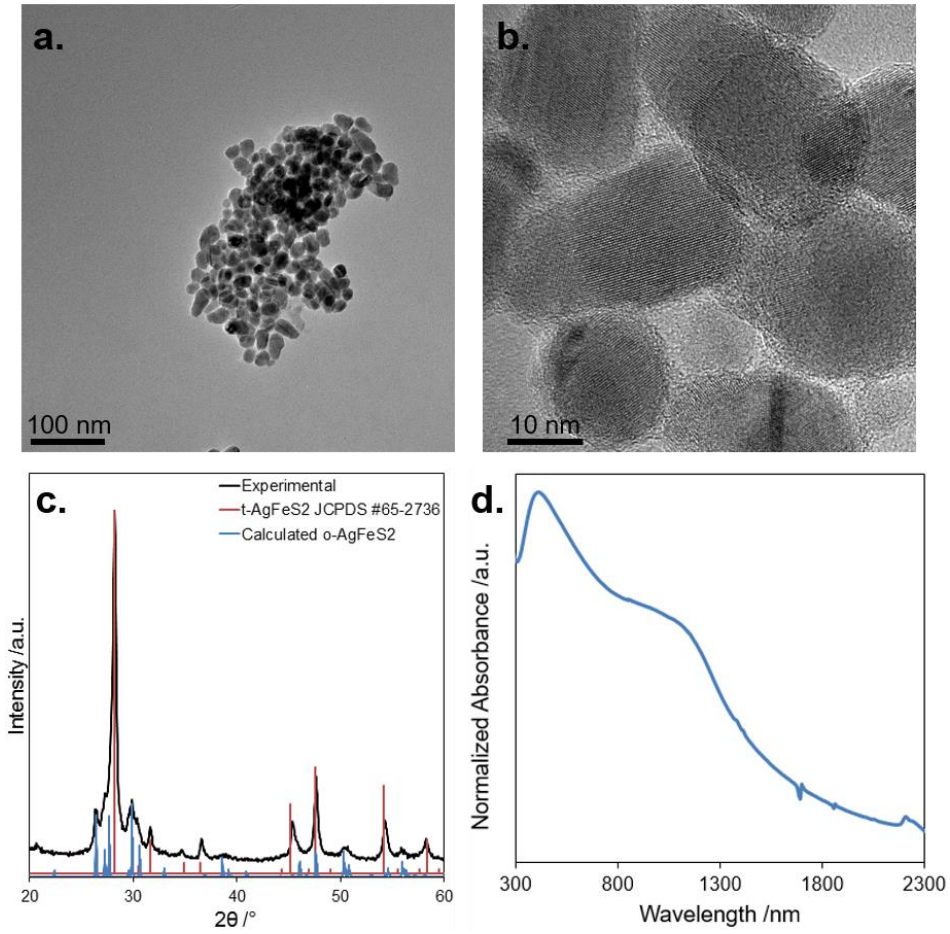

Figure F.3. Characterization of $AgFeS_2$ NCs synthesized at 210°C; **a.-b.** TEM images, **c.** XRD and **d.** UV-Vis absorbance.

F.5. Characterization of $AgFeS_2$ NCs synthesized at 240°C

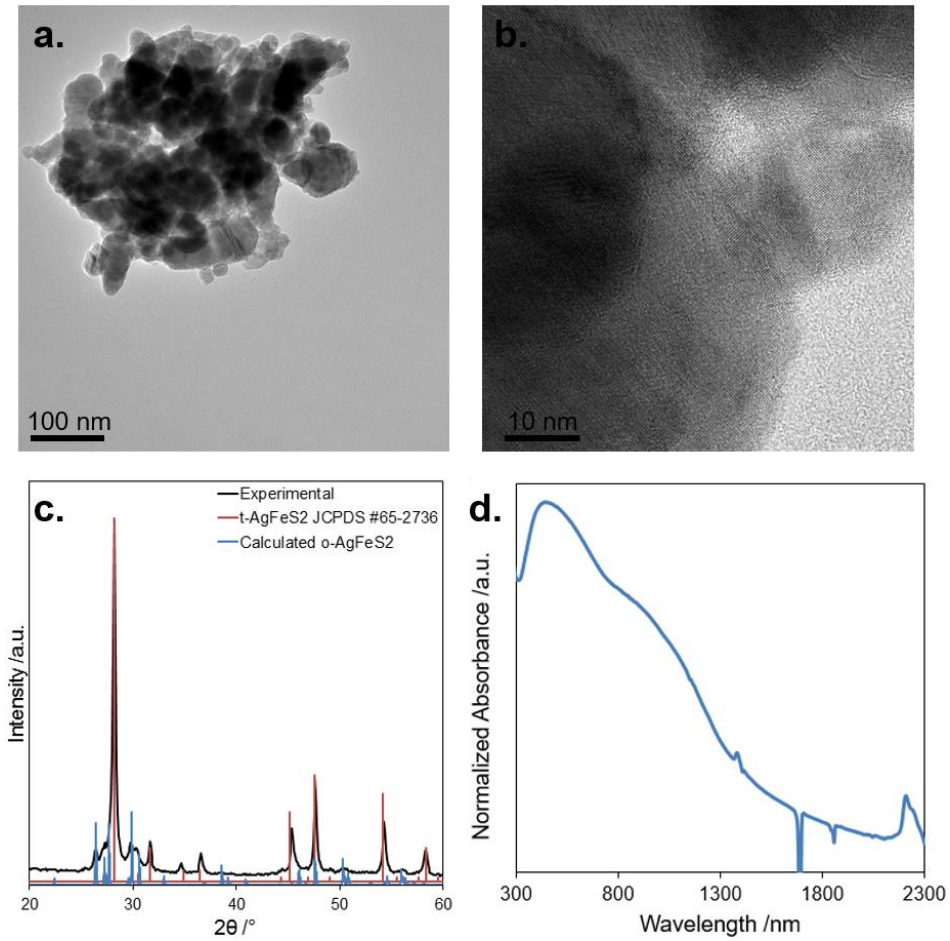

Figure F.4. Characterization of $AgFeS_2$ NCs synthesized at 240°C; **a.-b.** TEM images, **c.** XRD and **d.** UV-Vis absorbance.

F.6. Characterization of $AgFeS_2$ NCs synthesized with iron(III) stearate at 210°C

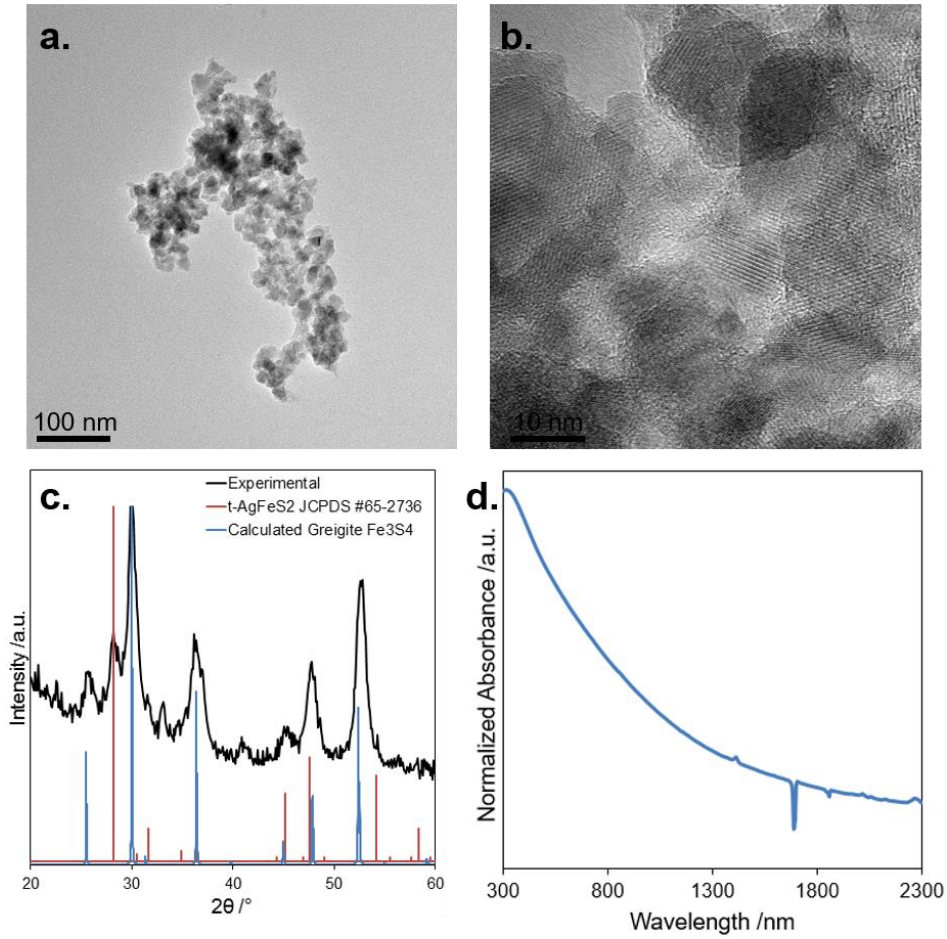

Figure F.5. Characterization of $AgFeS_2$ NCs synthesized with $Fe(stear)_3$ at 210°C; **a.-b.** TEM images, **c.** XRD and **d.** UV-Vis absorbance.

F.7. Characterization of t-$AgFeS_2$ NCs within mixed phase sample

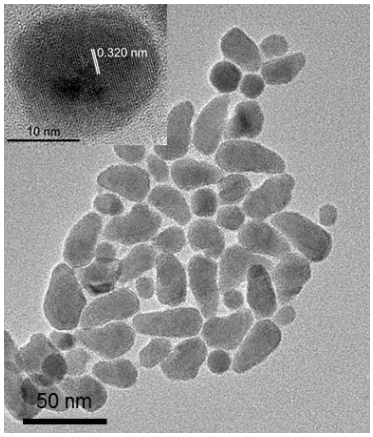

Figure F.6. Characterization of t-$AgFeS_2$ NCs in mixed phase sample; TEM image of o-$AgFeS_2$ sample with spherical and bullet-like morphologies (inset: HRTEM of spherical parting with lattice fringes characteristic of t-$AgFeS_2$, d = 0.320 nm, denoted).

F.8. Tauc plots for $AgFeS_2$ samples

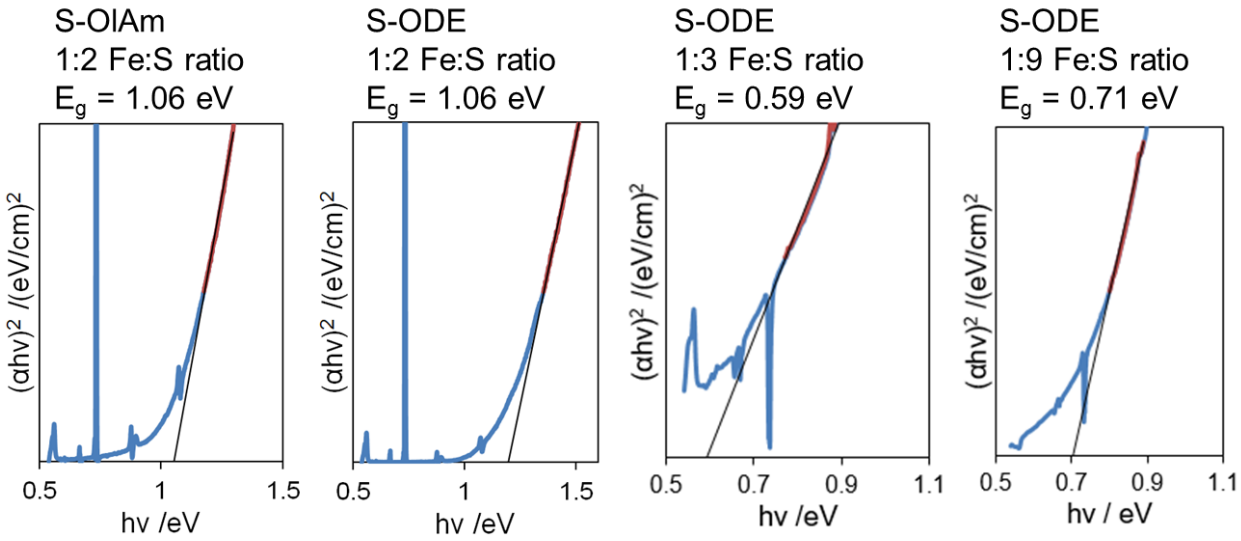

Figure F.7. Tauc plots used to estimate the band gap of $AgFeS_2$ NCs.

F.9. Characterization of $AgFeS_2$ NCs with increased S precursor concentration

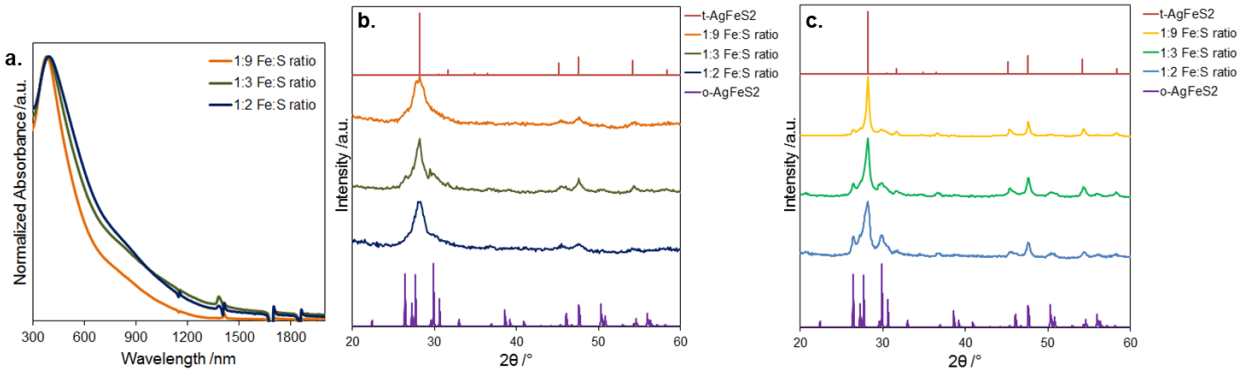

Figure F.8. Characterization of $AgFeS_2$ NCs with increased S precursor concentration; **a.** UV-Vis absorbance of $AgFeS_2$ NCs synthesized with S-OlAm with concentration 0.16 M, 0.24 M and 0.72 M resulting in Fe:S precursor ratio 1:2, 1:3, and 1:9 respectively, **b.** XRD patterns for the product NCs, and **c.** XRD patterns for $AgFeS_2$ NCs synthesized with S-ODE with concentration 0.16 M, 0.24 M and 0.72 M resulting in Fe:S precursor ratio 1:2, 1:3, and 1:9 respectively.

F.10. TEM images of $AgFeS_2$ NCs with different S precursor concentration

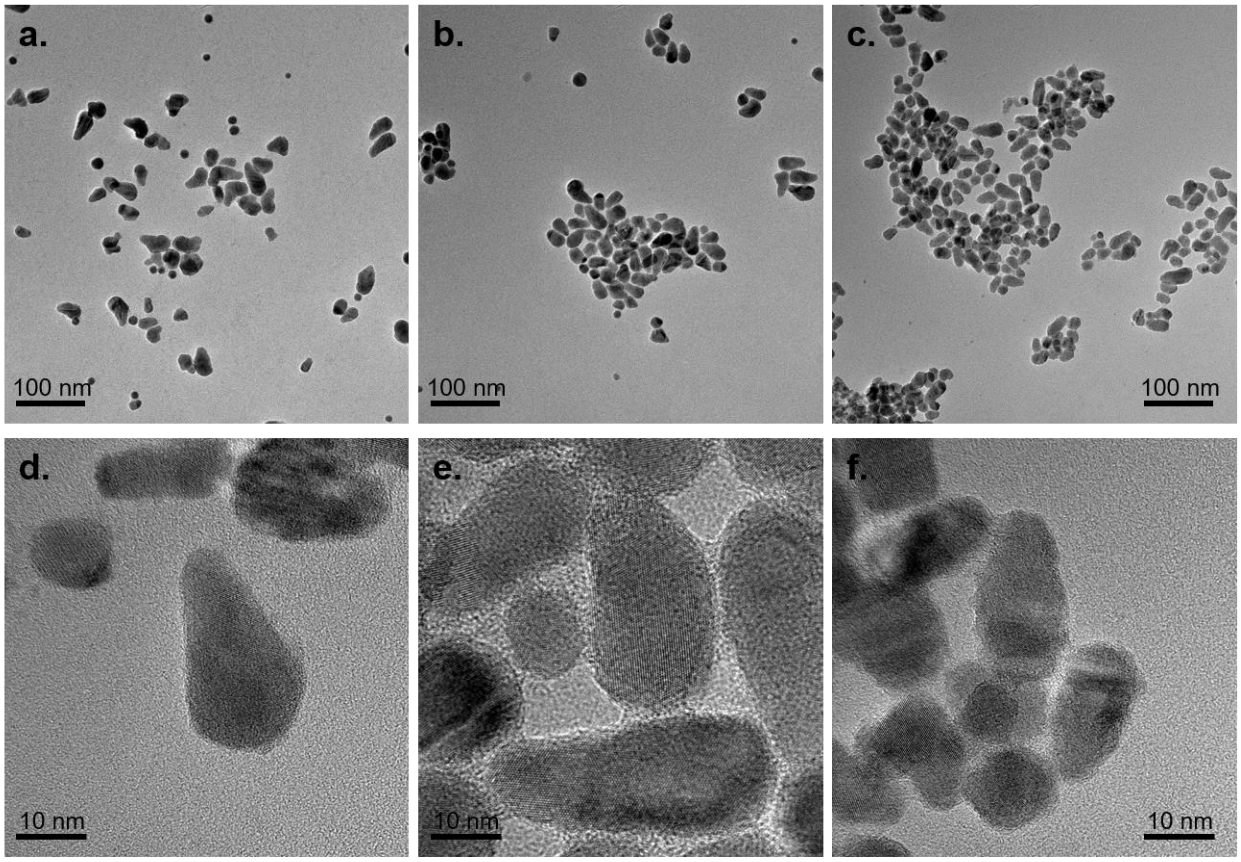

Figure F.9. TEM images of $AgFeS_2$ NCs with different S precursor concentration; **a.-c.** TEM images for 1:2, 1:3, and 1:9 Fe:S precursor ratio respectively, **d.-f.** HRTEM images for 1:2, 1:3, and 1:9 Fe:S precursor ratio respectively.

F.11. Characterization of $AgFeS_2$ NCs synthesized with excess $Fe(acac)_3$

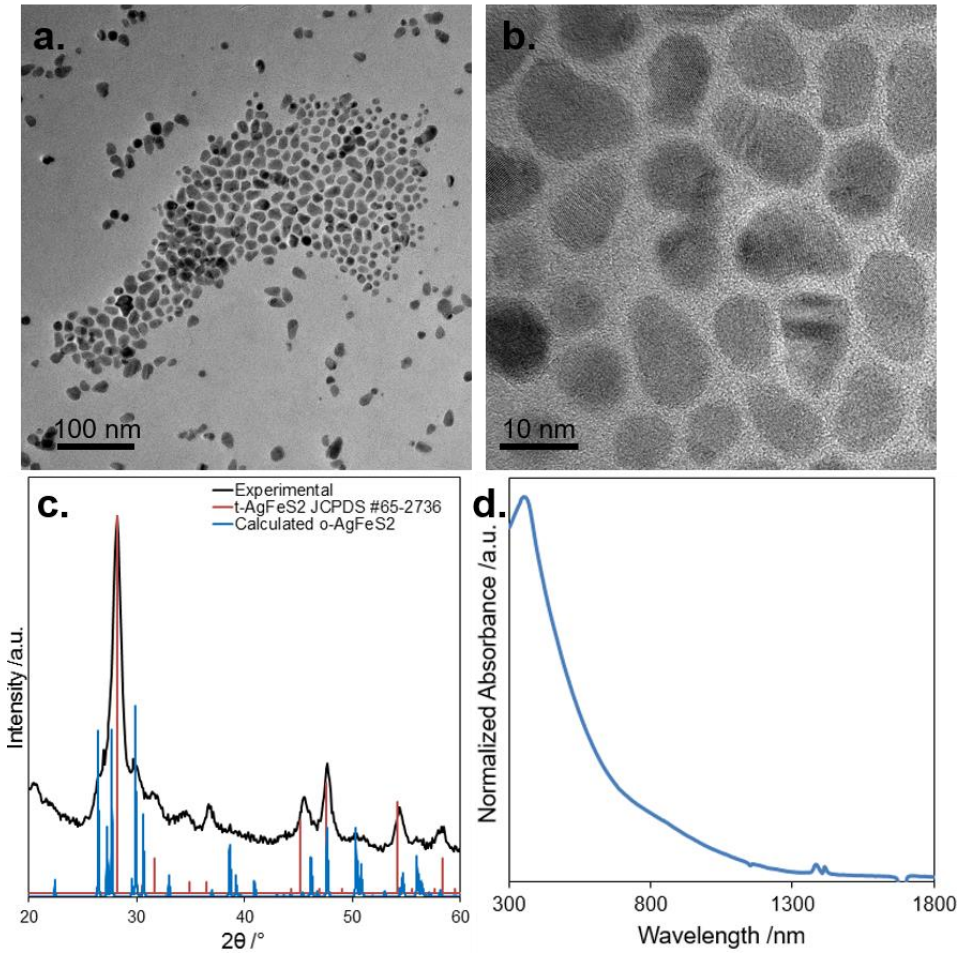

Figure F.10. Characterization of $AgFeS_2$ NCs synthesized with excess $Fe(acac)_3$; **a.-b.** TEM images, **c.** XRD and **d.** UV-Vis absorbance.

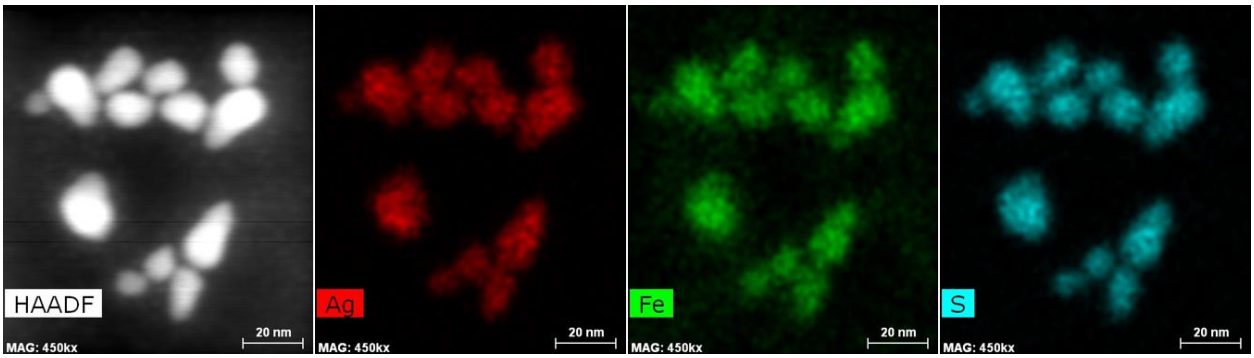

Figure F.11. EDS mapping images for $AgFeS_2$ NCs synthesized with excess $Fe(acac)_3$.

F.12. Characterization of $AgFeS_2$ NCs synthesized with iron(III) stearate at 180°C

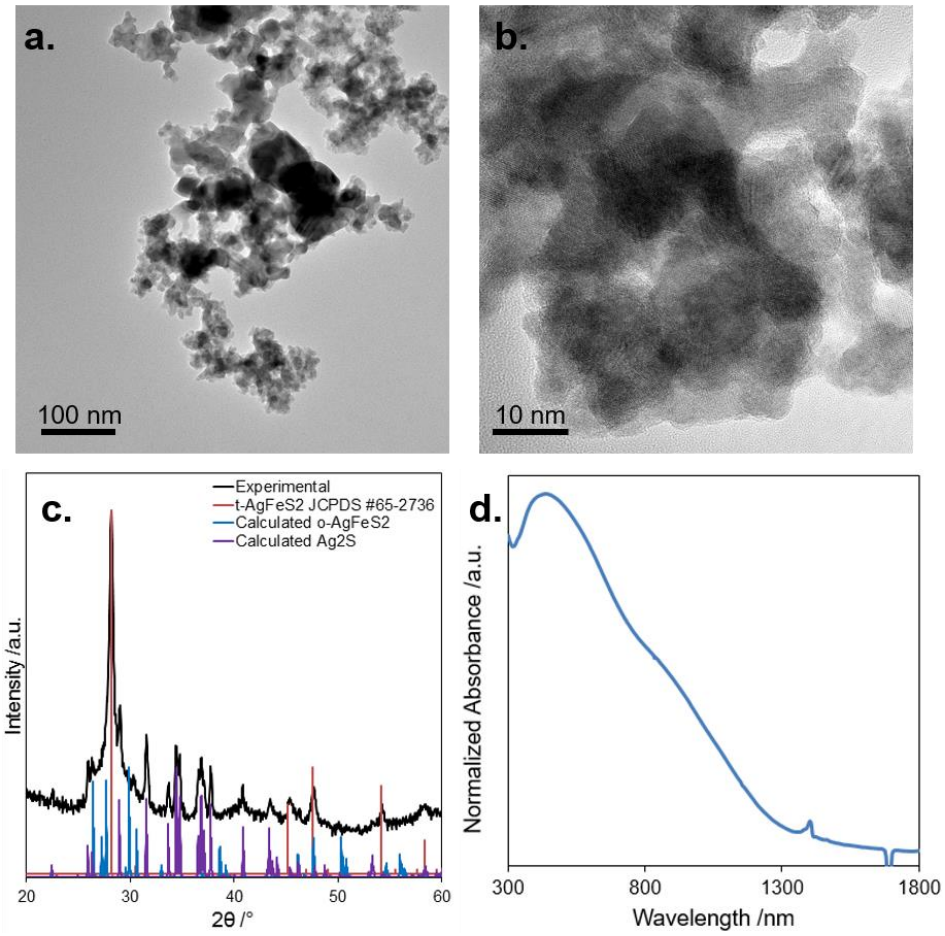

Figure F.12. Characterization of $AgFeS_2$ NCs synthesized with $Fe(stear)_3$ at 180°C; **a.- b.** TEM images, **c.** XRD and **d.** UV-Vis absorbance.

G. Adapted publications

Parts of this dissertation have appeared in previously published manuscripts. Copyright approval has been obtained for any reproduced figures or text as indicated below.

Chapter III

Adapted with permission from Leach, A.D.P. et al., *J. Phys. Chem. Lett.*, **2016**, *7* (3), pp 572–583. Copyright 2016 American Chemical Society.

Chapter IV

Reproduced from Ref. 163 with permission from the Royal Society of Chemistry.

Chapter V

Adapted with permission from Leach, A.D.P. et al., *J. Phys. Chem. C*, **2016**, *120* (9), pp 5207–5212. Copyright 2016 American Chemical Society.

Chapter VI

Adapted with permission from Hernández-Pagán, E.A. et al., *Chem. Mater.*, **2015**, *27* (23), pp 7969–7976. Copyright 2015 American Chemical Society.

Chapter VIII

Paper entitled ‘An Investigation of the Flexible Structure and Composition of $AgFeS_2$ Nanostructures’ is currently in preparation.

REFERENCES

(1) State of the Future. *The Millenium Project* http://www.millennium-project.org/millennium/challeng.html (accessed Jan. 31, 2017).

(2) Grand Challenges for Engineering. *National Academy of Engineering* http://www.engineeringchallenges.org/File.aspx?id=11574&v=ba24e2ed (accessed Jan. 31, 2017).

(3) The Future of Materials Science and Materials Engineering Education. *National Science Foundation* https://www.nsf.gov/mps/dmr/mse_081709.pdf (accessed Jan. 31, 2017).

(4) Ekimov, A. I.; Onushchenko, A. A. Quantum Size Effect in Three-Dimensional Microscopic Semiconductor Crystals *Letters to the Journal of Experimental and Theoretical Physics* **1981**, *34*, 345-349.

(5) Brus, L. E. A Simple Model for the Ionization-Potential, Electron-Affinity, and Aqueous Redox Potentials of Small Semiconductor Crystallites *Journal of Chemical Physics* **1983**, *79*, 5566-5571.

(6) Brus, L. E. Electron-Electron and Electron-Hole Interactions in Small Semiconductor Crystallites - the Size Dependence of the Lowest Excited Electronic State *Journal of Chemical Physics* **1984**, *80*, 4403-4409.

(7) Reed, M. A.; Bate, R. T.; Bradshaw, K.; Duncan, W. M.; Frensley, W. R.; Lee, J. W.; Shih, H. D. Spatial Quantization in GaAs-AlGaAs Multiple Quantum Dots *Journal of Vacuum Science & Technology B* **1986**, *4*, 358-360.

(8) Reed, M. A.; Randall, J. N.; Aggarwal, R. J.; Matyi, R. J.; Moore, T. M.; Wetsel, A. E. Observation of Discrete Electronic States in a Zero-Dimensional Semiconductor Nanostructure *Physical Review Letters* **1988**, *60*, 535-537.

(9) Moore, G. E. Cramming More Components onto Integrated Circuits (Reprinted from Electronics, pg 114-117, April 19, 1965) *Proceedings of the IEEE* **1998**, *86*, 82-85.

(10) Sharma, N.; Ojha, H.; Bharadwaj, A.; Pathak, D. P.; Sharma, R. K. Preparation and Catalytic Applications of Nanomaterials: A Review *RSC Advances* **2015**, *5*, 53381-53403.

(11) Clunan, A.; Rodine-Hardy, K. Nanotechnology in a Globalized World: Strategic Assessments of an Emerging Technology **2014**, 1-92.

(12) Nanomaterials. *National Institue of Environmental Health Sciences* https://www.niehs.nih.gov/health/topics/agents/sya-nano/ (accessed Nov. 20, 2016).

(13) Jariwala, D.; Sangwan, V. K.; Lauhon, L. J.; Marks, T. J.; Hersam, M. C. Carbon Nanomaterials for Electronics, Optoelectronics, Photovoltaics, and Sensing *Chemical Society Reviews* **2013**, *42*, 2824-2860.

(14) Prasanthi, P.; Rao, G. S.; Gowd, B. U. Mechanical Performance of Buckminster Fullerene-Reinforced Composite with Interface Defects Using Finite Element Method through Homogenization Techniques *Composite Interfaces* **2015**, *22*, 299-314.

(15) Partha, R.; Conyers, J. L. Biomedical Applications of Functionalized Fullerene-Based Nanomaterials *International Journal of Nanomedicine* **2009**, *4*, 261-275.

(16) Dennler, G.; Scharber, M. C.; Brabec, C. J. Polymer-Fullerene Bulk-Heterojunction Solar Cells *Advanced Materials* **2009**, *21*, 1323-1338.

(17) De Volder, M. F. L.; Tawfick, S. H.; Baughman, R. H.; Hart, A. J. Carbon Nanotubes: Present and Future Commercial Applications *Science* **2013**, *339*, 535.

(18) The Nobel Prize in Physics 2010. *Nobel Media AB* http://www.nobelprize.org/nobel_prizes/physics/laureates/2010/ (accessed Nov. 20, 2016).

(19) Graphene and Human Brain Project Win Largest Research Excellence Award in History, as Battle for Sustained Science Funding Continues. *European Commission* http://europa.eu/rapid/press-release_IP-13-54_en.htm (accessed Nov. 20, 2016).

(20) Geim, A. K. Graphene: Status and Prospects *Science* **2009**, *324*, 1530-1534.

(21) Gimenez-Lopez, M. D.; Chuvilin, A.; Kaiser, U.; Khlobystov, A. N. Functionalised Endohedral Fullerenes in Single-Walled Carbon Nanotubes *Chemical Communications* **2011**, *47*, 2116-2118.

(22) Smith, D. K.; Lee, D. C.; Korgel, B. A. High Yield Multiwall Carbon Nanotube Synthesis in Supercritical Fluids *Chemistry of Materials* **2006**, *18*, 3356-3364.

(23) Huang, P. Y.; Ruiz-Vargas, C. S.; van der Zande, A. M.; Whitney, W. S.; Levendorf, M. P.; Kevek, J. W.; Garg, S.; Alden, J. S.; Hustedt, C. J.; Zhu, Y.; et al. Grains and Grain Boundaries in Single-Layer Graphene Atomic Patchwork Quilts *Nature* **2011**, *469*, 389.

(24) Dreaden, E. C.; Alkilany, A. M.; Huang, X. H.; Murphy, C. J.; El-Sayed, M. A. The Golden Age: Gold Nanoparticles for Biomedicine *Chemical Society Reviews* **2012**, *41*, 2740-2779.

(25) Zrazhevskiy, P.; Sena, M.; Gao, X. H. Designing Multifunctional Quantum Dots for Bioimaging, Detection, and Drug Delivery *Chemical Society Reviews* **2010**, *39*, 4326-4354.

(26) Xia, Y. N.; Xiong, Y. J.; Lim, B.; Skrabalak, S. E. Shape-Controlled Synthesis of Metal Nanocrystals: Simple Chemistry Meets Complex Physics? *Angewandte Chemie-International Edition* **2009**, *48*, 60-103.

(27) Colomban, P. The Use of Metal Nanoparticles to Produce Yellow, Red and Iridescent Colour, from Bronze Age to Present Times in Lustre Pottery and Glass: Solid State Chemistry, Spectroscopy and Nanostructure *Journal of Nano Research* **2009**, *8*, 109-132.

(28) Pines, D.; Bohm, D. A Collective Description of Electron Interactions: II. Collective vs. Individual Particle Aspects of the Interactions *Physical Review* **1952**, *85*, 338-353.

(29) Daniel, M. C.; Astruc, D. Gold Nanoparticles: Assembly, Supramolecular Chemistry, Quantum-Size-Related Properties, and Applications Toward Biology, Catalysis, and Nanotechnology *Chemical Reviews* **2004**, *104*, 293-346.

(30) Jain, P. K.; Huang, X. H.; El-Sayed, I. H.; El-Sayed, M. A. Noble Metals on the Nanoscale: Optical and Photothermal Properties and Some Applications in Imaging, Sensing, Biology, and Medicine *Accounts of Chemical Research* **2008**, *41*, 1578-1586.

(31) Novotna, Z.; Reznickova, A.; Viererblova, L.; Kolafa, J.; Kolska, Z.; Riha, J.; Svorcik, V. Physicochemical Properties of Gold Nanostructures Deposited on Glass *Journal of Nanomaterials* **2014**, *2014*, 8.

(32) Rai, M.; Yadav, A.; Gade, A. Silver Nanoparticles as a New Generation of Antimicrobials *Biotechnology Advances* **2009**, *27*, 76-83.

(33) Dong, X. Y.; Gao, Z. W.; Yang, K. F.; Zhang, W. Q.; Xu, L. W. Nanosilver as a New Generation of Silver Catalysts in Organic Transformations for Efficient Synthesis of Fine Chemicals *Catalysis Science & Technology* **2015**, *5*, 2554-2574.

(34) Thompson, D. T. Using Gold Nanoparticles for Catalysis *Nano Today* **2007**, *2*, 40-43.

(35) Chen, J. Y.; Lim, B.; Lee, E. P.; Xia, Y. N. Shape-Controlled Synthesis of Platinum Nanocrystals for Catalytic and Electrocatalytic Applications *Nano Today* **2009**, *4*, 81-95.

(36) Thompson, S. E.; Parthasarathy, S. Moore's Law: the Future of Si Microelectronics *Materials Today* **2006**, *9*, 20-25.

(37) Wu, C. Z.; Xie, Y. Controlling Phase and Morphology of Inorganic Nanostructures Originated from the Internal Crystal Structure *Chemical Communications* **2009**, 5943-5957.

(38) Suresh, S. Semiconductor Nanomaterials, Methods and Applications: A Review *Nanoscience and Nanotechnology* **2013**, *3*, 62-74.

(39) Chiu, C. H.; Huang, Z.; Poh, C. T. Formation of Nanostructures by the Activated Stranski-Krastanow Transition Method *Physical Review Letters* **2004**, *93*, 136105.

(40) Tassev, V. L.; Bliss, D. F. Stranski, Krastanov, and Kaischew, and their Influence on the Founding of Crystal Growth Theory *Journal of Crystal Growth* **2008**, *310*, 4209-4216.

(41) Stranski, I. N.; Krastanov, L. Zur Theorie der orientierten Ausscheidung von Ionenkristallen aufeinander *Abhandlungen der Mathematisch-Naturwissenschaftlichen Klasse IIb. Akademie der Wissenschaften Wien* **1939**, *146*, 797-810.

(42) Yin, Y.; Alivisatos, A. P. Colloidal Nanocrystal Synthesis and the Organic-Inorganic Interface *Nature* **2005**, *437*, 664-670.

(43) Bowers, M. J.; McBride, J. R.; Rosenthal, S. J. White-Light Emission from Magic-Sized Cadmium Selenide Nanocrystals *Journal of the American Chemical Society* **2005**, *127*, 15378-15379.

(44) Boles, M. A.; Engel, M.; Talapin, D. V. Self-Assembly of Colloidal Nanocrystals: From Intricate Structures to Functional Materials *Chemical Reviews* **2016**, *116*, 11220-11289.

(45) Shevchenko, E. V.; Ringler, M.; Schwemer, A.; Talapin, D. V.; Klar, T. A.; Rogach, A. L.; Feldmann, J.; Alivisatos, A. P. Self-Assembled Binary Superlattices of CdSe and Au Nanocrystals and Their Fluorescence Properties *Journal of the American Chemical Society* **2008**, *130*, 3274-3275.

(46) Whitham, K.; Yang, J.; Savitzky, B. H.; Kourkoutis, L. F.; Wise, F.; Hanrath, T. Charge Transport and Localization in Atomically Coherent Quantum Dot Solids *Nature Materials* **2016**, *15*, 557-563.

(47) Sun, S. H.; Murray, C. B.; Weller, D.; Folks, L.; Moser, A. Monodisperse FePt Nanoparticles and Ferromagnetic FePt Nanocrystal Superlattices *Science* **2000**, *287*, 1989-1992.

(48) Shirasaki, Y.; Supran, G. J.; Bawendi, M. G.; Bulovic, V. Emergence of Colloidal Quantum-Dot Light-Emitting Technologies *Nature Photonics* **2013**, *7*, 13-23.

(49) Medintz, I. L.; Uyeda, H. T.; Goldman, E. R.; Mattoussi, H. Quantum Dot Bioconjugates for Imaging, Labelling and Sensing *Nature Materials* **2005**, *4*, 435-446.

(50) Kim, T.-H.; Cho, K.-S.; Lee, E. K.; Lee, S. J.; Chae, J.; Kim, J. W.; Kim, D. H.; Kwon, J.-Y.; Amaratunga, G.; Lee, S. Y.; et al. Full-Colour Quantum Dot Displays Fabricated by Transfer Printing *Nature Photonics* **2011**, *5*, 176-182.

(51) Lan, X.; Voznyy, O.; García de Arquer, F. P.; Liu, M.; Xu, J.; Proppe, A. H.; Walters, G.; Fan, F.; Tan, H.; Liu, M.; et al. 10.6% Certified Colloidal Quantum Dot Solar Cells via Solvent-Polarity-Engineered Halide Passivation *Nano Letters* **2016**, *16*, 4630-4634.

(52) Grim, J. Q.; Christodoulou, S.; Di Stasio, F.; Krahne, R.; Cingolani, R.; Manna, L.; Moreels, I. Continuous-Wave Biexciton Lasing at Room Temperature Using Solution-Processed Quantum Wells *Nature Nanotechnology* **2014**, *9*, 891-895.

(53) Keuleyan, S. E.; Guyot-Sionnest, P.; Delerue, C.; Allan, G. Mercury Telluride Colloidal Quantum Dots: Electronic Structure, Size-Dependent Spectra, and Photocurrent Detection up to 12 μm *ACS Nano* **2014**, *8*, 8676-8682.

(54) Kalisman, P.; Nakibli, Y.; Amirav, L. Perfect Photon-to-Hydrogen Conversion Efficiency *Nano Letters* **2016**, *16*, 1776-1781.

(55) Klimov, V. I.; Mikhailovsky, A. A.; Xu, S.; Malko, A.; Hollingsworth, J. A.; Leatherdale, C. A.; Eisler, H. J.; Bawendi, M. G. Optical Gain and Stimulated Emission in Nanocrystal Quantum Dots *Science* **2000**, *290*, 314.

(56) Kovalenko, M. V.; Manna, L.; Cabot, A.; Hens, Z.; Talapin, D. V.; Kagan, C. R.; Klimov, V. I.; Rogach, A. L.; Reiss, P.; Milliron, D. J.; et al. Prospects of Nanoscience with Nanocrystals *ACS Nano* **2015**, *9*, 1012-1057.

(57) Lhuillier, E.; Keuleyan, S.; Liu, H.; Guyot-Sionnest, P. Mid-IR Colloidal Nanocrystals *Chemistry of Materials* **2013**, *25*, 1272-1282.

(58) Lartigue, L.; Hugounenq, P.; Alloyeau, D.; Clarke, S. P.; Lévy, M.; Bacri, J.-C.; Bazzi, R.; Brougham, D. F.; Wilhelm, C.; Gazeau, F. Cooperative Organization in Iron Oxide Multi-Core Nanoparticles Potentiates Their Efficiency as Heating Mediators and MRI Contrast Agents *ACS Nano* **2012**, *6*, 10935-10949.

(59) Faraday, M. The Bakerian Lecture: Experimental Relations of Gold (and Other Metals) to Light *Philosophical Transactions Royal Society of London* **1857**, *147*, 145-181.

(60) Boles, M. A.; Ling, D.; Hyeon, T.; Talapin, D. V. The Surface Science of Nanocrystals *Nature Materials* **2016**, *15*, 141-153.

(61) Donega, C. D.; Liljeroth, P.; Vanmaekelbergh, D. Physicochemical Evaluation of the Hot-Injection Method, a Synthesis Route for Monodisperse Nanocrystals *Small* **2005**, *1*, 1152-1162.

(62) van Embden, J.; Chesman, A. S. R.; Jasieniak, J. J. The Heat-Up Synthesis of Colloidal Nanocrystals *Chemistry of Materials* **2015**, *27*, 2246-2285.

(63) Son, D. H.; Hughes, S. M.; Yin, Y. D.; Alivisatos, A. P. Cation Exchange Reactions in Ionic Nanocrystals *Science* **2004**, *306*, 1009-1012.

(64) Nag, A.; Kundu, J.; Hazarika, A. Seeded-Growth, Nanocrystal-Fusion, Ion-Exchange and Inorganic-Ligand Mediated Formation of Semiconductor-Based Colloidal Heterostructured Nanocrystals *CrystEngComm* **2014**, *16*, 9391-9407.

(65) Hodges, J. M.; Morse, J. R.; Fenton, J. L.; Ackerman, J. D.; Alameda, L. T.; Schaak, R. E. Insights into the Seeded-Growth Synthesis of Colloidal Hybrid Nanoparticles *Chemistry of Materials* **2016**, *29*, 106–119.

(66) Carbone, L.; Nobile, C.; De Giorgi, M.; Sala, F. D.; Morello, G.; Pompa, P.; Hytch, M.; Snoeck, E.; Fiore, A.; Franchini, I. R.; et al. Synthesis and Micrometer-Scale Assembly of Colloidal CdSe/CdS Nanorods Prepared by a Seeded Growth Approach *Nano Letters* **2007**, *7*, 2942-2950.

(67) Wang, W.; Banerjee, S.; Jia, S. G.; Steigerwald, M. L.; Herman, I. P. Ligand Control of Growth, Morphology, and Capping Structure of Colloidal CdSe Nanorods *Chemistry of Materials* **2007**, *19*, 2573-2580.

(68) Bouet, C.; Tessier, M. D.; Ithurria, S.; Mahler, B.; Nadal, B.; Dubertret, B. Flat Colloidal Semiconductor Nanoplatelets *Chemistry of Materials* **2013**, *25*, 1262-1271.

(69) Sear, R. P. Quantitative Studies of Crystal Nucleation at Constant Supersaturation: Experimental Data and Models *CrystEngComm* **2014**, *16*, 6506-6522.

(70) Pound, G. M.; Mer, V. K. L. Kinetics of Crystalline Nucleus Formation in Supercooled Liquid Tin *Journal of the American Chemical Society* **1952**, *74*, 2323-2332.

(71) Vengrenovich, R. D.; Gudyma, Y. V.; Yarema, S. V. Ostwald Ripening of Quantum-Dot Nanostructures *Semiconductors* **2001**, *35*, 1378-1382.

(72) Handelman, A.; Beker, P.; Amdursky, N.; Rosenman, G. Physics and Engineering of Peptide Supramolecular Nanostructures *Physical Chemistry Chemical Physics* **2012**, *14*, 6391-6408.

(73) Kutzelnigg, W. Friedrich Hund and Chemistry *Angewandte Chemie-International Edition in English* **1996**, *35*, 573-586.

(74) Mulliken, R. S. Spectroscopy Molecular Orbitals and Chemical Bonding *Science* **1967**, *157*, 13.

(75) Dick, R. Dimensional Effects on Densities of States and Interactions in Nanostructures *Nanoscale Research Letters* **2010**, *5*, 1546-1554.

(76) Rosson, T. E.; Claiborne, S. M.; McBride, J. R.; Stratton, B. S.; Rosenthal, S. J. Bright White Light Emission from Ultrasmall Cadmium Selenide Nanocrystals *Journal of the American Chemical Society* **2012**, *134*, 8006-8009.

(77) Issa, B.; Obaidat, I. M.; Albiss, B. A.; Haik, Y. Magnetic Nanoparticles: Surface Effects and Properties Related to Biomedicine Applications *International Journal of Molecular Sciences* **2013**, *14*, 21266-21305.

(78) Sperling, R. A.; Parak, W. J. Surface Modification, Functionalization and Bioconjugation of Colloidal Inorganic Nanoparticles *Philosophical Transactions of the Royal Society A-Mathematical Physical and Engineering Sciences* **2010**, *368*, 1333-1383.

(79) Chaudhuri, R. G.; Paria, S. Core/Shell Nanoparticles: Classes, Properties, Synthesis Mechanisms, Characterization, and Applications *Chemical Reviews* **2012**, *112*, 2373-2433.

(80) Burrows, N. D.; Vartanian, A. M.; Abadeer, N. S.; Grzincic, E. M.; Jacob, L. M.; Lin, W. N.; Li, J.; Dennison, J. M.; Hinman, J. G.; Murphy, C. J. Anisotropic Nanoparticles and Anisotropic Surface Chemistry *Journal of Physical Chemistry Letters* **2016**, *7*, 632-641.

(81) Sajanlal, P. R.; Sreeprasad, T. S.; Samal, A. K.; Pradeep, T. Anisotropic Nanomaterials: Structure, Growth, Assembly, and Functions *Nano Reviews* **2011**, *2*, 1-62.

(82) Mangel, S.; Houben, L.; Bar-Sadan, M. Revealing Growth Schemes of Nanoparticles in Atomic Resolution: Mapping Stacking Fault Formation and Distribution *Crystal Growth & Design* **2015**, *15*, 3114-3118.

(83) Chen, C. C.; Zhu, C.; White, E. R.; Chiu, C. Y.; Scott, M. C.; Regan, B. C.; Marks, L. D.; Huang, Y.; Miao, J. W. Three-Dimensional Imaging of Dislocations in a Nanoparticle at Atomic Resolution *Nature* **2013**, *496*, 74.

(84) Leite, E. R.; Giraldi, T. R.; Pontes, F. M.; Longo, E.; Beltran, A.; Andres, J. Crystal Growth in Colloidal Tin Oxide Nanocrystals Induced by Coalescence at Room Temperature *Applied Physics Letters* **2003**, *83*, 1566-1568.

(85) Leach, A. D. P.; Shen, X.; Faust, A.; Cleveland, M. C.; La Croix, A. D.; Banin, U.; Pantelides, S. T.; Macdonald, J. E. Defect Luminescence from Wurtzite $CuInS_2$ Nanocrystals: Combined Experimental and Theoretical Analysis *The Journal of Physical Chemistry C* **2016**, *120*, 5207-5212.

(86) Rodriguez, J. A.; Vasquez-Agustin, M. A.; Morales-Sanchez, A.; Aceves-Mijares, A. Emission Mechanisms of Si Nanocrystals and Defects in SiO_2 Materials *Journal of Nanomaterials* **2014**, *2014*, 1-17.

(87) Djurisic, A. B.; Leung, Y. H.; Tam, K. H.; Hsu, Y. F.; Ding, L.; Ge, W. K.; Zhong, Y. C.; Wong, K. S.; Chan, W. K.; Tam, H. L.; et al. Defect Emissions in ZnO Nanostructures *Nanotechnology* **2007**, *18*, 1-8.

(88) Allred, A. L. Electronegativity Values from Thermochemical Data *Journal of Inorganic and Nuclear Chemistry* **1961**, *17*, 215-221.

(89) Reiss, P.; Protiere, M.; Li, L. Core/Shell Semiconductor Nanocrystals *Small* **2009**, *5*, 154-168.

(90) Zhong, X. H.; Xie, R. G.; Zhang, Y.; Basche, T.; Knoll, W. High-Quality Violet- to Red-Emitting ZnSe/CdSe Core/Shell Nanocrystals *Chemistry of Materials* **2005**, *17*, 4038-4042.

(91) Battaglia, D.; Li, J. J.; Wang, Y. J.; Peng, X. G. Colloidal Two-Dimensional Systems: CdSe Quantum Shells and Wells *Angewandte Chemie-International Edition* **2003**, *42*, 5035-5039.

(92) Mews, A.; Eychmuller, A.; Giersig, M.; Schooss, D.; Weller, H. Preparation, Characterization, and Photophysics of the Quantum-Dot Quantum-Well System CdS/HgS/CdS *Journal of Physical Chemistry* **1994**, *98*, 934-941.

(93) Jia, Y. Y.; Chen, J. Q.; Wu, K. F.; Kaledin, A.; Musaev, D. G.; Xie, Z. X.; Lian, T. Q. Enhancing Photo-Reduction Quantum Efficiency Using Quasi-Type II Core/Shell Quantum Dots *Chemical Science* **2016**, *7*, 4125-4133.

(94) Chen, X. B.; Lou, Y. B.; Samia, A. C.; Burda, C. Coherency Strain Effects on the Optical Response of Core/Shell Heteronanostructures *Nano Letters* **2003**, *3*, 799-803.

(95) Povolotskaya, A. V.; Povolotskiy, A. V.; Manshina, A. A. Hybrid Nanostructures: Synthesis, Morphology and Functional Properties *Russian Chemical Reviews* **2015**, *84*, 579-600.

(96) Chomoucka, J.; Drbohlavova, J.; Huska, D.; Adam, V.; Kizek, R.; Hubalek, J. Magnetic Nanoparticles and Targeted Drug Delivering *Pharmacological Research* **2010**, *62*, 144-149.

(97) Guo, M. A.; Que, C. L.; Wang, C. H.; Liu, X. Z.; Yan, H. S.; Liu, K. L. Multifunctional Superparamagnetic Nanocarriers with Folate-Mediated and pH-Responsive Targeting Properties for Anticancer Drug Delivery *Biomaterials* **2011**, *32*, 185-194.

(98) Kang, H.; Yim, J.; Jeong, S.; Yang, J. K.; Kyeong, S.; Jeon, S. J.; Kim, J.; Eom, K. D.; Lee, H.; Kim, H. I.; et al. Polymer-Mediated Formation and Assembly of Silver Nanoparticles on Silica Nanospheres for Sensitive Surface-Enhanced Raman Scattering Detection *ACS Applied Materials & Interfaces* **2013**, *5*, 12804-12810.

(99) Kim, K. H.; Baek, Y. K.; Jeon, H. J.; Srinivasarao, M.; Jung, H. T. Cylindrical Posts of Ag/SiO_2/Au Multi-Segment Layer Patterns for Highly Efficient Surface Enhanced Raman Scattering *Nanotechnology* **2012**, *23*, 1-7.

(100) Wu, H. Y.; Cunningham, B. T. Plasmonic Coupling of SiO_2-Ag "Post-Cap" Nanostructures and Silver Film for Surface Enhanced Raman Scattering *Applied Physics Letters* **2011**, *98*, 153103.

(101) Banin, U.; Ben-Shahar, Y.; Vinokurov, K. Hybrid Semiconductor-Metal Nanoparticles: From Architecture to Function *Chemistry of Materials* **2014**, *26*, 97-110.

(102) Cozzoli, P. D.; Pellegrino, T.; Manna, L. Synthesis, Properties and Perspectives of Hybrid Nanocrystal Structures *Chemical Society Reviews* **2006**, *35*, 1195-1208.

(103) Li, J. J.; Wang, Y. A.; Guo, W. Z.; Keay, J. C.; Mishima, T. D.; Johnson, M. B.; Peng, X. G. Large-Scale Synthesis of Nearly Monodisperse CdSe/CdS Core/Shell Nanocrystals Using Air-Stable Reagents via Successive Ion Layer Adsorption and Reaction *Journal of the American Chemical Society* **2003**, *125*, 12567-12575.

(104) Lee, W. R.; Kim, M. G.; Choi, J. R.; Park, J. I.; Ko, S. J.; Oh, S. J.; Cheon, J. Redox-Transmetalation Process as a Generalized Synthetic Strategy for Core-Shell Magnetic Nanoparticles *Journal of the American Chemical Society* **2005**, *127*, 16090-16097.

(105) Park, J. I.; Cheon, J. Synthesis of "Solid Solution" and "Core-Shell" Type Cobalt-Platinum Magnetic Nanoparticles via Transmetalation Reactions *Journal of the American Chemical Society* **2001**, *123*, 5743-5746.

(106) Hernandez-Pagan, E. A.; Leach, A. D. P.; Rhodes, J. M.; Macdonald, J. E. A Synthetic Exploration of Metal-Semiconductor Hybrid Particles of $CuInS_2$ *Chemistry of Materials* **2015**, *27*, 7969–7976.

(107) Kim, H.; Achermann, M.; Balet, L. P.; Hollingsworth, J. A.; Klimov, V. I. Synthesis and Characterization of Co/CdSe Core/Shell Nanocomposites: Bifunctional Magnetic-Optical Nanocrystals *Journal of the American Chemical Society* **2005**, *127*, 544-546.

(108) Pastoriza-Santos, I.; Perez-Juste, J.; Liz-Marzan, L. M. Silica-Coating and Hydrophobation of CTAB-Stabilized Gold Nanorods *Chemistry of Materials* **2006**, *18*, 2465-2467.

(109) Tom, R. T.; Nair, A. S.; Singh, N.; Aslam, M.; Nagendra, C. L.; Philip, R.; Vijayamohanan, K.; Pradeep, T. Freely Dispersible Au@TiO_2, Au@ZrO_2, Ag@TiO_2, and Ag@ZrO_2 Core-Shell Nanoparticles: One-Step Synthesis, Characterization, Spectroscopy, and Optical Limiting Properties *Langmuir* **2003**, *19*, 3439-3445.

(110) Hirakawa, T.; Kamat, P. V. Charge Separation and Catalytic Activity of Ag@TiO_2 Core-Shell Composite Clusters Under UV-Irradiation *Journal of the American Chemical Society* **2005**, *127*, 3928-3934.

(111) Liz-Marzán, L. M.; Mulvaney, P. The Assembly of Coated Nanocrystals *The Journal of Physical Chemistry B* **2003**, *107*, 7312-7326.

(112) Wood, A.; Giersig, M.; Mulvaney, P. Fermi Level Equilibration in Quantum Dot-Metal Nanojunctions *Journal of Physical Chemistry B* **2001**, *105*, 8810-8815.

(113) Dawson, A.; Kamat, P. V. Semiconductor-Metal Nanocomposites. Photoinduced Fusion and Photocatalysis of Gold-Capped TiO_2 (TiO_2/Gold) Nanoparticles *Journal of Physical Chemistry B* **2001**, *105*, 960-966.

(114) Subramanian, V.; Wolf, E. E.; Kamat, P. V. Green Emission to Probe Photoinduced Charging Events in ZnO-Au Nanoparticles. Charge Distribution and Fermi-Level Equilibration *Journal of Physical Chemistry B* **2003**, *107*, 7479-7485.

(115) Choi, S. H.; Kim, E. G.; Hyeon, T. One-Pot Synthesis of Copper-Indium Sulfide Nanocrystal Heterostructures with Acorn, Bottle, and Larva Shapes *Journal of the American Chemical Society* **2006**, *128*, 2520-2521.

(116) Carbone, L.; Jakab, A.; Khalavka, Y.; Sonnichsen, C. Light-Controlled One-Sided Growth of Large Plasmonic Gold Domains on Quantum Rods Observed on the Single Particle Level *Nano Letters* **2009**, *9*, 3710-3714.

(117) Mokari, T.; Rothenberg, E.; Popov, I.; Costi, R.; Banin, U. Selective Growth of Metal Tips onto Semiconductor Quantum Rods and Tetrapods *Science* **2004**, *304*, 1787-1790.

(118) Teranishi, T.; Inoue, Y.; Nakaya, M.; Oumi, Y.; Sano, T. Nanoacorns: Anisotropically Phase-Segregated CoPd Sulfide Nanoparticles *Journal of the American Chemical Society* **2004**, *126*, 9914-9915.

(119) Han, S. K.; Gu, C.; Gong, M.; Wang, Z. M.; Yu, S. H. Colloidal Synthesis of Ternary $AgFeS_2$ Nanocrystals and Their Transformation to Ag_2S-Fe_7S_8 Heterodimers *Small* **2013**, *9*, 3765-3769.

(120) Shi, W. L.; Zeng, H.; Sahoo, Y.; Ohulchanskyy, T. Y.; Ding, Y.; Wang, Z. L.; Swihart, M.; Prasad, P. N. A General Approach to Binary and Ternary Hybrid Nanocrystals *Nano Letters* **2006**, *6*, 875-881.

(121) Peng, X. G.; Manna, L.; Yang, W. D.; Wickham, J.; Scher, E.; Kadavanich, A.; Alivisatos, A. P. Shape Control of CdSe Nanocrystals *Nature* **2000**, *404*, 59-61.

(122) Manna, L.; Milliron, D. J.; Meisel, A.; Scher, E. C.; Alivisatos, A. P. Controlled Growth of Tetrapod-Branched Inorganic Nanocrystals *Nature Materials* **2003**, *2*, 382-385.

(123) Caddeo, C.; Cazia, V.; Bagolini, L.; Lusk, M. T.; Mattoni, A. Pinpointing the Cause of Platinum Tipping on CdS Nanorods *Journal of Physical Chemistry C* **2015**, *119*, 22663-22668.

(124) Menagen, G.; Mocatta, D.; Salant, A.; Popov, I.; Dorfs, D.; Banin, U. Selective Gold Growth on CdSe Seeded CdS Nanorods *Chemistry of Materials* **2008**, *20*, 6900-6902.

(125) Liu, H. T.; Alivisatos, A. P. Preparation of Asymmetric Nanostructures Through Site Selective Modification of Tetrapods *Nano Letters* **2004**, *4*, 2397-2401.

(126) Hardman, R. A Toxicologic Review of Quantum Dots: Toxicity Depends on Physicochemical and Environmental Factors *Environmental Health Perspectives* **2006**, *114*, 165-172.

(127) Reiss, P.; Carriere, M.; Lincheneau, C.; Vaure, L.; Tamang, S. Synthesis of Semiconductor Nanocrystals, Focusing on Nontoxic and Earth-Abundant Materials *Chemical Reviews* **2016**, *116*, 10731-10819.

(128) Ueng, H. Y.; Hwang, H. L. The Defect Structure of $CuInS_2$. 1. Intrinsic Defects *Journal of Physics and Chemistry of Solids* **1989**, *50*, 1297-1305.

(129) Yue, W. J.; Han, S. K.; Peng, R. X.; Shen, W.; Geng, H. W.; Wu, F.; Tao, S. W.; Wang, M. T. $CuInS_2$ Quantum Dots Synthesized by a Solvothermal Route and their Application as Effective Electron Acceptors for Hybrid Solar Cells *Journal of Materials Chemistry* **2010**, *20*, 7570-7578.

(130) Nose, K.; Soma, Y.; Omata, T.; Otsuka-Yao-Matsuo, S. Synthesis of Ternary $CuInS_2$ Nanocrystals; Phase Determination by Complex Ligand Species *Chemistry of Materials* **2009**, *21*, 2607-2613.

(131) Xie, R.; Rutherford, M.; Peng, X. Formation of High-Quality I-III-VI Semiconductor Nanocrystals by Tuning Relative Reactivity of Cationic Precursors *Journal of the American Chemical Society* **2009**, *131*, 5691-5697.

(132) Deng, D.; Chen, Y.; Cao, J.; Tian, J.; Qian, Z.; Achilefu, S.; Gu, Y. High-Quality $CuInS_2$/ZnS Quantum Dots for In Vitro and In Vivo Bioimaging *Chemistry of Materials* **2012**, *24*, 3029-3037.

(133) Li, L.; Pandey, A.; Werder, D. J.; Khanal, B. P.; Pietryga, J. M.; Klimov, V. I. Efficient Synthesis of Highly Luminescent Copper Indium Sulfide-Based Core/Shell Nanocrystals with Surprisingly Long-Lived Emission *Journal of the American Chemical Society* **2011**, *133*, 1176-1179.

(134) Zhong, H.; Bai, Z.; Zou, B. Tuning the Luminescence Properties of Colloidal I-III-VI Semiconductor Nanocrystals for Optoelectronics and Biotechnology Applications *Journal of Physical Chemistry Letters* **2012**, *3*, 3167-3175.

(135) Nakajima, M.; Usami, M.; Nakazawa, K.; Arishima, K.; Yamamoto, M. Developmental Toxicity of Indium: Embryotoxicity and Teratogenicity in Experimental Animals *Congenital Anomalies* **2008**, *48*, 145-150.

(136) EPA National Primary Drinking Water Regulations. *United States Environmental Protection Agency* http://water.epa.gov/drink/contaminants/#List (accessed Sept. 30, 2015).

(137) Horne, M. T.; Dunson, W. A. Effects of Low pH, Metals, and Water Hardness on Larval Amphibians *Archives of Environment Contamination and Toxicology* **1995**, *29*, 500-505.

(138) Shannon, R. D. Revised Effective Ionic-Radii and Systematic Studies of Interatomic Distances in Halides and Chalcogenides *Acta Crystallographica Section A* **1976**, *32*, 751-767.

(139) Uehara, M.; Watanabe, K.; Tajiri, Y.; Nakamura, H.; Maeda, H. Synthesis of $CuInS_2$ Fluorescent Nanocrystals and Enhancement of Fluorescence by Controlling Crystal Defect *Journal of Chemical Physics* **2008**, *129*, 134709.

(140) Kolny-Olesiak, J.; Weller, H. Synthesis and Application of Colloidal $CuInS_2$ Semiconductor Nanocrystals *ACS Applied Materials & Interfaces* **2013**, *5*, 12221-12237.

(141) Zhong, H.; Lo, S. S.; Mirkovic, T.; Li, Y.; Ding, Y.; Li, Y.; Scholes, G. D. Noninjection Gram-Scale Synthesis of Monodisperse Pyramidal $CuInS_2$ Nanocrystals and Their Size-Dependent Properties *ACS Nano* **2010**, *4*, 5253-5262.

(142) Zhong, H.; Zhou, Y.; Ye, M.; He, Y.; Ye, J.; He, C.; Yang, C.; Li, Y. Controlled Synthesis and Optical Properties of Colloidal Ternary Chalcogenide $CuInS_2$ Nanocrystals *Chemistry of Materials* **2008**, *20*, 6434-6443.

(143) Nairn, J. J.; Shapiro, P. J.; Twamley, B.; Pounds, T.; von Wandruszka, R.; Fletcher, T. R.; Williams, M.; Wang, C. M.; Norton, M. G. Preparation of Ultrafine Chalcopyrite Nanoparticles via the Photochemical Decomposition of Molecular Single-Source Precursors *Nano Letters* **2006**, *6*, 1218-1223.

(144) Castro, S. L.; Bailey, S. G.; Raffaelle, R. P.; Banger, K. K.; Hepp, A. F. Synthesis and Characterization of Colloidal $CuInS_2$ Nanoparticles from a Molecular Single-Source Precursor *Journal of Physical Chemistry B* **2004**, *108*, 12429-12435.

(145) Castro, S. L.; Bailey, S. G.; Raffaelle, R. P.; Banger, K. K.; Hepp, A. F. Nanocrystalline Chalcopyrite Materials ($CuInS_2$ and $CuInSe_2$) via Low-Temperature Pyrolysis of Molecular Single-Source Precursors *Chemistry of Materials* **2003**, *15*, 3142-3147.

(146) Pan, D.; An, L.; Sun, Z.; Hou, W.; Yang, Y.; Yang, Z.; Lu, Y. Synthesis of Cu-In-S Ternary Nanocrystals with Tunable Structure and Composition *Journal of the American Chemical Society* **2008**, *130*, 5620-5621.

(147) Shay, J. L.; Tell, B. Energy-Band Structure of I-III-VI_2 Semiconductors *Surface Science* **1973**, *37*, 748-762.

(148) Courtel, F. M.; Hammami, A.; Imbeault, R.; Hersant, G.; Paynter, R. W.; Marsan, B.; Morin, M. Synthesis of n-type $CuInS_2$ Particles Using N-Methylimidazole, Characterization and Growth Mechanism *Chemistry of Materials* **2010**, *22*, 3752-3761.

(149) Chen, B.; Zhong, H.; Zhang, W.; Tan, Z. A.; Li, Y.; Yu, C.; Zhai, T.; Bando, Y.; Yang, S.; Zou, B. Highly Emissive and Color-Tunable $CuInS_2$-Based Colloidal Semiconductor Nanocrystals: Off-Stoichiometry Effects and Improved Electroluminescence Performance *Advanced Functional Materials* **2012**, *22*, 2081-2088.

(150) Draguta, S.; McDaniel, H.; Klimov, V. I. Tuning Carrier Mobilities and Polarity of Charge Transport in Films of $CuInSe_xS_{2-x}$ Quantum Dots *Advanced Materials* **2015**, *27*, 1701-1705.

(151) Yoshino, K.; Nomoto, K.; Kinoshita, A.; Ikari, T.; Akaki, Y.; Yoshitake, T. Dependence of Cu/In Ratio of Structural and Electrical Characterization of $CuInS_2$ Crystal *Journal of Materials Science - Materials in Electronics* **2008**, *19*, 301-304.

(152) Chen, B.; Chang, S.; Li, D.; Chen, L.; Wang, Y.; Chen, T.; Zou, B.; Zhong, H.; Rogach, A. L. Template Synthesis of $CuInS_2$ Nanocrystals from In_2S_3 Nanoplates and Their Application as Counter Electrodes in Dye-Sensitized Solar Cells *Chemistry of Materials* **2015**, *27*, 5949-5956.

(153) Jara, D. H.; Yoon, S. J.; Stamplecoskie, K. G.; Kamat, P. V. Size-Dependent Photovoltaic Performance of $CuInS_2$ Quantum Dot-Sensitized Solar Cells *Chemistry of Materials* **2014**, *26*, 7221-7228.

(154) Carbone, L.; Cozzoli, P. D. Colloidal Heterostructured Nanocrystals: Synthesis and Growth Mechanisms *Nano Today* **2010**, *5*, 449-493.

(155) Batabyal, S. K.; Tian, L.; Venkatram, N.; Ji, W.; Vittal, J. J. Phase-Selective Synthesis of $CuInS_2$ Nanocrystals *Journal of Physical Chemistry C* **2009**, *113*, 15037-15042.

(156) Kruszynska, M.; Borchert, H.; Parisi, J.; Kolny-Olesiak, J. Synthesis and Shape Control of $CuInS_2$ Nanoparticles *Journal of the American Chemical Society* **2010**, *132*, 15976-15986.

(157) Huang, W.-C.; Tseng, C.-H.; Chang, S.-H.; Tuan, H.-Y.; Chiang, C.-C.; Lyu, L.-M.; Huang, M. H. Solvothermal Synthesis of Zincblende and Wurtzite $CuInS_2$ Nanocrystals and Their Photovoltaic Application *Langmuir* **2012**, *28*, 8496-8501.

(158) Shen, X.; Hernández-Pagan, E. A.; Zhou, W.; Puzyrev, Y. S.; Idrobo, J.-C.; Macdonald, J. E.; Pennycook, S. J.; Pantelides, S. T. Interlaced Crystals Having a Perfect Bravais Lattice and Complex Chemical Order Revealed by Real-Space Crystallography *Nature Communications* **2014**, *5*, 5431.

(159) Peng, S.; Liang, Y.; Cheng, F.; Liang, J. Size-Controlled Chalcopyrite $CuInS_2$ Nanocrystals: One-Pot Synthesis and Optical Characterization *Science China - Chemistry* **2012**, *55*, 1236-1241.

(160) He, J.-J.; Zhou, W.-H.; Guo, J.; Li, M.; Wu, S.-X. Inorganic Ligand Mediated Synthesis of $CuInS_2$ Nanocrystals with Tunable Properties *CrystEngComm* **2012**, *14*, 3638-3644.

(161) Connor, S. T.; Hsu, C.-M.; Weil, B. D.; Aloni, S.; Cui, Y. Phase Transformation of Biphasic $Cu_2S{-}CuInS_2$ to Monophasic $CuInS_2$ Nanorods *Journal of the American Chemical Society* **2009**, *131*, 4962-4966.

(162) Kuzuya, T.; Hamanaka, Y.; Itoh, K.; Kino, T.; Sumiyama, K.; Fukunaka, Y.; Hirai, S. Phase Control and its Mechanism of $CuInS_2$ Nanoparticles *Journal of Colloid and Interface Science* **2012**, *388*, 137-143.

(163) Bao, N.; Qiu, X.; Wang, Y.-H. A.; Zhou, Z.; Lu, X.; Grimes, C. A.; Gupta, A. Facile Thermolysis Synthesis of $CuInS_2$ Nanocrystals with Tunable Anisotropic Shape and Structure *Chemical Communications* **2011**, *47*, 9441-9443.

(164) Leach, A. D. P.; Mast, L. G.; Hernandez-Pagan, E. A.; Macdonald, J. E. Phase Dependent Visible to Near-Infrared Photoluminescence of $CuInS_2$ Nanocrystals *Journal of Materials Chemistry C* **2015**, *3*, 3258-3265.

(165) Yu, C.; Zhang, L.; Tian, L.; Liu, D.; Chen, F.; Wang, C. Synthesis and Formation Mechanism of $CuInS_2$ Nanocrystals with a Tunable Phase *CrystEngComm* **2014**, *16*, 9596-9602.

(166) Yue, W.; Zhang, G.; Wang, S.; Sun, W.; Lan, M.; Nie, G. Influence of Crystal Phase for $CuInS_2$ on Device Performance of Polymer-$CuInS_2$/Oxide Nanoarrays Solar Cells *Materials Science in Semiconductor Processing* **2014**, *25*, 337-343.

(167) Chang, J.; Waclawik, E. R. Controlled Synthesis of $CuInS_2$, Cu_2SnS_3 and Cu_2ZnSnS_4 Nano-structures: Insight into the Universal Phase-Selectivity Mechanism *CrystEngComm* **2013**, *15*, 5612-5619.

(168) van der Stam, W.; Berends, A. C.; Rabouw, F. T.; Willhammar, T.; Ke, X.; Meeldijk, J. D.; Bals, S.; de Mello Donega, C. Luminescent $CuInS_2$ Quantum Dots by Partial Cation Exchange in $Cu_{2-x}S$ Nanocrystals *Chemistry of Materials* **2015**, *27*, 621-628.

(169) Akkerman, Q. A.; Genovese, A.; George, C.; Prato, M.; Moreels, I.; Casu, A.; Marras, S.; Curcio, A.; Scarpellini, A.; Pellegrino, T.; et al. From Binary Cu_2S to Ternary Cu–In–S and Quaternary Cu–In–Zn–S Nanocrystals with Tunable Composition via Partial Cation Exchange *ACS Nano* **2015**, *9*, 521-531.

(170) Niezgoda, J. S.; Harrison, M. A.; McBride, J. R.; Rosenthal, S. J. Novel Synthesis of Chalcopyrite $Cu_xIn_yS_2$ Quantum Dots with Tunable Localized Surface Plasmon Resonances *Chemistry of Materials* **2012**, *24*, 3294-3297.

(171) Azimi, H.; Kuhri, S.; Stahl, M. S.; Hou, Y.; Guldi, D. M.; Brabec, C. J. Elucidating the Excited-State Properties of $CuInS_2$ Nanocrystals upon Phase Transformation: Quasi-Quantum Dots Versus Bulk Behavior *Advanced Electronic Materials* **2015**, *1*, 1500040.

(172) Zhao, Y.; Burda, C. Development of Plasmonic Semiconductor Nanomaterials with Copper Chalcogenides for a Future with Sustainable Energy Materials *Energy & Environmental Science* **2012**, *5*, 5564-5576.

(173) Luther, J. M.; Jain, P. K.; Ewers, T.; Alivisatos, A. P. Localized Surface Plasmon Resonances Arising from Free Carriers in Doped Quantum Dots *Nature Materials* **2011**, *10*, 361-366.

(174) Niezgoda, J. S.; Yap, E.; Keene, J. D.; McBride, J. R.; Rosenthal, S. J. Plasmonic $Cu_xIn_yS_2$ Quantum Dots Make Better Photovoltaics Than Their Nonplasmonic Counterparts *Nano Letters* **2014**, *14*, 3262-3269.

(175) Chen, B. K.; Zhong, H. Z.; Zou, B. S. I-III-VI Semiconductor Nanocrystals *Progress in Chemistry* **2011**, *23*, 2276-2286.

(176) Nam, D.-E.; Song, W.-S.; Yang, H. Noninjection, One-Pot Synthesis of Cu-Deficient $CuInS_2$/ZnS Core/Shell Quantum Dots and Their Fluorescent Properties *Journal of Colloid and Interface Science* **2011**, *361*, 491-496.

(177) Wang, X.; Liang, Z.; Xu, X.; Wang, N.; Fang, J.; Wang, J.; Xu, G. A High Efficient Photoluminescence Zn-Cu-In-S/ZnS Quantum Dots with Long Lifetime *Journal of Alloys and Compounds* **2015**, *640*, 134-140.

(178) Tran, T. K. C.; Le, Q. P.; Nguyen, Q. L.; Li, L.; Reiss, P. Time-Resolved Photoluminescence Study of $CuInS_2$/ZnS Nanocrystals *Advances in Natural Sciences: Nanoscience and Nanotechnology* **2010**, *1*, 025007.

(179) Omata, T.; Nose, K.; Kurimoto, K.; Kita, M. Electronic Transition Responsible for Size-Dependent Photoluminescence of Colloidal $CuInS_2$ Quantum Dots *Journal of Materials Chemistry C* **2014**, *2*, 6867-6872.

(180) Kraatz, I. T.; Booth, M.; Whitaker, B. J.; Nix, M. G. D.; Critchley, K. Sub-Bandgap Emission and lntraband Defect-Related Excited-State Dynamics in Colloidal $CuInS_2$/ZnS Quantum Dots Revealed by Femtosecond Pump-Dump-Probe Spectroscopy *Journal of Physical Chemistry C* **2014**, *118*, 24102-24109.

(181) Sun, J. H.; Zhu, D. H.; Zhao, J. L.; Ikezawa, M.; Wang, X. Y.; Masumoto, Y. Ultrafast Carrier Dynamics in $CuInS_2$ Quantum Dots *Applied Physics Letters* **2014**, *104*, 023118.

(182) Cadirci, M.; Masala, O.; Pickett, N.; Binks, D. Ultrafast Charge Dynamics in $CuInS_2$ Nanocrystal Quantum Dots *Chemical Physics* **2014**, *438*, 60-65.

(183) De Trizio, L.; Prato, M.; Genovese, A.; Casu, A.; Povia, M.; Simonutti, R.; Alcocer, M. J. P.; D'Andrea, C.; Tassone, F.; Manna, L. Strongly Fluorescent Quaternary Cu-In-Zn-S Nanocrystals Prepared from $Cu_{1-x}InS_2$ Nanocrystals by Partial Cation Exchange *Chemistry of Materials* **2012**, *24*, 2400-2406.

(184) Rice, W. D.; McDaniel, H.; Klimov, V. I.; Crooker, S. A. Magneto-Optical Properties of $CuInS_2$ Nanocrystals *Journal of Physical Chemistry Letters* **2014**, *5*, 4105-4109.

(185) Chen, H.; Wang, C.-Y.; Wang, J.-T.; Hu, X.-P.; Zhou, S.-X. First-Principles Study of Point Defects in Solar Cell Semiconductor $CuInS_2$ *Journal of Applied Physics* **2012**, *112*, 084513.

(186) Krustok, J.; Schon, J. H.; Collan, H.; Yakushev, M.; Madasson, J.; Bucher, E. Origin of the Deep Center Photoluminescence in $CuGaSe_2$ and $CuInS_2$ Crystals *Journal of Applied Physics* **1999**, *86*, 364-369.

(187) Krustok, J.; Schon, J. H.; Collan, H.; Yakushev, M.; Madasson, J.; Bucher, E. Erratum: Origin of the Deep Center Photoluminescence in $CuGaSe_2$ and $CuInS_2$ Crystals *Journal of Applied Physics* **2001**, *89*, 8357-8358.

(188) Omata, T.; Nose, K.; Otsuka-Yao-Matsuo, S. Size Dependent Optical Band Gap of Ternary I-III-VI_2 Semiconductor Nanocrystals *Journal of Applied Physics* **2009**, *105*, 073106.

(189) Qin, L.; Li, D.; Zhang, Z.; Wang, K.; Ding, H.; Xie, R.; Yang, W. The Determination of Extinction Coefficient of $CuInS_2$, and $ZnCuInS_3$ Multinary Nanocrystals *Nanoscale* **2012**, *4*, 6360-6364.

(190) Booth, M.; Brown, A. P.; Evans, S. D.; Critchley, K. Determining the Concentration of $CuInS_2$ Quantum Dots from the Size-Dependent Molar Extinction Coefficient *Chemistry of Materials* **2012**, *24*, 2064-2070.

(191) Shay, J. L.; Kasper, H. M. Direct Observation of Cu d Levels in I-III-VI_2 Compounds *Physical Review Letters* **1972**, *29*, 1162-1164.

(192) Kono, S.; Okusawa, M. X-Ray Photoelectron Study of the Valence Bands in I–III–VI_2 Compounds *Journal of the Physical Society of Japan* **1974**, *37*, 1301-1304.

(193) Zhang, S. B.; Wei, S. H.; Zunger, A.; Katayama-Yoshida, H. Defect Physics of the $CuInSe_2$ Chalcopyrite Semiconductor *Physical Review B* **1998**, *57*, 9642-9656.

(194) Pan, Z.; Mora-Sero, I.; Shen, Q.; Zhang, H.; Li, Y.; Zhao, K.; Wang, J.; Zhong, X.; Bisquert, J. High-Efficiency "Green" Quantum Dot Solar Cells *Journal of the American Chemical Society* **2014**, *136*, 9203-9210.

(195) Park, J.; Kim, S.-W. $CuInS_2$/ZnS Core/Shell Quantum Dots by Cation Exchange and Their Blue-Shifted Photoluminescence *Journal of Materials Chemistry* **2011**, *21*, 3745-3750.

(196) Nam, D.-E.; Song, W.-S.; Yang, H. Facile, Air-Insensitive Solvothermal Synthesis of Emission-Tunable $CuInS_2$/ZnS Quantum Dots with High Quantum Yields *Journal of Materials Chemistry* **2011**, *21*, 18220-18226.

(197) Choi, H. S.; Kim, Y.; Park, J. C.; Oh, M. H.; Jeon, D. Y.; Nam, Y. S. Highly Luminescent, Off-Stoichiometric $Cu_xIn_yS_2$/ZnS Quantum Dots for Near-Infrared Fluorescence Bio-Imaging *RSC Advances* **2015**, *5*, 43449-43455.

(198) Nakamura, H.; Kato, W.; Uehara, M.; Nose, K.; Omata, T.; Otsuka-Yao-Matsuo, S.; Miyazaki, M.; Maeda, H. Tunable Photoluminescence Wavelength of Chalcopyrite $CuInS_2$-Based Semiconductor Nanocrystals Synthesized in a Colloidal System *Chemistry of Materials* **2006**, *18*, 3330-3335.

(199) Zhang, W.; Lou, Q.; Ji, W.; Zhao, J.; Zhong, X. Color-Tunable Highly Bright Photoluminescence of Cadmium-Free Cu-Doped Zn-In-S Nanocrystals and Electroluminescence *Chemistry of Materials* **2014**, *26*, 1204-1212.

(200) May, T. W.; Wiedmeyer, R. H. A Table of Polyatomic Interferences in ICP-MS *Atomic Spectroscopy* **1998**, *19*, 150-155.

(201) Rees, C. E.; Holt, B. D. The Isotopic Analysis of Sulfur and Oxygen In *Stable Isotopes: Natural and Anthropogenic Sulphur in the Environment*; H. R. Krouse and V. A. Grinenko Eds.; John Wiley & Sons: New York, 1991; pp 43-64.

(202) Tsuji, I.; Kato, H.; Kobayashi, H.; Kudo, A. Photocatalytic H_2 Evolution Under Visible-Light Irradiation Over Band-Structure-Controlled $(CuIn)_{(x)}Zn_{2(1-x)}S_2$ Solid Solutions *Journal of Physical Chemistry B* **2005**, *109*, 7323-7329.

(203) Zheng, L.; Xu, Y.; Song, Y.; Wu, C.; Zhang, M.; Xie, Y. Nearly Monodisperse $CuInS_2$ Hierarchical Microarchitectures for Photocatalytic H_2 Evolution Under Visible Light *Inorganic Chemistry* **2009**, *48*, 4003-4009.

(204) Lin, Y.; Zhang, F.; Pan, D.; Li, H.; Lu, Y. Sunlight-Driven Photodegradation of Organic Pollutants Catalyzed by $TiO_2/(ZnS)_{(x)}(CuInS2)_{(1-x)}$ Nanocomposites *Journal of Materials Chemistry* **2012**, *22*, 8759-8763.

(205) Shen, F.; Que, W.; Liao, Y.; Yin, X. Photocatalytic Activity of TiO_2 Nanoparticles Sensitized by $CuInS_2$ Quantum Dots *Industrial & Engineering Chemistry Research* **2011**, *50*, 9131-9137.

(206) Dutta, S. K.; Mehetor, S. K.; Pradhan, N. Metal Semiconductor Heterostructures for Photocatalytic Conversion of Light Energy *Journal of Physical Chemistry Letters* **2015**, *6*, 936-944.

(207) Ye, C.; Regulacio, M. D.; Lim, S. H.; Li, S.; Xu, Q.-H.; Han, M.-Y. Alloyed ZnS-$CuInS_2$ Semiconductor Nanorods and Their Nanoscale Heterostructures for Visible-Light-Driven Photocatalytic Hydrogen Generation *Chemistry - A European Journal* **2015**, *21*, 9514-9519.

(208) Witt, E.; Parisi, J.; Kolny-Olesiak, J. Selective Growth of Gold onto Copper Indium Sulfide Selenide Nanoparticles *Zeitschrift fur Naturforschung A: Journal of Physical Sciences* **2013**, *68*, 398-404.

(209) Park, S. H.; Hong, A.; Kim, J.-H.; Yang, H.; Lee, K.; Jang, H. S. Highly Bright Yellow-Green-Emitting $CuInS_2$ Colloidal Quantum Dots with Core/Shell/Shell Architecture for White Light-Emitting Diodes *ACS Applied Materials & Interfaces* **2015**, *7*, 6764-6771.

(210) Yong, K.-T.; Roy, I.; Hu, R.; Ding, H.; Cai, H.; Zhu, J.; Zhang, X.; Bergey, E. J.; Prasad, P. N. Synthesis of Ternary $CuInS_2$/ZnS Quantum Dot Bioconjugates and Their Applications for Targeted Cancer Bioimaging *Integrative Biology* **2010**, *2*, 121-129.

(211) Liu, Z. P.; Lin, Z. H.; Liu, L. L.; Su, X. G. A Convenient and Label-Free Fluorescence "Turn Off-On" Nanosensor with High Sensitivity and Selectivity for Acid Phosphatase *Analytica Chimica Acta* **2015**, *876*, 83-90.

(212) Kamat, P. V. Quantum Dot Solar Cells. The Next Big Thing in Photovoltaics *Journal of Physical Chemistry Letters* **2013**, *4*, 908-918.

(213) Carey, G. H.; Abdelhady, A. L.; Ning, Z.; Thon, S. M.; Bakr, O. M.; Sargent, E. H. Colloidal Quantum Dot Solar Cells *Chemical Reviews* **2015**, 12732–12763.

(214) Chang, J.-Y.; Su, L.-F.; Li, C.-H.; Chang, C.-C.; Lin, J.-M. Efficient "Green" Quantum Dot-Sensitized Solar Cells Based on Cu_2S-$CuInS_2$-ZnSe Architecture *Chemical Communications* **2012**, *48*, 4848-4850.

(215) Yao, R.-Y.; Zhou, Z.-J.; Hou, Z.-L.; Wang, X.; Zhou, W.-H.; Wu, S.-X. Surfactant-Free $CuInS_2$ Nanocrystals: An Alternative Counter-Electrode Material for Dye-Sensitized Solar Cells *ACS Applied Materials & Interfaces* **2013**, *5*, 3143-3148.

(216) Hodes, G.; Manassen, J.; Cahen, D. Electrocatalytic Electrodes for the Polysulfide Redox System *Journal of the Electrochemical Society* **1980**, *127*, 544-549.

(217) Radich, J. G.; Dwyer, R.; Kamat, P. V. Cu_2S Reduced Graphene Oxide Composite for High-Efficiency Quantum Dot Solar Cells. Overcoming the Redox Limitations of S_2^-/S_n^{2-} at the Counter Electrode *Journal of Physical Chemistry Letters* **2011**, *2*, 2453-2460.

(218) Hu, X. M.; Kang, R. D.; Zhang, Y. Y.; Deng, L. G.; Zhong, H. Z.; Zou, B. S.; Shi, L. J. Ray-Trace Simulation of $CuInS(Se)_{(2)}$ Quantum Dot Based Luminescent Solar Concentrators *Optics Express* **2015**, *23*, A858-A867.

(219) Knowles, K. E.; Kilburn, T. B.; Alzate, D. G.; McDowall, S.; Gamelin, D. R. Bright $CuInS_2$/CdS Nanocrystal Phosphors for High-Gain Full-Spectrum Luminescent Solar Concentrators *Chemical Communications* **2015**, *51*, 9129-9132.

(220) Tan, Z.; Zhang, Y.; Xie, C.; Su, H.; Liu, J.; Zhang, C.; Dellas, N.; Mohney, S. E.; Wang, Y.; Wang, J.; et al. Near-Band-Edge Electroluminescence from Heavy-Metal-Free Colloidal Quantum Dots *Advanced Materials* **2011**, *23*, 3553-3558.

(221) Zhang, Y.; Xie, C.; Su, H.; Liu, J.; Pickering, S.; Wang, Y.; Yu, W. W.; Wang, J.; Wang, Y.; Hahm, J.-I.; et al. Employing Heavy Metal-Free Colloidal Quantum Dots in Solution-Processed White Light-Emitting Diodes *Nano Letters* **2011**, *11*, 329-332.

(222) Song, W.-S.; Yang, H. Efficient White-Light-Emitting Diodes Fabricated from Highly Fluorescent Copper Indium Sulfide Core/Shell Quantum Dots *Chemistry of Materials* **2012**, *24*, 1961-1967.

(223) Chuang, P. H.; Lin, C. C.; Liu, R. S. Emission-Tunable $CuInS_2$/ZnS Quantum Dots: Structure, Optical Properties, and Application in White Light-Emitting Diodes with High Color Rendering Index *ACS Applied Materials & Interfaces* **2014**, *6*, 15379-15387.

(224) Chen, B. K.; Zhong, H. Z.; Wang, M. X.; Liu, R. B.; Zou, B. S. Integration of $CuInS_2$-Based Nanocrystals for High Efficiency and High Colour Rendering White Light-Emitting Diodes *Nanoscale* **2013**, *5*, 3514-3519.

(225) Chen, B. K.; Zhou, Q. C.; Li, J. F.; Zhang, F.; Liu, R. B.; Zhong, H. Z.; Zou, B. S. Red Emissive $CuInS_2$-Based Nanocrystals: A Potential Phosphor for Warm White Light-Emitting Diodes *Optics Express* **2013**, *21*, 10105-10110.

(226) Pons, T.; Pic, E.; Lequeux, N.; Cassette, E.; Bezdetnaya, L.; Guillemin, F.; Marchal, F.; Dubertret, B. Cadmium-Free $CuInS_2$/ZnS Quantum Dots for Sentinel Lymph Node Imaging with Reduced Toxicity *ACS Nano* **2010**, *4*, 2531-2538.

(227) Li, L.; Daou, T. J.; Texier, I.; Tran Thi Kim, C.; Nguyen Quang, L.; Reiss, P. Highly Luminescent $CuInS_2$/ZnS Core/Shell Nanocrystals: Cadmium-Free Quantum Dots for In Vivo Imaging *Chemistry of Materials* **2009**, *21*, 2422-2429.

(228) Liu, Z.; Chen, N.; Dong, C.; Li, W.; Guo, W.; Wang, H.; Wang, S.; Tan, J.; Tu, Y.; Chang, J. Facile Construction of Near Infrared Fluorescence Nanoprobe with Amphiphilic Protein-Polymer Bioconjugate for Targeted Cell Imaging *ACS Applied Materials & Interfaces* **2015**, *7*, 18997-19005.

(229) Kim, Y.; Park, K. Y.; Jang, D. M.; Song, Y. M.; Kim, H. S.; Cho, Y. J.; Myung, Y.; Park, J. Synthesis of Au-Cu_2S Core-Shell Nanocrystals and Their Photocatalytic and Electrocatalytic Activity *Journal of Physical Chemistry C* **2010**, *114*, 22141-22146.

(230) Yu, K.; Ng, P.; Ouyang, J.; Zaman, M. B.; Abulrob, A.; Baral, T. N.; Fatehi, D.; Jakubek, Z. J.; Kingston, D.; Wu, X.; et al. Low-Temperature Approach to Highly Emissive Copper Indium Sulfide Colloidal Nanocrystals and Their Bioimaging Applications *ACS Applied Materials & Interfaces* **2013**, *5*, 2870-2880.

(231) Guo, W.; Chen, N.; Tu, Y.; Dong, C.; Zhang, B.; Hu, C.; Chang, J. Synthesis of Zn-Cu-In-S/ZnS Core/Shell Quantum Dots with Inhibited Blue-Shift Photoluminescence and Applications for Tumor Targeted Bioimaging *Theranostics* **2013**, *3*, 99-108.

(232) Cheng, C.-Y.; Ou, K.-L.; Huang, W.-T.; Chen, J.-K.; Chang, J.-Y.; Yang, C.-H. Gadolinium-Based $CuInS_2$/ZnS Nanoprobe for Dual-Modality Magnetic Resonance/Optical Imaging *ACS Applied Materials & Interfaces* **2013**, *5*, 4389-4400.

(233) Shen, J.; Li, Y.; Zhu, Y.; Yang, X.; Yao, X.; Li, J.; Huang, G.; Li, C. Multifunctional Gadolinium-Labeled Silica-Coated Fe_3O_4 and $CuInS_2$ Nanoparticles as a Platform for In Vivo Tri-Modality Magnetic Resonance and Fluorescence Imaging *Journal of Materials Chemistry B* **2015**, *3*, 2873-2882.

(234) Zhao, C.; Bai, Z.; Liu, X.; Zhang, Y.; Zou, B.; Zhong, H. Small GSH-Capped $CuInS_2$ Quantum Dots: MPA-Assisted Aqueous Phase Transfer and Bioimaging Applications *ACS Applied Materials & Interfaces* **2015**, *7*, 17623-17629.

(235) Wang, M. N.; Chen, Z.; Cao, C. B. Preparation of Magnetic $CuInS_2$-ZnS Nanocomposites for Bioimaging *Materials Letters* **2014**, *120*, 50-53.

(236) Lin, Z.; Ma, Q.; Fei, X.; Zhang, H.; Su, X. A Novel Aptamer Functionalized $CuInS_2$ Quantum Dots Probe for Daunorubicin Sensing and Near Infrared Imaging of Prostate Cancer Cells *Analytica Chimica Acta* **2014**, *818*, 54-60.

(237) Tang, X.; Cheng, W.; Choo, E. S. G.; Xue, J. Synthesis of $CuInS_2$-ZnS Alloyed Nanocubes with High Luminescence *Chemical Communications* **2011**, *47*, 5217-5219.

(238) Bensebaa, F.; Durand, C.; Aouadou, A.; Scoles, L.; Du, X.; Wang, D.; Le Page, Y. A New Green Synthesis Method of $CuInS_2$ and $CuInSe_2$ Nanoparticles and Their Integration into Thin Films *Journal of Nanoparticle Research* **2010**, *12*, 1897-1903.

(239) Liu, S.; Zhang, H.; Qiao, Y.; Su, X. One-Pot Synthesis of Ternary $CuInS_2$ Quantum Dots with Near-Infrared Fluorescence in Aqueous Solution *RSC Advances* **2012**, *2*, 819-825.

(240) Wang, M.; Liu, X.; Cao, C.; Shi, C. Synthesis of Band-Gap Tunable Cu-In-S Ternary Nanocrystals in Aqueous Solution *RSC Advances* **2012**, *2*, 2666-2670.

(241) Chen, Y.; Li, S.; Huang, L.; Pan, D. Green and Facile Synthesis of Water-Soluble Cu-In-S/ZnS Core/Shell Quantum Dots *Inorganic Chemistry* **2013**, *52*, 7819-7821.

(242) Jiang, T.; Song, J.; Wang, H.; Ye, X.; Wang, H.; Zhang, W.; Yang, M.; Xia, R.; Zhu, L.; Xu, X. Aqueous Synthesis of Color Tunable Cu Doped Zn-In-S/ZnS Nanoparticles in the

Whole Visible Region for Cellular Imaging *Journal of Materials Chemistry B* **2015**, *3*, 2402-2410.

(243) Gabka, G.; Bujak, P.; Giedyk, K.; Kotwica, K.; Ostrowski, A.; Malinowska, K.; Lisowski, W.; Sobczak, J. W.; Pron, A. Ligand Exchange in Quaternary Alloyed Nanocrystals - A Spectroscopic Study *Physical Chemistry Chemical Physics* **2014**, *16*, 23082-23088.

(244) Permadi, A.; Fahmi, M. Z.; Chen, J.-K.; Chang, J.-Y.; Cheng, C.-Y.; Wang, G.-Q.; Ou, K.-L. Preparation of Poly(Ethylene Glycol) Methacrylate Coated $CuInS_2$/ZnS Quantum Dots and Their Use in Cell Staining *RSC Advances* **2012**, *2*, 6018-6022.

(245) Liu, H.; Gu, C.; Xiong, W.; Zhang, M. A Sensitive Hydrogen Peroxide Biosensor Using Ultra-Small $CuInS_2$ Nanocrystals as Peroxidase Mimics *Sensors and Actuators B - Chemical* **2015**, *209*, 670-676.

(246) Liu, S. Y.; Shi, F. P.; Zhao, X. J.; Chen, L.; Su, X. G. 3-Aminophenyl Boronic Acid-Functionalized $CuInS_2$ Quantum Dots as a Near-Infrared Fluorescence Probe for the Determination of Dopamine *Biosensors & Bioelectronics* **2013**, *47*, 379-384.

(247) Liu, Z. P.; Liu, L. L.; Sun, M. H.; Su, X. G. A Novel and Convenient Near-Infrared Fluorescence "Turn Off-On" Nanosensor for Detection of Glucose and Fluoride Anions *Biosensors & Bioelectronics* **2015**, *65*, 145-151.

(248) Liao, S.; Huang, Y.; Zuo, J.; Yan, Z. The Interaction of $CuInS_2$/ZnS/TGA Quantum Dots with Tyrosine Kinase Inhibitor and Its Application *Luminescence* **2015**, *30*, 362-370.

(249) Lin, Z.; Pan, D.; Hu, T.; Liu, Z.; Su, X. A Near-Infrared Fluorescent Bioassay for Thrombin Using Aptamer-Modified $CuInS_2$ Quantum Dots *Microchimica Acta* **2015**, *182*, 1933-1939.

(250) Yan, X.; Li, H.; Yan, Y.; Su, X. Selective Detection of Parathion-Methyl Based on Near-Infrared $CuInS_2$ Quantum Dots *Food Chemistry* **2015**, *173*, 179-184.

(251) Liu, S.; Shi, F.; Chen, L.; Su, X. Dopamine Functionalized $CuInS_2$ Quantum Dots as a Fluorescence Probe for Urea *Sensors and Actuators B - Chemical* **2014**, *191*, 246-251.

(252) Liu, Z.; Ma, Q.; Wang, X.; Lin, Z.; Zhang, H.; Liu, L.; Su, X. A Novel Fluorescent Nanosensor for Detection of Heparin and Heparinase Based on $CuInS_2$ Quantum Dots *Biosensors & Bioelectronics* **2014**, *54*, 617-622.

(253) Demillo, V. G.; Liao, M.; Zhu, X.; Redelman, D.; Publicover, N. G.; Hunter, K. W., Jr. Fabrication of $MnFe_2O_4$-$CuInS_2$/ZnS Magnetofluorescent Nanocomposites and Their Characterization *Colloids and Surfaces A - Physicochemical and Engineering Aspects* **2015**, *464*, 134-142.

(254) Rao, P.; Yao, W.; Li, Z.; Kong, L.; Zhang, W.; Li, L. Highly Stable $CuInS_2$@ZnS:Al Core@Shell Quantum Dots: The Role of Aluminium Self-Passivation *Chemical Communications* **2015**, *51*, 8757-8760.

(255) Song, W.-S.; Jang, E.-P.; Kim, J.-H.; Jang, H. S.; Yang, H. Unique Oxide Overcoating of $CuInS_2$/ZnS Core/Shell Quantum Dots with $ZnGa_2O_4$ for Fabrication of White Light-Emitting Diode with Improved Operational Stability *Journal of Nanoparticle Research* **2013**, *15*, 1-10.

(256) Song, W.-S.; Kim, J.-H.; Yang, H. Silica-Embedded Quantum Dots as Downconverters of Light-Emitting Diode and Effect of Silica on Device Operational Stability *Materials Letters* **2013**, *111*, 104-107.

(257) Chen, C.-W.; Wu, D.-Y.; Chan, Y.-C.; Lin, C. C.; Chung, P.-H.; Hsiao, M.; Liu, R.-S. Evaluations of the Chemical Stability and Cytotoxicity of $CuInS_2$ and $CuInS_2$/ZnS Core/Shell Quantum Dots *Journal of Physical Chemistry C* **2015**, *119*, 2852-2860.

(258) Howes, P. D.; Chandrawati, R.; Stevens, M. M. Colloidal Nanoparticles as Advanced Biological Sensors *Science* **2014**, *346*, 1247390.

(259) Silvester, E. J.; Healy, T. W.; Grieser, F.; Sexton, B. A. Hydrothermal Preparation and Characterization of Optically Transparent Colloidal Chalcopyrite ($CuFeS_2$) *Langmuir* **1991**, *7*, 19-22.

(260) Hu, J.; Lu, Q.; Deng, B.; Tang, K.; Qian, Y.; Li, Y.; Zhou, G.; Liu, X. A Hydrothermal Reaction to Synthesize $CuFeS_2$ Nanorods *Inorganic Chemistry Communications* **1999**, *2*, 569-571.

(261) Austin, I. G.; Goodman, C. H. L.; Pengelly, A. E. New Semiconductors with the Chalcopyrite Structure *Journal of the Electrochemical Society* **1956**, *103*, 609-610.

(262) Sato, K.; Harada, Y.; Taguchi, M.; Shin, S.; Fujimori, A. Characterization of Fe 3d States in $CuFeS_2$ by Resonant X-ray Emission Spectroscopy *physica status solidi (a)* **2009**, *206*, 1096-1100.

(263) Tsujii, N.; Mori, T.; Isoda, Y. Phase Stability and Thermoelectric Propertiesof $CuFeS_2$-Based Magnetic Semiconductor *Journal of Electronic Materials* **2014**, *43*, 2371-2375.

(264) Bhattacharyya, B.; Pandey, A. $CuFeS_2$ Quantum Dots and Highly Luminescent $CuFeS_2$ Based Core/Shell Structures: Synthesis, Tunability, and Photophysics *Journal of the American Chemical Society* **2016**, *138*, 10207-10213.

(265) Ghosh, S.; Avellini, T.; Petrelli, A.; Kriegel, I.; Gaspari, R.; Almeida, G.; Bertoni, G.; Cavalli, A.; Scotognella, F.; Pellegrino, T.; et al. Colloidal $CuFeS_2$ Nanocrystals: Intermediate Fe d-Band Leads to High Photothermal Conversion Efficiency *Chemistry of Materials* **2016**, *28*, 4848-4858.

(266) Disale, S. D.; Garje, S. S. A Convenient Synthesis of Nanocrystalline Chalcopyrite, $CuFeS_2$ Using Single-Source Precursors *Applied Organometallic Chemistry* **2009**, *23*, 492-497.

(267) Wang, Y.-H. A.; Bao, N.; Gupta, A. Shape-Controlled Synthesis of Semiconducting $CuFeS_2$ Nanocrystals *Solid State Sciences* **2010**, *12*, 387-390.

(268) Kumar, P.; Uma, S.; Nagarajan, R. Precursor Driven One Pot Synthesis of Wurtzite and Chalcopyrite $CuFeS_2$ *Chemical Communications* **2013**, *49*, 7316-7318.

(269) Liang, D.; Ma, R.; Jiao, S.; Pang, G.; Feng, S. A Facile Synthetic Approach for Copper Iron Sulfide Nanocrystals with Enhanced Thermoelectric Performance *Nanoscale* **2012**, *4*, 6265-6268.

(270) Gabka, G.; Bujak, P.; Zukrowski, J.; Zabost, D.; Kotwica, K.; Malinowska, K.; Ostrowski, A.; Wielgus, I.; Lisowski, W.; Sobczak, J. W.; et al. Non-Injection Synthesis of Monodisperse Cu-Fe-S Nanocrystals and Their Size Dependent Properties *Physical Chemistry Chemical Physics* **2016**, *18*, 15091-15101.

(271) Boon, J. W. The Crystal Structure of Chalcopyrite ($CuFeS_2$) and $AgFeS_2$: The Permutoidic Reactions $KFeS_2 \rightarrow CuFeS_2$ and $KFeS_2 \rightarrow AgFeS_2$ *Recueil des Travaux Chimiques des Pays-Bas* **1944**, *63*, 69-80.

(272) Shen, X.; Hernández-Pagan, E. A.; Zhou, W.; Puzyrev, Y. S.; Idrobo, J.-C.; Macdonald, J. E.; Pennycook, S. J.; Pantelides, S. T. Interlaced Crystals Having a Perfect Bravais Lattice and Complex Chemical Order Revealed by Real-Space Crystallography *Nature Communications* **2014**, *5*, 1-6.

(273) Boekema, C.; Krupski, A. M.; Varasteh, M.; Parvin, K.; van Til, F.; van der Woude, F.; Sawatzky, G. A. Cu and Fe Valence States in $CuFeS_2$ *Journal of Magnetism and Magnetic Materials* **2004**, *272–276, Part 1*, 559-561.

(274) Oguchi, T.; Sato, K.; Teranishi, T. Optical Reflectivity Spectrum of a $CuFeS_2$ Single Crystal *Journal of the Physical Society of Japan* **1980**, *48*, 123-128.

(275) Kvande, R.; Geerligs, L. J.; Coletti, G.; Arnberg, L.; Di Sabatino, M.; Øvrelid, E. J.; Swanson, C. C. Distribution of Iron in Multicrystalline Silicon Ingots *Journal of Applied Physics* **2008**, *104*, 064905.

(276) Xie, H.; Su, X.; Zheng, G.; Zhu, T.; Yin, K.; Yan, Y.; Uher, C.; Kanatzidis, M. G.; Tang, X. The Role of Zn in Chalcopyrite $CuFeS_2$: Enhanced Thermoelectric Properties of $Cu_{1-x}Zn_xFeS_2$ with In Situ Nanoprecipitates *Advanced Energy Materials* **2016**, 1601299.

(277) Ang, R.; Khan, A. U.; Tsujii, N.; Takai, K.; Nakamura, R.; Mori, T. Thermoelectricity Generation and Electron–Magnon Scattering in a Natural Chalcopyrite Mineral from a Deep-Sea Hydrothermal Vent *Angewandte Chemie International Edition* **2015**, *54*, 12909-12913.

(278) Li, J.; Tan, Q.; Li, J.-F. Synthesis and Property Evaluation of $CuFeS_{2-x}$ as Earth-Abundant and Environmentally-Friendly Thermoelectric Materials *Journal of Alloys and Compounds* **2013**, *551*, 143-149.

(279) Ding, W.; Wang, X.; Peng, H.; Hu, L. Electrochemical Performance of the Chalcopyrite $CuFeS_2$ as Cathode for Lithium Ion Battery *Materials Chemistry and Physics* **2013**, *137*, 872-876.

(280) Wu, Y.; Zhou, B.; Yang, C.; Liao, S.; Zhang, W.-H.; Li, C. $CuFeS_2$ Colloidal Nanocrystals as an Efficient Electrocatalyst for Dye Sensitized Solar Cells *Chemical Communications* **2016**, *52*, 11488-11491.

(281) Sciacca, B.; Yalcin, A. O.; Garnett, E. C. Transformation of Ag Nanowires into Semiconducting $AgFeS_2$ Nanowires *Journal of the American Chemical Society* **2015**, *137*, 4340-4343.

(282) Bindi, L.; Spry, P. G.; Pratesi, G. Lenaite from the Gies Gold-Silver Telluride Deposit, Judith Mountains, Montana, USA: Occurrence, Composition, and Crystal Structure *Canadian Mineralogist* **2006**, *44*, 207-212.

(283) Shay, J. L.; Tell, B.; Schiavone, L. M.; Kasper, H. M.; Thiel, F. Energy Bands of $AgInS_2$ in the Chalcopyrite and Orthorhombic Structures *Physical Review B* **1974**, *9*, 1719-1723.

(284) Hong, S. P.; Park, H. K.; Oh, J. H.; Yang, H.; Do, Y. R. Comparisons of the Structural and Optical Properties of o-$AgInS_2$, t-$AgInS_2$, and c-$AgIn_5S_8$ Nanocrystals and Their Solid-Solution Nanocrystals with ZnS *Journal of Materials Chemistry* **2012**, *22*, 18939-18949.

(285) Park, Y. J.; Oh, J. H.; Han, N. S.; Yoon, H. C.; Park, S. M.; Do, Y. R.; Song, J. K. Photoluminescence of Band Gap States in $AgInS_2$ Nanoparticles *Journal of Physical Chemistry C* **2014**, *118*, 25677-25683.

(286) Hamanaka, Y.; Ogawa, T.; Tsuzuki, M.; Kuzuya, T. Photoluminescence Properties and Its Origin of $AgInS_2$ Quantum Dots with Chalcopyrite Structure *Journal of Physical Chemistry C* **2011**, *115*, 1786-1792.

(287) Mao, B. D.; Chuang, C. H.; Wang, J. W.; Burda, C. Synthesis and Photophysical Properties of Ternary I-III-VI $AgInS_2$ Nanocrystals: Intrinsic versus Surface States *Journal of Physical Chemistry C* **2011**, *115*, 8945-8954.

(288) Gasanly, N. M.; Serpengüzel, A.; Aydinli, A.; Gürlü, O.; Yilmaz, I. Donor-Acceptor Pair Recombination in $AgIn_5S_8$ Single Crystals *Journal of Applied Physics* **1999**, *85*, 3198-3201.

(289) Gong, G.; Liu, Y.; Mao, B.; Wang, B.; Tan, L.; Li, D.; Liu, Y.; Shi, W. Mechanism Study on the Photocatalytic Efficiency Enhancement of MoS_2 Modified Zn-$AgIn_5S_8$ Quantum Dots *RSC Advances* **2016**, *6*, 99023-99033.

(290) Li, K.; Chai, B.; Peng, T.; Mao, J.; Zan, L. Preparation of $AgIn_5S_8/TiO_2$ Heterojunction Nanocomposite and Its Enhanced Photocatalytic H_2 Production Property under Visible Light *ACS Catalysis* **2013**, *3*, 170-177.

(291) Song, J.; Jiang, T.; Guo, T.; Liu, L.; Wang, H.; Xia, T.; Zhang, W.; Ye, X.; Yang, M.; Zhu, L.; et al. Facile Synthesis of Water-Soluble Zn-Doped $AgIn_5S_8$/ZnS Core/Shell Fluorescent Nanocrystals and Their Biological Application *Inorganic Chemistry* **2015**, *54*, 1627-1633.

(292) Leach, A. D. P.; Macdonald, J. E. Optoelectronic Properties of $CuInS_2$ Nanocrystals and Their Origin *The Journal of Physical Chemistry Letters* **2016**, *7*, 572-583.

(293) El-Sayed, M. A. Small Is Different: Shape-, Size-, and Composition-Dependent Properties of Some Colloidal Semiconductor Nanocrystals *Accounts of Chemical Research* **2004**, *37*, 326-333.

(294) Eychmuller, A. Structure and Photophysics of Semiconductor Nanocrystals *Journal of Physical Chemistry B* **2000**, *104*, 6514-6528.

(295) Kim, M. R.; Xu, Z.; Chen, G.; Ma, D. Semiconductor and Metallic Core-Shell Nanostructures: Synthesis and Applications in Solar Cells and Catalysis *Chemistry - A European Journal* **2014**, *20*, 11256-11275.

(296) Parak, W. J.; Gerion, D.; Pellegrino, T.; Zanchet, D.; Micheel, C.; Williams, S. C.; Boudreau, R.; Le Gros, M. A.; Larabell, C. A.; Alivisatos, A. P. Biological Applications of Colloidal Nanocrystals *Nanotechnology* **2003**, *14*, R15-R27.

(297) Chng, L. L.; Erathodiyil, N.; Ying, J. Y. Nanostructured Catalysts for Organic Transformations *Accounts of Chemical Research* **2013**, *46*, 1825-1837.

(298) Vaneski, A.; Schneider, J.; Susha, A. S.; Rogach, A. L. Colloidal Hybrid Heterostructures Based on II-VI Semiconductor Nanocrystals for Photocatalytic Hydrogen Generation *Journal of Photochemistry and Photobiology C-Photochemistry Reviews* **2014**, *19*, 52-61.

(299) Esteves, A. C. C.; Trindade, T. Synthetic Studies on II/VI Semiconductor Quantum Dots *Current Opinion in Solid State & Materials Science* **2002**, *6*, 347-353.

(300) Hullavarad, N. V.; Hullavarad, S. S.; Karulkar, P. C. Cadmium Sulphide (CdS) Nanotechnology: Synthesis and Applications *Journal of Nanoscience and Nanotechnology* **2008**, *8*, 3272-3299.

(301) Rzigalinski, B. A.; Strobl, J. S. Cadmium-Containing Nanoparticles: Perspectives on Pharmacology and Toxicology of Quantum Dots *Toxicology and Applied Pharmacology* **2009**, *238*, 280-288.

(302) Osterloh, F. E. Inorganic Materials as Catalysts for Photochemical Splitting of Water *Chemistry of Materials* **2008**, *20*, 35-54.

(303) Vaneski, A.; Susha, A. S.; Rodriguez-Fernandez, J.; Berr, M.; Jaeckel, F.; Feldmann, J.; Rogach, A. L. Hybrid Colloidal Heterostructures of Anisotropic Semiconductor Nanocrystals Decorated with Noble Metals: Synthesis and Function *Advanced Functional Materials* **2011**, *21*, 1547-1556.

(304) Lu, X. T.; Zhuang, Z. B.; Peng, Q.; Li, Y. D. Controlled Synthesis of Wurtzite $CuInS_2$ Nanocrystals and Their Side-By-Side Nanorod Assemblies *CrystEngComm* **2011**, *13*, 4039-4045.

(305) Klenk, R.; Klaer, J.; Scheer, R.; Lux-Steiner, M. C.; Luck, I.; Meyer, N.; Ruhle, U. Solar Cells Based on $CuInS_2$ - an Overview *Thin Solid Films* **2005**, *480*, 509-514.

(306) Sheng, X.; Wang, L.; Luo, Y. P.; Yang, D. R. Synthesis of Hexagonal Structured Wurtzite and Chalcopyrite $CuInS_2$ via a Simple Solution Route *Nanoscale Research Letters* **2011**, *6*, 1-6.

(307) Xia, C.; Cao, L.; Liu, W.; Su, G.; Gao, R.; Qu, H.; Shi, L.; He, G. One-Step Synthesis of Near-Infrared Emitting and Size Tunable $CuInS_2$ Semiconductor Nanocrystals by Adjusting Kinetic Variables *CrystEngComm* **2014**, *16*, 7469-7477.

(308) Coughlan, C.; Singh, A.; Ryan, K. M. Systematic Study into the Synthesis and Shape Development in Colloidal $CuIn_xGa_{1-x}S_2$ Nanocrystals *Chemistry of Materials* **2013**, *25*, 653-661.

(309) Shemesh, Y.; Macdonald, J. E.; Menagen, G.; Banin, U. Synthesis and Photocatalytic Properties of a Family of CdS-PdX Hybrid Nanoparticles *Angewandte Chemie-International Edition* **2011**, *50*, 1185-1189.

(310) Kruszynska, M.; Borchert, H.; Parisi, J.; Kolny-Olesiak, J. Investigations of Solvents and Various Sulfur Sources Influence on the Shape-Controlled Synthesis of $CuInS_2$ Nanocrystals *Journal of Nanoparticle Research* **2011**, *13*, 5815-5824.

(311) Tomic, S.; Bernasconi, L.; Searle, B. G.; Harrison, N. M. Electronic and Optical Structure of Wurtzite $CuInS_2$ *Journal of Physical Chemistry C* **2014**, *118*, 14478-14484.

(312) Chang, J.-Y.; Cheng, C.-Y. Facile One-Pot Synthesis of Copper Sulfide-Metal Chalcogenide Anisotropic Heteronanostructures in a Noncoordinating Solvent *Chemical Communications* **2011**, *47*, 9089-9091.

(313) Han, W.; Yi, L.; Zhao, N.; Tang, A.; Gao, M.; Tang, Z. Synthesis and Shape-Tailoring of Copper Sulfide/Indium Sulfide-Based Nanocrystals *Journal of the American Chemical Society* **2008**, *130*, 13152-13161.

(314) Koo, B.; Patel, R. N.; Korgel, B. A. Wurtzite-Chalcopyrite Polytypism in $CuInS_2$ Nanodisks *Chemistry of Materials* **2009**, *21*, 1962-1966.

(315) Liu, Z. P.; Wang, L. L.; Hao, Q. Y.; Wang, D. K.; Tang, K. B.; Zuo, M.; Yang, Q. Facile Synthesis and Characterization of $CuInS_2$ Nanocrystals with Different Structures and Shapes *CrystEngComm* **2013**, *15*, 7192-7198.

(316) Komarala, V. K.; Xie, C.; Wang, Y.; Xu, J.; Xiao, M. Time-Resolved Photoluminescence Properties of $CuInS_2$/ZnS Nanocrystals: Influence of Intrinsic Defects and External Impurities *Journal of Applied Physics* **2012**, *111*, 1-4.

(317) Jones, M.; Scholes, G. D. On the Use of Time-Resolved Photoluminescence as a Probe of Nanocrystal Photoexcitation Dynamics *Journal of Materials Chemistry* **2010**, *20*, 3533-3538.

(318) Zhang, W.; Zhong, X. Facile Synthesis of ZnS-$CuInS_2$-Alloyed Nanocrystals for a Color-Tunable Fluorchrome and Photocatalyst *Inorganic Chemistry* **2011**, *50*, 4065-4072.

(319) Wuensch, B. J.; Buerger, M. J. The Crystal Structure of Chalcocite, Cu_2S **1963**, *Paper 1*, 164-170.

(320) Rietveld, H. M. A Profile Refinement Method For Nuclear and Magnetic Structures *Journal of Applied Crystallography* **1969**, *2*, 65.

(321) Larson, A. C.; Von Dreele, R. B. General Structure Analysis System (GSAS) *Los Alamos National Laboratory Report LAUR 86-748* **1994**, 1-224.

(322) Toby, B. H. EXPGUI, a Graphical User Interface for GSAS *Journal of Applied Crystallography* **2001**, *34*, 210-213.

(323) Rurack, K.; Spieles, M. Fluorescence Quantum Yields of a Series of Red and Near-Infrared Dyes Emitting at 600-1000 nm *Analytical Chemistry* **2011**, *83*, 1232-1242.

(324) Wojdyr, M. Fityk: A General-Purpose Peak Fitting Program *Journal of Applied Crystallography* **2010**, *43*, 1126-1128.

(325) Toby, B. H. R Factors in Rietveld Analysis: How Good is Good Enough? *Powder Diffraction* **2006**, *21*, 67-70.

(326) Lu, X.; Zhuang, Z.; Peng, Q.; Li, Y. Wurtzite Cu_2ZnSnS_4 Nanocrystals: A Novel Quaternary Semiconductor *Chemical Communications* **2011**, *47*, 3141-3143.

(327) Tauc, J.; Grigorov.R; Vancu, A. Optical Properties and Electronic Structure of Amorphous Germanium *Journal of the Physical Society of Japan* **1966**, *S 21*, 123.

(328) Weibel, A.; Bouchet, R.; Boulc'h, F.; Knauth, P. The Big Problem of Small Particles: A Comparison of Methods for Determination of Particle Size in Nanocrystalline Anatase Powders *Chemistry of Materials* **2005**, *17*, 2378-2385.

(329) Ge, M.; Guo, C.; Liu, L.; Zhang, B.; Zhou, Z. Synthesis of $CuInS_2$ Microspheres Using In_2S_3 Microspheres as Templates *Australian Journal of Chemistry* **2009**, *62*, 1690-1694.

(330) Kim, Y. H.; Lee, J. H.; Shin, D.-W.; Park, S. M.; Moon, J. S.; Nam, J. G.; Yoo, B. Synthesis of Shape-Controlled Beta-In_2S_3 Nanotubes Through Oriented Attachment of Nanoparticles *Chemical Communications* **2010**, *46*, 2292-2294.

(331) Xing, Y.; Zhang, H.; Song, S.; Feng, J.; Lei, Y.; Zhao, L.; Li, M. Hydrothermal Synthesis and Photoluminescent Properties of Stacked Indium Sulfide Superstructures *Chemical Communications* **2008**, 1476-1478.

(332) Kino, T.; Kuzuya, T.; Itoh, K.; Sumiyama, K.; Wakamatsu, T.; Ichidate, M. Synthesis of Chalcopyrite Nanoparticles via Thermal Decomposition of Metal-Thiolate *Materials Transactions* **2008**, *49*, 435-438.

(333) Turo, M. J.; Macdonald, J. E. Crystal-Bound vs. Surface-Bound Thiols on Nanocrystals *ACS Nano* **2014**, *8*, 10205-10213.

(334) Bryks, W.; Wette, M.; Velez, N.; Hsu, S.-W.; Tao, A. R. Supramolecular Precursors for the Synthesis of Anisotropic Cu_2S Nanocrystals *Journal of the American Chemical Society* **2014**, *136*, 6175-6178.

(335) Saldanha, P. L.; Brescia, R.; Prato, M.; Li, H.; Povia, M.; Manna, L.; Lesnyak, V. Generalized One-Pot Synthesis of Copper Sulfide, Selenide-Sulfide, and Telluride-Sulfide Nanoparticles *Chemistry of Materials* **2014**, *26*, 1442-1449.

(336) Larsen, T. H.; Sigman, M.; Ghezelbash, A.; Doty, R. C.; Korgel, B. A. Solventless Synthesis of Copper Sulfide Nanorods by Thermolysis of a Single Source Thiolate-Derived Precursor *Journal of the American Chemical Society* **2003**, *125*, 5638-5639.

(337) Kruszynska, M.; Borchert, H.; Bachmatiuk, A.; Rümmeli, M. H.; Büchner, B.; Parisi, J.; Kolny-Olesiak, J. Size and Shape Control of Colloidal Copper(I) Sulfide Nanorods *ACS Nano* **2012**, *6*, 5889-5896.

(338) Ning, J. J.; Men, K. K.; Xiao, G. J.; Zhao, L. Y.; Wang, L.; Liu, B. B.; Zou, B. Synthesis, Optical Properties and Growth Process of In_2S_3 Nanoparticles *Journal of Colloid and Interface Science* **2010**, *347*, 172-176.

(339) Aldakov, D.; Lefrancois, A.; Reiss, P. Ternary and Quaternary Metal Chalcogenide Nanocrystals: Synthesis, Properties and Applications *Journal of Materials Chemistry C* **2013**, *1*, 3756-3776.

(340) Hofhuis, J.; Schoonman, J.; Goossens, A. Elucidation of the Excited-State Dynamics in $CuInS_2$ Thin Films *Journal of Physical Chemistry C* **2008**, *112*, 15052-15059.

(341) Knowles, K. E.; Nelson, H. D.; Kilburn, T. B.; Gamelin, D. R. Singlet–Triplet Splittings in the Luminescent Excited States of Colloidal Cu^+:CdSe, Cu^+:InP, and $CuInS_2$ Nanocrystals: Charge-Transfer Configurations and Self-Trapped Excitons *Journal of the American Chemical Society* **2015**, *137*, 13138-13147.

(342) Uehara, M.; Watanabe, K.; Tajiri, Y.; Nakamura, H.; Maeda, H. Synthesis of $CuInS_2$ Fluorescent Nanocrystals and Enhancement of Fluorescence by Controlling Crystal Defect *Journal of Chemical Physics* **2008**, *129*, 1-6.

(343) Zhong, X.; Feng, Y.; Knoll, W.; Han, M. Alloyed $Zn_xCd_{1-x}S$ Nanocrystals with Highly Narrow Luminescence Spectral Width *Journal of the American Chemical Society* **2003**, *125*, 13559-13563.

(344) Dierick, R.; Van den Broeck, F.; De Nolf, K.; Zhao, Q.; Vantomme, A.; Martins, J. C.; Hens, Z. Surface Chemistry of $CuInS_2$ Colloidal Nanocrystals, Tight Binding of L-Type Ligands *Chemistry of Materials* **2014**, *26*, 5950-5957.

(345) Heyd, J.; Scuseria, G. E.; Ernzerhof, M. Hybrid Functionals Based on a Screened Coulomb Potential *Journal of Chemical Physics* **2003**, *118*, 8207-8215.

(346) Heyd, J.; Scuseria, G. E.; Ernzerhof, M. Hybrid Functionals Based on a Screened Coulomb Potential (vol 118, pg 8207, 2003) *Journal of Chemical Physics* **2006**, *124*, 1.

(347) Chen, H.; Wang, C.-Y.; Wang, J.-T.; Hu, X.-P.; Zhou, S.-X. First-Principles Study of Point Defects in Solar Cell Semiconductor $CuInS_2$ *Journal of Applied Physics* **2012**, *112*, 1-6.

(348) Kresse, G.; Joubert, D. From Ultrasoft Pseudopotentials to the Projector Augmented-Wave Method *Physical Review B* **1999**, *59*, 1758-1775.

(349) Kresse, G.; Furthmuller, J. Efficient Iterative Schemes for Ab Initio Total-Energy Calculations Using a Plane-Wave Basis Set *Physical Review B* **1996**, *54*, 11169-11186.

(350) Shen, X.; Dhar, S.; Pantelides, S. T. Atomic Origin of High-Temperature Electron Trapping in Metal-Oxide-Semiconductor Devices *Applied Physics Letters* **2015**, *106*, 1-3.

(351) Castleton, C. W. M.; Hoglund, A.; Mirbt, S. Density Functional Theory Calculations of Defect Energies Using Supercells *Modelling and Simulation in Materials Science and Engineering* **2009**, *17*, 1-12.

(352) van der Stam, W.; Bladt, E.; Rabouw, F. T.; Bals, S.; de Mello Donega, C. Near-Infrared Emitting $CuInSe_2/CuInS_2$ Dot Core/Rod Shell Heteronanorods by Sequential Cation Exchange *ACS Nano* **2015**, *9*, 11430–11438.

(353) Ogawa, T.; Kuzuya, T.; Hamanaka, Y.; Sumiyama, K. Synthesis of Ag-In Binary Sulfide Nanoparticles-Structural Tuning and their Photoluminescence Properties *Journal of Materials Chemistry* **2010**, *20*, 2226-2231.

(354) Torimoto, T.; Ogawa, S.; Adachi, T.; Kameyama, T.; Okazaki, K.-I.; Shibayama, T.; Kudo, A.; Kuwabata, S. Remarkable Photoluminescence Enhancement of ZnS-$AgInS_2$ Solid Solution Nanoparticles by Post-Synthesis Treatments *Chemical Communications* **2010**, *46*, 2082-2084.

(355) Rao, M. J.; Shibata, T.; Chattopadhyay, S.; Nag, A. Origin of Photoluminescence and XAFS Study of $(ZnS)_{1-x}(AgInS_2)_x$ Nanocrystals *Journal of Physical Chemistry Letters* **2014**, *5*, 167-173.

(356) Du, Y.; Xu, B.; Fu, T.; Cai, M.; Li, F.; Zhang, Y.; Wang, Q. Near-Infrared Photoluminescent Ag_2S Quantum Dots from a Single Source Precursor *Journal of the American Chemical Society* **2010**, *132*, 1470-1471.

(357) Mir, W. J.; Swarnkar, A.; Sharma, R.; Katti, A.; Adarsh, K. V.; Nag, A. Origin of Unusual Excitonic Absorption and Emission from Colloidal Ag_2S Nanocrystals: Ultrafast Photophysics and Solar Cell *The Journal of Physical Chemistry Letters* **2015**, *6*, 3915-3922.

(358) Costi, R.; Saunders, A. E.; Banin, U. Colloidal Hybrid Nanostructures: A New Type of Functional Materials *Angewandte Chemie-International Edition* **2010**, *49*, 4878-4897.

(359) Shen, S.; Wang, Q. Rational Tuning the Optical Properties of Metal Sulfide Nanocrystals and Their Applications *Chemistry of Materials* **2013**, *25*, 1166-1178.

(360) Wang, X.; Swihart, M. T. Controlling the Size, Shape, Phase, Band Gap, and Localized Surface Plasmon Resonance of $Cu_{2-x}S$ and Cu_xIn_yS Nanocrystals *Chemistry of Materials* **2015**, *27*, 1786-1791.

(361) Motl, N. E.; Bondi, J. F.; Schaak, R. E. Synthesis of Colloidal Au-Cu_2S Heterodimers via Chemically Triggered Phase Segregation of AuCu Nanoparticles *Chemistry of Materials* **2012**, *24*, 1552-1554.

(362) Macdonald, J. E.; Bar Sadan, M.; Houben, L.; Popov, I.; Banin, U. Hybrid Nanoscale Inorganic Cages *Nature Materials* **2010**, *9*, 810-815.

(363) Dilsaver, P. S.; Reichert, M. D.; Hallmark, B. L.; Thompson, M. J.; Vela, J. Cu_2ZnSnS_4-Au Heterostructures: Toward Greener Chalcogenide-Based Photocatalysts *Journal of Physical Chemistry C* **2014**, *118*, 21226-21234.

(364) Buck, M. R.; Bondi, J. F.; Schaak, R. E. A Total-Synthesis Framework for the Construction of High-Order Colloidal Hybrid Nanoparticles *Nature Chemistry* **2012**, *4*, 37-44.

(365) Amirav, L.; Alivisatos, A. P. Photocatalytic Hydrogen Production with Tunable Nanorod Heterostructures *Journal of Physical Chemistry Letters* **2010**, *1*, 1051-1054.

(366) Bao, N.; Shen, L.; Takata, T.; Domen, K. Self-Templated Synthesis of Nanoporous CdS Nanostructures for Highly Efficient Photocatalytic Hydrogen Production Under Visible Light *Chemistry of Materials* **2008**, *20*, 110-117.

(367) Berr, M.; Vaneski, A.; Susha, A. S.; Rodriguez-Fernandez, J.; Doblinger, M.; Jackel, F.; Rogach, A. L.; Feldmann, J. Colloidal CdS Nanorods Decorated with Subnanometer Sized Pt Clusters for Photocatalytic Hydrogen Generation *Applied Physics Letters* **2010**, *97*, 093108.

(368) Guo, S.; Zhang, S.; Sun, S. Tuning Nanoparticle Catalysis for the Oxygen Reduction Reaction *Angewandte Chemie-International Edition* **2013**, *52*, 8526-8544.

(369) Mieszawska, A. J.; Mulder, W. J. M.; Fayad, Z. A.; Cormode, D. P. Multifunctional Gold Nanoparticles for Diagnosis and Therapy of Disease *Molecular Pharmaceutics* **2013**, *10*, 831-847.

(370) Thakor, A. S.; Jokerst, J.; Zavaleta, C.; Massoud, T. F.; Gambhir, S. S. Gold Nanoparticles: A Revival in Precious Metal Administration to Patients *Nano Letters* **2011**, *11*, 4029-4036.

(371) Wang, W.; Feng, W.; Ding, T.; Yang, Q. Phosphine-Free Synthesis and Characterization of Cubic-Phase Cu_2SnTe_3 Nanocrystals with Optical and Optoelectronic Properties *Chemistry of Materials* **2015**, *27*, 6181-6184.

(372) Lee, J.-S.; Bodnarchuk, M. I.; Shevchenko, E. V.; Talapin, D. V. "Magnet-in-the-Semiconductor" FePt-PbS and FePt-PbSe Nanostructures: Magnetic Properties, Charge Transport, and Magnetoresistance *Journal of the American Chemical Society* **2010**, *132*, 6382-6391.

(373) Baaziz, W.; Pichon, B. P.; Liu, Y.; Greneche, J.-M.; Ulhaq-Bouillet, C.; Terrier, E.; Bergeard, N.; Halte, V.; Boeglin, C.; Choueikani, F.; et al. Tuning of Synthesis Conditions by Thermal Decomposition Toward Core-Shell $Co_xFe_{1-x}O@Co_yFe_{3-y}O_4$ and $CoFe_2O_4$ Nanoparticles with Spherical and Cubic Shapes *Chemistry of Materials* **2014**, *26*, 5063-5073.

(374) Mourdikoudis, S.; Liz-Marzan, L. M. Oleylamine in Nanoparticle Synthesis *Chemistry of Materials* **2013**, *25*, 1465-1476.

(375) Shevchenko, E. V.; Talapin, D. V.; Schnablegger, H.; Kornowski, A.; Festin, O.; Svedlindh, P.; Haase, M.; Weller, H. Study of Nucleation and Growth in the Organometallic Synthesis of Magnetic Alloy Nanocrystals: The Role of Nucleation Rate in Size Control of $CoPt_3$ Nanocrystals *Journal of the American Chemical Society* **2003**, *125*, 9090-9101.

(376) Yang, Z.; Klabunde, K. J. Synthesis of Nearly Monodisperse Palladium (Pd) Nanoparticles by Using Oleylamine and Trioctylphosphine Mixed Ligands *Journal of Organometallic Chemistry* **2009**, *694*, 1016-1021.

(377) Ortiz, N.; Skrabalak, S. E. Manipulating Local Ligand Environments for the Controlled Nucleation of Metal Nanoparticles and Their Assembly into Nanodendrites *Angewandte Chemie-International Edition* **2012**, *51*, 11757-11761.

(378) Patra, B. K.; Shit, A.; Guria, A. K.; Sarkar, S.; Prusty, G.; Pradhan, N. Coincident Site Epitaxy at the Junction of Au-Cu_2ZnSnS_4 Heteronanostructures *Chemistry of Materials* **2015**, *27*, 650-657.

(379) Howard, B. C. Development of a Novel Synthesis of Quantum-Confined, Wurtzite $CuInS_2$ Nanoparticles and Subsequent Characterization *Master's Thesis*, Vanderbilt University, Nashville, TN **2014**.

(380) Supran, G. J.; Shirasaki, Y.; Song, K. W.; Caruge, J. M.; Kazlas, P. T.; Coe-Sullivan, S.; Andrew, T. L.; Bawendi, M. G.; Bulovic, V. QLEDs for Displays and Solid-State Lighting *MRS Bulletin* **2013**, *38*, 703-711.

(381) Murray, C. B.; Norris, D. J.; Bawendi, M. G. Synthesis and Characterization of Nearly Monodisperse CdE (E = S, Se, Te) Semiconductor Nanocrystallites *Journal of the American Chemical Society* **1993**, *115*, 8706-8715.

(382) Fu, H. Y.; Tsang, S. W. Infrared Colloidal Lead Chalcogenide Nanocrystals: Synthesis, Properties, and Photovoltaic Applications *Nanoscale* **2012**, *4*, 2187-2201.

(383) Steckel, J. S.; Yen, B. K. H.; Oertel, D. C.; Bawendi, M. G. On the Mechanism of Lead Chalcogenide Nanocrystal Formation *Journal of the American Chemical Society* **2006**, *128*, 13032-13033.

(384) Henckens, M. L. C. M.; van Ierland, E. C.; Driessen, P. P. J.; Worrell, E. Mineral Resources: Geological Scarcity, Market Price Trends, and Future Generations *Resources Policy* **2016**, *49*, 102-111.

(385) Choi, S. H.; An, K.; Kim, E. G.; Yu, J. H.; Kim, J. H.; Hyeon, T. Simple and Generalized Synthesis of Semiconducting Metal Sulfide Nanocrystals *Advanced Functional Materials* **2009**, *19*, 1645-1649.

(386) Binetti, E.; Striccoli, M.; Sibillano, T.; Giannini, C.; Brescia, R.; Falqui, A.; Comparelli, R.; Corricelli, M.; Tommasi, R.; Agostiano, A.; et al. Tuning Light Emission of PbS Nanocrystals from Infrared to Visible Range by Cation Exchange *Science and Technology of Advanced Materials* **2015**, *16*, 1-10.

(387) Kambara, T. Optical Properties of a Magnetic Semiconductor - Chalcopyrite CuFeS.II. Calculated Electronic Structures of $CuGaS_2$:Fe and $CuFeS_2$ *Journal of the Physical Society of Japan* **1974**, *36*, 1625-1635.

(388) Perdew, J. P.; Burke, K.; Ernzerhof, M. Generalized Gradient Approximation Made Simple *Physical Review Letters* **1996**, *77*, 3865-3868.

(389) Blöchl, P. E. Projector Augmented-Wave Method *Physical Review B* **1994**, *50*, 17953-17979.

(390) Monkhorst, H. J.; Pack, J. D. Special Points for Brillouin-Zone Integrations *Physical Review B* **1976**, *13*, 5188-5192.

(391) Dudarev, S. L.; Botton, G. A.; Savrasov, S. Y.; Humphreys, C. J.; Sutton, A. P. Electron-Energy-Loss Spectra and the Structural Stability of Nickel Oxide: An LSDA+U Study *Physical Review B* **1998**, *57*, 1505-1509.

(392) Gusain, M.; Kumar, P.; Nagarajan, R. Wurtzite $CuInS_2$: Solution Based One Pot Direct Synthesis and Its Doping Studies with Non-Magnetic Ga^{3+} and Magnetic Fe^{3+} Ions *RSC Advances* **2013**, *3*, 18863-18871.

(393) Wada, T.; Nakamura, S.; Maeda, T. Ternary and Multinary Cu-Chalcogenide Photovoltaic Materials from $CuInSe_2$ to Cu_2ZnSnS_4 and Other Compounds *Progress in Photovoltaics* **2012**, *20*, 520-525.

(394) Cheng, K. C.; Law, W. C.; Yong, K. T.; Nevins, J. S.; Watson, D. F.; Ho, H. P.; Prasad, P. N. Synthesis of Near-Infrared Silver-Indium-Sulfide ($AgInS_2$) Quantum Dots as Heavy-Metal Free Photosensitizer for Solar Cell Applications *Chemical Physics Letters* **2011**, *515*, 254-257.

(395) Hu, J. Q.; Deng, B.; Tang, K. B.; Wang, C. R.; Qian, Y. T. Preparation and Phase Control of Nanocrystalline Silver Indium Sulfides via a Hydrothermal Route *Journal of Materials Research* **2001**, *16*, 3411-3415.

(396) Wang, D. S.; Zheng, W.; Hao, C. H.; Peng, Q.; Li, Y. D. General Synthesis of I-III-VI_2 Ternary Semiconductor Nanocrystals *Chemical Communications* **2008**, 2556-2558.

(397) Bai, T. Y.; Xing, S. H.; Li, C. G.; Shi, Z.; Feng, S. H. Phase-Controlled Synthesis of Orthorhombic and Tetragonal $AgGaSe_2$ Nanocrystals with High Quality *Chemical Communications* **2016**, *52*, 8581-8584.

(398) Xu, L. C.; Wang, R. Z.; Liu, L. M.; Chen, Y. P.; Wei, X. L.; Yan, H.; Lau, W. M. Wurtzite-Type $CuInSe_2$ for High-Performance Solar Cell Absorber: Ab Initio Exploration of the New Phase Structure *Journal of Materials Chemistry* **2012**, *22*, 21662-21666.

(399) Teranishi, T.; Sato, K.; Kondo, K. i. Optical Properties of a Magnetic Semiconductor: Chalcopyrite $CuFeS_2$.: I. Absorption Spectra of $CuFeS_2$ and Fe-Doped $CuAlS_2$ and $CuGaS_2$ *Journal of the Physical Society of Japan* **1974**, *36*, 1618-1624.

(400) Bai, P. P.; Zheng, S. Q.; Chen, C. F.; Zhao, H. Investigation of the Iron-Sulfide Phase Transformation in Nanoscale *Crystal Growth & Design* **2014**, *14*, 4295-4302.

(401) Sadovnikov, S. I.; Gusev, A. I.; Rempel, A. A. Nonstoichiometry of Nanocrystalline Monoclinic Silver Sulfide *Physical Chemistry Chemical Physics* **2015**, *17*, 12466-12471.

(402) Delgado, G.; Mora, A. J.; Pineda, C.; Tinoco, T. Simultaneous Rietveld Refinement of Three Phases in the Ag-In-S Semiconducting System from X-ray Powder Diffraction *Materials Research Bulletin* **2001**, *36*, 2507-2517.

(403) Ng, M. T.; Boothroyd, C. B.; Vittal, J. J. One-Pot Synthesis of New-Phase $AgInSe_2$ Nanorods *Journal of the American Chemical Society* **2006**, *128*, 7118-7119.

(404) Thomson, J. W.; Nagashima, K.; Macdonald, P. M.; Ozin, G. A. From Sulfur−Amine Solutions to Metal Sulfide Nanocrystals: Peering into the Oleylamine−Sulfur Black Box *Journal of the American Chemical Society* **2011**, *133*, 5036-5041.

(405) Bartlett, P. D.; Cox, E. F.; Davis, R. E. Reactions of Elemental Sulfur. IV. Catalytic Effects in the Reaction of Sulfur with Triphenylphosphine *Journal of the American Chemical Society* **1961**, *83*, 103-109.

(406) Cho, N.; Li, F.; Turedi, B.; Sinatra, L.; Sarmah, S. P.; Parida, M. R.; Saidaminov, M. I.; Murali, B.; Burlakov, V. M.; Goriely, A.; et al. Pure Crystal Orientation and Anisotropic

Charge Transport in Large-Area Hybrid Perovskite Films *Nature Communications* **2016**, *7*, 1-11.

(407) Tanaka, M.; Hasegawa, M.; Takei, H. Growth and Anisotropic Physical Properties of $PdCoO_2$ Single Crystals *Journal of the Physical Society of Japan* **1996**, *65*, 3973-3977.

(408) He, W. D.; Osmulski, M. E.; Lin, J. H.; Koktysh, D. S.; McBride, J. R.; Park, J. H.; Dickerson, J. H. Remarkable Optical and Magnetic Properties of Ultra-Thin Europium Oxysulfide Nanorods *Journal of Materials Chemistry* **2012**, *22*, 16728-16731.

(409) Ibanez, M.; Luo, Z. S.; Genc, A.; Piveteau, L.; Ortega, S.; Cadavid, D.; Dobrozhan, O.; Liu, Y.; Nachtegaal, M.; Zebarjadi, M.; et al. High-Performance Thermoelectric Nanocomposites from Nanocrystal Building Blocks *Nature Communications* **2016**, *7*, 1-7.

(410) Meruga, J. M.; Cross, W. M.; May, P. S.; Luu, Q.; Crawford, G. A.; Kellar, J. J. Security Printing of Covert Quick Response Codes Using Upconverting Nanoparticle Inks *Nanotechnology* **2012**, *23*, 1-9.

(411) Dijksman, A. T. Spectroscopy of Colloidal Quantum Dots of Controlled Shape and Size *PhD Thesis*, L'Université Pierre et Marie Curie, Paris, France **2013**.

(412) Aharoni, A.; Oron, D.; Banin, U.; Rabani, E.; Jortner, J. Long-Range Electronic-to-Vibrational Energy Transfer from Nanocrystals to their Surrounding Matrix Environment *Physical Review Letters* **2008**, *100*, 057404.

(413) Kuzuya, T.; Yamamuro, S.; Hihara, T.; Sumiyama, K. Water-Free Solution Synthesis of Monodisperse Cu_2S Nanocrystals *Chemistry Letters* **2004**, *33*, 352-353.

(414) Bai, T.; Li, C.; Li, F.; Zhao, L.; Wang, Z.; Huang, H.; Chen, C.; Han, Y.; Shi, Z.; Feng, S. A Simple Solution-Phase Approach to Synthesize High Quality Ternary $AgInSe_2$ and Band Gap Tunable Quaternary $AgIn(S_{1-x}Se_x)_2$ Nanocrystals *Nanoscale* **2014**, *6*, 6782-6789.